University of Southern Queensland

Faculty of Engineering & Surveying

Initial Development of Ice Crystal Ice Accretion at Conditions Related to Turbofan Operation at High Altitude

A thesis submitted by

Khalid Hashim Saleh

in fulfilment of the requirements of

Doctor of Philosophy

2013

Abstract

Ice accretion on external surfaces of aircraft is a widely recognised problem, but more recently identified problem of ice crystal ice accretion within aero-engine compressors during flight through deep convection systems also represents a significant hazard and forms the motivation for the present work. The experimental studies targeting solid phase ice accretion are very limited due to the high wind tunnel facilities operational cost and safety concern for in-flight icing testing, which requires flight through severe weather conditions.

In this study, a small wind tunnel was established to simulate some of the conditions relevant to aircraft engine icing from ice crystals and explore the application of a model for the initiation of ice accretion. In this facility, liquid nitrogen was used to freeze liquid water droplets generated using an ultrasonic nozzle. The liquid nitrogen section reduces the droplet temperature to less than $-40\,^{\circ}\mathrm{C}$ and maintains this temperature for sufficient time to ensure complete freezing occurs. The particle diameters were controlled by the air and water pressure delivered to the ultrasonic nozzle and particle diameters around $50\,\mu\mathrm{m}$ were generated. The ice water content was also measured experimentally and it was found to be around $0.42\,\mathrm{g/m^3}$. A temperature controller was developed to keep the specimen surface temperature essentially constant and four specimen surface temperatures were tested: -9, -5, 0, and $5\,^{\circ}\mathrm{C}$.

The wind tunnel duct had a diameter of 70 mm and was operated at the relatively low flow speed of 6.5 m/s. A cylinder with diameter of 10 mm and flat plate surface with length of 3.6 cm and a leading edge diameter of 3 mm were used as the test specimens. A microscope video camera was used to visualise a small area on the specimen surface of

9×9 mm and record the initiation of the accretion process. The experimental data were analysed using image processing techniques, and different locations around the centre line of the test specimens in the vicinity of the stagnation point were investigated. Two regions with different roughness were used on both specimens with an average roughness (R_a) for the smooth side of 0.5 μm and 1.0 μm for the rough side, but no effect of the surface roughness was observed in the experimental accretion results for these conditions.

The mathematical model for accretion initiation which was developed considers the aerodynamic, adhesive, and friction force affecting the particles in contact with the surface. The model indicates that ice accretion can occur at subfreezing conditions in the stagnation region and this effect was observed in the present experiments. The model also indicates that accretion is less likely to occur as the temperature increases due to reductions in the coefficient of friction. Such an effect was also observed in the experiments: accretion occurred most rapidly in the $-9\,^{\circ}$C case but virtually no accretion was registered in the $0\,^{\circ}$C and $5\,^{\circ}$C cases.

Although the mathematical model suggested the accretion could also initiate on a flat plate with a laminar boundary layer, this was not observed experimentally. The lack of the accretion in the laminar boundary layer configuration is attributed to the finite leading edge diameter on which substantial ice accretion was observed. The rate of accretion development on the leading edge of the flat plate was comparable to that on the large diameter cylinder specimen which is not consistent with the trends suggested by the mathematical model.

The new wind tunnel duct conditions can be controlled and solid ice particles of a uniform shape and known size distribution can be produced. The development of the new facility and the force-balance model has established useful tools which can be further enhanced in future ice accretion studies.

Associated Publications

The following publications were produced during the period of candidature:

Saleh, Khalid H. and Buttsworth, David R. and Yusaf, Talal , "Development of a small icing wind tunnel for simulating the initial stages of solid phase ice accretion", *17th Australasian Fluid Mechanics Conference*, 5-9 Dec 2010, Auckland, New Zealand.

Buttsworth, DR, Saleh, KH & Yusaf, T, "Discrete particle simulation for the initial stages of ice accretion in aircraft engines: initial model development", *3rd International Conference on Energy and Environment (ICEE)*, 7-8 December 2009, Malacca, Malaysia.

Certification of Dissertation

I certify that the ideas, designs and experimental work, results, analyses and conclusions set out in this dissertation are entirely my own effort, except where otherwise indicated and acknowledged.
I further certify that the work is original and has not been previously submitted for assessment in any other course or institution, except where specifically stated.

Khalid Hashim Saleh

W0079456

_____

Signature of Candidate

_____

Date

ENDORSEMENT

_____

Signature of Supervisor/s

_____

Date

Acknowledgments

First and foremost I would like to extend my sincere appreciation and gratitude to my supervisor Prof. David Buttsworth for his support and guidance throughout my Ph.D. study. I am also grateful to him for giving me the opportunity to work on this research project which has helped me to broaden my knowledge and develop new skills.

I acknowledge the contribution of technical staff of the University of Southern Queensland for their contributions to the work resulting in this thesis. I would like to thank FoES Associated Dean (Research) A/Prof. Armando Apan and his assistant Mrs Juanita Ryan for their support. Also my deep appreciation goes to Ms Angela Windsor and Mrs Kelly Baron for helping me through my language course and for proof reading of this thesis.

I would like also to thank all of my friends and the Iraqi students at USQ especially Ahmed Al-Sabawy for his encouragement and thoughtful opinion in my personal and study issues.

Finally, I am very grateful to my father and my mother for all their efforts to raise me. Thanks to my wife for taking care of me and my son Anas through my study.

Khalid Hashim Saleh

University of Southern Queensland

2013

Contents

List of Figures

List of Tables

Notation

A_s	Water droplet surface area in mm^2
A_T	Particle cross sectional area in mm^2
C	Specific heat of water in J/kg.K
C_D	Drag coefficient
D	Leading edge diameter in mm
D_{force}	Drag force in N
d_{par}	Ice particle diameter in μm
d_w	Water droplet diameter in μm
F_{ad}	Adhesion force in N
g	Gravitational acceleration in m/s^2
Gr_d	Grashof number
h_c	Convection heat transfer coefficient in $W/m^2.K$
H	Shortest distance between ice particle and the surface in μm
k	Air thermal conductivity in W/m.K
Nu_d	Nusselt number
R_a	Centre line average value in μm
Re	Reynolds number
R_z	Average peak to valley height in μm
t	Time in s
T	Temperature in °C
T_s	Air and water mixture temperature in °C
T_∞	Cold stream temperature in °C
u_e	Air speed external to the boundary layer in m/s
u_p	Ice particle speed in m/s

$\bar{u}$	Air speed in the boundary layer in m/s
U_∞	Free stream flow velocity in m/s
V	Water droplet volume in m^3
V_L	Liquid bridge volume in m^3
β	Air coefficient of thermal expansion in K^{-1}
γ	Dimensionless boundary layer thickness
δ	Boundary layer thickness in μm
ϵ	Embracing angle
η	Collection efficiency
μ	Friction coefficient
ν	Kinematic viscosity in m^2/s
ρ	Density in kg/m^3
σ	Surface tension coefficient in N/m
ϕ	Contact angle

Acronyms & Abbreviations

AERTS	Adverse Environment Rotor Test Stand
AIWT	Altitude Icing Wind Tunnel
BRAIT	Boeing Research Aerodynamic Icing Tunnel
CIRA	Italian Aerospace Research Centre
C-MAPSS40K	Commercial Modular Aero-Propulsion System Simulation 40K
FAA	Federal Aviation Administration
FENSAP-ICE	Finite Element Navier-Stokes Analysis Package
FSSP	Forward Scattering Spectrometer Probe
GRC	Glenn Research Centre
HSV	Hue Saturation Value
IRT	Icing Research Tunnel
IWC	Ice Water Content
JKR	Johnson, Kendal and Robert
LIRL	LeClerc Icing Research Laboratory
LWC	Liquid Water Content
NRC	National Research Council
RANS	Reynolds Averaged Navier-Stokes
RATFac	Research Altitude Test Facility
RGB	Red Green Blue
SLD	Supercooled Large Droplet
SLW	Supercooled Liquid Water content
TWC	Total Water Content
UHV	Ultra High Vacuum

Chapter 1

Introduction

1.1 Background

Ice accretion occurs when freezing water droplets, snow or ice particles accumulate on engineered structures. Icing was originally studied in the context of marine applications. Lozowski et al. (2000) reviewed the history of marine icing model development and reported that ice accretion on ships occurs because of the freezing and adhesion of fog, rain, and various kinds of spray, which impinge on the vessel surfaces. Marine icing as shown in Figure 1.1, normally involves ice accretion from brine water and the ice mass accumulated can be large enough to alter the location of the centre of the gravity of a ship. Under typical marine icing conditions, the impinging median volume droplet diameter is around $1100\,\mu$m and the air temperature range is -4.1 to $-10.1\,^{\circ}$C (Ryerson and Gow, 2000).

Power transmission lines are also subjected to ice growth as revealed in Figure 1.2 under certain rates of impingement of the frozen rain and external heat transfer. Each year, countries like Canada, United States, England, Finland, Japan, and China, report failures of a large number of structures due to ice accretion (Poots, 1996). Ice accretion research programs are established in these countries and a database is being developed for ice load and wind-on-ice load on the power system structures. Development of mathematical models for the flow field, droplet trajectory and ice accretion process

Figure 1.1: Photograph showing ice deposits on surface of a marine vessel and spray which can contribute to ice accretion. (Photo courtesy of the Fishing Vessel Safety Division of the USCG.)

are essential to improve structure design under conditions of ice accretion (Makkonen, 2000). Four distinct ice accretion regimes for structures can generally be identified: rime, glaze, frost, and wet snow (Poots, 1996).

In aircraft applications, ice accretion generally occurs during flight through clouds at a temperature equal to or below the water freezing point. This phenomenon may contribute to serious power loss and possible aircraft destruction, thus, endangering human life. Therefore, the ice accretion on aircraft components has received significant attention. Gent et al. (2000) demonstrated that the ice accretion on aircraft at higher altitudes depends on the shape of the part, the size of the surface, the travelling speed of the body, the ambient temperature, Liquid Water Content (LWC), and the droplet size within the cloud.

If flight occurs at a low ambient temperature (-40 to $-10\,^{\circ}\mathrm{C}$) (Thomas et al., 1996), at a modest speed (such that there is little kinetic heating), and at a low value of cloud water concentration ($0.05\,\mathrm{g/m^3}$), the droplets can freeze immediately on impact (Gent et al., 2000). This type of ice formation is known as “rime ice” and it tends

Figure 1.2: Photograph of power transmission line and structure with ice deposits. (Photo courtesy of the Landsnet (Transmission lines).)

to have a white opaque appearance and a density of around $880\,\mathrm{kg/m^3}$ (Griffiths and Korkan, 1992), with a surface roughness greater than the part on which it accretes as it can be seen in Figure 1.3. The rime ice appears white because air is captured between the frozen droplets. Although rime ice normally has a streamlined profile, it can sometimes take on the shape of a pointed spearhead (Gent et al., 2000).

At warmer temperatures between -18 and $0\,^{\circ}\mathrm{C}$, and with high flight speeds which lead to an increase in the capture of mass of water, or with high water content of the cloud ($1\,\mathrm{g/m^3}$), "glaze ice" forms. In glaze icing, not all the liquid droplets freeze on impact, the droplets run back as a thin liquid film, and then start to freeze. Therefore, this form of accretion is translucent in appearance with a density of $917\,\mathrm{kg/m^3}$ (Griffiths and Korkan, 1992). In the case of icing of aircraft wings, two ice horns can grow away from the stagnation point, if the icing is present for sufficient time (Gent et al., 2000).

At transitional conditions between rime and glaze accretion, "mixed ice" accretion can occur. The type and shape of ice accretion within any regime are dependent on a range of interrelated factors including aerofoil geometry, altitude, air speed, liquid water content, droplet collection efficiency, ambient temperature, droplet size, and cloud extent (Thomas et al., 1996).

Figure 1.3: Photograph of ice deposits on the wing of the NASA Twin Otter. (`http://www.wearherjackwilliams.com`)

Aircraft engines are also prone to ice accretion and this has been identified as relevant for commuter and commercial aircraft engines (Mason et al., 2006). Supercooled large droplets are not an engine problem but supercooled *small* droplets can accrete within the air intake and slightly beyond the fan (Mason et al., 2006). GE has established a $US 50 million ice testing facility in Canada to test the performance, endurance, and the capability of aircraft engines to handle such icing conditions at temperature between -20 and $0\,^{\circ}\mathrm{C}$ (Tarantola, 2013).

Ice crystals also represent a threat to engines (Mason et al., 2006). Ice crystal icing can occur at an altitude higher than 10000 m where the temperature is generally less than $-40\,^{\circ}\mathrm{C}$. The temperature of the first stage of the engine compressor is around $0\,^{\circ}\mathrm{C}$ at such conditions. Flights through clouds with an ambient temperature of less than $-40\,^{\circ}\mathrm{C}$ were previously considered benign from an icing perspective because at these conditions, any cloud water content is already in the solid phase. Solid ice particles do not tend to adhere to external aircraft surfaces which are already at sub-freezing temperatures. However, ice particles will partially melt as they travel inside the engine, and when they hit the surfaces of the compressor, a water layer can form. The ice particles that adhere to surfaces can reduce the surface temperature to the

freezing point. The icing may continue to build up causing engine blockage, rotor blade damage, engine rollback, and surge which all lead to a serious loss of engine functionality (Mason et al., 2006; Mason et al., 2011). In this study, the adhesion of fully frozen ice particles to model surfaces over a range of surface temperatures from well below freezing, to above the melting temperature will be investigated.

1.2 Research Aim

Former icing research has concentrated mainly on the physical and numerical simulation of glaze and rime icing accretion on aircraft structures. A very limited number of experimental works have targeted solid phase ice accretion because of the high wind tunnel operational cost and safety concern for in-flight icing testing, which requires flight through severe weather conditions. The process outlined in Section 1.1 for accretion of solid ice particles on aircraft engine components at high altitude is supported by a range of observations (Mason et al., 2006; Mason et al., 2011) but detailed experimental data on the physical process leading to the initiation of this mode of accretion is not yet available.

The overall aim of this project is to develop a reliable, small scale experimental facility and related experimental techniques which can be used in the study of the initiation of ice accretion from the solid ice particles at thermal conditions relevant to turbofan operation at high altitude. The new ice accretion measurements to be obtained as part of the current work should help to better understand the engine icing problem and should aid in the development of a mathematical model for the accretion process.

1.3 Thesis Objectives

The main objectives of this study are:

1. Design and build a small wind tunnel to simulate some aspects of the turbo fan engine icing problem.

2. Develop a mathematical model for the initiation of icing.

3. Perform experiments which target a range of conditions relevant to the initiation of icing.

4. Review the applicability of the model for the initiation of icing.

1.4 Scope of the Dissertation

This dissertation contributes to understanding the initiation of solid ice accretion through experiments and the development of an ice accretion model based on the forces affecting ice particles in the boundary layer. Below is a description of the content presented in each chapter of this thesis.

Chapter 2 Literature Review.

This chapter is devoted to the literature review in order to provide the reader with an adequate overview of the engine icing conditions, icing physical processes, engine icing experimental studies, simulation studies on turbofan engine icing, and finally a general description of some of the major icing wind tunnels.

Chapter 3 Mathematical Model

The results from the literature that are relevant to the modelling of ice accretion: the ice friction coefficient, the adhesion force of ice particles, and the aerodynamic forces in the boundary layer are reviewed. The balance of these forces is considered to define conditions leading to the initiation of icing.

Chapter 4 Experimental Apparatus Design and Characterisation.

The experimental apparatus dimensions and operation, thermal conditions for droplet freezing, apparatus characterisation tests, and some preliminary results will be discussed.

Chapter 5 Ice Water Content.

The experimental results for the ice water content, ice particle size distribution, and the capture efficiency for the collection test specimen will be presented.

Chapter 6 Ice Accretion on Cylindrical Specimen.

The testing and analysis methods for four surface temperature cases on the cylindrical specimen are presented. Applicability of the mathematical model to the cylindrical specimen results is discussed.

Chapter 7 Ice Accretion on Flat Plate Specimen.

The testing and analysis methods for four surface temperature cases on the flat plate specimen are presented. Applicability of the mathematical model to the flat plate specimen results is discussed.

Chapter 8 Conclusion.

The conclusions drawn throughout this work in addressing the objective list in Section 1.3 are presented. The chapter also describes the most significant contributions of this study and makes suggestions for future work.

Chapter 2

Literature Review

2.1 Introduction

A general introduction to the icing problem has been presented in the previous chapter. Here, the conditions and physical processes relevant to ice crystal icing engines are reviewed. Turbofan engine icing experiments and simulation works are also reviewed. A description and the general layout of the icing wind tunnels which have been used to validate ice accretion simulation studies are also presented.

The locations over which ice accretion can be initiated in aircraft engines are extensive as illustrated in Figure 2.1 hence there will be a corresponding wide range of thermofluids conditions under which ice accretion can be initiated. The supercooled liquid water accretion can accumulate on the spinner, fan, core inlet while the ice crystal accretion occurs deep inside the engine and it is difficult to collect visual data of the latter phenomenon from the restricted space (Mason et al., 2006). This study will focus on the ice crystal accretion.

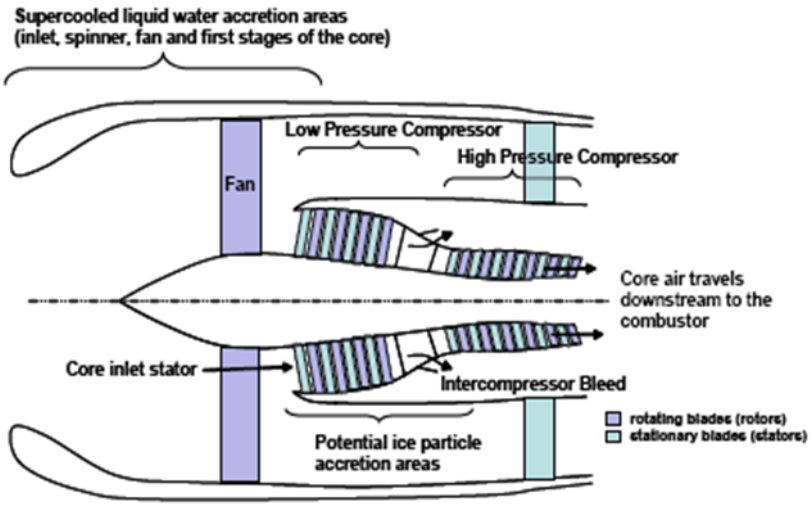

Figure 2.1: Illustration of a typical turbo fan engine system and potential ice accretion areas. Reproduced from Mason et al. (2006).

2.2 Ice Crystal Engine Icing Meteorological Conditions

In the last decade, it was claimed that the size of storm and tropical clouds have increased because of climate change (Bengtsson et al., 2006). Increased temperatures enhance the evaporation process from the ocean surfaces. When a mass of vapour rises to a high level and condenses, super saturation can produce storm clouds (cumulonimbus) with large water content and severe icing conditions.

During a typical flight of a commuter or commercial aircraft, altitudes of around 10 km above sea level are reached with atmospheric pressure around 25 kPa. At that level, the ambient temperature will be less than $-40\,^{\circ}\mathrm{C}$. Water cannot remain in a supercooled state at this temperature, so the cloud moisture content will be in the solid phase. Such conditions were previously considered benign from the aircraft icing perspective because the ice particles appeared to be deflected from the wings and other structures without observable accretion. However, recent evidence suggests ice accretion can occur in the compressor stages of certain engines and this can lead to a reduction or total loss of engine power (Mason et al., 2006).

The distribution and densities of ice crystal was studied during the Tropical experiment

at Darwin in 1987 in the tops of tropical cumulonimbus anvils related to the tropical cyclones and associated clouds (Knollenberg et al., 1993). A two dimensional probe was designed to cover particle diameters from 0.1 μm to 78 μm. The measurements were recorded at temperatures varying between $-60\,^{\circ}$C and $-90\,^{\circ}$C and altitudes ranging from 13 to 18 km. These measurements were compared with other measurements performed in continental cumulonimbus anvils in the western United States. The measurement results revealed that the tropical anvil has a higher concentration of ice crystals, which is between $10\,\mathrm{cm}^{-3}$ and $100\,\mathrm{cm}^{-3}$. The sizes of the particles in continental United States anvils are much larger than the crystal size in the tropical storms; the mean mass size in tropical conditions is usually between 20 and 40 μm. In addition, it was found that the ice crystals are almost spherical or of low aspect ratio and relatively dense. A two dimensional Grey Images instrument was used to obtain the ice water content. This technique gives reasonable results for the large crystals only. To overcome this difficulty, it would be preferable to have an independent IWC instrument capability (Knollenberg et al., 1993).

The cloud particles in thunderstorm anvils and the probability of weather threat to aviation were studied by Lawson et al. (1998). The engine power loss, which is also known as engine rollback, has been attributed to the ingestion of high mass concentrations of ice particles, snow, and possibly a small amount of supercooled liquid water (within a temperature range between -30 to $-40\,^{\circ}$C) in the anvil region. The outcomes of this research and aircraft observations in the anvils of mid-latitude and tropical thunderstorms show that most anvils have small particles with thunderstorms holding less than $0.4\,\mathrm{g/m}^3$ mass concentrations. The ice water contents may vary between 1 to $3\,\mathrm{g/m}^3$ in large, more intense mid-latitude storms, with the maximum particle size being about 2 mm. The centre of thunderstorms have the highest mass concentration and concentration decreases rapidly away from the core. In regions of high radar reflectivity, the concentration of the ice particles decreases well below $1\,\mathrm{g/m}^3$ at a distance of 50 km from a thunderstorm centre (Lawson et al., 1998). It can be concluded that conditions leading to high ice mass concentration are: large amounts of moisture available, strong updraft velocity, low precipitation efficiency, and low tropopause. The tropopause is the boundary between the stratosphere and the troposphere.

Grzych and Mason (2010) discussed the engine incident database to understand the convective environment related to the engine icing events. By analysing the meteorological data for the engine incidents, Grzych and Mason (2010) concluded that all the recorded incidents occurred in the convective cloud anvil, the environment that is characterised by high precipitable water and modest wind shear. In nine engine incidents, the radar showed both a tropical mesoscale convective system and hurricane vertical profiles. It was concluded that the atmospheric characterisation effort must focus on the particle size and the ice water content to assess the engine capability to handle the ice conditions. The aircraft engine designer needs to know the maximum ice water content to evaluate the location in the engine where it is possible for the ice to accumulate (Grzych and Mason, 2010).

Temperatures are expected to be near $-40\,^{\circ}\mathrm{C}$ at altitudes from 3.5 km to 11.9 km, and at such conditions, the environment is dominated by ice particles with particle sizes of less than $50\,\mu$m. Ice crystals can be found in a wide range of shapes and sizes. The small ice particles were found mostly in spherical shape, while the large particles can be in a hexagonal shape or other shapes depending on the temperature and vapour pressure. In the case of engines where extreme bends or flow reversals exist, it is expected that large ice particles will be reduced in size by colliding with the fan and early compressor stages, allowing only smaller crystal to accrete downstream on the static components. In the next few paragraph the deep convective clouds condition will be introduced.

A deep convective cloud is a cloud that ingests air mainly through its base and delivers at least some of that air through to the cloud top (Rosenfeld and Lensky, 1998). For the deep convection clouds to exist, thermodynamically, two requirements must be satisfied: conditional instability throughout the lower troposphere and a means for air parcels to rise to the level of free convection. The instability can be caused by: heating at the bottom of an air layer; cooling at the top of an air layer; or lifting or saturation of potentially unstable layer. The second condition is determined by the altitude of the level of free convection, which depends on temperature of the planetary boundary layer and the humidity. Altitude of the level of free convection is also affected by the depth of the planetary boundary layer, which is controlled by low level wind convergence and

turbulence (Fu et al., 1990). The tops of convective clouds become colder with height in accordance with adjacent atmospheric sounding (Rosenfeld and Lensky, 1998).

Data on the microphysical properties of deep convective clouds is limited. Jorgensen and Lemone (1989) documented convection cloud properties near Taiwan, and concluded that there was a rapid decline of cloud water and radar reflectivity at altitudes above the freezing level. This implies a rapid conversion of cloud water and rain to ice at high altitude. The microphysical properties of the tropical clouds in Brazil and the Marshall Islands were studied by Stith et al. (2002). At a temperature of $-12\,^{\circ}\mathrm{C}$, significant supercooled liquid water was found, while at $-18\,^{\circ}\mathrm{C}$ and lower, there was not a significant amount of supercooled liquid water. Heymsfield and Miloshevich (1993) reported the measurements of the clouds properties in the temperature range $-31\,^{\circ}\mathrm{C}$ to $-40\,^{\circ}\mathrm{C}$, which indicate a transition from liquid phase to solid ice: disappearance of liquid water droplets and an increase in the ice particle concentration. Although the water droplets vanished rapidly close to $-40\,^{\circ}\mathrm{C}$, there was no clear conclusion about the ice particle concentration and size, and the area in the cloud with highest ice concentration.

Rosenfeld and Woodley (2000) reported that the deep convective cloud droplets can reach a median volume diameter of $17\,\mu$m and amount to $1.8\,\mathrm{g\,m^{-3}}$, and at slightly colder than $-37.5\,^{\circ}\mathrm{C}$ only ice was found from an aircraft measurement, suggesting homogeneous freezing occurred.

2.3 Engine Icing Physics

Engine icing can occur on the engine inlet, spinner, fan and engine core (Heinrich, 1991). The solid ice particle are believed to be the main cause of the turbofan engine core icing. As the small ice crystals move inside the engine, they melt down to be a mixture of solid and liquid phases due to the engine temperature and the compression process. The harder the ice particle, the deeper into the engine core ice accretion can happen. As the mixed phase water impinges on the engine inner surfaces, the surface temperature decreases until the freezing point is reached (Heinrich, 1991). Before the

freezing point, some of the water droplet may run back and solidify on the surface, depending on the particle size and liquid water content. After the surface reaches the freezing point, the mixed phase droplet may accumulate on impact. If the flow rate through the engine is suddenly dropped at high water content, the surface temperature may reach the freezing point faster than at cruising conditions and the water droplet will freeze at the impact. Al-Khalil (2003) indicates the higher is a chance of ice accretion if the water content increases. The process of the ice crystals or mixed phase droplets decreasing the surface temperature for the ice accretion to start is still a subject of research.

Under mixed phase and super cooled droplet engine icing conditions, the tools and technique developed for the study and analysis of aircraft icing have relevance and are discussed in the following. Aircraft icing can be caused by supercooled water droplets at a temperature range of $-40\,^{\circ}\mathrm{C}$ to $0\,^{\circ}\mathrm{C}$. These droplets have a metastable condition and follow trajectories that strike the surface or carry it away from the body. When the aircraft enters the freezing clouds, the droplets may freeze rapidly on impact, or they may flow back as a thin layer of water and accumulate into droplets (Poots, 2000; Gent et al., 2000).

One of the significant variables in icing phenomena is the freezing fraction, as identified by Messinger (1953). The freezing fraction is the ratio of the amount of water which is intercepted by the body and freezes on the surface to the mass flow rate of Total Water Content (TWC) that enters the control volume. Another characteristic that affects the ice accretion process is the rate of freezing development. This is governed by the heat transfer from the freezing layer to and from the surface. The latent heat resulting from fusion of the colliding droplets which freeze must be dissipated. The principle mechanisms of heat loss are evaporation and convection. Evaporative cooling, which is a function of the surface pressure of the body, will drive the surface temperature and water layer pressure to the freezing point. The convection heat transfer relies on the speed, body shape, and the temperature difference between the surface and the surrounding air (Gent et al., 2000).

The liquid water content of the clouds plays a significant role in the freezing fraction value. With low LWC the freezing fraction tends to be unity because the rate of

convection heat loss, in this case, is sufficient to remove all of the latent heat, and all the liquid droplets will freeze on the impact. This is known as rime icing, which has an opaque milky appearance, due to air trapping, and has a rough surface which may cause high aerodynamic penalty (Gent et al., 2000; Kind et al., 1998).

On the other hand, at high LWC the released latent energy is higher than the energy removed by convection heat transfer and the liquid droplet will freeze partially, so the freezing fraction will be less than one. Glaze icing conditions prevail. This accretion tends to be glassy in appearance and the surface roughness can range from fractions of a millimetre up to localised three-dimensional nodules several millimetres in height. This type of icing is more difficult to analyse than the rime cases because of the unfrozen run-back droplets on the surface (Kind et al., 1998; Poots, 2000).

Jin and Hu (2010) presented an experiment on icing physics to quantify the heat transfer process and the transient behaviour of the phase changing for small water droplets impinging on a frozen cold plate. Molecular tagging thermometry was used to measure simultaneously the droplet size and temperature. It was observed that the bottom of the impinged water droplet surface would change to solid ice, while the upper portion of the droplet was still in the liquid phase. The interface surface between the liquid phase and the solid ice phase was found to move upward with time. The temperature measurement for the remaining liquid water within the small icing droplet was noticed to increase, and Jin and Hu (2010) concluded that this increase was due to the latent heat release during the solidification process. During the icing process, the volume expansion of the water droplet was found to be primarily upward to cause droplet height growth.

2.4 Engine Icing Experimental Work

Experimental observation of ice accretion of super cooled droplet in the axial compressor of a small jet engine was reported by Minoya et al. (2010). The experiments were conducted in a cold room with a temperature range between $-11\,^{\circ}\mathrm{C}$ and $-1\,^{\circ}\mathrm{C}$, the test was conducted at temperatures between $-10\,^{\circ}\mathrm{C}$ and $-4\,^{\circ}\mathrm{C}$, and the water droplet

size ranging from 10 μm to 70 μm. Ice accretion was observed in the vicinity of the leading edge of the blade and on the suction side of the fan blade. In addition, it was found that the ice accretion starts earlier with low temperatures and the accumulation rate is more rapid in comparison with high temperature conditions.

Mason et al. (2011) suggested testing on a simplified rig for the engine ice accretion problem because it has the benefit of good visibility of the accretion process and uncomplicated video documentation, in comparison with the real icing which occurs inside an operating engine. The facility test section of Mason et al. (2011) contains a duct which replicates the real transition duct between the low and high pressure compressor in a typical turbofan engine, as well as an aerofoil, simulating the strut. Ice particles were produced using a grinder and were injected as an ice jet with an exit velocity of 90 m/s and temperature from $-15\,^{\circ}$C to $-10\,^{\circ}$C. Atomisation nozzles were also used to spray water at a median volume diameter between 20 μm and 40 μm. Mason et al. (2011) found that the accretion occurs on the aerofoil and the duct surfaces at warm temperatures above 10 $^{\circ}$C, and no accretion was observed when the air and the surface temperature were held under zero degrees Celcius. It was concluded that the ice accreted on the warm aerofoil surface when mixed phase conditions were generated. This study did not analyse the heat transfer and the cause of the ice particle adhesion and accretion.

A series of experiments were performed by NASA, the National Research Council (NRC) of Canada and the Federal Aviation Administration (FAA), to study the physical mechanism of ice accretion on surfaces exposed to ice crystals and mixed phase conditions similar to the conditions of engines during power loss incidents (Struk et al., 2012). At the NRC Research Altitude Test Facility (RATFac), the tests took place using a single wedge type aerofoil fitted inside a small wind tunnel. This rig can produce ice-crystals and mixed phase conditions. This study involved the testing and characterisation of the wedge aerofoil aerodynamics, and the determination of the range of the conditions which leads to the ice accretion. Tests conditions were: angles of attack at $0\,^{\circ}$ and $-6\,^{\circ}$, Mach numbers of 0.2, 0.3 and 0.4, and nominal stagnation pressures of 45 and 93 kPa. Ice accretion tests were carried out for total temperatures ranging from 5 to 15 $^{\circ}$C, and ice and liquid water contents were varied up to

20 and 3 g/m^3 respectively. At the lowest stagnation pressure of 45 kPa and the wet bulb surface temperature in the range of $-2.7\,^{\circ}$C to $-4\,^{\circ}$C, the test showed strong ice adhesion to the surface and continuous ice accumulation on the leading edge until it reached 15 mm in height after 3 minutes in one case for test specimen which has 3.173 mm leading edge diameter. The ice accretion usually occurred in the vicinity of the leading edge and at lower surface temperatures, while the leeward side of the wedge was typically ice free in the entire range of high pressure tests and some of the low pressure test. High levels of ice accumulation on the leading edge imply significant aerodynamic performance degradation, and it could be the cause of major damage to the downstream parts, if the ice was shed from the blade (Struk et al., 2012).

To explore the sensitivity of the ice accretion process to the wet bulb temperature, Currie et al. (2012) conducted a mixed phase experimental study which confirmed that the wet bulb temperature should be less than $0\,^{\circ}$C for the ice accretion to be well-adhered to the surface. It was found that at sub-freezing wet bulb temperature, adding ice particles in the free stream enhance significantly the ice accretion near the leading edge, compared to the accretion due to liquid phase only. Currie et al. (2012) performed the test at Mach numbers of 0.25 and 0.4, median mass diameter of ice crystals between 90 to 200 μm, liquid water content varying between 0 to 5 g/m^3, and ice water content ranging from 0 to 17 g/m^3.

Knezevici et al. (2012) presented data and sample images to explain the role of the particle size and wet bulb temperature on the ice crystal phenomenon. It was found that the particle size and the wet bulb temperature have a significant influence on the amount of accretion under the mixed phase test conditions. This is because small particles can melt faster, and the large particles have higher erosive effects than the smaller particles. The wet bulb temperature was found to have a significant affect on the natural melting of the ice particles (Knezevici et al., 2012).

Knezevici et al. (2013) added a shadowgraphy imaging system to their earlier work to characterise ice crystal particle size distribution. In this study, the leading edge ice accretion rate was measured and found to be 1 % to 25 % of the theoretical growth rate based on the edge tracking image processing measurement technique, which was verified with ice tracings results. Knezevici et al. (2013) concluded that erosion and

splashing affected the mixed droplet retention significantly at a test speed of 80 m/s, with the median mass diameter of the ice crystals between 45 to 300 μm.

2.5 Engine Icing Simulation

A numerical simulation for three dimensional super cooled droplet trajectories through an aero-engine rotating machinery was performed by Hamed et al. (2005). This simulation solved the droplets and flow equations in the reference frame of the rotating blades using the Eulerian - Lagrangian approach to simulate the influence of aerodynamics on the droplet trajectories. As a consequence, the calculation of the amount of water that collides with the rotating and stationary surfaces was presented depending on the proposed flux - based collection efficiency (Hamed et al., 2005). Das et al. (2006) added to the work of Hamed et al. (2005), which involved a quasi-three dimensional analysis of the ice accretion over the rotor blade at different design speeds and included results for the radial variation in ice shape. Both of these articles considered the drag force as the primary aerodynamic force on the droplets and neglected the forces due to inter-droplet interactions and pressure gradients.

The mechanics of ice crystals as a sole cause of ice accretion in the commercial aircraft turbofan engine core was discussed by Ríos and Cho (2008). In this study, a new code which treats the coupling between the ice crystals and the flow as a multiphase flow has been developed. The results from this code show that the ice crystals in a flow which is highly loaded with non-spherical particles tend to bypass the stators and penetrate deep inside the engine compressor more than liquid droplets of the same size. This study concluded that flight in a rich ice crystal environment (9 g/m^3, and 200 μm) can be the cause of the engine icing.

To study the effect of the ice accretion on the two dimensional stator cascade in the first stage of the compressor, a numerical investigation was performed by Lee and Loth (2008). This study focused on the ice shape and the aerodynamic penalties for the 67A stator blade. The computational methodology included a steady state flow field calculation using a Reynolds-Averaged Navier-Stokes (RANS) solver to predict

the super cooled droplet trajectories and the impingement efficiency in the Lagrangian frame. The RANS solver static pressure distributions were used in LEWICE to identify the ice accretion on the surface of the stator blade. Lee and Loth (2008) found that the ice accretion is sensitive to temperature, droplet size, and integration time. Ice accretion can lead to flow field changes and as a consequence, boundary layer separation can occur causing an increase in the total pressure loss and mass flow rate as well as flow turning angle. Lee and Loth (2008) simulations require more validation effort.

A computational study of super cooled small water droplet (around 20 μm) to examine the outcomes of the rime and glaze icing formation shapes on the flow field of the M2129 diffusing S-duct has been conducted by Taghavi and Jin (2008) using a steady state Reynolds Averaged Navier Stokes solver at different Mach numbers ranging from 0.13 to 0.85. The results show significant performance degradations due to the massive flow separation from the horn in the glaze icing conditions, while the consequence of rime ice accretion is negligible. It was revealed in this study that the glaze icing conditions were more hazardous than the rime ice in terms of the secondary flow region, total pressure recovery, air inlet mass flow rate, and that these effects can increase with the Mach number.

Wright et al. (2010) describes an overview of the GlennICE software and the modification made to GlennICE in order to model the ice crystal accretion inside the engine. These modifications included a new particle trajectory algorithm and the energy equation to code the engine icing phenomena. The results have been compared with experimental tests done previously in the Cox icing wind tunnel by Al-Khalil (2003) and the results of the preliminary ice erosion test show that the ice shape was eliminated from the surface by the impact of other ice particles, probably due to the high engine flow speed.

The influence of the inlet diameter, flight Mach number, modified inertia parameter and droplet Reynolds number on the collection efficiency of the ice crystal and water droplet were investigated by Liao et al. (2011). This study used CFD simulation of an axisymmetric inlet of a turbofan engine. The collection efficiency was identified as the ratio of the water mass flow per unit area at the inlet throat to the water mass flow per unit area in the free stream. The results of the water collection efficiency were

associated with air mass flow ratio instead of the velocity ratio, and were evaluated with published experimental data. The results show the significance of the local ice/water concentration effect within the engine inlet in designing and placing the engine inlet probe. Liao et al. (2011) assumed the droplet trajectory was decoupled from the flow field simulation based on the low mass fraction of the droplets.

To study the consequence of the ice crystal accretion on the low pressure compressor performance and to compute its effects on the engine system, a computational tool was developed by Jorgenson et al. (2011). This tool can be divided into: engine thermodynamic cycle code, a compressor mean line flow analysis code, and an ice accretion code. The engine modelling code and the mean line compressor flow analysis code were used to estimate the flow conditions in low pressure compressor regions and to recognise locations where the ice may accumulate inside the compressor. A small temperature range for engine ice accretion conditions was assumed to allow the computational code to parametrically include ice accretion blockage effects on the low pressure compressor. The results from this tool confirm the supercooled droplet code outcomes, which show that the accretion takes place primarily on the leading edge. In addition, the code demonstrates that the accretion may occur at different compressor stages depending on engine temperature and flight conditions.

By advancing the work by Jorgenson et al. (2011), the effect of the ice accretion on the engine performance, detection and mitigation of the engine rollback was investigated by May et al. (2011). The engine rollback is the engine decelerating and or shutdown due to engine fuel system fault or ice accretion. . May et al. (2011) used the Commercial Modular Aero-Propulsion System Simulation 40K (C−MAPSS40K). In this study, the performance of the C−MAPSS40K software for ice crystal accretion was compared to real aircraft engine behaviour during the ice accretion events and good agreement has been achieved. May et al. (2011) conclude that the engine rollback is initiated by the engine hitting maximum safety restrictions and the engine controller switching to a conservative control approach.

2.6 Icing Wind Tunnels

In 1944, the Icing Research Tunnel (IRT) was built by the Advisory Committee for Aeronautics (NACA) in Cleveland, Ohio, to investigate the loss of more than 100 aeroplanes over the Himalayas in World War II. This tunnel, now known as NASA - IRT is a closed loop atmospheric wind tunnel with a 2100 ton refrigeration capability that uses water spray bars to produce the cloud. The spray bars produce a water mean volume droplet diameter between 15 μm to 50 μm with total water content varying from 0.2 to 2.5 g/m^3 according to the NASA - IRT website. The distance between the spray bars and the test section is 13.41 m. The facility test section dimensions are: height 1.8 m, width 2.7 m, and length 6.1 m, and the test section also includes a turntable to change the angle of attack of the model to a maximum of 20°. The tunnel can operate over a wide speed range: from 25.7 m/s to 180 m/s. The minimum operating temperature is −30 °C and this can be established with 0.5 °C accuracy. Figure 2.2 is a plan view of the NASA - IRT wind tunnel. This facility operation is costed at 34,000 USD/day and scheduling is required at least nine months in advance (Ríos, 2012).

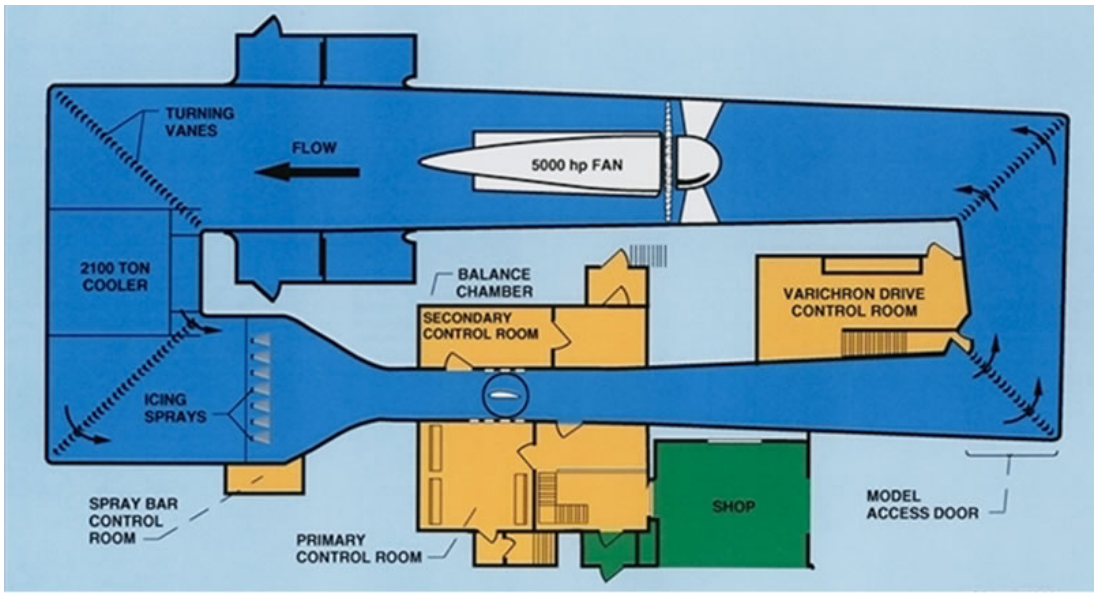

Figure 2.2: Plan view of NASA IRT. Reproduced from Irvine et al. (2001).

The Cox LeClerc Icing Research Laboratory (LIRL) is smaller in size than the IRT, and is located in Manhattan, New York. Cox LIRL is also a closed loop tunnel and

has two test sections, a high speed main test area (Test Section 1) and a second larger test section that operates at a lower test speed (Test Section 2). The dimensions of Test Section 1 are 0.71 m × 1.17 m × 2 m with a maximum speed of 89.5 m/s, while the speed in Test Section 2 is 53.6 m/s with dimensions of 1.22 m × 1.22 m × 1.52 m. These test sections also contain turntables for dynamic control of the angle of attack of a model. Spray and ice shaver systems can be used to produce different droplet sizes and shapes. The particle generation devices are located 5.72 m from the test section. The liquid water content can be varied between 0.25 and 3 g/m^3. The minimum temperature in this tunnel is −30 °C; the refrigeration system has a cooling capacity of 80 ton. Testing in Cox LIRL is costed at 9,000 USD/day and reservations for a test should be made at least two months in advance (Al-Khalil, 2003; AI-Khalil and Salamon, 1998; Ríos, 2012). Figure 2.3 presents a general layout of the Cox Icing Research Laboratory Wind Tunnel.

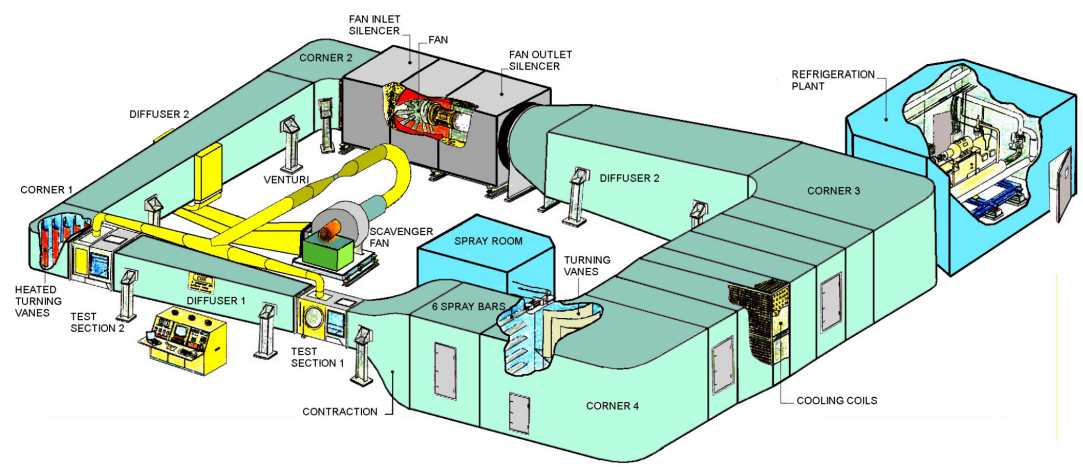

Figure 2.3: Illustration of Cox Icing Research Laboratory Wind Tunnel. Reproduced from AI-Khalil and Salamon (1998).

The National Research Council (NRC) in Ottawa, Canada built another test facility which serves the icing/aerodynamic testing requirements of government agencies, research institutes and private companies. This facility has multiple test sections and can produce a wide range of flow speeds from 5 m/s to 298 m/s depending on the type of test. The Altitude Icing Wind Tunnel (AIWT) specialises in icing testing with 0.57 m × 0.57 m × 1.83 m test section for which the air velocity can vary from 5 m/s to 100 m/s. The liquid water content in this tunnel can be varied between 0.1 and

$3.0\,\mathrm{g/m^3}$, with a droplet median volume diameter between 8 and 120 μm. The minimum temperature in the AIWT under the maximum speed conditions is $-35\,^{\circ}\mathrm{C}$. The AIWT tunnel was built to simulate flight at altitudes as high as 7 km.

The Italian Centre for Aerospace Research (CIRA) has its own icing wind tunnel called IWT. The CIRA facility has three exchangeable test sections and for large models an open jet configuration can be used. The main test section dimension are 2.35 m × 2.24 m × 8 m, for which a maximum speed of 214 m/s can be achieved with a minimum temperature of $-40\,^{\circ}\mathrm{C}$ simulating the flight conditions at 7 km altitude. This icing tunnel also uses a spray bar and it can produce particles with a mean volume diameter of 50 to 300 μm (De Gregorio et al., 1997). The distance between the spray bar and the test section is 18.42 m. A schematic diagram of the CIRA icing wind tunnel is shown in Figure 2.4.

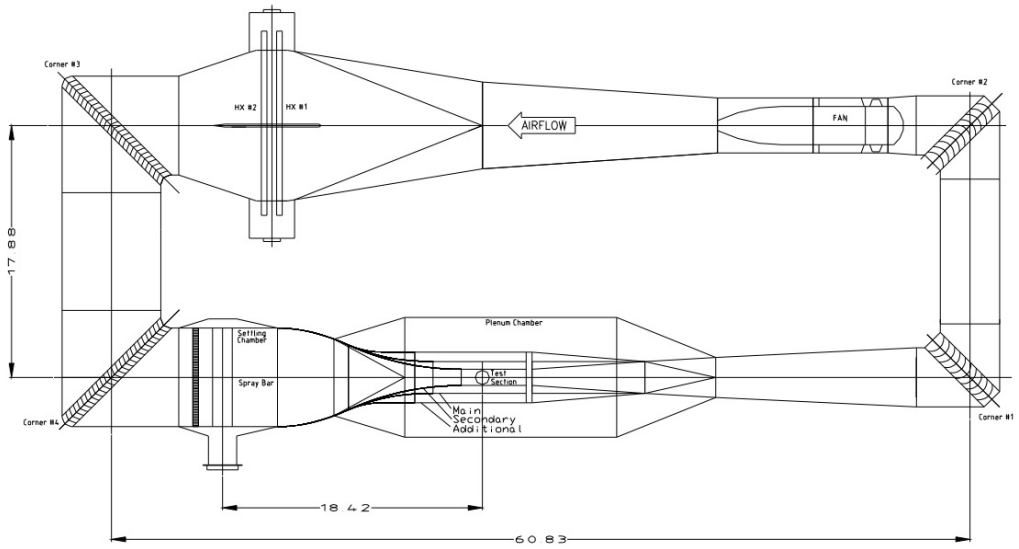

Figure 2.4: CIRA icing wind tunnel layout. Reproduced from Bellucci (2007).

To simplify the airworthiness certification process, Boeing proposed upgrading their tunnel to include an icing test facility. Figure 2.5 is an illustration of the Boeing Research Aerodynamic Icing Tunnel. The Boeing Research Aerodynamic Icing Tunnel (BRAIT) has three test sections, the largest test section has a cross-section of 1.52 m × 2.44 m, a maximum flow speed of 130 m/s, and minimum temperature of $-40\,^{\circ}\mathrm{C}$. A spray bar device can generate a liquid water content of 0.25 to $3.0\,\mathrm{g/m^3}$, with droplet sizes from 15 to 40 μm. This facility was built to simulate flight at 4.6 km altitude. It

has been reported that the uniformity of the flow is within 1% of the centreline velocity (Chintamani et al., 1997).

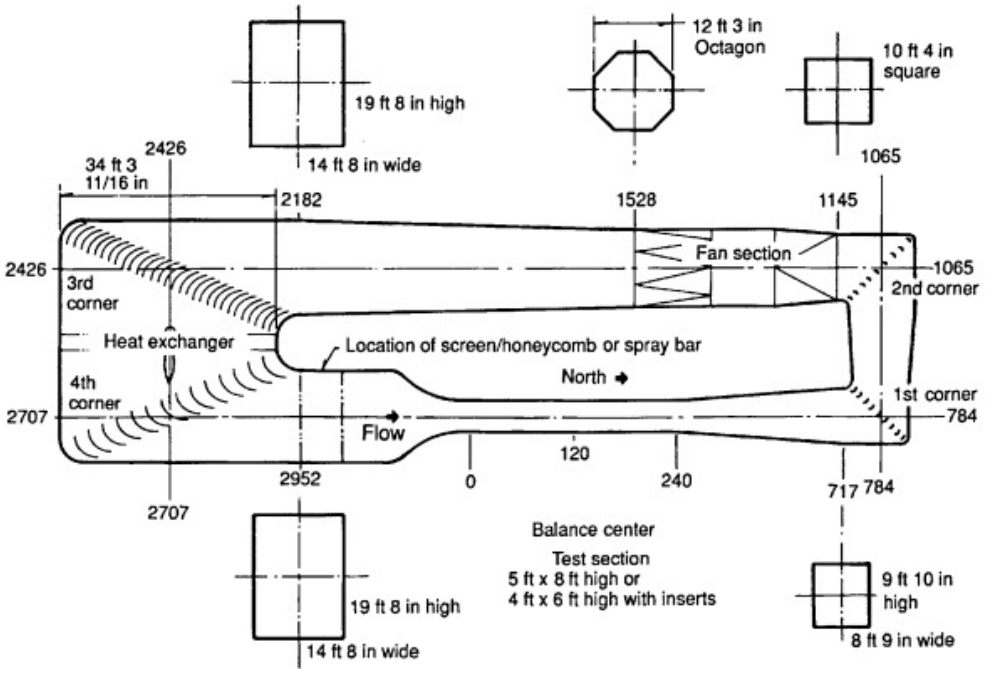

Figure 2.5: Illustration of Boeing Research Aerodynamic Icing Tunnel. Reproduced from Chintamani et al. (1997)

2.7 Conclusion

Ice accretion is a problem of practical interest. Turbofan engine icing and power loss accidents with no ice accretion on the aircraft external surfaces only started to be reported during the 90's and only during flights through the high convective cloud regions (Mason et al., 2006). There is limited experimental data on the turbofan engine ice crystal icing problem. Since ice crystal icing occurs in a very confined space and there is generally no optical access to the relevant engine spaces during operation, direct observations of accretion during flight have not been possible. The engine icing simulation studies still in progress and there is limited experimental data to evaluate the simulation results. The simulations also show that the accretion occurs in the leading edge area. The thermodynamic conditions under which engine icing is initiated have not been fully identified.

The cloud water particle sizes that vary from one to several hundred micrometres. These particles can be in a supercooled or a solid phase depending on the surrounding air temperature, and both of these phases can contribute to the initiation of icing on aircraft surfaces, and on engine components.

The supercooled icing conditions have been investigated by many researchers theoretically and to less extent, experimentally. Most of the numerical simulations have not been thoroughly validated due to lack of resources, so the reliability of any model is limited to the conditions close to those used in the validation work. The experimental icing studies used for code validation have been mostly performed in a few, expensive, large scale testing facilities.

The low temperatures in the high altitude clouds make it impossible for the water within the cloud to be in super cooled liquid phase. However, liquid water is likely to play a role in the initiation of ice accretion within aero-engine compressor because some melting of ice particles can occur due to the elevated air and surface temperature within the compressor.

Previous wind tunnel experiments targeting aero-engine icing conditions have used a suspension of solid and liquid water in high speed ($\geq 70\,\mathrm{m/s}$) air flows at surface temperatures between $5\,^{\circ}\mathrm{C}$ and $15\,^{\circ}\mathrm{C}$. Results demonstrate ice accretion across a range of conditions. However, it is very difficult to analyse such results to yield the physics which drives the initiation of accretion because of the complexity of the flows and the uncertainty in the conditions. For example, ice shavers used in previous works produce a wide variety of shapes and sizes for the particles. This adds considerable complexity. Furthermore, while the ratio of liquid to solid phases in the air suspension can be specified based on the their respective rates of delivery, melting of small ice particles in higher air temperature conditions increases the uncertainty of the actual test conditions.

For the generation of fundamental data which can be used for testing an initiation hypotheses or validation of basic models for the ice accretion process under simplified conditions, construction of a new, small scale icing wind tunnel is justified.

Chapter 3

Mathematical Model

3.1 Introduction

Mathematical models which explain the ice accretion normally focus on the energy equilibrium between the surface and the droplet. In this chapter, to illustrate the fundamental physics of ice particle adhesion to a surface, a mathematical model will be developed based on the aerodynamic and friction force balance on the particles. The adhesion force affects the friction and must therefore also be considered. A comprehensive understanding of the forces is crucial for development of a model for the initial stage of ice accretion. This chapter discusses results from the literature which are relevant to the modelling of ice accretion initiation. Friction coefficients, adhesive force, and aerodynamic force models for the initiation of ice accretion at the stagnation point of cylindrical specimen and on a flat plate are introduced.

3.2 Ice Coefficient of Friction

3.2.1 Literature Review

The coefficient of friction μ is the ratio of the friction force between two bodies and the force pressing them together. The friction coefficient of ice is relevant to studies in the

areas of winter sports, glaciology, and ship hull design. It is generally recognised that the friction force on ice is very low and relies mainly on three parameters: temperature, velocity and the normal load. The composition and the surface state of the connection may also affect the ice coefficient of friction. Measurements of ice friction coefficient have considered the coefficient of friction between ice and other materials, and the coefficient of friction between ice and ice.

Friction physical theories are explained for dry and lubrication friction as reported by (Liang et al., 2003). Dry friction theory involves frictional heating of the sliding contact of two surfaces, creep, and fracture of ice surface, and assumes the absence of a lubricant layer. On ice particles under atmospheric pressure and even at temperatures as low as 130 K (Pan et al., 2011), a very thin liquid layer appears and lubricates the contact surfaces on a molecular size particle. In the crystal ice case, a more substantial water layer can arise from the conversion of the kinetic energy of the particle to thermal energy due to the impact of the particle with the surface.

Experimental work to assess the influence of temperature and the physical nature of the surfaces on the friction of snow and ice was performed by (Bowden, 1953). At lower temperatures, the static friction of the snow is very high. If the sliding speed increases, there is a very marked drop in the friction coefficient due to localised ice melting produced due to the frictional heating. A friction melting theory based on the appearance of the melted water film preventing the direct contact of two surfaces and lubrication between slider and ice as self-lubrication, was also developed by Bowden (1953).

Evans et al. (1976) described a series of experiments to investigate the dependence of ice friction on temperature, velocity, load and the slider material. The tests were conducted at temperatures between -1 and $-15\,^{\circ}\mathrm{C}$, load in the range of 5 to 20 N, and velocities from 0.2 to 10 m/s. Based on a melting friction theory, the analysis demonstrated that a thin water film is created at the sliding ice interface by frictional heat and the film acts as a lubricant. In contrast, Oksanen and Keinonen (1982) assumed that the water layer, which is formed by frictional heat on the contact surfaces, is the only cause of friction. This conclusion was reached based on experimental measurements at similar conditions to those of Evans et al. (1976) (normal loads in

range of 10 to 45 N, velocities from 0.5 to 3 m/s and temperatures between −1 and −15 °C) except that the case of ice - ice friction was being considered.

Experimental work by Kuroiwa (1977) concluded that, at temperatures higher than −10 °C, the friction (at speed less than 10^{-4} m/s) was caused by plastic deformation within the snow. As the speed increased, stick-slip friction dominated and was associated with fractures and abrasions of the snow grain.

Tusima and Tabata (1979) study shows that the kinetic friction with smooth surfaces including glass, stainless steel and plastic (PTFE) are in the range of 0.01 to 0.04, whereas the friction coefficient between sea ice and materials with rough surfaces is from 0.05 to 0.24. The friction measurements were carried out by sliding the specimens at different speeds between 3.5×10^{-7} to 2×10^{-3} m/s, with normal load over a range of 13 to 1000 N and over a temperature range of −1.8 °C to −10 °C (Tusima and Tabata, 1979).

Akkok et al. (1987) studied the mechanics of ice friction and compared the experimental results with various theoretical models. The conclusion of this study provides evidence that the friction of ice is subject to a thermal control mechanism under certain conditions (Akkok et al., 1987).

Colbeck (1988) described the components of the kinetic friction of snow and detailed the coefficient of friction due to the lubricating layer theoretically. The performance of the lubrication layer depends on the thickness of the water films which supports the load on snow grains. The ambient temperature and the surface thermal conductivity also affects the thickness of water film. It was concluded that, at any freezing temperature, the minimum friction can be achieved at an intermediate velocity because the friction coefficient decreases as the slider first starts to move. After that, the water films form which increases the friction coefficient because of the shear resistance (Colbeck, 1988).

Casassa et al. (1991) investigated the kinematic friction coefficients between ice and ice at different conditions: temperatures from 0 to −25 °C, normal stresses between 205 and 1292 Pa, and velocities from 0.9 to 25.3 m/s. Casassa et al. (1991) observed the ice-

ice friction coefficient to be less than 0.04, increasing with velocity at low temperatures. It was also noticed that the dry friction involves Coulomb friction and adhesion, and both of these are dependent on temperature and hardness of ice. On the other hand, although snow viscosity is independent of hardness and temperature, it was found to be strongly dependent on the snow grain characteristics.

Döppenschmidt et al. (1998) used atomic force microscopy to study the surface properties of ice over a range of temperatures varying from -24 to $-0.7\,^{\circ}\mathrm{C}$. It was noticed that the liquid layer thickness on the ice surface varied between 12 nm at $-24\,^{\circ}\mathrm{C}$ and 70 nm at $-0.7\,^{\circ}\mathrm{C}$. As a function of velocity in the range of 0.2 to 60 μm/s, and temperature around $-23\,^{\circ}\mathrm{C}$, and normal force of 5 nN, the friction was measured and it was found that the friction increased with decreased sliding velocity.

The kinetic coefficient of friction for ice on ice contact was investigated for fresh water ice, granular ice and salt water ice by Kennedy et al. (2000). The influence of ambient temperature (-3 to $-40\,^{\circ}\mathrm{C}$), contact load (0.007 to 1.0 MPa), and speed (5×10^{-7} to 5×10^{-2} m/s), on the coefficient of friction were examined. The effect of the grain size of the ice sample was also studied. The appearance of the surface of the fresh water ice samples changed from clear to opaque after the sliding experiments. This change happened due to surface fracture and granulation near the contact surfaces at velocities in the range of 10^{-5} to 10^{-3} m/s. Three different regimes were identified. First, creep happened at temperatures between $-30\,^{\circ}\mathrm{C}$ and $-40\,^{\circ}\mathrm{C}$ and with speeds less than 10^{-5} m/s. Second, fracture governed the transitional speeds between 10^{-5} and 10^{-4} m/s. Third, adhesion and surface melting dominated at speeds of around 10^{-3} m/s when sufficient frictional heating took place to produce a lubricating layer of the melting water.

The static friction coefficient was found to be 0.29, while the kinetic coefficient decreased as the speed increased: a value around 0.1 was obtained at 0.01 m/s, whereas a value around 0.04 was obtained at 0.1 m/s for the painted steel (Frederking and Barker, 2002).

Maeno et al. (2003) examined the two proposed physical mechanisms of ice friction: the water lubrication and the adhesion-shear deformation. Ice-ice friction measurements

were performed for temperatures between 0 and $-30\,^{\circ}\mathrm{C}$, with normal pressures varying from 1.2 to 370 kPa. The results show that with a reduction in the sliding velocity from 0.1 m/s, the ice-ice friction coefficient rises because the reduction of the frictional heat reduces the water layer thickness, and stick-slip behaviour becomes dominant at approximately at 10^{-3} m/s (Maeno et al., 2003).

The nature of the liquid film is still a subject of a given research, but it is clear that the coefficient of friction declines with an increase in temperature due to the development of the lubricant film, which reduces solid to solid contact. However with increases in temperature above $-4\,^{\circ}\mathrm{C}$, the friction coefficient increases, as a consequence of the additional resistance caused by capillary bridges and viscous shearing of the melting film (Colbeck, 1988; Kietzig, 2010).

The ice roughness plays a significant role in the heat transfer between the ice/water layer and the surface. As a result, it will affect the freezing rate and the final shape and location of the ice. Another important factor is the ice density, which may vary under different circumstances. It was found that the effective ice density can be as low as $300\,\mathrm{kg/m^3}$ (Cebeci and Kafyeke, 2003) due to the amount of air trapped in the ice, while the figure of $917\,\mathrm{kg/m^3}$ was used for aircraft icing simulation (Thomas et al., 1996; Griffiths and Korkan, 1992).

Studies have considered ice friction with different materials such as synthetic polymers, polyethylene, steel with no reference to the surface roughness. Although works on surface roughness are available, the focus of such studies is the effect of the roughness depth and orientation on the friction coefficient between ice/snow layers and the surface (Kietzig et al., 2009). In the present icing problem, individual ice particles will be considered and the question is whether or not the particles move on the surface or adhere to the surface at the impact location. Consequently this study will focus on the ice friction at different surface temperatures and two different surface roughnesses.

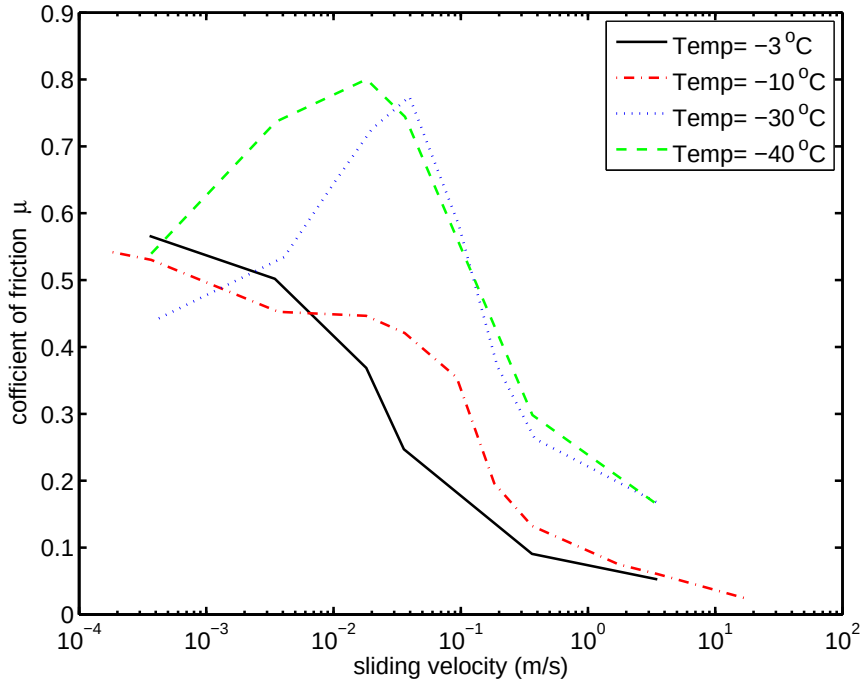

Figure 3.1: Temperature dependence of coefficient of friction of ice as a function of sliding velocity, data from Kennedy et al. (2000).

3.2.2 Application of Ice Friction Results to Current Study

The experimental data of Kennedy et al. (2000) is used in this study, which is shown in Figure 3.1 for velocities less than 0.1 m/s. Theoretical results of Colbeck (1988) are shown in Figure 3.2 for velocities between 1 and 25 m/s. To make the data of Kennedy et al. (2000) consistent with those of Colbeck (1988), Kennedy et al. (2000) velocity values have been scaled up by a factor of 100 as illustrated in Figure 3.3. The reported Colbeck (1988) data does not include results for $-3\,^{\circ}\mathrm{C}$ whereas Kennedy et al. (2000) does, so an interpolation on the Colbeck (1988) data has been performed using $0\,^{\circ}\mathrm{C}$ and $-10\,^{\circ}\mathrm{C}$ data. The average slope of the curves between 10 and 25 m/s was used to extrapolate the friction coefficient values up to 100 m/s. Based on the results in Figure 3.3, an interpolation function was written to define the coefficient of friction at any temperature between $-3\,^{\circ}\mathrm{C}$ and $-40\,^{\circ}\mathrm{C}$ and at any velocity between 10^{-4} and 100 m/s.

These two dataset were used to cover low and high speed realistically, and the scaling appropriate due to the gap between the two datasets. In Kennedy tests the minimum

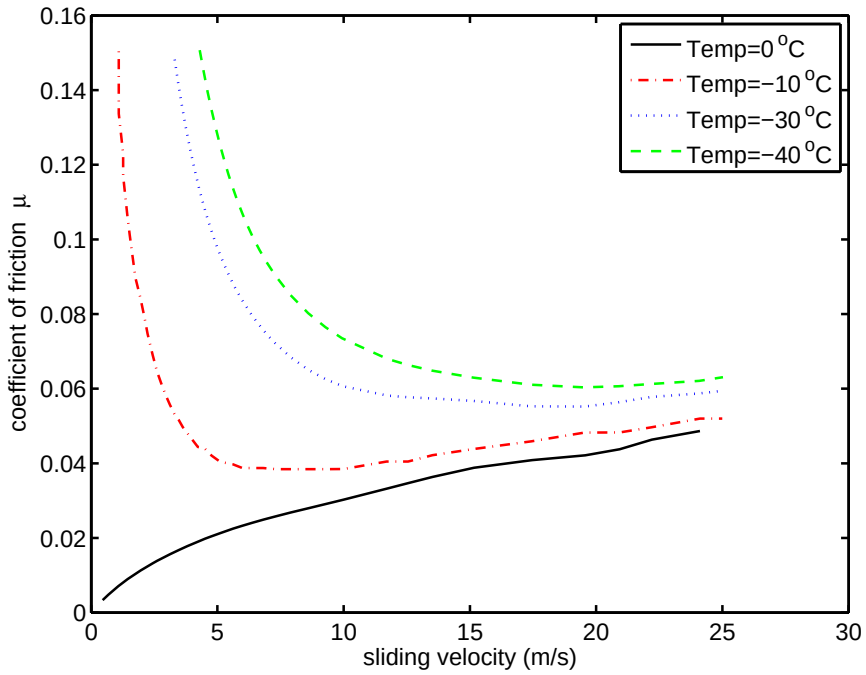

Figure 3.2: Temperature dependence of coefficient of friction of ice as a function of sliding velocity, results from Colbeck (1988).

standard deviation was ± 0.005 for grain size 2.5 mm and under 5×10^{-2} m/s sliding velocity . The standard deviation increases with decreasing of the sliding velocity to reach ± 0.07 at 5×10^{-7} m/s. The Colbeck study disregarded the capillary attraction between the ice grains and the slider as well as the variation of heat transfer through the slider surface was ignored.

3.3 Adhesion Force of Ice Particles

3.3.1 Literature Review

An adhesive force between ice particles and a surface will exist due to a liquid bridge, which is also known as a capillary bridge. This liquid bridge is usually present because of the condensation of liquid from the surrounding vapour. The capillary force has been reported by Israelachvili (2011) for a thermodynamic non-equilibrium case and it depends on the shape of the capillary bridge which is a function of particle size, contact angle, and the volume of the water liquid (Hwang et al., 1987).

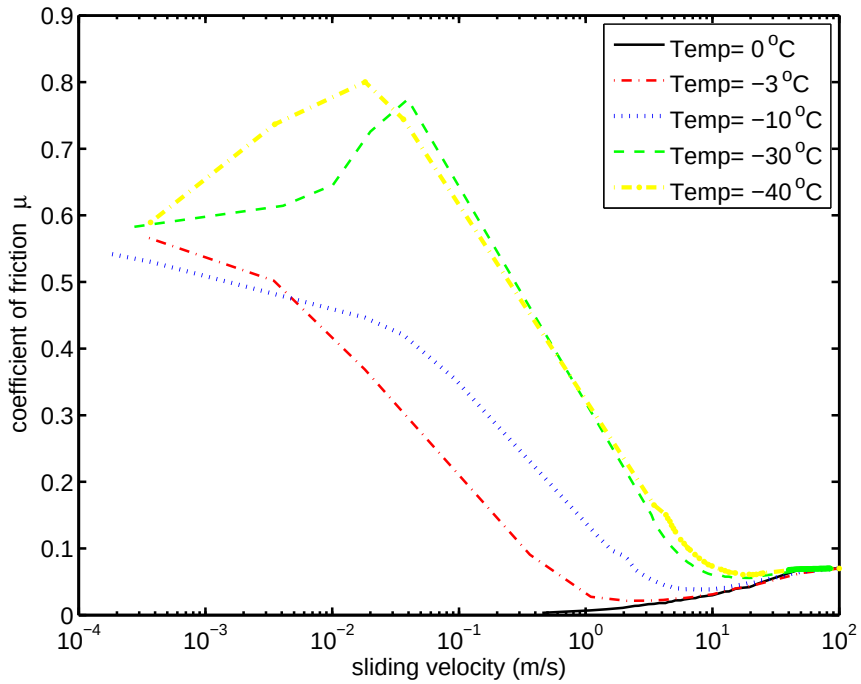

Figure 3.3: Temperature dependence of coefficient of friction of fresh water granular ice as a function of sliding velocity, combined results from Kennedy et al. (2000) and Colbeck (1988) including a velocity offset of 100 times on the data of Kennedy et al. (2000).

Experiments on ice/stainless steel and ice/optically flat fused quartz as a function of surface roughness and rates of shear were performed by Jellinek (1960). Jellinek (1960) found that the adhesive strength decreases with reducing the roughness of the steel surfaces. The results of this study also showed that the shear force was resisted by the friction force, whereas in the tensile case, the surface tension forces are involved, which are much larger than the frictional forces. It was also found that there was a linear increase in the strength of the bond with decreasing temperature until the temperature was reached where the cohesive strength becomes smaller than the adhesive force. The Raraty and Tabor (1958) and Jellinek (1960) results agreed well because of the assumption of the liquid-like film.

A numerical solution of the capillary force between spheres during agglomeration was presented by Hwang et al. (1987). The calculations covered a wide range of variables: particle size ratio, inter-particle distance, contact angle, and liquid volume. The capillary force achieved from these calculations appears more accurate than using a circular profile approximation for the inter-particle liquid bridge. A large capillary force is as-

sociated with a small contact angle, a small separation distance between the spheres, and uniform distribution of the liquid film. Separation conditions were identified using an energy analysis. The equilibrium separation between particles occurs at large contact angle when zero force conditions exist (Hwang et al., 1987).

To investigate the force and rupture behaviour, Willett et al. (2000) suggested an experimental method for measuring the capillary forces occurring due to microscopic liquid bridges. This study considered spheres of equal diameter and sphere-flat plate cases with perfect wetting bridges. The experimental results were compared with the numerical solution in order to establish the accuracy of the methods. The results indicate that the existing criteria for gravitational distortion are too restrictive and that the effect of separation pressure is negligible. The accuracy of the Derjaguin approximation for extending the method to spheres of unequal size was evaluated. The extent of decline in the rupture distances at a contact angle of zero and 40 ° was predicted numerically and a simple correlation was proposed.

To measure the adhesive force between ice particles in air and in a sucrose solution, a micromanipulation method was designed by Fan et al. (2003). Ice particles were produced in a heating/cooling stage chamber under a microscope. The ice particles' diameter varied from 10 to 300 μm. The results of this study show that the adhesive force between ice particles increases with their size and contact time. It was also noted that the adhesive force between the particles generated in aqueous solution is significantly smaller than that in the air. Fan et al. (2003) suggested using the Johnson, Kendal and Robert theory (JKR) to enhance knowledge of the ice particle interface. This technique can be implemented to study the adhesive force and interaction between ice particles in a wide range of contexts.

The particle-particle adhesion forces were measured in ice and clathrate hydrates using a micro-mechanical testing technique by Yang et al. (2004). In this work, the particle radius was approximately 200 μm with a temperature range from -10 to 2 °C at atmospheric pressure. The results show that the hydrate and ice curves overlap, suggesting that there is a similar adhesion system which relies on the melting temperature of the solid. Also, the measured forces declined as the temperature was reduced from the freezing temperature of the particles. The recorded forces and trends were explained

using a model for capillary cohesion with rough surfaces.

By analysing the liquid bridge force, the physical mechanism of liquid bridge and rupture energy were calculated by Mu and Su (2007). The viscous force and rupture energy of a pair of central moving spherical particles connected by a pendular liquid bridge with an interstitial Newtonian fluid were considered. The effects of liquid volume and separation distance on the static liquid bridge were also studied. The results indicated that with an increase in the liquid bridge volume, an increase in the rupture energy occurs when the granularity of the particles is constant. It was also found that the rupture energy increased with increasing particle size at constant liquid bridge volume, and the liquid bridge force approaches zero if the particle is dry or if the liquid bridge volume is very small.

A thermodynamic approach for the calculation of the capillary adhesion force at zero separation was introduced by Sprakel et al. (2008). This study discussed sphere-plate and sphere-sphere geometries. The results of this approach were validated by comparison with experimental tests and self-consistent field calculations. The self-consistent field calculation results were presented to study capillary condensation and capillary forces. The capillary condensation is the process of forming a new stable phase between two surfaces. The results show a deviation in the numerical technique of the thermodynamic approach from the self-consistent field calculations, which can be attributed to finite size effects of the system.

3.3.2 Adhesion Force Formula

An analytical solution for the Laplace-Young pressure equation was developed by Orr et al. (1975) for all potential types of pendular rings and liquid bridges when the effect of gravity is insignificant. The adhesion force of a rigid sphere-sphere and a sphere-flat plate has been discussed by a large number of researchers (Antonini et al., 2009; de Lazzer et al., 1999; Hwang et al., 1987; Israelachvili, 2011; Mu and Su, 2007; Sprakel et al., 2008; Willett et al., 2000). Figure 3.4 illustrates the typical arrangement that is considered.

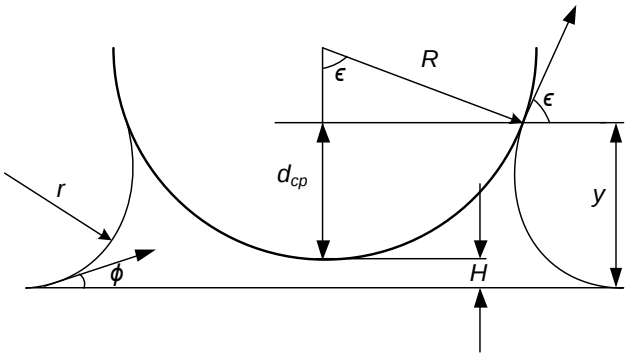

Figure 3.4: Illustration of the liquid bridge between a sphere and a flat plate.

Based on the Gorge method, the adhesion force between particle and plate is given by Rabinovich et al. (2005),

$$F_{ad} = -\frac{4\pi\sigma R\cos(\phi)}{1+\frac{H}{d_{cp}}} - 2\pi\sigma R\sin(\epsilon)\sin(\phi+\epsilon) \tag{3.1}$$

where R is the particle radius, ϵ is the embracing angle, ϕ is the contact angle that the liquid makes with the wall, σ is the water surface tension coefficient, and H is the shortest distance between the particle and the plate. In this equation the first term is the attractive force between the particle and the surface due to the liquid bridge, while the second term is the vertical component of the surface tension force of the liquid bridge. This equation is consistent with JKR theory, which assumes that the real particles are elastic and on colliding with a surface, they deform elastically under the influence of the impact load. Because the ice particles are never completely rigid, this assumption replicates the ice impinging on a surface and with adhesive force. This will lead to an increase in the finite contact area between the ice particle and the surface.

In the case of a small volume of liquid bridge, it was found that the second term on the right hand side of the adhesion equation is insignificant in comparison with the first one and it can be neglected (Rabinovich et al., 2005). On the other hand, for any geometry considered, if the volume of the liquid bridge is big enough so the contact angle ϕ is close to 90 °, the surface tension force and its contribution in the total magnitude of the adhesion forces is going to be more significant. The surface tension

force may reach the order of the first term in the capillary force equation and could even exceed it (de Lazzer et al., 1999). d_{cp} can be found from the following expression:

$$d_{cp} = -H + \sqrt{H^2 + V_L/(\pi R)} \tag{3.2}$$

where V_L is the volume of the liquid bridge. The embracing angle can be calculated with respect to volume from (Rabinovich et al., 2005):

$$\epsilon^2 = \frac{2H}{R}\left(-1 + \sqrt{1 + \frac{V_L}{\pi R H^2}}\right) \tag{3.3}$$

3.3.3 Application of Adhesion Results to Current Study

It can be assumed a thin layer of water exists on the ice particle (Pan et al., 2011) prior to colliding with the surface and at the initiation of the ice accretion. Due to the accumulated particles impact energy, a thick water layer can appear later. In the present study, both terms of the adhesion force will be considered. Figure 3.5 shows the adhesion force variation with particle radius at a constant liquid bridge volume fraction of 0.05, and different values for the contact angle. The surface tension for water at 0.01 °C is 75.7 mN/m (Vargaftik et al., 1983). The liquid bridge volume fraction is the ratio of the liquid volume in the liquid bridge to the total ice particle volume.

The effect of the volume fraction on the adhesion force can be seen in Figure 3.6 at constant particle diameter of 50 μm and with different values of the contact angle (ϕ). The range of volume fractions considered in Figure 3.6 is from 0 to 0.2 as discussed by Hwang et al. (1987). The range of the contact angles (ϕ) in both Figures 3.5 and 3.6 varies from 0 to $\pi/2$ as reported by Sprakel et al. (2008).

The adhesion force is a linear function of the ice particle size and varies with particle diameter more strongly for small contact angles as shown in Figure 3.5; as the particle diameter increases the magnitude of the adhesion force increases. Increases in the contact angle lead to a decrease in the adhesion force magnitude due to the cosine function in the first term of the adhesion force formula, and at $\phi = \pi/2$ the first term in Equation (3.1) will vanish and the adhesion force is equal to the vertical component of the surface tension force. Figure 3.6 shows that the liquid bridge volume fraction

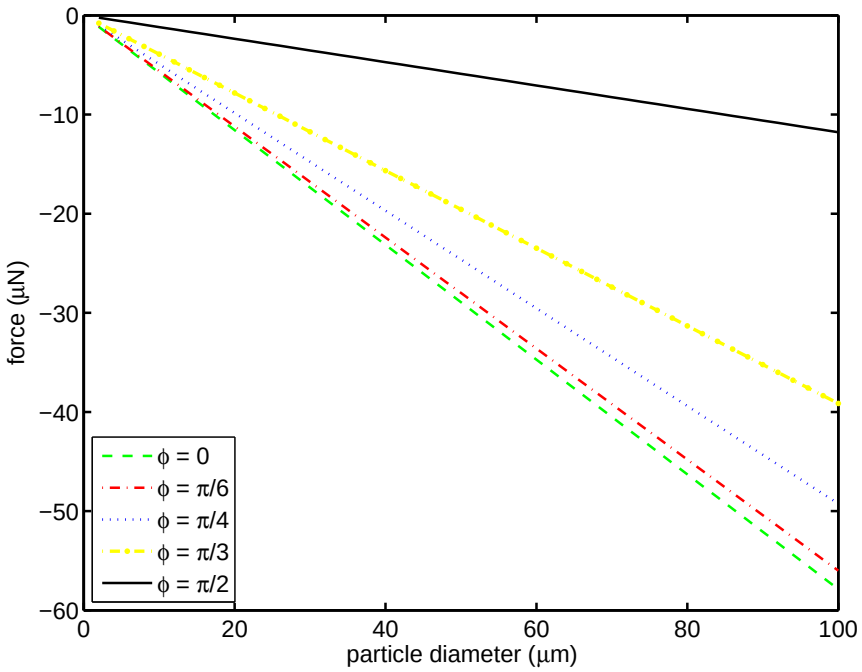

Figure 3.5: Adhesion force variation with particle diameter and contact angle (ϕ) at constant liquid bridge volume fraction of 0.05.

has a relatively minor influence on the magnitude of the adhesion force. For $\phi = 0$ and with a variation of the volume fraction from 0 to 0.2, the adhesion force decreases from $-24\,\mu$N to $-33\,\mu$N.

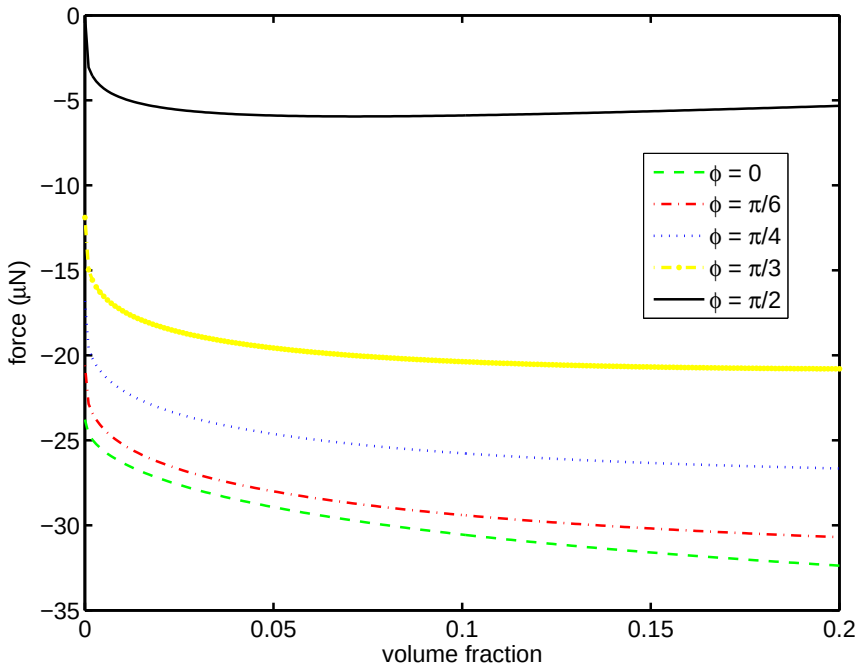

Figure 3.6: Adhesion force variation with liquid bridge volume fraction and contact angle (ϕ) at a constant particle diameter of 50 μm.

The adhesion force for a particle of 100 μm diameter is 55 μN as shown in Figure 3.5, so the pressure is 0.007 MPa and for a particle of 20 μm diameter, the adhesion force is found to be 13 μN, which produces a pressure of 0.042 MPa. The condition for Kennedy test was confirmed by this calculation.

Many researchers have discussed the effect of the liquid bridge volume fraction and the contact angle on the adhesion force (Rabinovich et al., 2005; Willett et al., 2000; Hwang et al., 1987). For the rest of this chapter, the liquid bridge volume fraction will be taken as 0.05. In the absence of more complete information, adopting this volume fraction as a representative value appears reasonable.

3.3.4 Saffman Force

The Saffman force for a relatively slow flow field (up to 12 m/s) was found experimentally by Mollinger and Nieuwstadt (1996) for a particle of around 100 μm in size. In this test the velocity gradient of the turbulent boundary layer was measured in a horizontal wind tunnel. In the present study, comparable conditions were used with the

duct flow velocity around 10 m/s, and the maximum particle diameter around 100 μm. Based on the Mollinger and Nieuwstadt (1996) data, a Saffman force around 30 nN will be generated. As this value of the Saffman force is several orders of magnitude smaller than the capillary bridge force, the Saffman force will not be considered in the model.

3.3.5 Electrostatic Adhesion Force

The electrostatic adhesion force is the adhesion of charged particles to surface and it depends on the particle size, shape, and particle charge. According to Walton (2008) and Hays (1995), electrostatic adhesion forces are on the order of 100 nN. From the results of Takeuchi (2006), the electrostatic force was found to be 342 nN for a 50 μm particle diameter and surface roughness (Ra) is 1.97 μm. These electrostatic adhesion figures are substantially smaller than the capillary bridge forces identified in this work and therefore will not be considered any further in this work.

3.4 Aerodynamic Forces

3.4.1 Stagnation Point

The drag force on ice particles in the vicinity of a stagnation point of a cylinder is considered in the present work. In the stagnation region, the flow speed aligned with the surface and external to the boundary layer u_e increases linearly with distance from the stagnation point as illustrated in Figure 3.7. The rate of velocity change in the flow external to the boundary layer is dependent on the diameter of the cylinder D, the on-coming flow speed U_∞, and the Mach number. For low Mach numbers, the relationship can be approximated using (White, 1991):

$$\frac{u_e}{x} \approx 4\frac{U_\infty}{D} \tag{3.4}$$

The local velocity external to the boundary layer can therefore be estimated if the values of U_∞ and D are specified, and the distance from the stagnation point x is

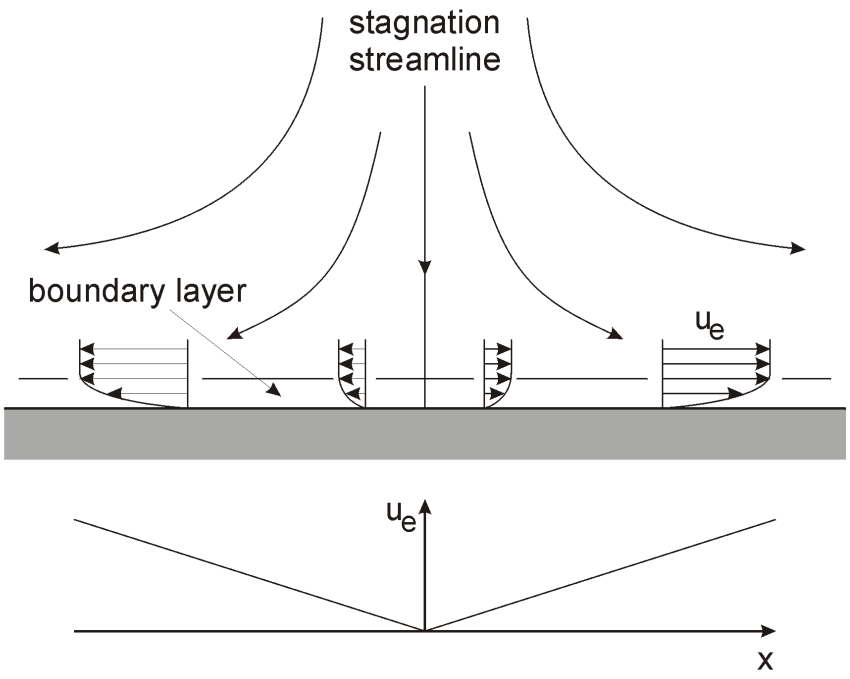

Figure 3.7: Illustration showing stagnation point flow field.

known. The D value in this chapter will be the diameter of the cylindrical specimen, which is approximately 10 mm.

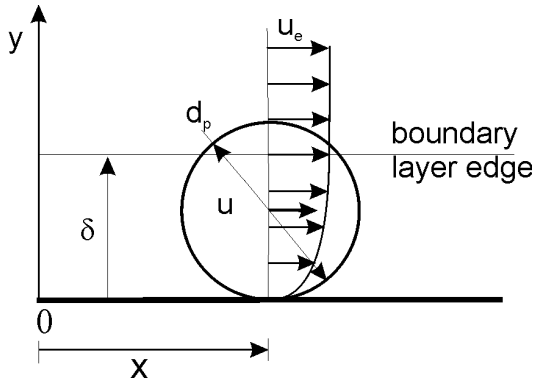

Figure 3.8: Illustration of a particle in the vicinity of the stagnation point.

The flow is assumed to be laminar in the stagnation region. The dimensionless boundary layer coordinate is defined as (White, 1991)

$$\gamma = y\sqrt{\frac{B}{\nu}} \tag{3.5}$$

where y is the boundary layer coordinate measured from the surface, ν is the kinematic viscosity of the air, and $B = 4\frac{U_\infty}{D}$. The velocity profile u/u_e in the boundary layer is

Table 3.1: Velocity profile in the stagnation point boundary layer.

$\gamma = y\sqrt{\frac{B}{\nu}}$	u/u_e	$\gamma = y\sqrt{\frac{B}{\nu}}$	u/u_e
0	0.00000	1.3	0.87381
0.1	0.11826	1.4	0.89681
0.2	0.22661	1.5	0.91617
0.3	0.32524	1.6	0.93235
0.4	0.41446	1.7	0.94578
0.5	0.49465	1.8	0.95684
0.6	0.56628	1.9	0.96588
0.7	0.62986	2	0.97322
0.8	0.68594	2.2	0.98386
0.9	0.73508	2.4	0.99055
1	0.77787	2.6	0.99464
1.1	0.81487	2.8	0.99705
1.2	0.84667	3	0.99843

presented in Table 3.1 (White, 1991). The boundary layer thickness δ_{99} occurs when $\gamma = 2.4$.

To find the average flow velocity to which a particle placed at the plate in the boundary layer is exposed, a kinetic approach is taken. The average flow velocity is then defined as:

$$\bar{u} = \sqrt{\frac{1}{A_T}\int_0^{d_p} u^2 dA} \tag{3.6}$$

where A_T is the particle cross sectional area, u is the local air speed, which is a function of y, d_p is the particle diameter, and dA indicates the integration proceeds relative to the particle cross sectional area. The particle cross section is circular so Equation (3.6) will be:

$$\bar{u} = \sqrt{\frac{8}{\pi \cdot d_p^2}\int_0^{d_p} u^2 \cdot \sqrt{y \cdot d_p - y^2}\, dy} \tag{3.7}$$

Since y is equal to $\gamma\sqrt{\frac{\nu}{B}}$, Equation (3.7) can be written as:

$$\frac{\bar{u}}{u_e} = \sqrt{\frac{8}{\pi \cdot d_p^2} \int_0^{d_p \cdot \sqrt{\frac{B}{\nu}}} (\frac{u}{u_e})^2 \cdot \sqrt{\gamma \cdot \sqrt{\frac{\nu}{B}} \cdot d_p - (\gamma \cdot \sqrt{\frac{\nu}{B}})^2} \cdot \sqrt{\frac{\nu}{B}} \cdot d\gamma} \tag{3.8}$$

By integrating Equation (3.8) numerically, the average (normalised) velocity to which a particle is exposed, was obtained. The results of Equation (3.8) for different free stream speeds can be seen in Figure 3.9.

It was assumed that there is no rotating movement of the particle and that the particle has a linear velocity only. The relative Reynolds number (Re) was calculated for the ice particle based on the difference between the average flow speed $\bar{u}$ and the particle speed u_p along the surface. For particle Reynolds numbers less than 2×10^5 and greater than zero, the drag coefficient was taken as (White, 1991):

$$C_D = \frac{24}{Re} - \frac{6}{1 + \sqrt{Re}} + 0.4 \tag{3.9}$$

Equation (3.9) is only suitable for laminar flow and sphere-shaped particles. The reference area (A_T) of the drag coefficient is the cross sectional area of the particles.

The drag force can be written in terms of the drag coefficient, the reference area of drag, and the dynamic pressure

$$D_{force} = 0.5 \cdot C_D \cdot \rho \cdot (\bar{u} - u_p)^2 \cdot A_T \tag{3.10}$$

As the free stream speed increases, the drag force increases as a function of $(\bar{u} - u_p)^2$ at any particle size. Figure 3.10 shows the relation between the drag force and the particle size at different free stream velocities on the assumption that the particle is stationary ($u_p = 0$) and centred at a distance of one particle diameter away from the stagnation point ($x = d_p$). The distance of $x = d_p$ is considered in this work because a particle centred precisely at the stagnation point is theoretically not subjected to any aerodynamic forces and hence the distance of one particle diameter is the nearest location to the stagnation point worthy of further consideration.

The drag force magnitude in Figure 3.10 is relatively small until the particle diameter reaches 100 μm. In the stagnation point case, the boundary layer thickness remains

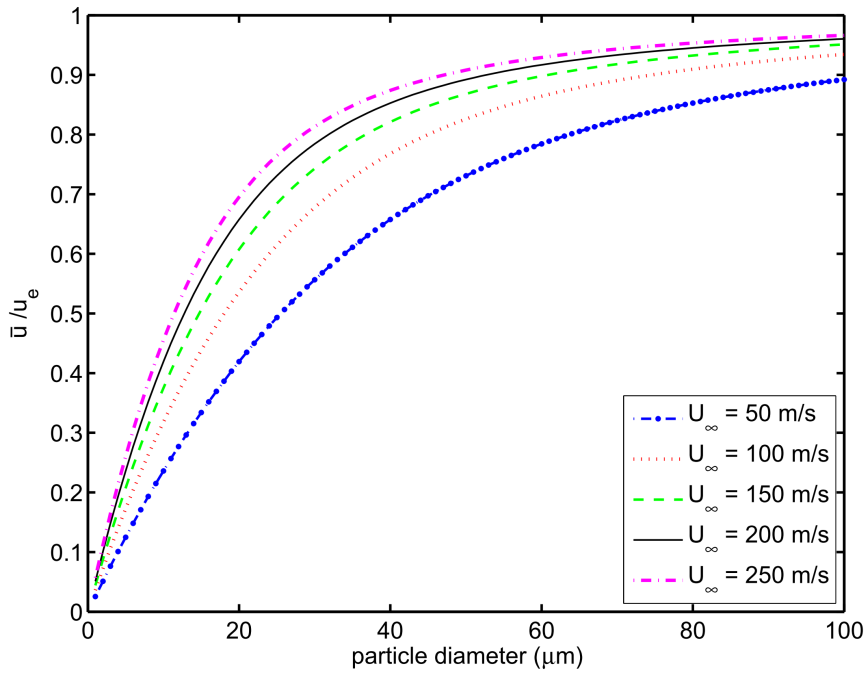

Figure 3.9: The average flow velocity to which a particle in the stagnation region boundary layer is exposed for different ice particle diameters and free stream speeds.

constant. The stagnation region boundary layer thickness varies from 8.81 μm for a free stream flow speed of 250 m/s to 19.7 μm for 50 m/s. As the distance from the stagnation point increases with particle size, the effective external flow speed becomes more significant and a rapid increase in aerodynamic drag is observed as the particle diameter increases.

In the case of $x = d_p$, the aerodynamic drag increases with particle diameter and due to the increase of the boundary layer thickness with x but if the distance x has constant value, the average velocity affecting the particle will increase with the particle diameter only as the boundary layer thickness is constant.

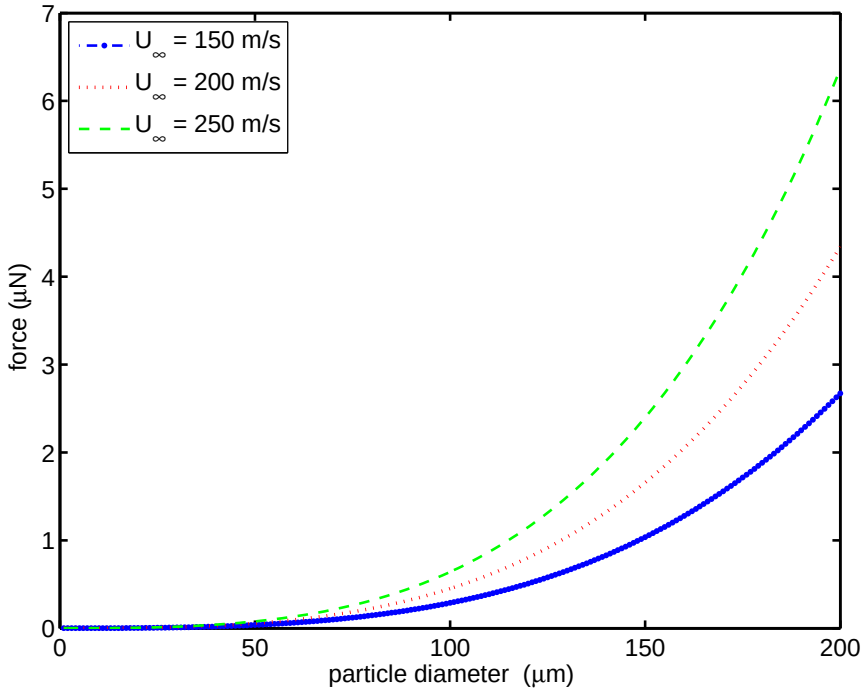

Figure 3.10: Variation of aerodynamic force on particles in the stagnation region boundary layer with the particle diameter and free stream speeds.

3.4.2 Flat Plate

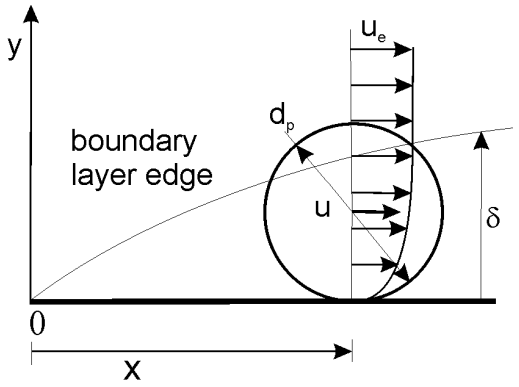

Figure 3.11: Illustration of a particle in the flat plate boundary layer.

For the flat plate arrangement, the boundary layer thickness increases with the distance from the leading edge, as illustrated in Figure 3.11. For this reason, it is expected that only small ice particles can accumulate near the leading edge and that the maximum diameter of particles which can adhere to the surface increases with the distance from the leading edge. From Schlichting (1979), the dimensionless boundary layer coordinate

is:

$$\gamma = y \cdot \sqrt{\frac{U_\infty}{\nu x}} \tag{3.11}$$

The velocity profile u/U_∞ in the boundary layer is presented in Table 3.2 (Schlichting, 1979). The boundary layer thickness δ_{99} for the flat plate occurs when $\gamma = 5$. If y is equal to $\gamma\sqrt{\frac{\nu x}{U_\infty}}$ and by substituting in Equation (3.7) and by dividing by U_∞:

$$\frac{\bar{u}}{U_\infty} = \sqrt{\frac{2}{A_T}\int_0^{d_p\cdot\sqrt{\frac{U_\infty}{\nu x}}} (\frac{u}{U_\infty})^2 \cdot \sqrt{\gamma \cdot \sqrt{\frac{\nu x}{U_\infty}} \cdot d_p - (\gamma \cdot \sqrt{\frac{\nu x}{U_\infty}})^2} \cdot \sqrt{\frac{\nu x}{U_\infty}} \cdot d\gamma} \tag{3.12}$$

where A_T is equal to $\pi \cdot d_p^2/4$. Figure 3.12 shows the result from a numerical integration of Equation (3.12). By taking $x = d_p$ and calculating the aerodynamic force, Figure 3.13 was generated using Equations (3.9) and (3.10). Figure 3.13 shows that as the particle size increases, the drag force also increases. The laminar boundary layer thickness increases with the square root of distance from the leading edge, and the particle distance from the the leading edge increases in direct proportion to the particle diameter. In Figure 3.13, drag force increases with particle diameter because the frontal area increases with the square of the particle diameter.

Table 3.2: Velocity profile in the boundary layer on a flat plate at zero incidence

$\gamma = y\sqrt{\frac{U_\infty}{\nu x}}$	$\frac{u}{U_\infty}$	$\gamma = y\sqrt{\frac{U_\infty}{\nu x}}$	$\frac{u}{U_\infty}$
0	0.00000	3.2	0.87609
0.2	0.06641	3.4	0.90177
0.4	0.13277	3.6	0.92333
0.6	0.19894	3.8	0.94112
0.8	0.26471	4.0	0.95552
1.0	0.32979	4.2	0.96696
1.2	0.39378	4.4	0.97587
1.4	0.4527	4.6	0.98269
1.6	0.51676	4.8	0.98779
1.8	0.57477	5.0	0.99155
2.0	0.62977	5.2	0.99425
2.2	0.68132	5.4	0.99616
2.4	0.72899	5.6	0.99748
2.6	0.77246	5.8	0.99838
2.8	0.81152	6.0	0.99898
3.0	0.84605	7.0	0.99992

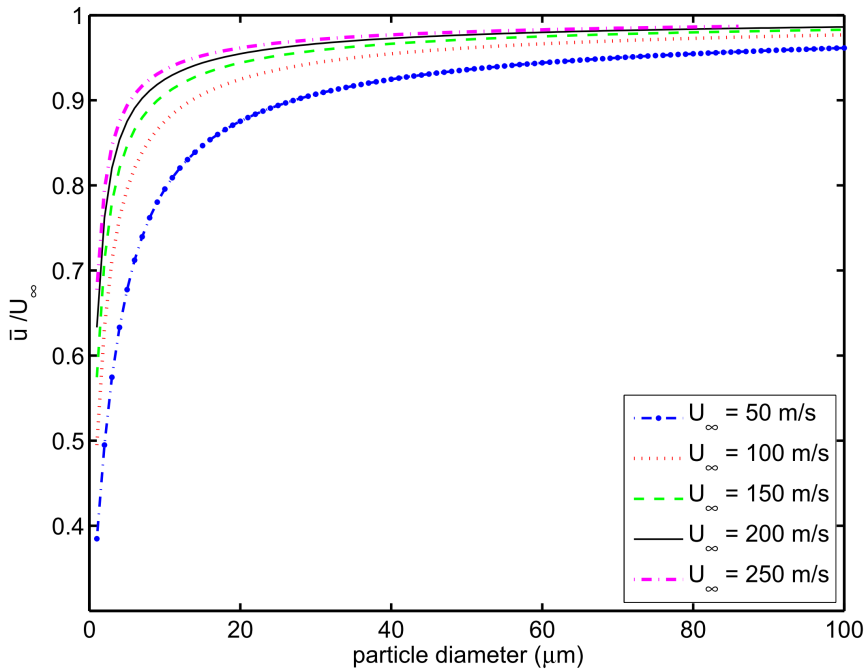

Figure 3.12: The average flow velocity to which a particle in a flat plate boundary layer is exposed for different ice particle diameters and free stream speeds.

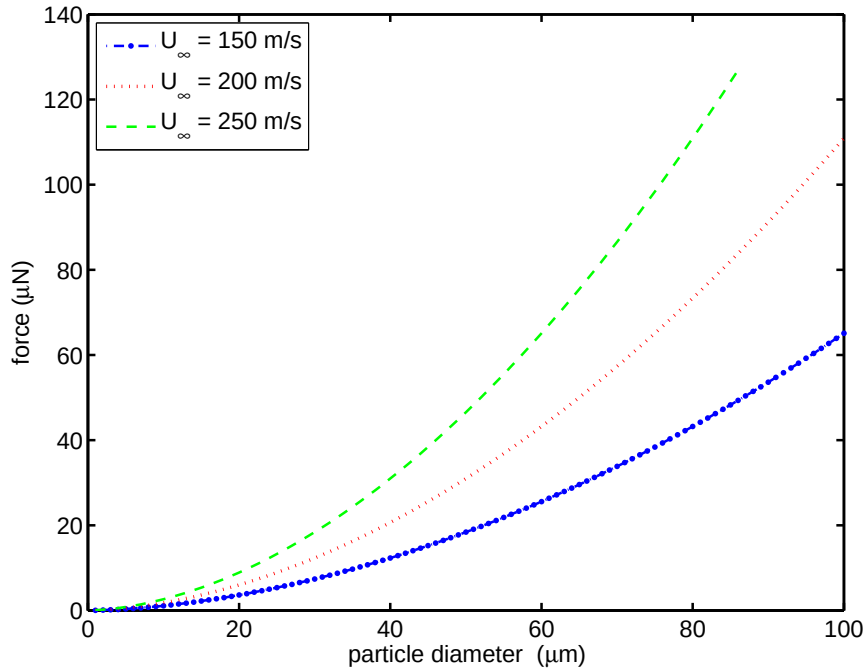

Figure 3.13: Variation of aerodynamic force on particles in a flat plate boundary layer with particle diameter and different free stream speeds.

3.5 Results

The combination of the forces considered in this work and their effect on the ice particle is illustrated in Figure 3.14. If the particle size, the liquid bridge volume fraction, and contact angle are known, the adhesion force for the particle can be obtained. The friction coefficient for the ice particle can be calculated from the particle/surface temperature and the particle speed on the surface. The friction force can then be determined from the adhesion force and friction coefficient and the particle acceleration can be deduced from the balance of the aerodynamic and friction forces.

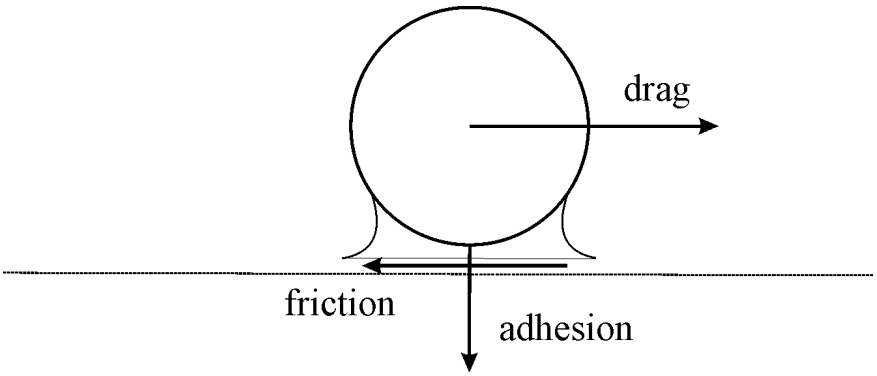

Figure 3.14: Illustration of the forces applied to the ice particle.

3.5.1 Ice Adhesion and Friction Force Results - Two Limiting Cases

From Figure 3.3, a representative maximum value for the ice particle friction coefficient at speeds approaching 0 m/s will be taken as 0.6. The limiting value of friction coefficient at high speeds will be taken as 0.07 (see Figure 3.3). The distance from the stagnation point was taken as $x = d_p$, and at 0.05 volume fraction, Figure 3.15 was produced, for $\mu = 0.6$. It can be seen from Figure 3.15 that at contact angles of $\phi = 0$ and $\pi/6$ the friction forces are similar in both cases because of the cosine function in Equation (3.1). At higher contact angles, the ice particles have a lower associated friction force. For the friction coefficient case $\mu = 0.07$, Figure 3.16 was produced, illustrating the same trends at different magnitude of forces.

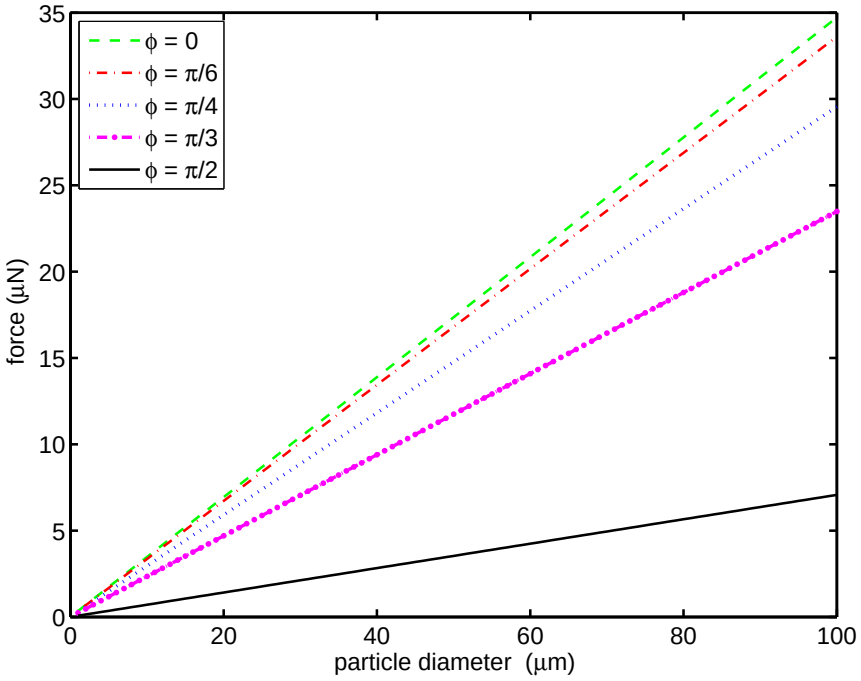

Figure 3.15: Friction force relation with the particle diameter for $\mu = 0.6$, $u_p = 0\,\mathrm{m/s}$, $x = d_p$, volume fraction of 0.05, and different contact angles.

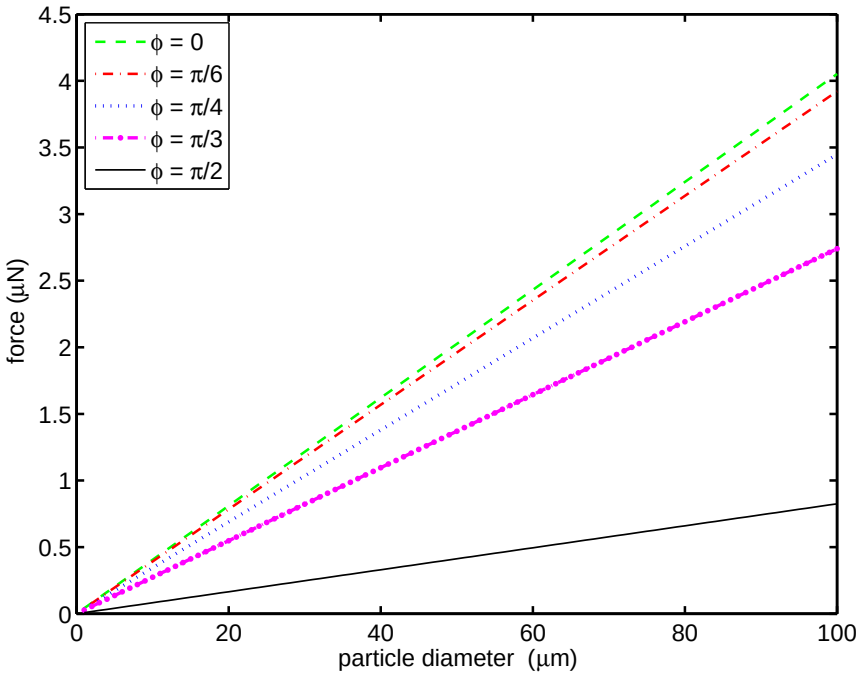

Figure 3.16: Friction force relation with the particle diameter for $\mu = 0.07$, $u_p = 0\,\mathrm{m/s}$, $x = d_p$, volume fraction of 0.05, and different contact angles.

3.5.2 Friction and Aerodynamic Results

3.5.2.1 Stagnation Point Case

For varying particle diameter at locations close to the stagnation point ($x = d_p$) the aerodynamic and friction forces were determined for different free stream speeds as illustrated in Figure 3.17. In this case the friction coefficient $\mu = 0.07$ was assumed, with liquid bridge volume fraction of 0.05. Figure 3.17 suggests that the probability of accretion with a high flow speed is lower than at lower speeds since the drag force increases with flow speed. For low contact angles, the ice particle is more likely to adhere to the surface. With higher values of the friction coefficient or lower values of the contact angle, it appears very likely that a particle at rest will remain permanently in the vicinity of the stagnation point.

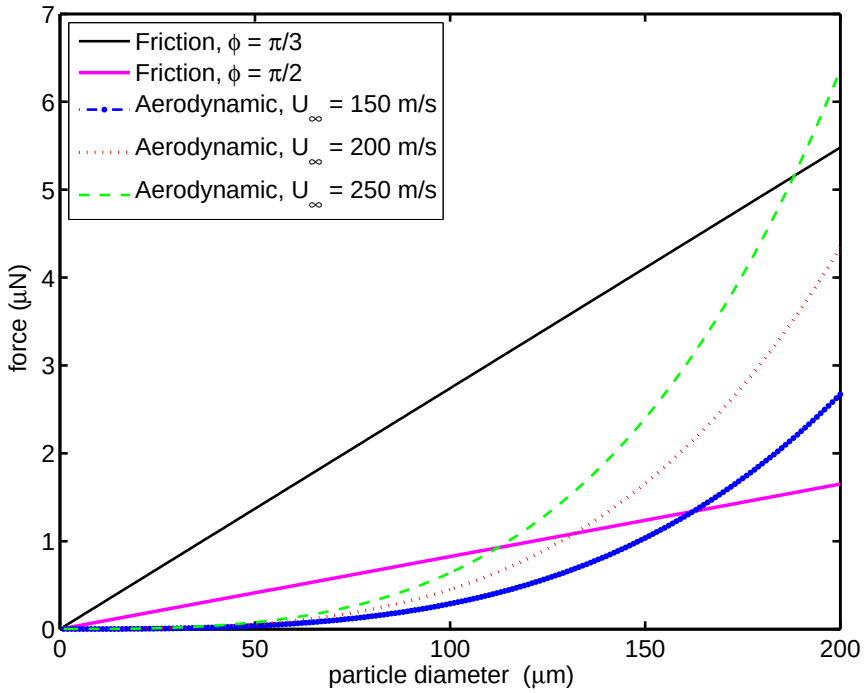

Figure 3.17: Drag force and the friction force variation with particle diameter for $\mu = 0.07$, $x = d_p$, $u_p = 0$, volume fraction of 0.05, at specified contact angles, and free stream speeds.

For a fixed distance from the stagnation point of $x = 1\,\text{mm}$, and otherwise the same conditions of Figure 3.17, Figure 3.18 was generated. In this case, Figure 3.18 shows that the drag force has increased significantly due to the increase of the distance from

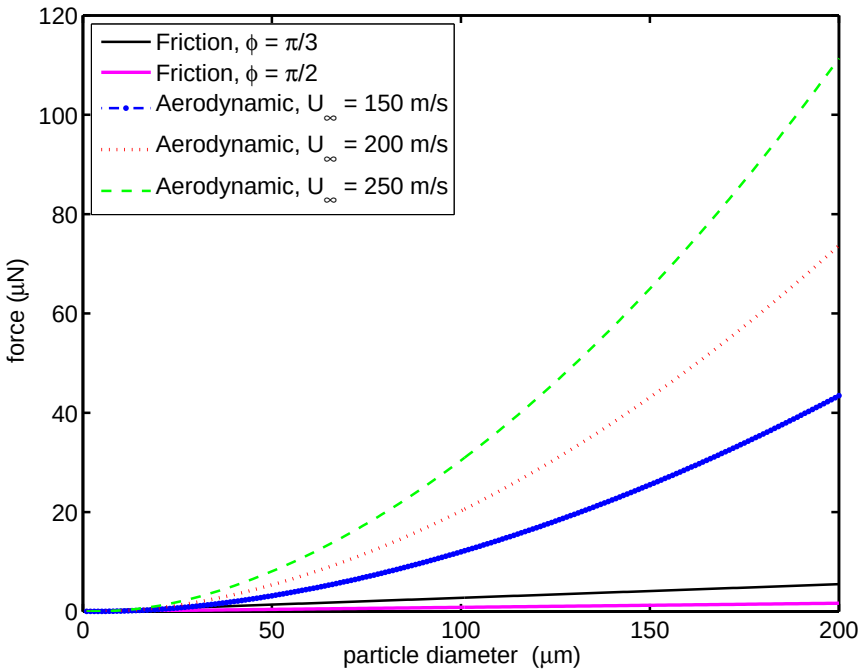

Figure 3.18: Drag force and the friction force variation with particle diameter for $\mu = 0.07$, $x = 1\,\text{mm}$, $u_p = 0$, volume fraction of 0.05, at specified contact angles, and free stream speeds.

the stagnation point, while the friction force did not change as it only depends on the friction coefficient and the contact angle of the particle. In this case, the aerodynamic forces are substantially higher than the friction forces so particles will not accrete under these conditions. However, if the highest friction coefficient value is now considered ($\mu = 0.6$) with otherwise the same conditions, a different situation arises as illustrated in Figure 3.19. At the higher coefficient of friction, Figure 3.19 demonstrates that there are some particle diameters for which the friction force is higher than the aerodynamic force and hence accumulation may initiate for these particles at this distance from the stagnation point.

By finding the point where the drag force equals the friction force at a constant contact angle and different free stream speeds, Figure 3.20 was produced. Figure 3.20 shows that at a given speed there is a critical distance from the stagnation point where the friction and the drag force are equal. Larger particles will be less likely to stick to the surface at locations further from the stagnation point. It also shows that with increasing the free stream speed, only smaller particles can accumulate on the surface

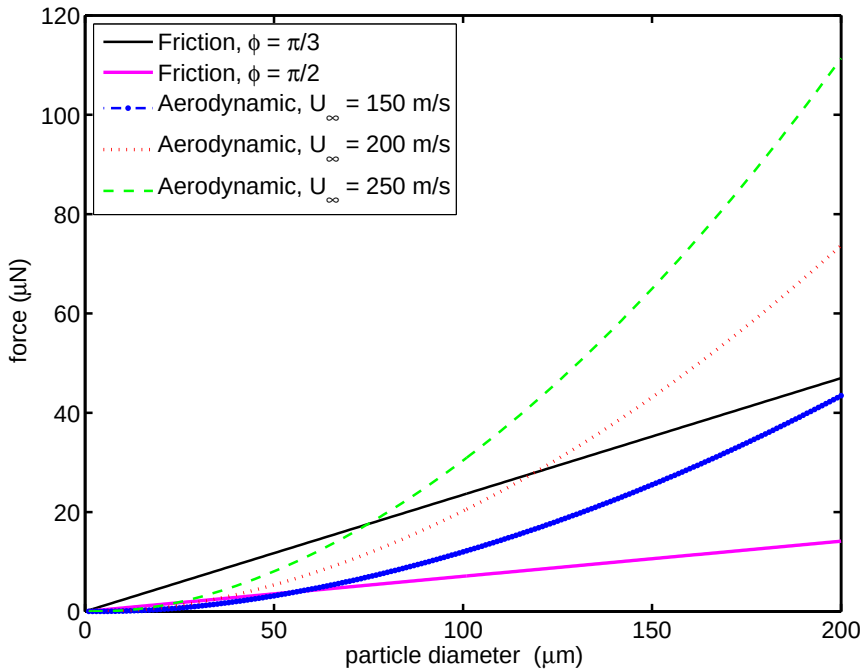

Figure 3.19: Drag force and the friction force variation with particle diameter for $\mu = 0.6$, $x = 1\,\text{mm}$, $u_p = 0$, volume fraction of 0.05, at specified contact angles, and free stream speeds.

at a given distance from the stagnation point.

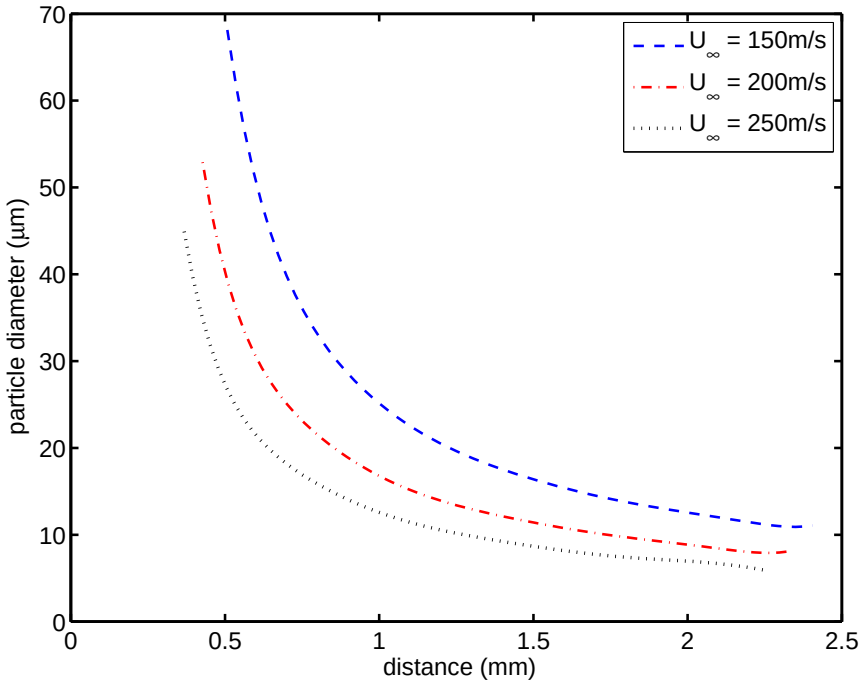

Figure 3.20: The relation between ice particle size which can accumulate on the cylinder surface and distance from the stagnation point for $\mu = 0.07$, $u_p = 0\,\mathrm{m/s}$, volume fraction of 0.05, $\phi = \pi/3$, and different free stream speeds.

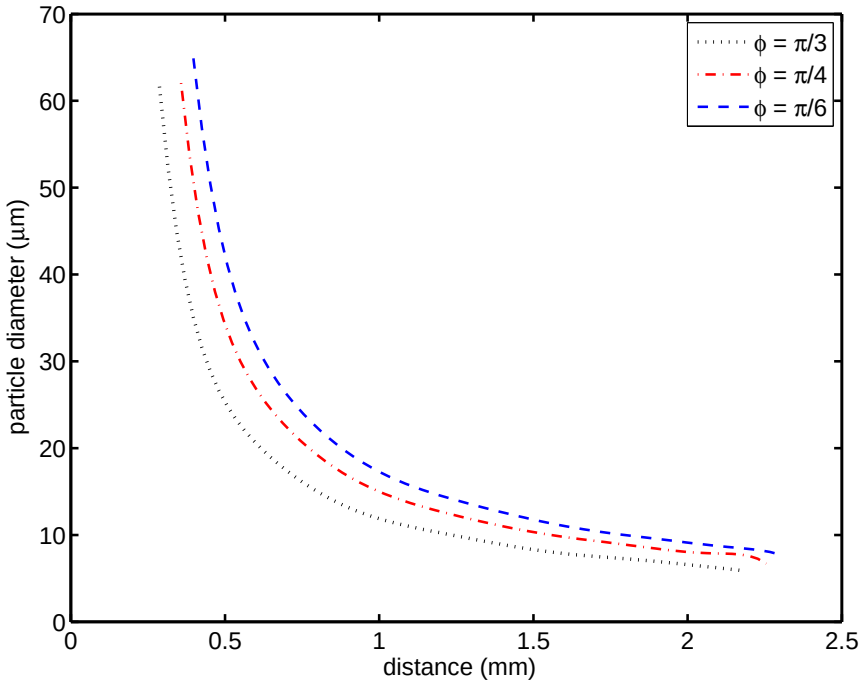

Figure 3.21: The relation between ice particle size which can accumulate on the cylinder surface and the distance from the stagnation point for $\mu = 0.07$, $u_p = 0$, $U_\infty = 200\,\mathrm{m/s}$, volume fraction of 0.05, and different contact angles.

Figure 3.21 was generated by determining the points where the the drag force equalled the friction force at a constant free stream speed for different contact angles. It can be noticed that with decreasing the contact angle, larger ice particles can accumulate at a given distance from the stagnation point due to the increase of the adhesion force and hence friction force with decreasing contact angle.

3.5.2.2 Flat Plate Case

For the flat plate case at a friction coefficient of 0.6 and the lowest contact angle, results were plotted in Figure 3.22 to compare the ice particle friction force and the drag force. It can be seen that at a distance of $x = d_p$, only small particles ($d_p < 50\,\mu$m) can accumulate. Results for a fixed distance of $x = 1\,$mm are presented in Figure 3.23 which shows a decrease in the aerodynamic force because of increased boundary layer thickness at this fixed location of x in comparison with the $x = d_p$ results in Figure 3.22. This results in an increase in the ice particle sizes which may remain stationary on the plate at this location or further downstream. The maximum ice particle diameter for which the friction force is higher than the aerodynamic force is around $60\,\mu$m for the conditions considered in Figure 3.23. If the friction coefficient is lower than 0.6, or if the contact angle increases, the current model indicates that only particles with diameters lower than $60\,\mu$m would be able to remain stationary on the surface at the location $x = 1\,$mm.

Figure 3.24 shows the relationship between the size of the particle and the nearest distance to the leading edge where it can remain stationary at a constant contact angle, friction coefficient, volume fraction, for different flow speeds. This figure was obtained by identifying the conditions where the drag force equals the friction force. As the flow speed increases, the boundary layer thickness decreases and the drag force increases so only smaller particles can remain stationary on the surface at a given distance from the leading edge as indicated in Figure 3.24.

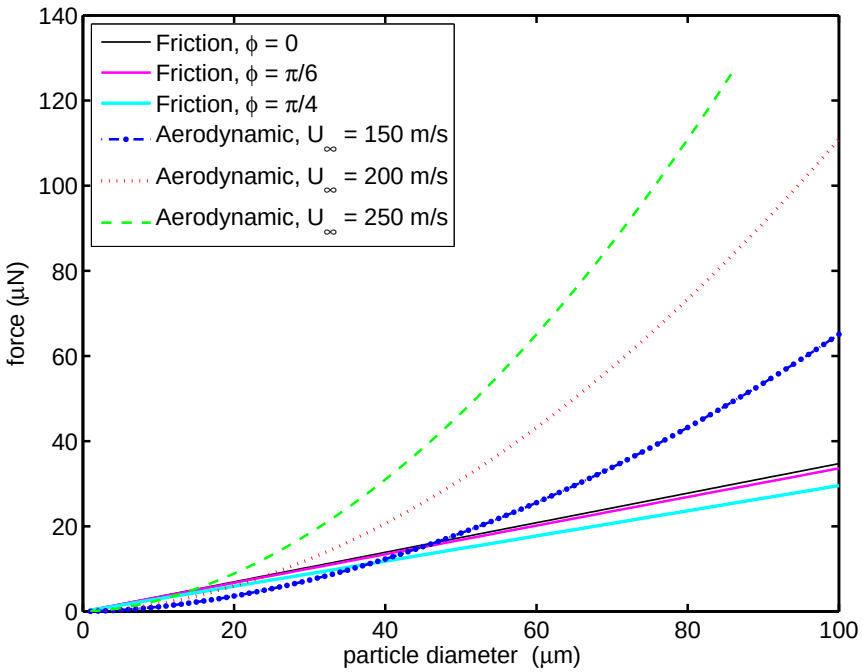

Figure 3.22: Drag force and friction force variation with particle diameter for $x = d_p$, $\mu = 0.6$, volume fraction of 0.05, at specified contact angles and free stream speeds.

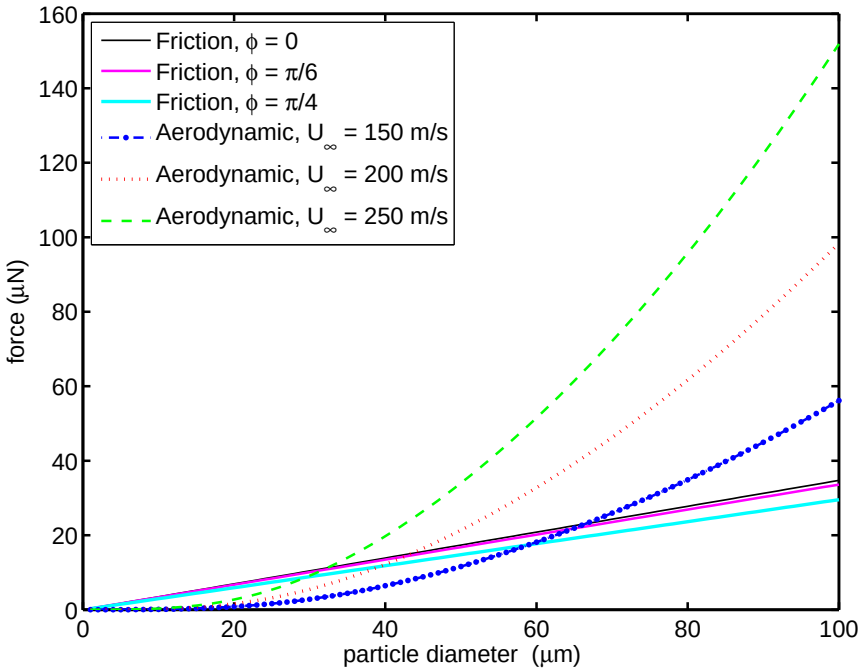

Figure 3.23: Drag force and friction force variation with particle diameter for $x = 1\,\mathrm{mm}$, $\mu = 0.6$, volume fraction of 0.05, at specified contact angles and free stream speeds.

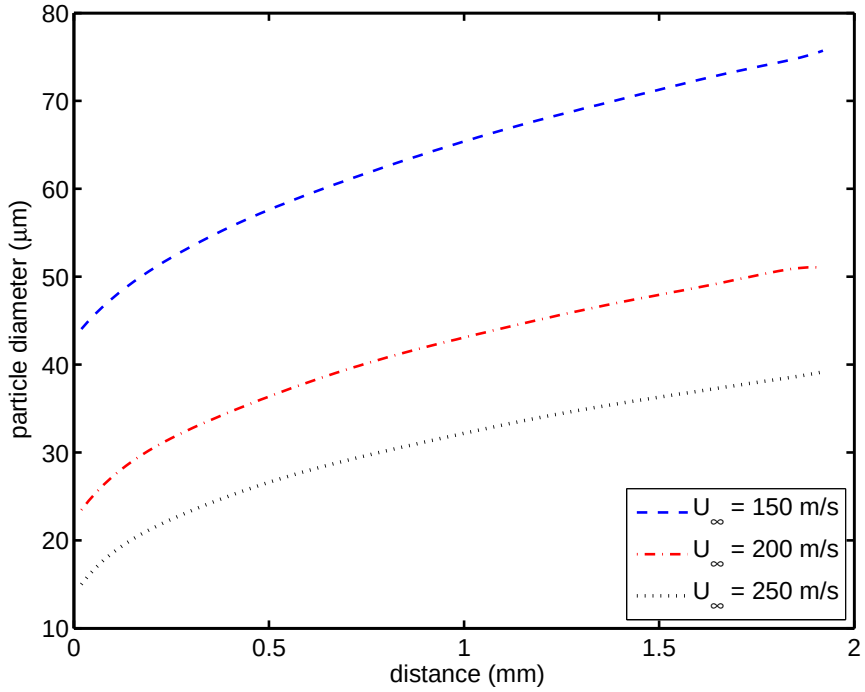

Figure 3.24: The relation between ice particle size which can accumulate on the flat plate surface and the distance from the leading edge for $\mu = 0.6$, $u_p = 0$, volume fraction of 0.05, $\phi = \pi/6$, and different free stream speeds.

3.6 Discussion

The friction, adhesion, and the aerodynamic forces which affect the ice particle on the surfaces have been discussed in this chapter. Two aerodynamic configurations have been considered: the stagnation point region of cylinder and a flat plate surface. The ice particle friction coefficients were adopted from previous studies and two particular coefficient of friction values have been studied 0.07 and 0.6, corresponding to the friction coefficient values at high speed and zero velocity respectively.

The adhesion force between an ice particle and a surface depends on the volume of the liquid bridge, the liquid contact angle, and the particle diameter. It was found that the contact angle and the particle diameter have stronger influence than the liquid bridge volume. So, a volume fraction (the liquid bridge volume to the particle volume) of 0.05 was adopted and the range of the contact angle considered was varied from 0 to $\pi/2$. The results show that with increasing the contact angle, the adhesion force decreases in magnitude, and the highest adhesion force value can be reached at $\phi = 0$.

The drag forces for ice particles near the stagnation point of a cylinder and on a flat plate were discussed. The drag force increases as the particle diameter and the distance from the stagnation point increases. For the flat plate case, as the distance from the leading edge increases, the drag force on a given size particle decreases.

Based on a balance of aerodynamic and friction forces, the maximum ice particle size which can remain stationary on the surface can be found. In the stagnation point case, and at the smallest friction coefficient considered of $\mu = 0.07$ and liquid film contact angles of $\phi = \pi/3$ and $\phi = \pi/2$ results at $x = d_p$ show the particles friction force to be higher than the aerodynamic force and hence particle adhesion in the stagnation region is very likely. By increasing x to 1 mm, at $\mu = 0.07$ and $\phi = \pi/3$ and $\phi = \pi/2$, particles cannot remain stationary at this location as the aerodynamic forces are much higher than the friction forces. However, if the friction coefficient changed to $\mu = 0.6$ with same contact angles, particles with diameters less than 200 μm could remain stationary on the surface if free stream flow speed was 150 m/s or less.

In the flat plate case, the highest friction coefficient considered of $\mu = 0.6$ and relatively low contact angles of 0, $\pi/6$, and $\pi/4$ should generate the highest friction forces. The results for $x = d_p$ show that a 50 μm diameter particle is the maximum particle size that can remain stationary at low flow stream speed, and decreases as the free flow speed increases. At $x = 1$ mm, the boundary layer is thicker than the leading edge, this lead to bigger than 60 μm particle diameter can accumulate. If the $\mu = 0.07$ was considered there is no accumulation can occur.

Although both cases show a possibility for the friction force to overcome the aerodynamic force, the stagnation point in the cylinder model is more likely to have higher accumulation rate, because the conditions considered will produce a much lower friction force than in the flat plate case. The high accumulation rate because of the boundary layer thickness is thicker near the stagnation point and decreases at further distance from the stagnation point. While the flat plate boundary layer thickness increases with distance from the leading edge and even with extreme conditions were assumed of high friction coefficient (0.6) and low contact angles only smaller size ice particle can accumulate on the surface.

3.7 Conclusion

The model introduced herein considers the balance between the aerodynamic drag forces with the boundary layer and the friction force on ice particles due to the surface adhesion through a liquid film. Results indicate that the ice particles can remain stationary near the stagnation point of a cylinder because of the low aerodynamic drag relative to the friction forces on the ice particles. With an increase of the distance from the stagnation line, the aerodynamic drag force increases and only the smaller particles can stay stationary on the surface. At locations away from the stagnation point, the initiation of accretion depends more strongly on the assumed friction coefficient and the assumed contact angle between the liquid film and the surface. In general, the stagnation point case will have more accumulation for higher values of the friction coefficient and smaller values of the contact angle. The friction coefficient is a function of both the temperature and the speed of the particle along the surface and the contact angle is likely to be function of the surface conditions.

Ice accretion within a flat plate boundary layer was also considered. In this case, the aerodynamic drag force is high relative to the friction force close to the leading edge. Hence, only small particle sizes can remain stationary on the surface close to the leading edge of the plate. By increasing the distance from the leading edge, the boundary layer thickness increases, and this leads to a decrease in the aerodynamic drag forces and increases the prospects for large size particles to stay stationary on the surface.

Chapter 4

Apparatus Design and Characterisation

4.1 Introduction

A new, small scale wind tunnel with the capacity to simulate aspects of the thermal and particle conditions relevant to the problem of ice accretion initiation in turbofan engines has been developed. In this tunnel, it is possible to take the approximately spherical water droplets to a temperature less than $-40\,^{\circ}\mathrm{C}$ for sufficient time to ensure all particles are ice. In addition, the tunnel allows for a microscopic focus on a small area of the test specimen to aid the understanding of the ice accretion initiation.

In this chapter, the apparatus arrangement and operation details will be discussed. The performance characteristics of the individual components are defined. The ultrasonic atomiser performance, the temperature distributions through different sections and on the test specimen, wind tunnel velocity profile, and the ice water content in this facility have been measured. The whole rig was also tested with all components together and its overall performance will be introduced.

A preliminary version of the icing wind tunnel is presented in Appendix A. In this earlier version of the facility, a different spray nozzle was used and the temperatures

were not sufficiently low to ensure all water droplets formed ice.

Although the aircraft engine ice crystal icing environment is likely to include a mixed phase of crystals and liquid droplets, this chapter will focus on fully frozen ice crystal icing as a first step to understand the fundamental icing crystal physics.

4.2 Experimental Apparatus Dimensions and Operation

Since the solid phase ice accretion problem in turbofan engines appears to depend on the solid-liquid phase transition in water and the aeroplanes of interest fly at high altitudes where the local static temperatures range from -30 to $-50\,^{\circ}\mathrm{C}$, it is important to duplicate the relevant local compressor first stage temperatures for the air ($\approx -15\,^{\circ}\mathrm{C}$) and the surfaces ($\approx +5\,^{\circ}\mathrm{C}$). Such conditions can be conveniently achieved by establishing an open circuit wind tunnel for producing ice particles and injecting them onto test specimens as illustrated in Figure 4.1. The facility is positioned inside a cold room.

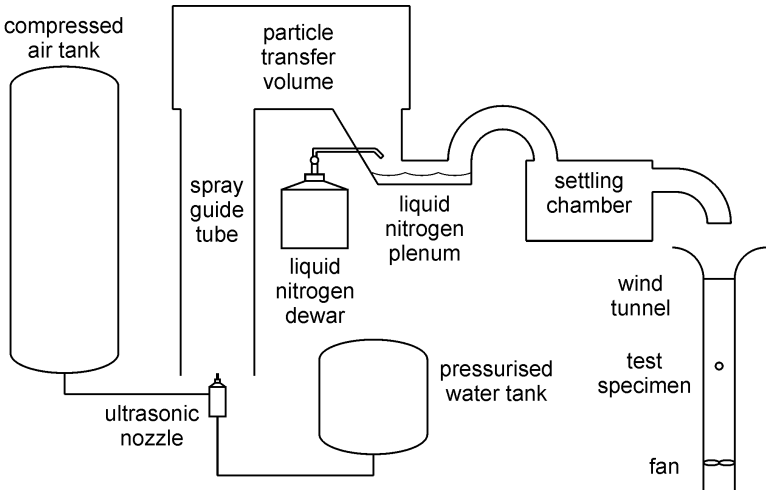

Figure 4.1: Schematic diagram for the icing wind tunnel arrangement.

In this facility the ice crystal icing will be considered as a first step toward more the complex mixed phase study in the engine icing field. This experimental arrangement generates relatively slow air flows, up to a maximum of 12 m/s. In addition, the wind tunnel duct is also small, 7.2 cm in diameter. Consequently, direct replication of the aircraft engine icing conditions will not be achieved in this facility. Nevertheless, this

apparatus can produce some solid phase icing data under thermal conditions relevant to the turbofan engine icing problem.

The apparatus operates in a cold room which has a set point temperature of between $-20\,^{\circ}\mathrm{C}$ and $0\,^{\circ}\mathrm{C}$. Air temperatures within this range are encountered in the early stages of those engine compressors exposed to potential high altitude solid phase ice accretion conditions. The tests described in the present work were performed with the cold room temperature around $-10\,^{\circ}\mathrm{C}$.

To aid the elimination of the larger water droplets during transit through the spray guide (Figure 4.1) and to minimise the vertical gradients in particle concentrations which can occur in the wind tunnel flow due to the gravity, a vertical orientation for the wind tunnel has been adopted as suggested by Brennen (2005). Brennen (2005) identifies different multiphase flow regimes and one of these is the Homogeneous Flow regime, which takes place when the particles are small and the volume fraction of the suspended phase is low or moderate. This flow regime happens when the particles sizes are of the order of tens of microns or less, which represents the particle sizes of interest in this project.

The apparatus consists of: a compressed air vessel, pressurised water tank, ultrasonic atomiser, spray guide tube, particle transfer volume, liquid nitrogen dewar, liquid nitrogen plenum, settling chamber, Perspex vertical wind tunnel, and the test specimen. All the equipment mentioned above is assembled inside a cold room. The cold room operating conditions are between -20 and $0\,^{\circ}\mathrm{C}$ and the temperature can be set with $0.1\,^{\circ}\mathrm{C}$ accuracy. The cold room measures $2 \times 2.2 \times 3\,\mathrm{m}$, a volume of $13.2\,\mathrm{m}^3$.

The maximum operating pressure for the compressed air vessel is 12 bar at a minimum temperature of $-15\,^{\circ}\mathrm{C}$. The compressed air vessel has a $2.2\,\mathrm{m}^3$ volume. The main function of this vessel is to supply sub-freezing pressurised air to an ultrasonic atomiser (PNR Nozzles model MAD 0331 B1), and as the air expands through the nozzle, it will enhance the water droplet phase changing process. The air regulator at the outlet of the air vessel is maintained at 4 bar. While the function of the pressurised water tank is to supply the nozzle with pressurised water, the water pressure also affects the outlet droplet size. The volume of the water tank is 18 L with a maximum operating

pressure of 1 MPa. Distilled water with no chemical agents has been used in this study.

The injected water droplets interact with the freezing air induced from the cold room through the spray guide tube, which is a PVC pipe of 1.45 m height and 254 mm diameter, and in so doing, the particles slow down during mixing with the air. The small droplets are carried out of the spray guide tube with the flow while the larger droplets tend to sink down towards the ultrasonic nozzle. The small water droplets transit through the particle transfer volume and enter the liquid nitrogen plenum. Water droplets can remain in the liquid phase until $-40\,^{\circ}\mathrm{C}$ (Kuhns, Mason, Kuhns and Mason, 1968; Mossop, 1955; Langham and Mason, 1958). As detailed in Section 4.3, the liquid nitrogen is used to absorb energy from the water droplets, taking them to temperatures less than $-40\,^{\circ}\mathrm{C}$ for a sufficiently long period of time to ensure that the droplets change to solid particles.

The liquid nitrogen plenum is built from steel and has a cross section dimension of 101.6×76.2 mm and is 40 cm long. The liquid nitrogen is supplied from a 20 L (MVE) dewar fitted with a manual discharge device to maintain a certain level of the nitrogen in the duct. The liquid nitrogen level is checked using a thermocouple at a particular point, and as the liquid level rises, the temperature rapidly drops down to $-150\,^{\circ}\mathrm{C}$. When the air-water droplet mixture travels over the liquid nitrogen, the mixture temperature dropped from $-5\,^{\circ}\mathrm{C}$ at the inlet of the liquid nitrogen duct to much less than $-40\,^{\circ}\mathrm{C}$ at the exit of the steel duct.

The settling chamber had dimensions of $600 \times 450 \times 370$ mm. It receives the flow from the liquid nitrogen plenum and gives it additional residence time at a temperature lower than $-40\,^{\circ}\mathrm{C}$ and it also works as a thermal shock absorber, damping the effects of rapid temperature changes from the dewar valve opening. With the help of a small fan inside the settling chamber, which works as an agitator, the particle-laden flow continually mixes and the temperature at the outlet of the settling chamber was around $-40\,^{\circ}\mathrm{C}$.

The mixture of ice particles and the cold air stream leaves the settling chamber and mixes again with the cold room air as it is drawn in to the wind tunnel. The air flow speed inside the perspex tunnel is controlled by a suction fan which can vary the speed between 0 to 12 m/s. The suction in this case is preferable to the blowing process to

reduce the turbulence as indicated in Pruppacher and Neiburger (1968). The relative humidity of the mixed flow in the wind tunnel duct was found to be 20 %.

4.3 Thermal Conditions for Liquid Freezing

An important feature in designing the icing wind tunnel is the water droplet residence time in the flow before it collides with the surface. To estimate the residence time in the liquid nitrogen duct and the settling chamber, the total volume of the two components can be divided by the volume flow rate giving 10.4 s as an upper estimate of the residence time. Another estimate of the residence time can be obtained from the shortest possible flight distance travelled by a droplet through the liquid nitrogen duct and the settling chamber (approximately 2.0 m) divided by an exit flow speed of 2 m/s giving a value of 1.0 s as lower estimate of the residence time. Natural convection heat transfer between the droplet and the cold air/nitrogen is considered as the main cause of droplet temperature decrease. In reality, an additional heat transfer component due to forced-convection will also be present, but the assumption of zero relative velocity between the particle and the cold air/nitrogen stream will result in a conservative calculation. As well, the liquid water droplets are assumed to have a spherical shape. Under these conditions, the Nusselt number can be calculated from the empirical formula (Kreith and Bohn, 2001):

$$Nu_d = 2 + 0.392 \times (Gr_d)^{1/4} \tag{4.1}$$

where Gr_d is the Grashof number, which can be estimated from:

$$Gr_d = \frac{g\beta(T_s - T_\infty).{d_w}^3}{\nu^2} \tag{4.2}$$

where: g gravitational acceleration in m/s^2.

T_s the water droplet temperature measured at the inlet of the liquid nitrogen duct, taken as 0 °C.

T_∞ the cold air stream temperature, within the nitrogen duct, taken as −80 °C.

ν air kinematic viscosity at T_s, taken as $13.3\times10^{-6}\,m^2/s$.

d_w water droplet diameter, taken as 100 μm.

β air coefficient of thermal expansion at T_s, taken as $3.67\times10^{-3}\,K^{-1}$.

If the Grashof number approaches zero because of the small size of the water droplet, the Nusselt number will become equal to 2, that is, $h_c d_w/k \to 2$.

where: h_c convection heat transfer coefficient in $W/m^2.K$.

k the air thermal conductivity at bulk air temperature in the liquid nitrogen plenum is $T_b = -50\,°C$, taken as 0.0204 W/m.K.

From these conditions, h_c will be 409.2 W/m^2K, and from the transient heat transfer equation between the cold air in the liquid nitrogen duct and the water droplet, the time t for the water droplet to achieve −40 °C is:

$$t = -\frac{C\rho V}{h_c A_s} \times \ln \frac{T - T_\infty}{T_s - T_\infty} \tag{4.3}$$

where: C specific heat of water, taken as 4217 J/kg.K.

A_s the water droplet surface area in m^2.

V the water droplet volume in m^3.

ρ droplet density at T_s, $\rho = 999.9\,kg/m^3$.

The quantity $\frac{C\rho V}{h_C A_s}$ is the time constant of the cooling process. From Equation (4.3), the time for the water droplet to reach −40 °C can be estimated as, 0.12 s, an order of magnitude shorter than the minimum residence time estimated for the plenum chamber and the settling chamber. This calculation approach ignores the evaporation and sublimation effect in calculating the time required for the droplet to cool to −40 °C, resulting in a conservative analysis of the problem. The force convection heat transfer which may take place due to the relative velocity of the water droplet and the air/evaporated nitrogen, is also ignored. If the force convection is included, it will

cause a higher value of h_c which yields a shorter time for the droplet to reach the required temperature.

Although a constant heat load applied to the blade surface is more realistic in the engine icing test, this study will focus on a constant surface temperature, to understand the effect of the constant surface temperature on the ice friction coefficient. The friction coefficient depends on the surface temperature and it is difficult to validate the model in Chapter 3, with constant heat flux to the surface. A combination of decreasing the temperature and increasing of the friction coefficient, will add another dimension of complexity to the work.

Most of the major icing wind tunnels are closed loop systems, which helps in maintaining the low temperatures. In addition, they all use spray bar systems to supply the water droplet to the cold stream, although some tunnels such as the Cox tunnel have both spray bars and ice shavers. Spray bar systems produce uniform shapes and controllable small droplet sizes, while the ice shavers generate non-uniform sizes and shapes of ice particles. The spray droplet size is controlled by the pressure of the water and the air supplied to the nozzles. In the ice shaver case, the residence time in the cold stream is not so important whereas water droplets residence time is critical since droplets potentially go through a phase change while suspended in the cold stream.

The chiller unit in the major icing wind tunnels cools the air stream before the spray bar introduces the droplets in order to reduce the blockage due to ice accumulation on the chiller. Nevertheless, with this arrangement there is the potential to freeze the spray bar nozzles, so hot water is usually fed into them to keep the nozzles in an operating condition. Keeping the initial water droplets temperature as cold as possible is helpful in reducing the required residence time in the cold stream. The new solid ice wind tunnel developed herein adopts the open loop system and the water is supplied at room temperature but mixed with subfreezing pressurised air to cool the water droplet in the injection process. The temperature of the air stream loaded with water droplets is monitored at entry to the liquid nitrogen section, and usually it is between $-5\,^{\circ}\mathrm{C}$ and $-0\,^{\circ}\mathrm{C}$.

In the open loop icing tunnel, the water droplets travel through a very cold cooling

section at a relatively low speed to give them the residence time required. Then, the frozen water particles are mixed with another stream at a higher temperature, though still sub-freezing, during the induction to the wind tunnel duct. In this case, the water droplets will undoubtedly be in solid form and will no longer be in a supercooled droplet state.

4.4 Characterisation Tests

The complete experimental apparatus has been tested as a unit and every part has also been characterised separately. The temperatures and the pressures throughout the apparatus were recorded using a data acquisition system which was coded using LabView software. The LabView circuit diagram can be found in Appendix C. Two types of cameras were used: a microscope video camera and a high speed camera.

4.4.1 Droplet and Ice Particles Sizes

The Ultrasonic Atomiser was operated without the ultrasonic generator at a range of different working pressures for the water and air inlets, in order to characterise the ice particle size, shape and distribution. Samples of the droplets were collected on microscope slides at the end of the spray guide tube. The sampling slides were treated with a vegetable oil to improve the capture efficiency, but because bubbles appeared on the surface, which affect the accuracy of the optical measurement, the oil treatment was not continued. Instead, the capture efficiency was demonstrated to be high through computational simulation.

The sampled droplets were found to have a pixel aspect ratio close to one and for this reason, the droplets are assumed to be in spherical shape. A reference image for scaling and image analysis software were used to obtain the droplet sizing from the droplet microscopic photographs. The reference image size was $0.767\,\text{mm} \times 0.575\,\text{mm}$ which represent $1376\,\text{pixel} \times 1032\,\text{pixel}$ and included a total number of particles in excess of 100 particles from several sampling slides. Results from the image analysis of the droplets at different nozzle working pressures of between 3.5 and 5.5 bar for the air,

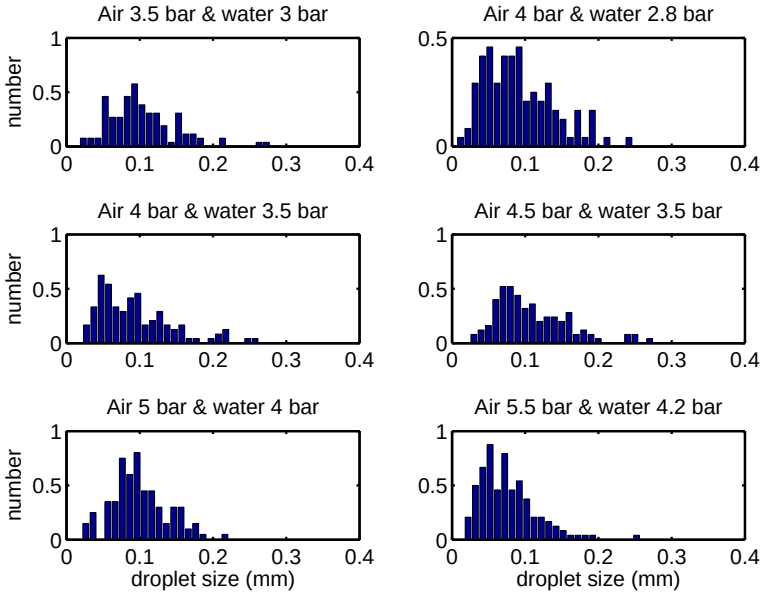

Figure 4.2: Droplets size distribution histograms for different nozzle operating pressures.

and between 2.8 and 4.2 bar for the water are presented in Figure 4.2. These tests were performed at an ambient temperature of 23 °C and another set of ice particle size and distribution were conducted in the cold room at −10 °C as shown in Section 5.3.

For the 2.8 and 3.5 bar tests for the water, the droplet sizes varied from 0.02 to 0.26 mm in mean volume diameter. With an increase in the working pressure for the water and air, the smaller droplet sizes becomes more significant. In the case of 4 and 4.2 bar, the majority of the observed droplet sizes were less than 0.1 mm size.

The droplets sizes collected at the end of spray guide tube were larger than the particle size anticipated in high altitude clouds where ice particle sizes between 1 and 50 μm are expected. The sources of error in these sampling tests include the evaporation of the small water droplets and the spreading of the big droplet which may give bigger water droplet size measurement than the real size in the flow. Two nozzles were tested and only the ultrasonic atomiser was used due to the smaller particle sizes generated by this nozzle. (The second nozzle tested was a UniJet model TX with an orifice of 0.36 mm and the droplet size distribution is described in Appendix A.)

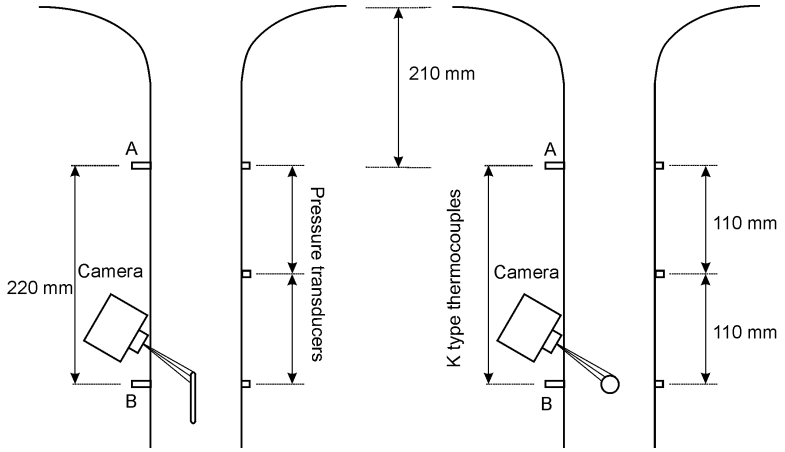

Figure 4.3: Illustration of the wind tunnel duct showing thermocouples, pressure transducers, and microscope camera locations.

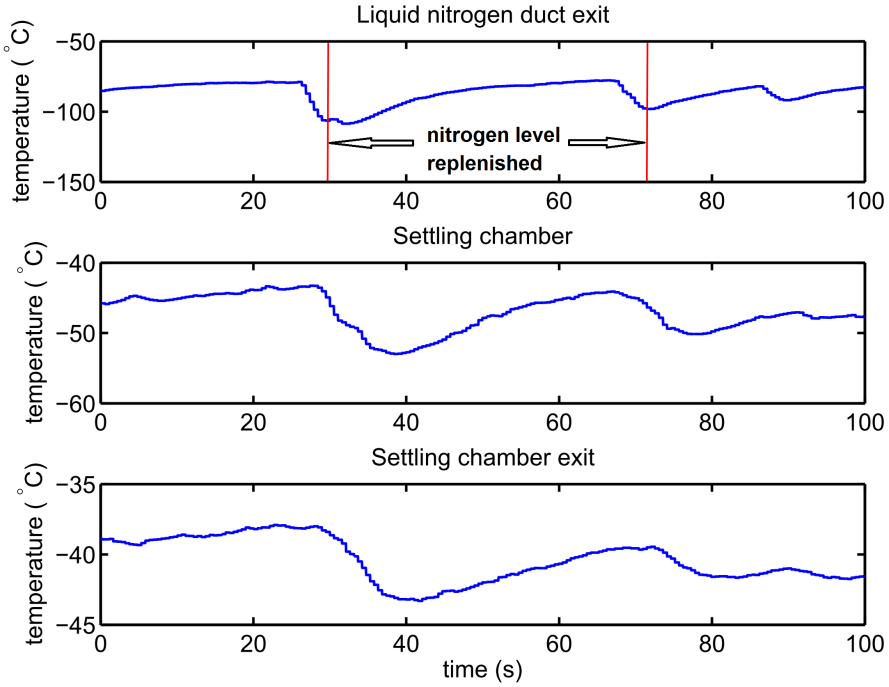

Figure 4.4: Air-water droplet flow temperature measurements within the apparatus upstream of the wind tunnel duct for a wind tunnel flow speed of 6.5 m/s. (Representative result.)

4.4.2 Apparatus Temperature Distribution

The temperatures within the apparatus have been measured at seven different locations to confirm the operating consistency of the facility and that the temperature distribution is sufficient for the required water-to-ice phase change. The measurement

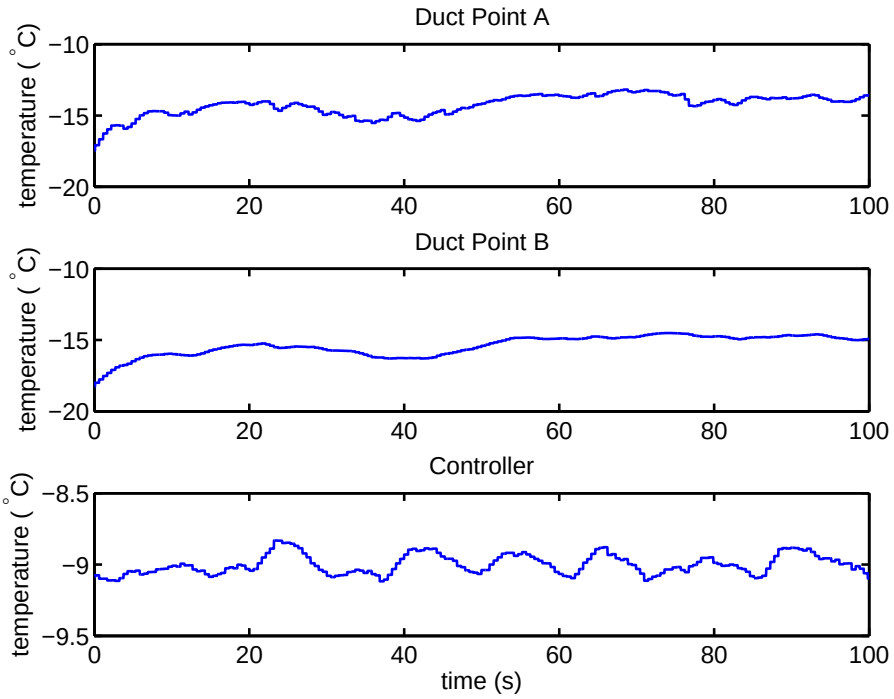

Figure 4.5: Air-water droplet flow temperature measurements within wind tunnel duct for a wind tunnel flow speed of 6.5 m/s. (Representative result.)

locations are: the inlet and exit of the liquid nitrogen plenum, the settling chamber, mixing area between the settling chamber exit and the wind tunnel duct, and two locations inside the duct (points A and B) as shown in Figure 4.3, and the surface of the test specimen.

Temperature measurements from selected points within the apparatus are presented in Figure 4.4 and Figure 4.5. In this test, the data acquisition recording was started and then the liquid nitrogen plenum filled and as a result, the plenum temperature dropped rapidly to less than −100 °C as shown in Figure 4.4. Both Figure 4.4 and Figure 4.5 show the temperature measurements after the video camera recording was started. As the liquid nitrogen filling process continued, the mixed flow temperature at the exit of the plenum chamber fluctuated between −70 °C and −110 °C. Although the flow temperature rises in the settling chamber, it remains less than −40 °C. At the exit of the settling chamber, the flow mixes with cold room air and the temperature again rises but remains uniform in temperature between duct point A and duct point B.

The temperature was measured by a hot wire anemometer-thermostat across the duct close to the test specimen location (at point B) and the variation from the mean value was found to be a maximum of 0.25 °C and for this reason the duct temperature was assumed to be constant.

4.4.3 Wind Tunnel

The wind tunnel duct was built from Perspex to aid the visualisation of the ice particles and cold stream flow. To aid the uniformity of the air flow in the duct, a well rounded entrance arrangement and a downstream fan were used. The air speed in this duct can be controlled to between 0 and 12 m/s. The test specimen was located 40 cm from the entrance of the wind tunnel duct and there are three pressure transducers distributed along this length. There are also two thermocouples along the flow at point A and B for monitoring the flow temperature before the test specimen region as shown in Figure 4.3.

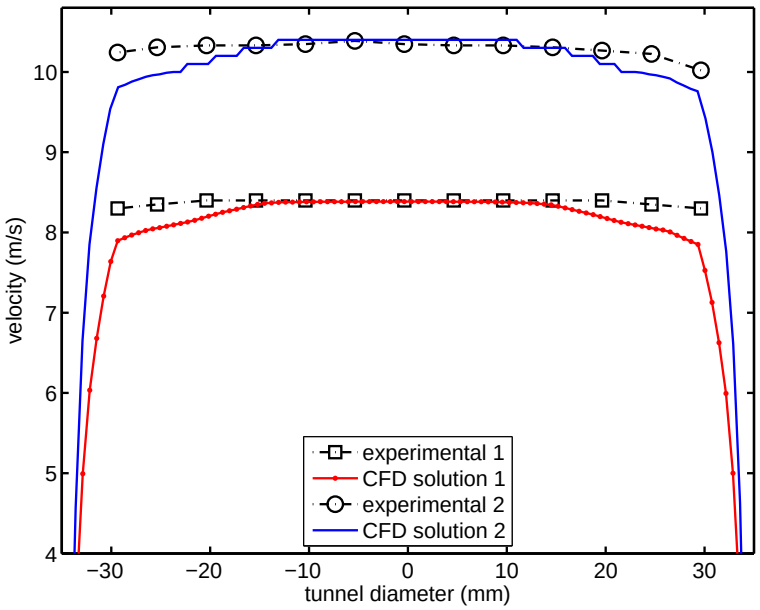

Figure 4.6: Velocity profiles across the wind tunnel duct at the test specimen position for peak flow speeds of 8.4 m/s and 10.2 m/s.

The velocity profile in the perspex tube was measured using a pitot tube and a hot wire anemometer. Results are presented in Figure 4.6 for two flow speeds. Figure 4.6 also presents a comparison of the measured data with a computational fluid dynam-

ics (CFD) simulation of the wind tunnel duct using Fluent. Laminar and turbulent boundary layer simulation were trialled and both tests show a better agreement with laminar CFD solution for the flow field. For these Reynolds numbers, the transition location would be further downstream. The flow speed will be set to less than 10 m/s to confirm the uniformity of the flow and the ice particles.

Two cameras were used to visualise the flow field and the development of icing on the surface: a Photron SA3 with frame rate of 500 frame/second in conjunction with a video recordings of ice accretion on the specimen over longer periods of time using a digital microscope camera was used with a 200X magnification. The general positioning of the cameras is illustrated in Figure 4.3 and Figure 4.7.

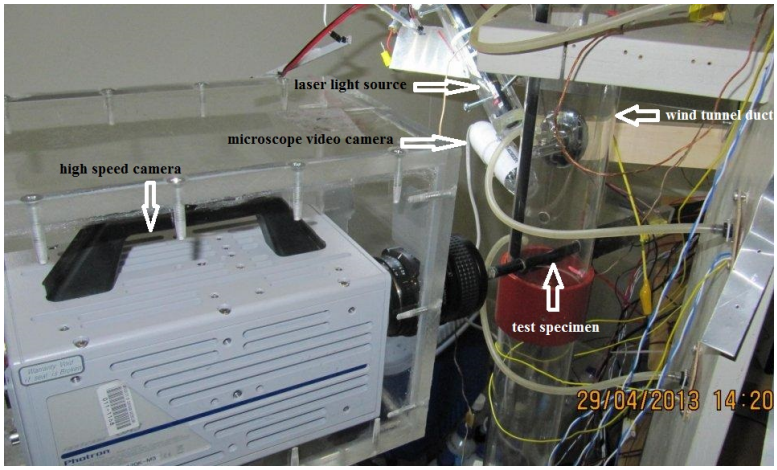

Figure 4.7: Photograph of the wind tunnel duct showing laser light source, high speed and microscope camera locations.

4.4.4 Cylinder and Flat Plate Specimen

The cylindrical specimen was installed perpendicular to the direction of the flow in the perspex duct. It was built from a 10 mm diameter copper tube, with an internal cartridge heater. The gap between the heater and the copper tube was filled with a high thermal conductive material (Silicone Heat Transfer Compound) to ensure a uniform heat transfer around the copper. The ends of the tube were closed with an insulating material (Araldite). Two foil k type thermocouples were bounded onto the cylinder surface. Each thermocouple had a thickness of 0.0005". Figure 4.8 presents a schematic diagram for the cylinder model.

(a)

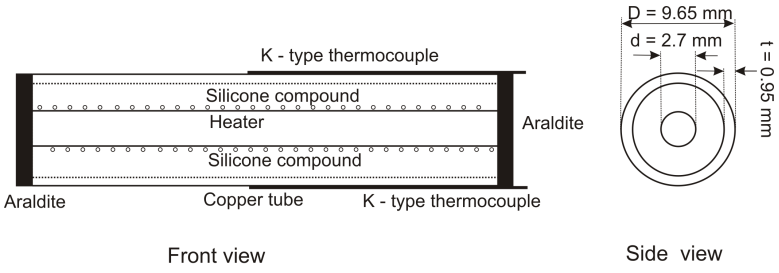

(b)

Figure 4.8: Illustration of the cylindrical test specimen: (a) Photograph, (b) Schematic diagram.

The cylinder was painted matt black, and to decrease the effect of the roughness, it was treated with multiple grades of sand paper until the roughness reading reached an average peak-to-valley height (R_z) of 2.105 μm and a centre line average value (R_a) of 0.433 μm.

To examine the surface temperature distribution around the cylinder, the cylinder was warmed up until the surface temperature stabilised at around 63 °C. The wind tunnel fan was switched on, and an air flow speed of approximately 10 m/s was established. The copper cylinder cooled down to an equilibrium temperature around 32 °C, when the room temperature air drawn through the wind tunnel was around 22 °C. The cylindrical specimen with the thermocouples bonded to the surface was slowly rotated to different orientations and the temperature was recorded for ten different angles starting from zero (corresponding to the stagnation point) up to 180° as shown in Figure 4.9.

The cylinder model temperature distribution shown in Figure 4.9 is compared with a

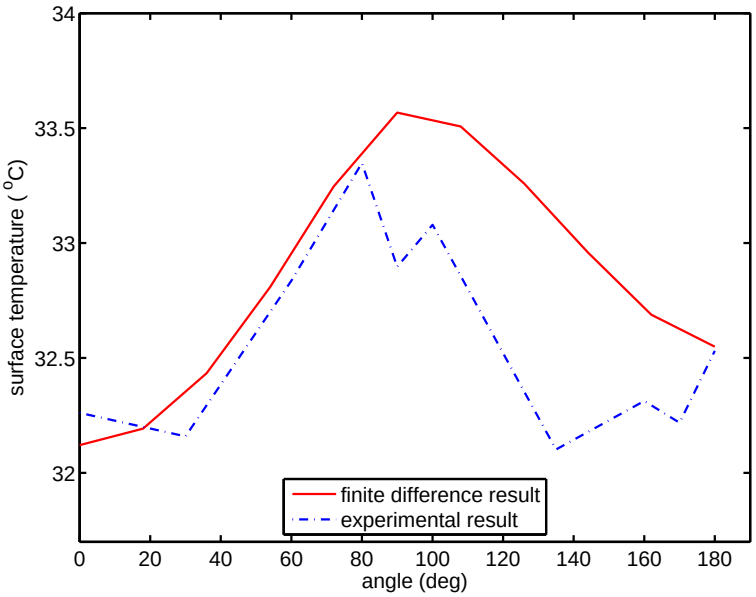

Figure 4.9: Temperature distribution around the cylindrical test specimen flow speed of 10 m/s and an ambient temperature of 22 °C.

one dimensional finite difference thermal simulation based on experimental data for the spatial distribution of Nusselt number from Scholten and Murray (1998). The result in Figure 4.9 shows adequate agreement between the present experimental data and simulation, given the modelling approximations used in the simulation.

In the flat plate arrangement, a copper sheet of thickness 0.5 mm with a heater wire underneath it was constructed as shown in Figure 4.10. The flat plate leading edge diameter was 3 mm. It is important in the arrangements used in the present work to keep a stable and constant temperature through the specimen.

The flat plate was painted matt black and polished in a similar manner to the cylindrical specimen. The roughness of the plate was measured in terms of the average peak-to-valley height (R_z) of 3 μm and the centre line average value (R_a) is 0.62 μm. Both samples were painted in black to obtain high contrast quality from the ice which may build on the surface.

Tests have been performed to measure the temperature distribution on the plate. The flat plate temperatures have been recorded using a thin foil thermocouple and an infrared camera. The infrared photos taken with a FLIR camera (model i5) were

(a)

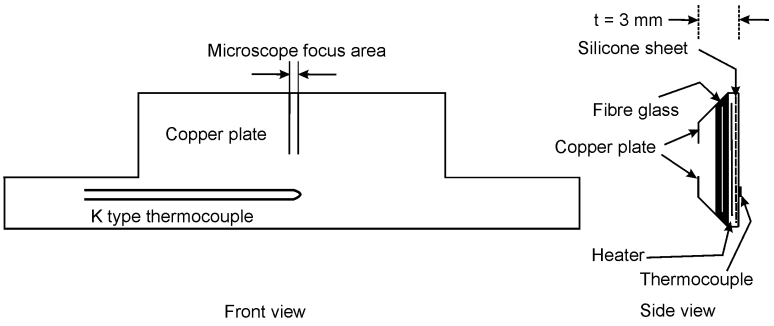

(b)

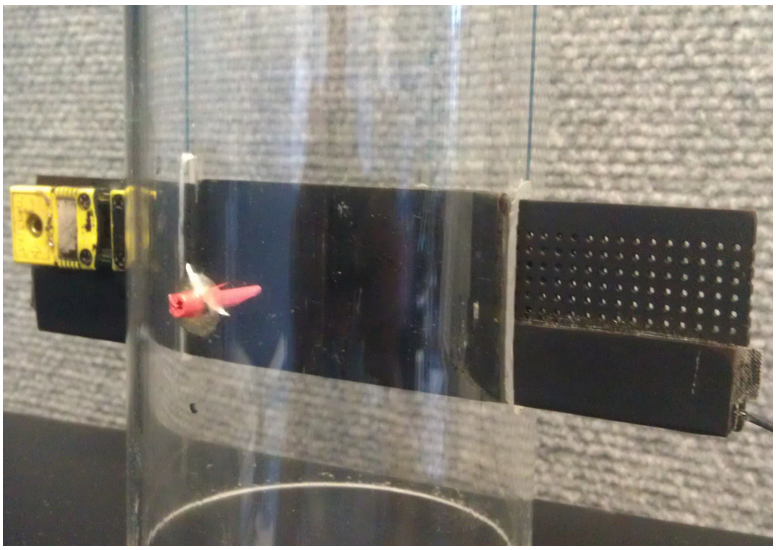

(c)

Figure 4.10: Illustration of the flat plate test specimen: (a) Photograph, (b) Schematic diagram, (c) Location in the tunnel.

converted through a standard colour map to the temperature distribution on the flat plate as illustrated in Figure 4.11. The temperature increases towards the rear of the plate because the boundary layer increases in the direction of the flow.

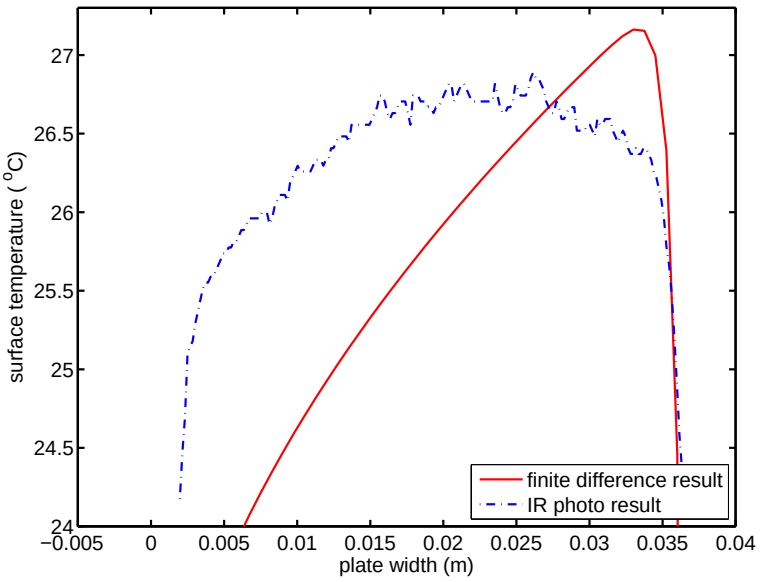

Figure 4.11: Temperature distribution on the flat plate test specimen (centreline profile) at flow speed of 10 m/s and an ambient temperature of 20 °C.

Figure 4.11 also presents simulation results from a one dimensional finite difference model for the flat plate and heater combination. Nusselt numbers for the flat plate boundary layer were adopted from Kreith and Bohn (2001) and the heat input to the plate was estimated from the dimensions of the flat plate and the measured power input to the heater.

It was found that the temperature non-uniformity for the cylindrical specimen was around 1.5 °C with a difference between the surface and the room temperature of 10 °C, and for the flat plate was around 2 °C with a mean difference between the surface and the room temperatures of 6.5 °C. The temperature non-uniformity for the cylindrical specimen is not significant as the ice accretion initiated near the stagnation point and at angle of around 80 ° from the stagnation point there are high aerodynamic force effects, so the particles will likely be swept away from the surface. In the flat plate case, according to the mathematical model, the initiation will not start near the leading edge. The plate temperature rises in the downstream direction and this may effect the accumulation, especially at temperatures close to 0 °C. To reduce the effect of temperature non-uniformity at locations away from leading edge, the thermocouple was mounted on the middle of the plate. This will aid in the identification and control of the temperature on the plate at locations downstream from the leading edge.

In both figures of the temperature distribution of the cylinder and the flat plate models (Figure 4.9 and Figure 4.11), there was differences in the experimental measurements and finite difference results. This variation can be caused by a combination of the lateral conduction, Nusselt number differences, and the spatial location of the heater inside both models.

4.4.5 Temperature Controller

A temperature controller was built from National Instrument hardware and software. This controller takes the temperature reading of the surface (from the foil thermocouple) and calculates the error relative to the set point. The error value is used in a mathematical model to specify an increase or decrease in the pulse width of the current delivery through the heater. The model parameters were defined based on performance testing over a range of set point temperatures between -10 to $5\,^{\circ}\mathrm{C}$.

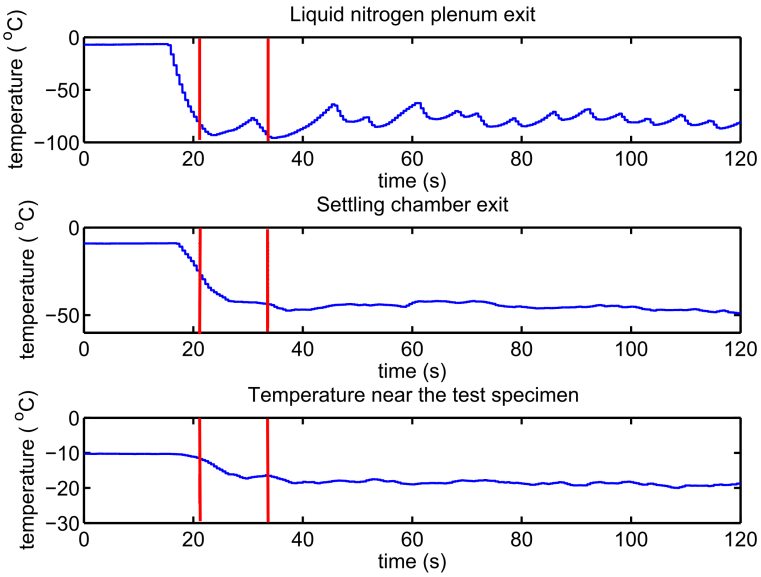

Figure 4.12: Facility temperatures with time for the cylinder model, surface temperature $-4\,^{\circ}\mathrm{C}$, air flow speed $6.5\,\mathrm{m/s}$, and cold room temperature $-10\,^{\circ}\mathrm{C}$.

An illustration of the controller performance can be seen from Figure 4.13, where the surface temperature was set to $-4\,^{\circ}\mathrm{C}$ and the room temperature was approximately $-10\,^{\circ}\mathrm{C}$. The data acquisition system frequency was set to $40\,\mathrm{Hz}$ and the controller thermocouple time response is between 2 and $5\,\mathrm{ms}$.

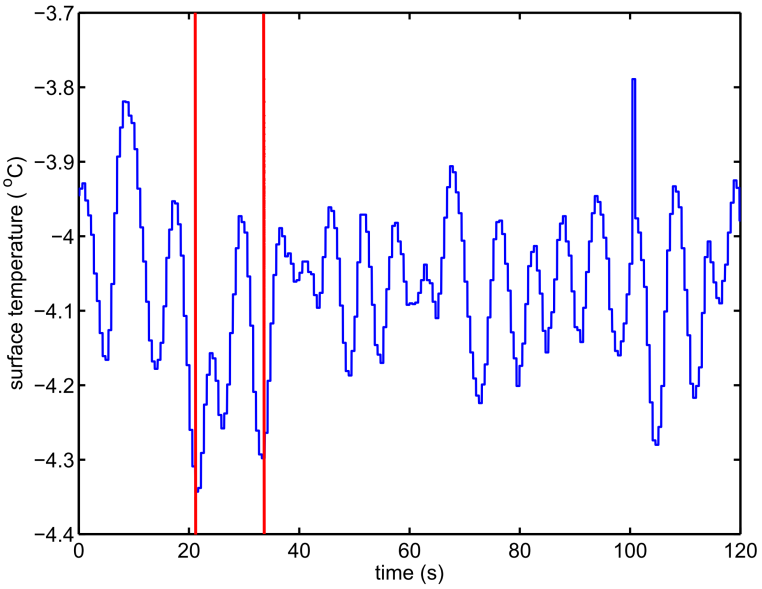

Figure 4.13: Temperature controller performance with time for the cylinder model, surface temperature $-4\,^{\circ}\mathrm{C}$, air flow speed 6.5 m/s, and cold room temperature $-10\,^{\circ}\mathrm{C}$.

The accuracy of the controller was found to be better than $\pm 0.3\,^{\circ}\mathrm{C}$, which is acceptable for the ice accretion experimental work. At about 20 s on the time scale in Figure 4.13 there was a sudden change in the external flow temperature due to the filling of the liquid nitrogen plenum as shown in Figure 4.12 and this is registered on the surface thermocouple as a drop in temperature at about $-4.35\,^{\circ}\mathrm{C}$. The controller works to bring the surface temperature back to the set point.

4.5 Illustration Accretion Results

Illustrative results from the wind tunnel are presented in this section. Photographs from the microscope camera, focused on an area of 9×9 mm near the stagnation region for the cylindrical model are presented in Figure 4.14. Only a $16\,\mathrm{mm}^2$ area near the centred on the stagnation region has been analysed for the ice accumulation results shown in Figure 4.15. A full description of the data post-processing method to estimate the amount of ice accumulation on the surface is discussed in Section 6.4. Details of the facility operating conditions for the cylindrical specimen and the flat plate are presented in Section 6.3 and Section 7.3 respectively.

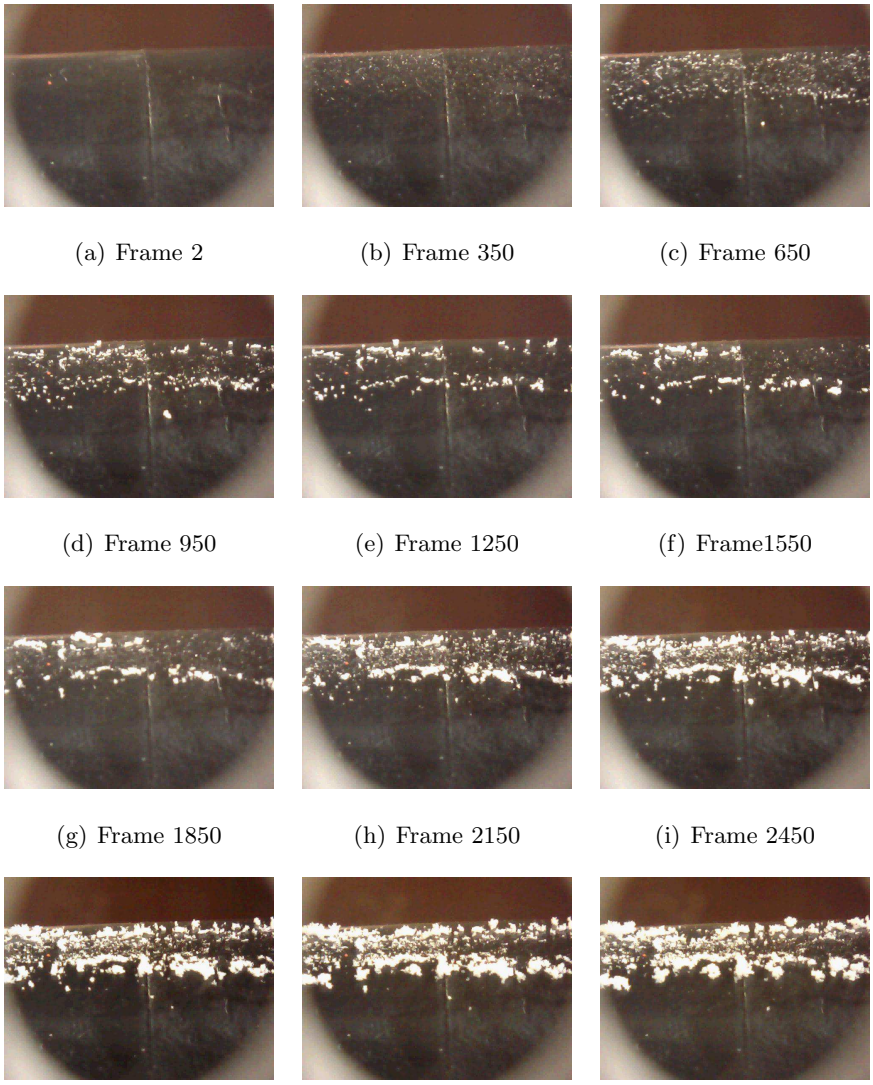

(a) Frame 2 (b) Frame 350 (c) Frame 650

(d) Frame 950 (e) Frame 1250 (f) Frame1550

(g) Frame 1850 (h) Frame 2150 (i) Frame 2450

(j) Frame 2750 (k) Frame 3050 (l) Frame 3350

Figure 4.14: Frames extracted from the video record of ice accretion on the cylinder model with a surface temperature of $-9\,^{\circ}\mathrm{C}$ and a 30 f/s recording rate.

4.6 Conclusion

A description of the experimental apparatus and a demonstration of the performance of the new apparatus developed for this project has been presented. Components have been tested separately to confirm the performance, and the overall operation of the

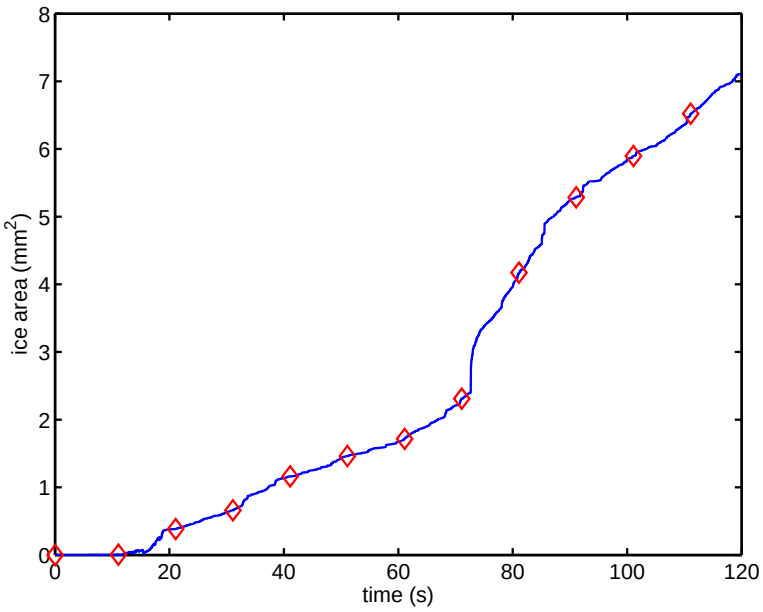

Figure 4.15: Ice area deduced from the video record on the cylindrical model near the stagnation region. The symbols represent the frames shown in Figure 4.14.

system has also been confirmed.

The temperatures of air/particle flow in the apparatus were recorded from a variety of locations. Sufficiently low temperatures and sufficiently long residence times are achieved to ensure the water droplets formed ice particles. The specimen surface temperature controller parameters were identified in order to keep the surface temperature constant within $\pm 0.3\,^{\circ}\mathrm{C}$ during any particular test. To verify the quality of the flow conditions, the uniformity of the flow within the wind tunnel was also measured and it was found to be around $\pm 0.2\,\mathrm{m/s}$ within the core wind tunnel flow.

The construction of the cylindrical and flat plate specimens was discussed and the temperature distributions on the specimens were documented using thermocouples and an infra red camera. The lowest surface temperature of the cylinder model was at the stagnation line and the temperature increased by a maximum of around $1.5\,^{\circ}\mathrm{C}$ at a position around $90\,^{\circ}$ from the stagnation line when the temperature difference between the surface and the flow was about $10\,^{\circ}\mathrm{C}$. The flat plate also registered a $1.5\,^{\circ}\mathrm{C}$ increase in surface temperature with increasing distance from the leading edge, but in this case the temperature difference between the surface and the flow was about $6.5\,^{\circ}\mathrm{C}$.

Chapter 5

Measurement of Ice Water Content

5.1 Introduction

In this chapter, the methods used to determine the ice water content generated in the facility is described: the ice sampling method, the analysis of the images to find the IWC and ice particle size distribution are discussed.

5.2 Experimental Setup

To determine the actual size distribution of the ice particles at the test section and to determine the actual ice water content, sampling tests were performed in the cold room at freezing flow condition similar to the tests in Chapter 6. In these tests, a cylinder, which has the same diameter as the actual cylinder test specimen, was cut in half. A flat sampling slide made of a clear plastic sheet was cut to the same size as the sampling test specimen as shown in Figure 5.1. The centre line of the wind tunnel duct is the area of interest and this location was marked on the sampling slide. The slide was divided into three areas, one in the middle and two close to the edges. Different areas were identified on the slide, to assess the influence of local capture efficiency

variations. A 2.0 Mp digital microscopic camera was used for the ice sampling work. (The same camera was also used in the ice accretion experiments.)

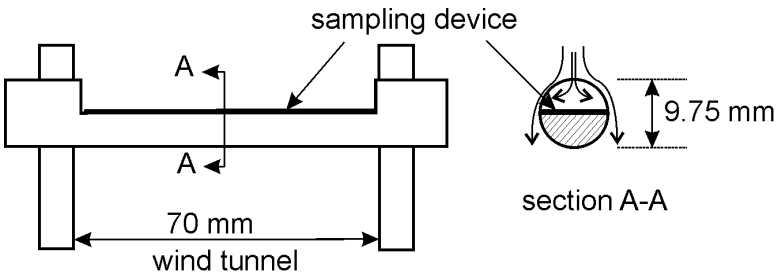

Figure 5.1: Illustration of the sampling apparatus located in the wind tunnel at the test specimen location.

The sampling slide was treated by cooking oil but unfortunately it reduced the measurement precision due to light reflection on the oil surface and for this reason, untreated sampling slides were used. By examining the high speed video, it was found that particle bounce was affecting only a small percentage of the particles even with untreated sampling slides. The sampling tests followed the same procedure as a standard ice accretion test in terms of establishing the flow conditions in the facility (see Section 6.3 for more details), nozzle air and water pressure, tunnel temperature, and humidity. Matters of procedure unique to the ice sampling tests are:

- The digital microscope camera was prepared and a standard reference image was recorded, to identify the magnification scale of the camera.
- The test slides were cleaned and one was positioned in the sampling device.
- The liquid nitrogen duct was filled and after one minute, the sampling device was positioned in the flow with the sampling slide on the leeward side.
- The sampling device was rapidly rotated through 180 ° so that the slide was on the windward side for a period of 10 seconds. the sampling device was then rapidly withdrawn from the wind tunnel duct.
- Photographs of the three different areas of the slide were then obtained using the digital microscope camera.

Under higher speed conditions particle bouncing, agglomeration, shedding and erosion

can have a significant effect on the icing process, ice water content measurement, and the particle size distribution.

5.3 Ice Water Content

For each sampling test, photos were recorded for the centre and the two edge regions. The dimensions of the microscope photos were 1.84 mm×1.39 mm, corresponding to an area of 640×480 pixels and includes a total number of particles in excess of 200. Two types of slides were trialled, one was painted black and the other was unpainted in an effort to achieve the optimum contrast between the ice and the surface. Figure 5.2 shows an example photograph of an unpainted ice sampling test slide near the centre line of the duct. A better contrast was achieved using the unpainted slides.

Figure 5.2: Photograph of an ice sampling slide obtained from sampling conditions of 6.5 m/s flow speed and ultrasonic nozzle water tank pressure of 3.5 bar.

To analyse the photos, two methods were used. A manual sizing and counting method using micro capturing software was trialled and a Matlab code was also developed to identify the icing area in a more automated (less subjective) manner. The code

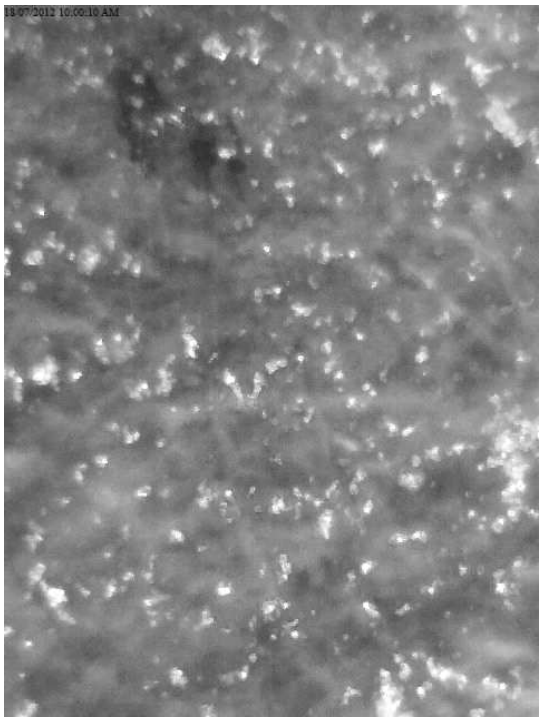

Figure 5.3: The value image after changing the original image to the HSV format. (6.5 m/s flow speed and water tank pressure was 3.5 bar.)

adopted the following procedure:

- The imported image was converted to Hue Saturation Value (HSV) format instead of the original Red Green Blue (RGB) mapping. Figure 5.3 shows the brightness (value) component of the image from the HSV format.
- The optimal threshold value was determined. The threshold value can have a strong impact on the IWC value because adoption of a high value can results in small particles being neglected and using a low threshold value can results in an over estimation the IWC. Thus, for each photo the threshold value was adjusted until it showed most of the ice particles on the sample. Figure 5.4 shows the photograph in Figure 5.3 after choosing a threshold value of 0.62 and eliminating pixels with values lower than the threshold. The 0.62 threshold value was found after trying different threshold values within the range from 0.5 to 0.75, as discussed in Section 5.4.
- The gray scale image, Figure 5.4 was converted to a binary image as shown in Figure 5.5.

- Standard Matlab (Image Processing Toolbox) functions were then used to find all the connected objects and compute the areas and perimeters of each object.
- The impact of agglomeration on the analysis was reduced by finding the highest reoccurrence particle size. If an ice area was bigger than three times the highest reoccurrence particle size on the slide, the analysis substitutes it with an equivalent area of particles having a diameter equal to the mean diameter. (The fraction of particles with diameters greater than three times the most frequent diameter was between 2 to 6% of the total number of the particles.)

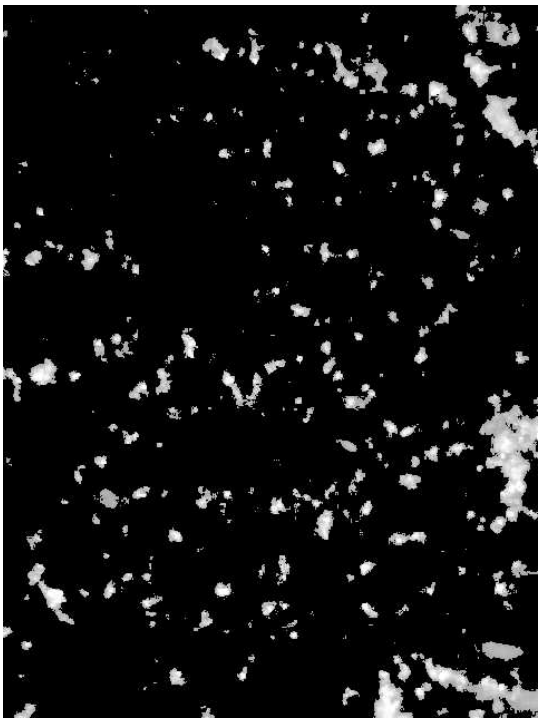

Figure 5.4: The example image after choosing the threshold value of 0.62.

The particle shape was assumed to be spherical due to the atomiser used in this work. The particle sizes were examined again to find the size distribution at the test section location. By normalising the number of particles in the analysis of each photograph and by taking the average histogram of a number of the sampling photographs, the particle diameters were found. Figure 5.6 and 5.7 show the average diameter histograms for the collected particles from nine sampling slides at the test section for the centre and the edge of the sampling specimen slide respectively. The sampling slide size in this tests was 1.84 mm×1.39 mm which represent 640 pixel×480 pixel. The error bar on these figures represent the standard deviation for the specified particle diameter.

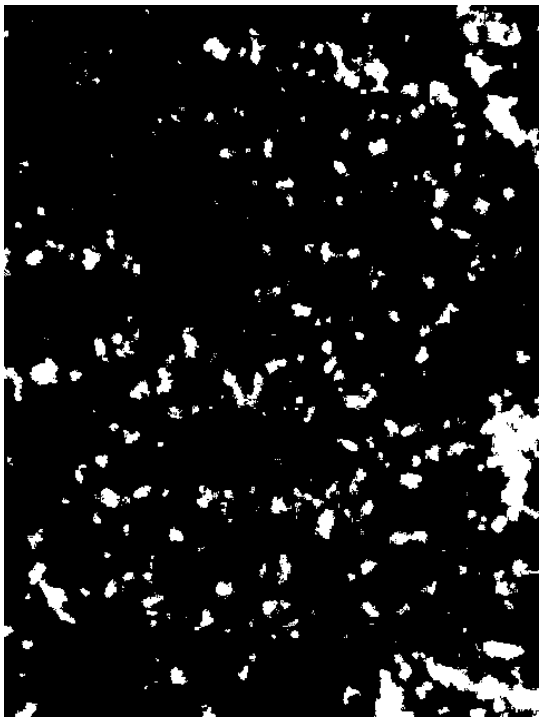

Figure 5.5: The binary image for the example image after choosing the threshold value of 0.62.

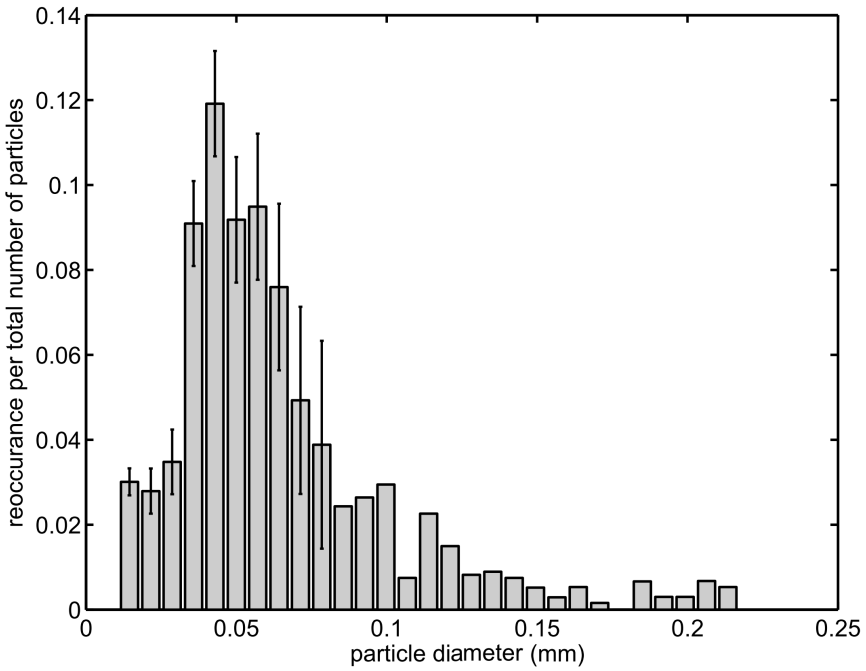

Figure 5.6: Average normalised particle diameter for the centre of the slide specimen.

A comparison of Figures 5.7 and 5.6 demonstrates that the particle size distribution is similar for the centre and the edges. It can also be noticed that larger particle size

were on the edges in comparison with the centre due to the starting of the ice accretion process.

After finding the total icing area, and with the known air volume flow rate within the wind tunnel, the ice water content was estimated to be $0.42\,\mathrm{g/m^3}$ with an uncertainty of $\pm 0.26\,\mathrm{g/m^3}$, which represents 2σ.

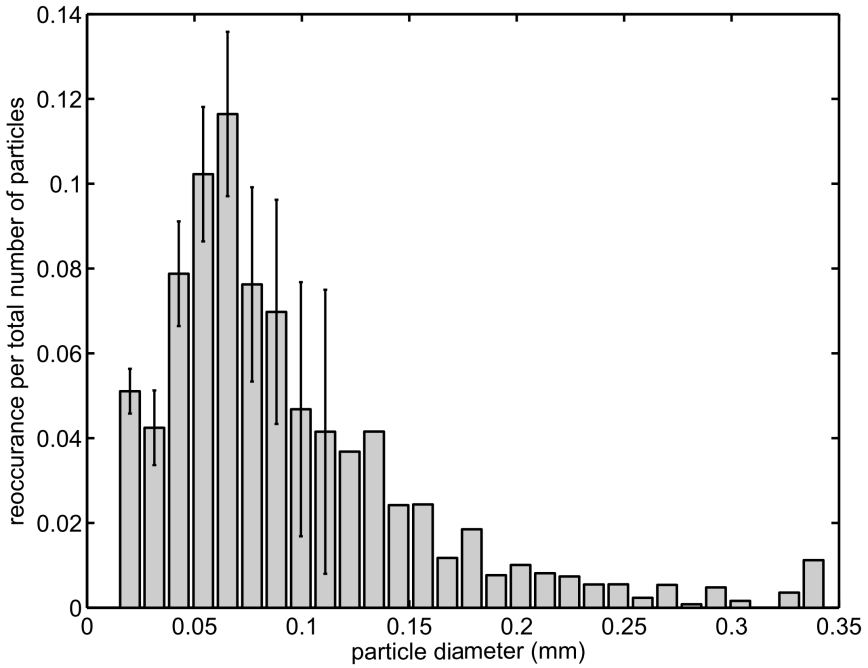

Figure 5.7: Average normalised particle diameter for the edge of the slide specimen.

5.4 Threshold Effects

The choice of the threshold value (introduced in Section 5.3) can affect the apparent ice water content deduced using the optical method. One of the sampling slides was analysed using the image processing Matlab code with variable threshold level to find the sensitivity of parameters to the threshold value.

Figure 5.8 shows the effect of the threshold value on the ice particle diameter distribution. The general trend for all three cases in Figure 5.8, is similar and as the threshold value increases, bigger particle diameters are identified in the size distribution.

In Figure 5.9 the particle diameters at maximum reoccurance were found at different

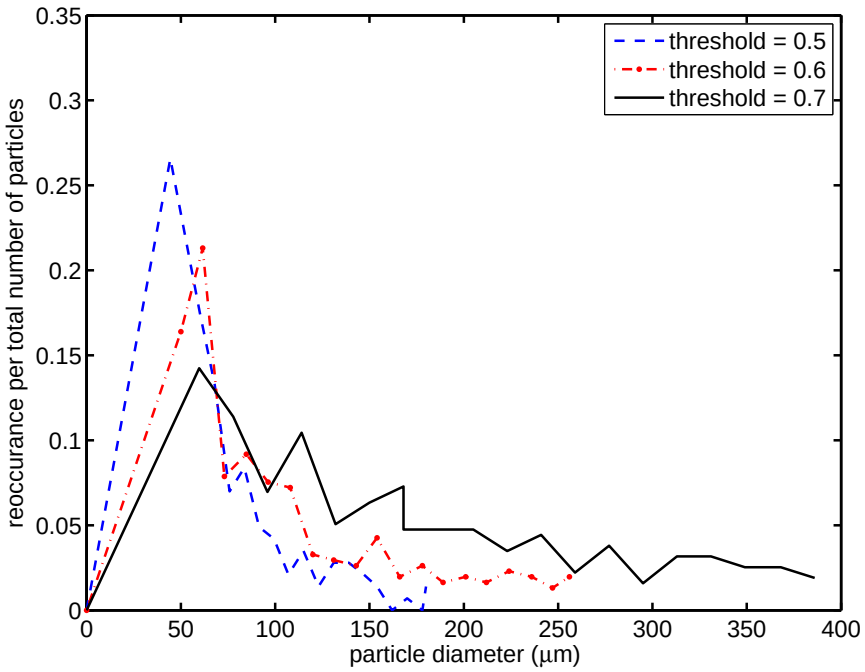

Figure 5.8: Ice particle reoccurance per total number of particles at different threshold values.

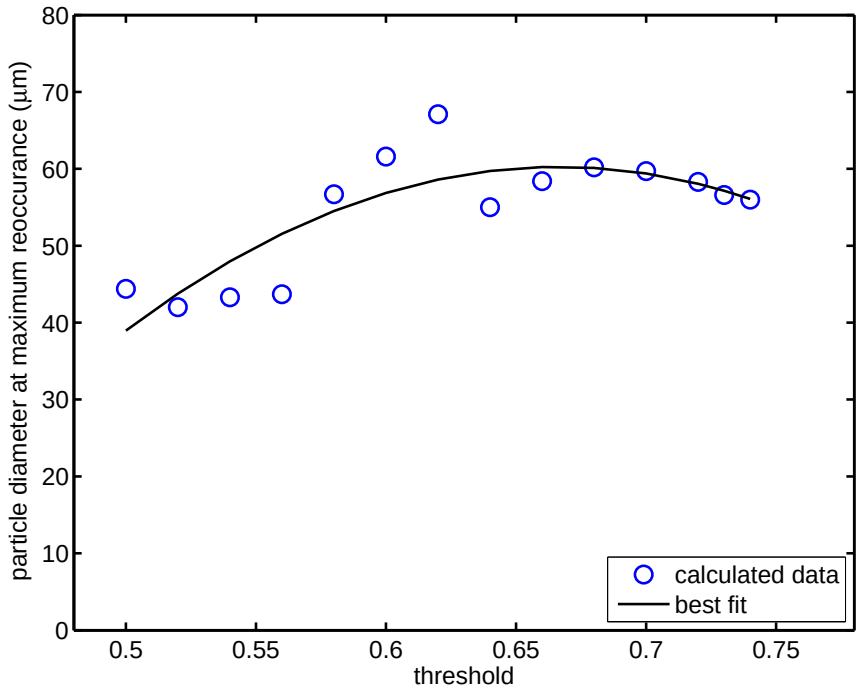

Figure 5.9: Variation of ice particle diameter for maximum reoccurance with different threshold values.

values of the threshold. The particle diameter at maximum reoccurance was found to vary between 45 and 65 μm and according to the quadratic line of best fit, approached a relatively constant value at a threshold of 0.62 (Figure 5.9). Figure 5.10 shows the reoccurance per total number of particles for the particle diameters identified in Figure 5.9. In Figure 5.10, the variation of the maximum reoccurance per total number of particles for the diameter shown in Figure 5.9 is around 3%.

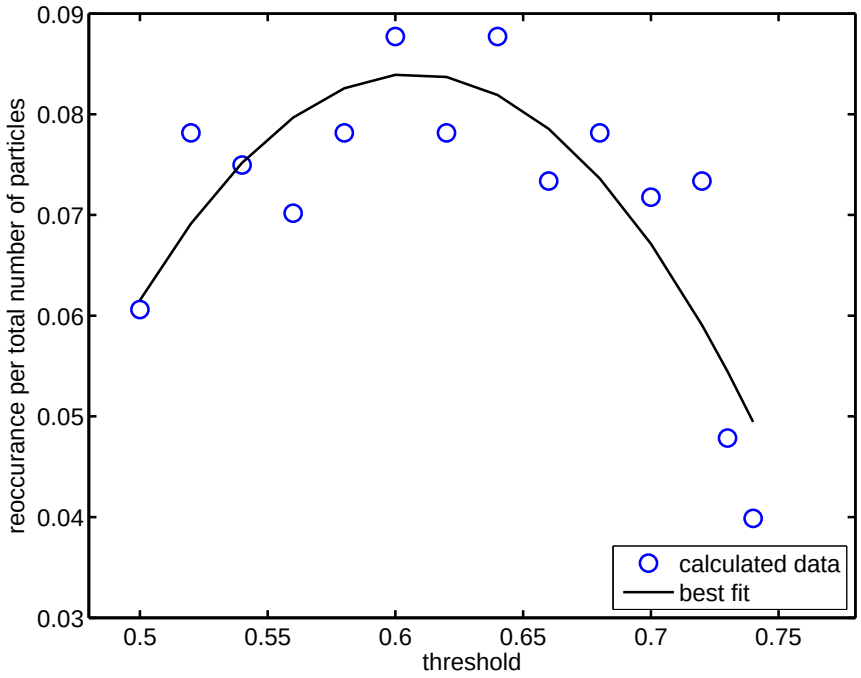

Figure 5.10: Variation of ice particle roccurance per total number of particles with different threshold value.

Figure 5.9 shows that the maximum reoccurance particle diameters stabilise for threshold values larger than about 0.62 and the reoccurrence of these diameters with the threshold variation in Figure 5.10 indicates that the maximum reoccurrence value is achieved between threshold values 0.6 and 0.62. Based on this analysis, the threshold value of 0.62 was used in subsequent analysis.

To find the influence of the threshold variation on the apparent ice water content, Figure 5.11 was generated. In Section 5.3, the ice average water content was found to be 0.42 g/m^3 from a number of different samples at a constant threshold value of 0.62 and the double standard deviation (2σ) was 0.26 g/m^3. In this study, the ice water content will be taken as 0.42 ± 0.26 g/m^3.

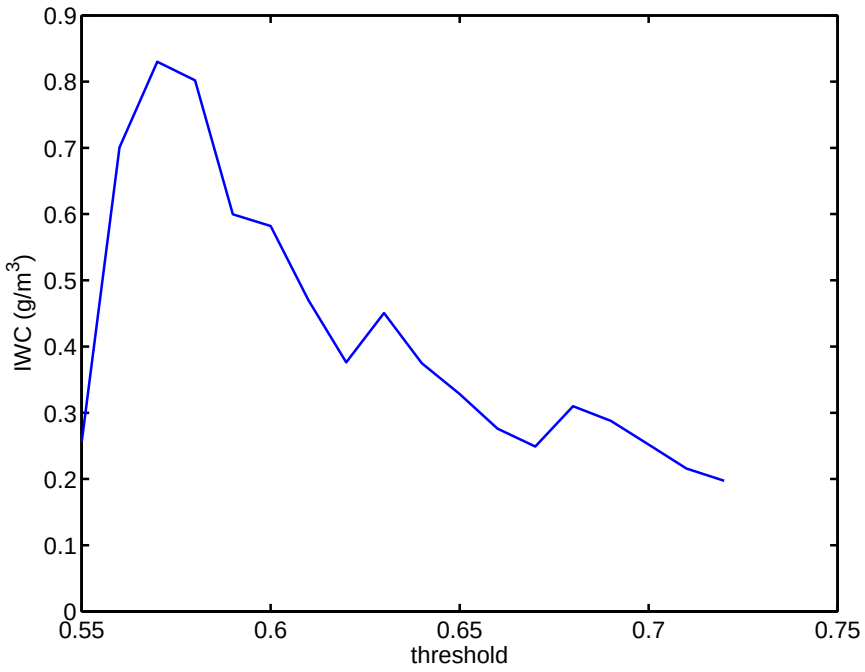

Figure 5.11: Apparent ice water content variation with threshold value.

5.5 Capture Efficiency

To confirm that the calculated ice water content is representative of the field particle distribution, the collection efficiency of the sampling configuration was calculated. A CFD Fluent simulation was used to specify the flow field around the sampling specimen as shown in Figure 5.12. The value of y_{max} for the sampling specimen was 5 mm. Figure 5.12 illustrates the geometry of the particle path tracking used in the capture efficiency analysis.

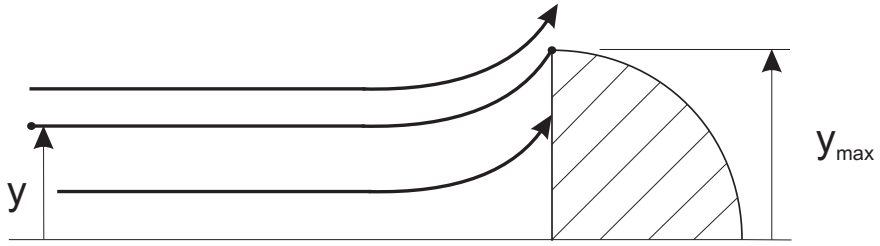

Figure 5.12: Illustration of the particle capture efficiency geometry.

Both turbulent and laminar CFD solvers were trialled and both of them gave the same results due to the low flow speed conditions. The velocity vector field from the CFD simulation was imported into Matlab and an ODE solver was implemented to track

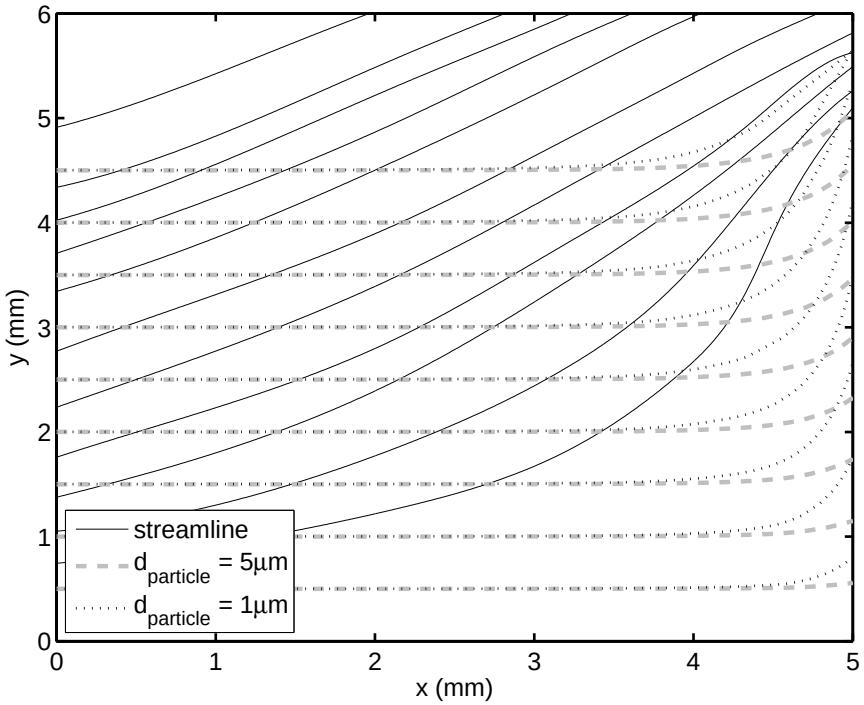

Figure 5.13: Streamlines around the sampling test specimen obtained using ANSYS software, and particle trajectories for 1 μm and 5 μm particle diameters.

the particle paths based on the aerodynamic drag forces on the particles due to the relative velocity between the flow and the particles. Figure 5.13 shows the streamlines and the particle trajectories for two different sized particles.

By considering a range of particle diameters as identified in Figure 5.6 and Figure 5.7 and starting from a distance of 10 cm upstream of the sampling specimen, the particle impinging point can be identified. The particle trajectories were found by tracking a particle released upstream at the initial air flow speed until it reached the streamwise location of the surface and either impacted on the surface or continued downstream. For particles released further from the stagnation streamline, (increasing values on the y axis in Figure 5.12) the particle drift increased. Also, the smallest particles are subjected to further drift as indicated in Figure 5.13.

The overall collection efficiency as a function of particle diameter is presented in Figure 5.14. As the particle size increases, the collection efficiency increases due to the increase in the inertia of the particles; the flow stream produces a lower drifting effect on the large particles.

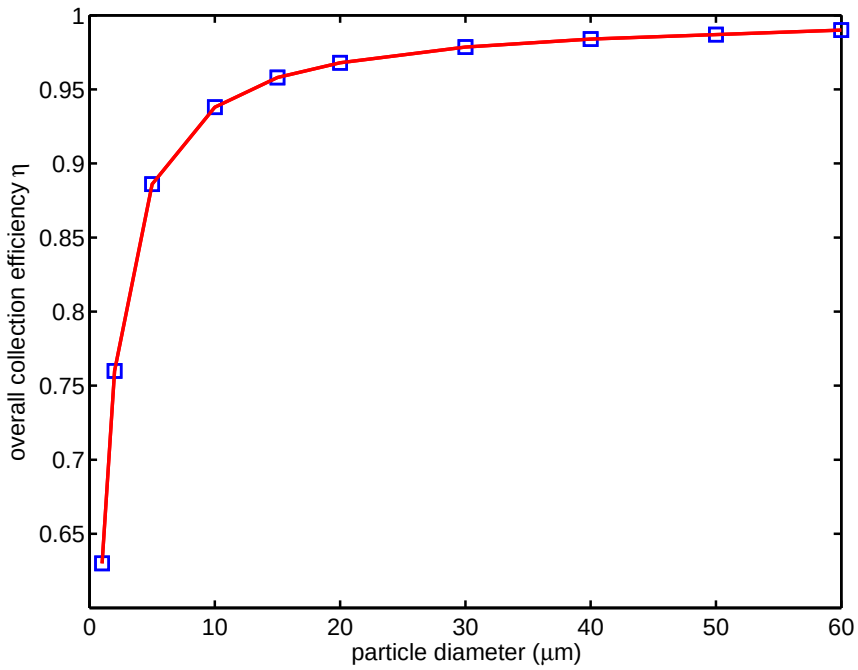

Figure 5.14: Ice capture efficiency as a function of particle diameter at 6.5 m/s flow velocity.

For particle sizes of 5, 10, 20, 30, 40, and 50 μm, the collection efficiency was calculated with respect to the non-dimensional distance from the stagnation point along the specimen as shown in Figure 5.15. This figure shows the local collection efficiency for each particle size over the region from 0 (the stagnation point) up to the point y on the specimen. It can be noticed that the highest local collection efficiency for any particle size occurs if the particle trajectory is close to a stagnation streamline and decreases as the distance from the stagnation streamline increases. For the particle sizes considered, the local collection efficiency reaches a minimum in the region where the $(\frac{y}{y_{max}})$ value is between 0.4 and 0.6; the local collection efficiency increase slightly for larger values of $\frac{y}{y_{max}}$. This is because of the compression of the flow streamlines near the edges of the sampling specimen as shown in Figure 5.13.

The collection efficiency presented in Figure 5.14 shows that for particle sizes above 5 μm, the collection efficiency is more than 85 % and if the size increases, the collection efficiency increases. Even at 1 μm particle diameter, the collection efficiency around 65 %. The cylinder model was assumed to have a capture efficiency similar to that of the sampling slide in this chapter.

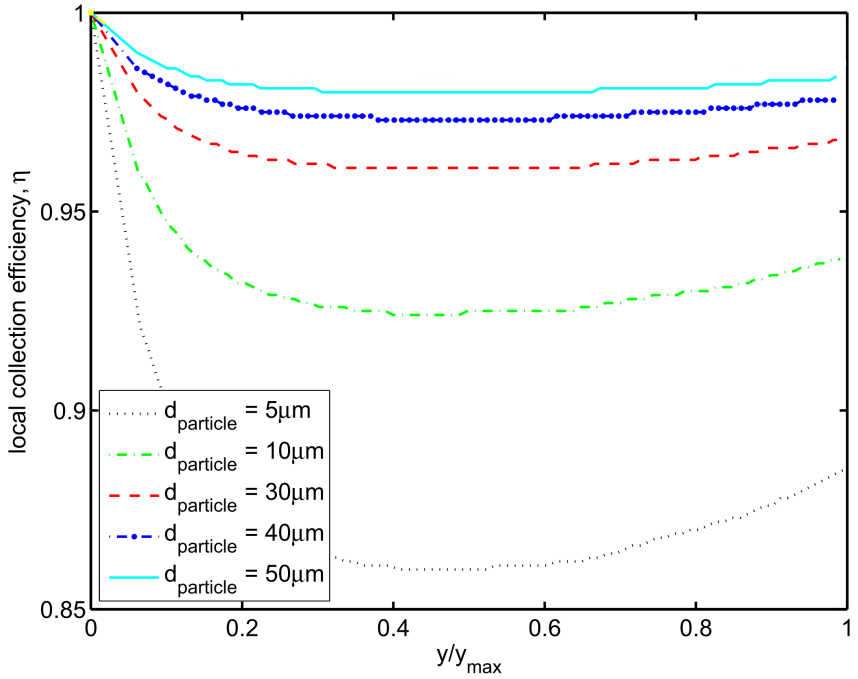

Figure 5.15: Ice capture efficiency with respect to the y/y_{max} for different particle diameters at a flow speed of 6.5 m/s.

5.6 Conclusion

The measurement method for the ice water content was described, and for the present operating conditions it was found to be 0.42 g/m^3 with an uncertainty of $\pm$0.26 g/m^3 based on a $\pm 2\sigma$ condition. The actual particle size distribution was also measured at the test section and the particle diameters were found to be around 50 μm at the centre and the edges of the sampling specimen. The capture efficiency of the sampling specimen was identified with aid of CFD simulation and a Matlab code for tracking particle trajectories. The code suggested high collection efficiency (around 95 % and above) for particle sizes of 20 μm or larger at the free stream speed of 6.5 m/s. For particles of 1 μm diameter, the collection efficiency is around 65 %. These values of the collection efficiency demonstrate that the particle size distribution and the ice water content obtained using the present technique should be sufficiently accurate: systematic errors introduced by the collection efficiency of the present device are likely to be small relative to the overall variability of the ice water content.

Chapter 6

Ice Accretion on Cylindrical Specimen

6.1 Introduction

Ice accretion initiation results on the cylinder specimen are presented in this chapter to demonstrate the accretion process on a microscopic scale. This chapter describes the motivation and the methodology used to obtain the experimental results as well as the data analysis methods. The ice accretion results on cold and warm surface temperatures with nominally identical external flow conditions are reported. The specimen was divided into two area having different roughness. The results show that the initiation of the ice accretion process depends strongly on the surface temperature.

6.2 Motivation and Experiment Design

The apparatus developed in this study cannot duplicate turbofan engine conditions encountered at high altitudes. For example, because it is important to preserve thermal conditions of the air, ice, and surface relevant to the ice melting and friction, at least according to the model developed in Chapter 3, the viscosity of the air and water will be duplicated in the present physical simulation. However, the wind tunnel speed is

currently limited to around 10 m/s which is an order of magnitude lower than in a turbofan engine, and the wind tunnel is relatively small (diameter is 70 mm) so this makes it difficult to achieve representative turbofan Reynolds numbers. Furthermore, the kinetic energy of the ice particles, which can play a role in the mechanics and thermal effects associated with the surface interaction, will not be duplicated.

This experimental study will focus on the duplication of thermal conditions relevant to local compressor air temperature around $-10\,^{\circ}\mathrm{C}$ and surface temperatures between $-10\,^{\circ}\mathrm{C}$ and $+10\,^{\circ}\mathrm{C}$ in the region where icing is expected to initiate. A small and controlled amount of heating was applied to the model to achieve the required surface temperatures. The particle state and size produced in this study was also selected in an effort to simulate the environmental conditions in the deep convection clouds.

Previous observations suggest that ice particles are unable to adhere to the cold external surfaces of the aircraft. Therefore solid ice particles were previously considered benign for aircraft and for this reason there have been a limited number of studies focusing on the problem of solid ice accretion until recent years. However, the mathematical model presented in Chapter 3 shows that even in a high flow speed at 150 m/s, with an ice friction coefficient of 0.6 (appropriate for cold ice on a cold surface), and at a 1 mm distance from the stagnation point on a 10 mm diameter cylinder, particles with a diameter less than 40 μm can stay stationary on the surface. The question therefore arises, can ice accretion occur in the vicinity of the stagnation point at subfreezing conditions in an aerodynamic flow of air and ice particles?

Results from the model for the relatively low flow speeds that can be achieved in the present facility are presented in Figure 6.1. The results show that the friction forces are higher than the drag force even at the very high contact angle of $\pi/2$ and the low friction coefficient of $\mu = 0.07$ for the range of particle sizes generated in the facility. Figure 6.1 was produced considering a distance of 1 mm from the stagnation point and if the distance from the stagnation point decreases the aerodynamic force also decreases making the initiation of accretion even more likely. It should therefore be feasible to address the possibility of stagnation region accretion initiation at subfreezing conditions using the present facility.

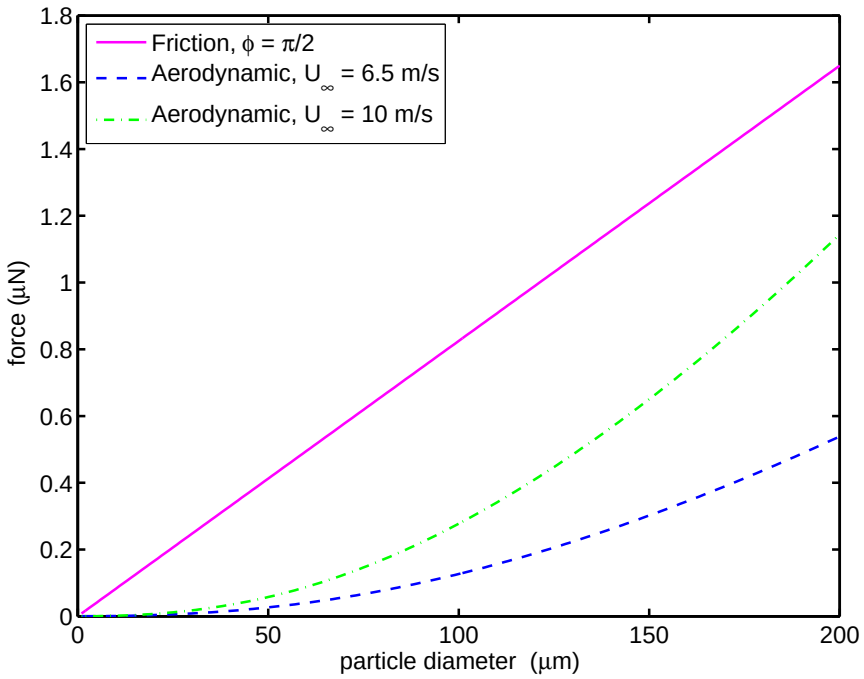

Figure 6.1: Aerodynamic drag force and the friction force variation with particle diameter for $\mu = 0.07$, $x = 2\,\text{mm}$, $u_p = 0$, volume fraction of 0.05, $\phi = \pi/2$, and different free stream speeds.

Another question which arises relates to the role of the surface temperature on the initiation of accretion. Previous studies have suggested the presence of suspended liquid water and surface temperatures that are initially above 0 °C are requisites for compressor ice accretion during transit through deep convective systems. In the present work, only suspended water in the solid phase is considered, but a range of surface temperatures is simulated in an effect to identify the role of the surface temperature in an unambiguous manner.

Figure 6.2 shows results from the model for the variation with temperature of the maximum possible diameter of ice particle which could remain stationary near the stagnation point on a 10 mm diameter cylinder in the present wind tunnel. As the temperature decreases, the maximum particle size increases for any distance from the stagnation point, and this is because the friction coefficient increases with decreasing temperature. As the distance from the stagnation point increases, the maximum particle size decreases due to the increase in the flow speed external to the boundary layer. As the temperature increases, the maximum size of the particles that can re-

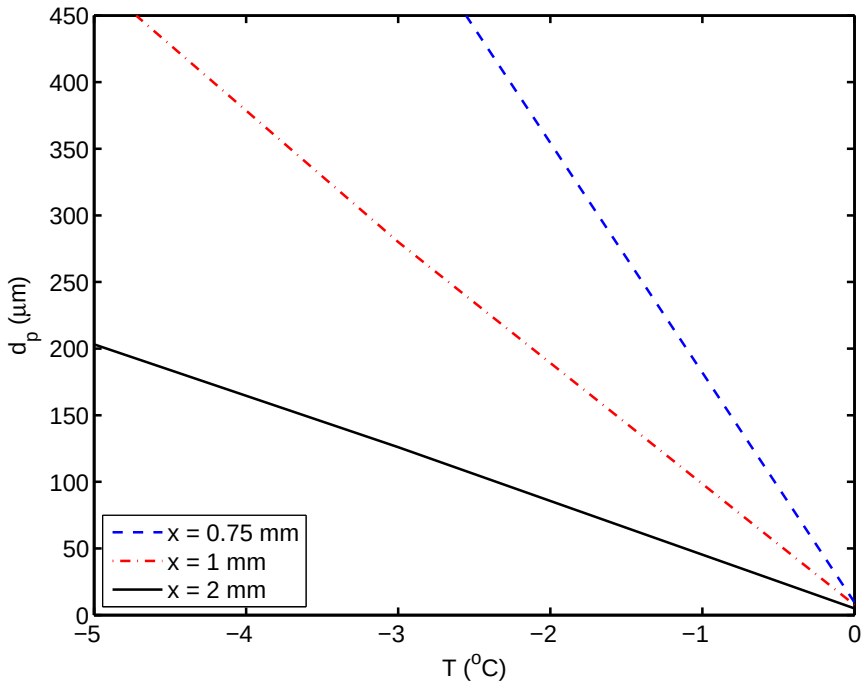

Figure 6.2: Variation of the maximum particle diameter that can adhere in the vicinity of the stagnation point with temperature for stagnation region of 10 mm diameter specimen, $u_p = 0.5$ m/s, volume fraction of 0.05, $\phi = \pi/2$, and free stream speed of 6.5 m/s.

main stationary near the stagnation point decreases, and at around 0 °C, particles of almost any size will be swept away, according to the model presented in Chapter 3. The validity of the model presented in Chapter 3 as an explanation of temperature effects is another matter that can be addressed using the present facility.

The work in the thesis represents an attempt to validate the mathematical model in Chapter 3 using the experimental data generated in this study. There is no other suitable data in the literature can be used in the validation process.

6.3 Testing Methods

Prior to an ice accretion test, reference images were obtained using a reference specimen to relate physical locations on the actual test cylinder to pixels in the video record. The reference cylindrical specimen was divided spatially into a grid of 1×1 mm areas marked on the cylinder surface, and these regions were analysed to assess the spatial

differences in ice accretion on the specimen. The marked reference cylinder was the same diameter as the test cylinder and it was placed in the position of the actual test cylinder as shown in Figure 6.3. The centre line of the wind tunnel and the stagnation line of the cylinder were marked as broken lines on the reference cylinder. The area of interest corresponds to two millimetres on either side of the stagnation line.

On the actual cylindrical specimen, the right hand side of the centre line was a rough area, where it has been painted black only. The left hand side of the specimen was the smooth surface, which was painted black and polished using a fine-grade sandpaper. Although Dotan, Dodiuk, Laforte and Kenig (2009) suggested that the level of the solid surface roughness may affect the crystallisation and nucleation of ice, Dotan et al. (2009) did not give any information about what the surface roughness should be. So for each test, ice accretion data for two different roughnesses on either side of the centre of the tunnel and specimen were recorded.

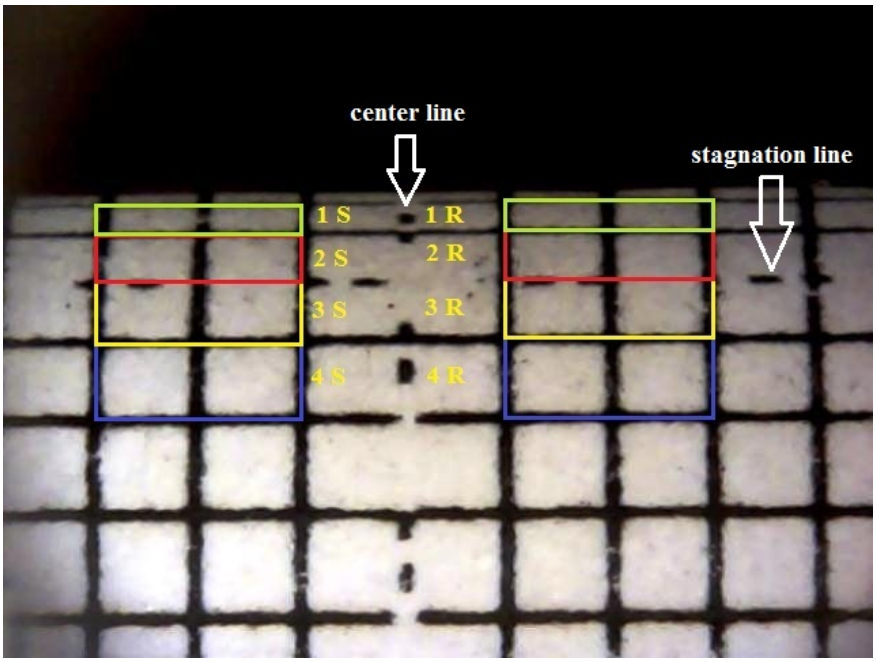

Figure 6.3: Annotated photograph of the cylindrical reference model with 1×1 mm grid.

To analyse the accretion results, both sides (rough and smooth) were treated separately and each side was divided into four areas. These four areas were designated: 1 Smooth (1S), 2 Smooth (2S), 3 Smooth (3S), and 4 Smooth (4S) for the smooth side and for the rough side as 1 Rough (1R), 2 Rough (2R), 3 Rough (3R), and 4 Rough (4R) as indicated in Figure 6.3. The $2\,\text{mm}^2$ area on the cylindrical model contains

148×20 pixels for area 1S and 1R, 148×36 pixels for area 2S and 2R, 148×43 pixels for 3S and 3R, and 148×59 pixel for area 4S and 4R. The equivalent area of each pixel was identified and the particle diameter having the same cross sectional area was calculated. Pixels in 1R or 1S are equivalent to a particle size of 29 μm, and the pixels in 4R or 4S are equivalent to the particle size of 17 μm. After recording the reference image, the reference cylinder was replaced by the actual cylinder, which is shown in Figure 6.4.

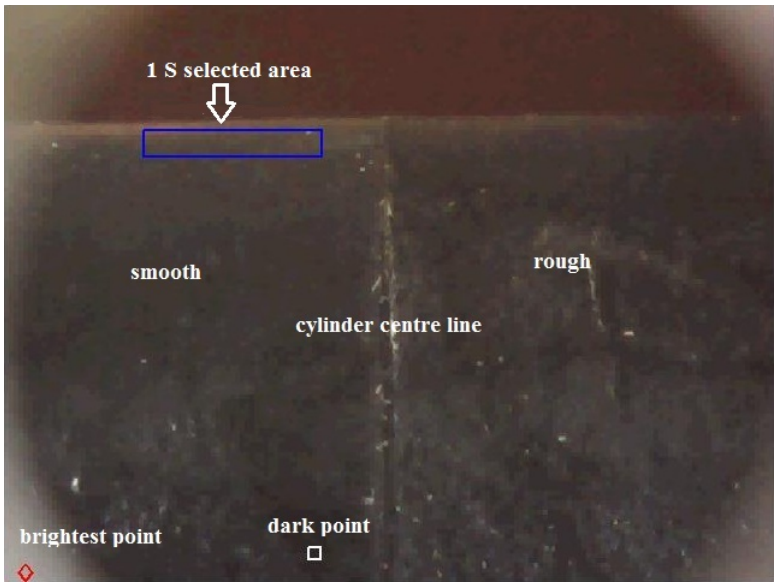

Figure 6.4: Annotated photograph of the cylindrical model after removing the plastic protector.

The ice accretion tests followed the procedure:

- The liquid nitrogen duct was filled with liquid nitrogen and the whole system was left to cool down for around five minutes.
- The video recording was started.
- The compressed air and the pressurised water were turned on.
- After approximately 60 s, the data acquisition system, the settling chamber fan, and the wind tunnel fan were turned on to establish a steady flow of particles through the wind tunnel.
- During the establishment of a steady particle flow through the tunnel, the surface of the test specimen was kept clear of ice particles and protected by a plastic

sheet. After between 10 and 15 s of the flow through the tunnel, the plastic protector was removed.

- A stop watch was used to record the starting time for the data acquisition system and the time of the removal of the protector sheet.

The icing test was run to around 3 min and the cover on the model was removed after 10 to 15 sec from the starting of the video recording and it took less than 1 sec to remove the plastic cover. The plastic sheet (the model cover) was formed into a shape closely fitting that of the cylinder so that its presence and removal caused minimal disturbance to the flow patterns in the tunnel. Tests were performed for surface temperatures of $-9\,^{\circ}\mathrm{C}$, $-5\,^{\circ}\mathrm{C}$, $0\,^{\circ}\mathrm{C}$, and $+5\,^{\circ}\mathrm{C}$. The relative humidity was measured with the water injection system on and it was found to be 20 %.

The surface roughness of both smooth and rough sides for the cylindrical specimen were measured using a MITATOYO Surftest-4 surface roughness stylus. The average roughness for the smooth side was found to be $R_a = 0.5\,\mu$m, and the average peak to valley height R_z was $2.5\,\mu$m. For the rough area the R_a was $1.0\,\mu$m and R_z was $4.6\,\mu$m.

6.4 Analysis methods

To find the ice accretion area on the surface, a code was built using Matlab. The method used by the code is described in the following steps:

- Read a frame from the reference cylinder video and identify corner pixels corresponding to the four smooth and rough regions, and other geometric feature of the reference model.
- Read each frame of the video file separately and identify clean dark and bright pixels on the specimen where there is no accretion recorded. These regions provide the reference values for the correction of the intensity of the images since background levels can change with time due to the auto iris on the camera.

- Identify the upper edge and the centre line of the actual cylinder specimen and compare it with the reference model.
- If there is difference between the images of the reference specimen and the real specimen, the difference in the x and y directions are added to the pixels of the selected areas, which is identified from the reference model.
- Change the images from Red, Green, Blue (RGB) colour mapping to Hue, Saturation, and Value (HSV) mapping. The code saves the value matrix, or the brightness, which is within the range from 0 to 1.0.
- The intensity of the light on each pixel of the two millimetre areas on the surface is compared with the selected dark pixel.
- Subtract the background value from each pixel to find the absolute brightness change during the recording time.
- If the brightness value on any pixel exceeds a value 0.1 larger than the scaled background value for that pixel, it is counted as having ice on it.
- Search across the entire selected area of the image, to find the total icing area in pixel^2 for each frame, and through the analysis of the reference images (as in Figure 6.3), the icing area in mm^2 is obtained.
- Repeat the above analysis for each frame in the video sequence to obtain the ice accretion in mm^2 with respect to the recording time.

The number of pixels in R1 and S1 is less than the number of pixels in R4 and S4, due to the viewing angle of the camera and the curvature of the cylinder. This difference in areas causes a depth effect of the ice particles on the surface. As the viewing angle is not perpendicular to the surface, the ice particles block a larger portion of the surface by the cosine of the viewing angle of each particular area as illustrated in Figure 6.5. This effect was also accommodated in the Matlab code during the early stage of the ice accretion. The uncertainty in the analysis method can be seen as higher accumulation than 100 % coverage or the starting of the accumulation above 0 %, as shown in the figures in Appendix D.

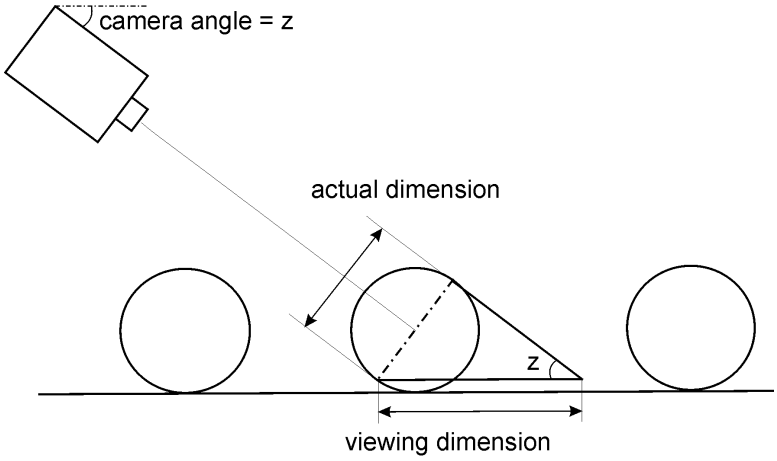

Figure 6.5: Illustration of the viewing angle and depth effect correction analysis.

The actual dimension of the cylinder and its location in the duct has been recorded and with the aid of the grid in Figure 6.3, the viewing angle at the stagnation point has been confirmed. When the grid appears to have equal horizontal and vertical distances, the viewing angle of the local surface is 90 ° and for other locations along the stagnation line in Figure 6.3, the viewing angle decreases. The actual viewing angle for each region was found by calculating the inverse tangent of the apparent vertical to the horizontal dimensions of the reference grid.

Tests have been performed for different surface temperatures and in one case, a different particle concentration was used. In each test the surface temperature was set to a specific value with optimum input parameters for the controller to keep the surface temperature at the required value with a temporal variation of less than ±0.3 °C.

6.5 Cold Surface Temperatures

Complete tests results are presented in Appendix D. Each test was repeated three times or more and in general, the reported data for −9 °C shows that the ice accretion happened faster close to the stagnation line and in all cases a complete coverage of the area is achieved between 60 s and 80 s. Ice accretion occurs more slowly further away from the stagnation line and it can take up to 100 s to achieve a complete coverage of the local area. At −5 °C, although the results show some delay in the accretion

process, they demonstrate identical behaviour of the accumulation to the −9 °C case. In the following sections the results for −9 °C and −5 °C will be discussed in more detail. The erosive shear force or the aerodynamic drag of the air flow increases with increase of the free stream speed, and these forces can eliminate the accreted ice from the surface.

6.5.1 Surface Temperature −9 °C

The cold room temperature was set to −10 °C, flow speed was set to 6.5 m/s, and the water tank pressure was set to 3.5 bar, and the test specimen temperature was set to −9 °C. Figure 6.6 and Figure 6.7 show the typical temperatures of the flow through the wind tunnel duct at different locations. The combination of duct temperatures, flow speed and thermal modelling indicates that the droplets are most likely to be in solid state as discussed in Section 4.3.

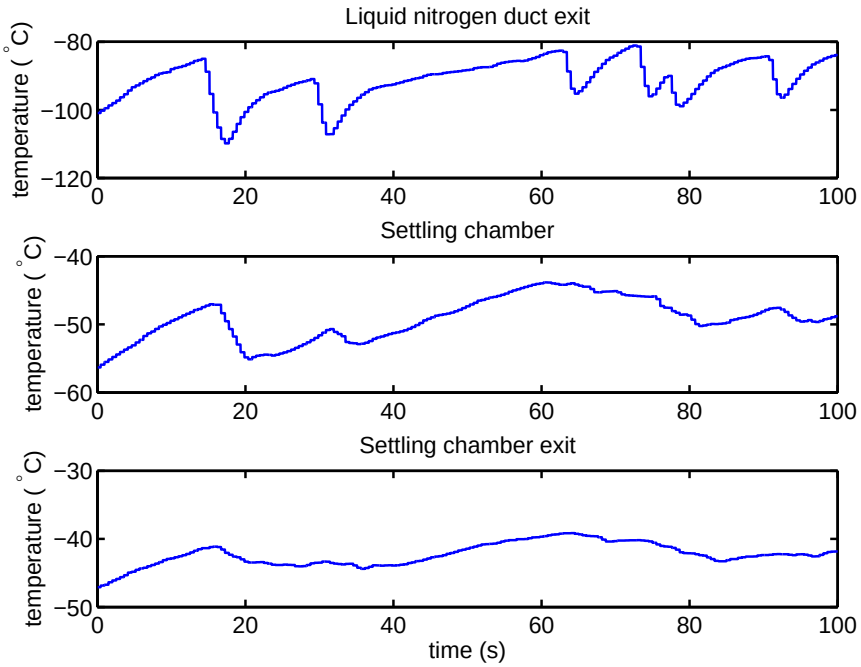

Figure 6.6: Temperatures within the facility upstream of the wind duct. Specimen temperature −9 °C. (Test: SM9T1HP)

In Figure 6.6 the liquid nitrogen duct exit temperatures show a variation of the temperature between −100 °C and −80 °C, and this arises due to the decrease in the liquid nitrogen level and the refilling process of the duct. Although, corresponding

temperature fluctuations are also observed in the settling chamber and at the exit of the chamber, the variation in amplitude decreases from ±10 °C in the liquid nitrogen duct down to ±5 °C at the settling chamber exit (see Figure 6.6). The flow temperatures rise through out the facility from the liquid nitrogen duct onwards due to heat transfer from the relatively warm cold room environment at −10 °C. At the inlet of the wind tunnel duct and near the test specimen, an additional temperature increase is observed in Figure 6.7 due to mixing between the particle laden flow and the cold room air. Within the duct at point A and B, the temperature is constant with time to within about ±2 °C and a variation of about ±0.2 °C is recorded on the surface of the test specimen as shown in Figure 6.7.

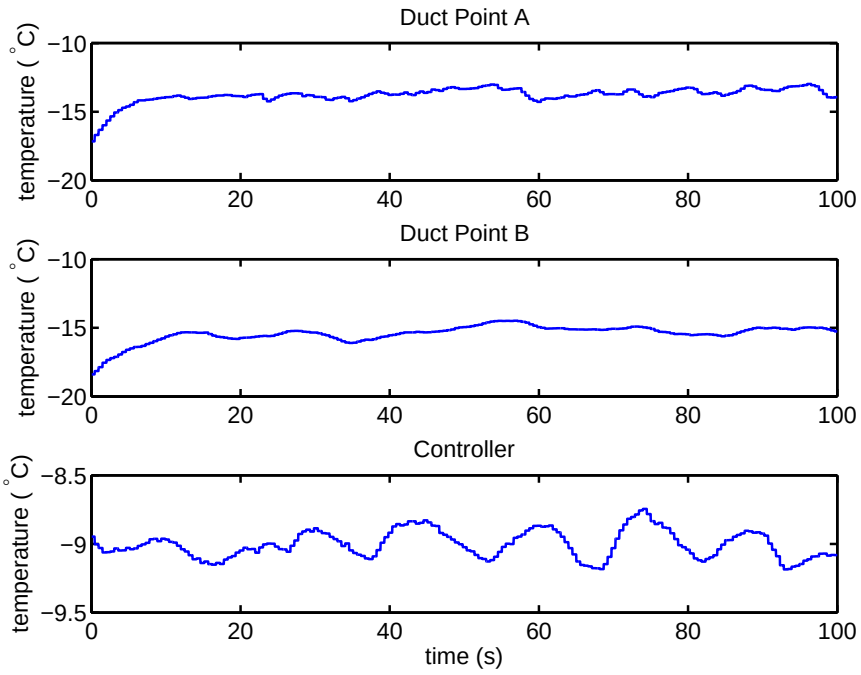

Figure 6.7: Temperatures within the wind tunnel duct for the test specimen temperature of −9 °C. (Test: SM9T1HP)

The area of the ice accretion was determined for each of the 2 mm^2 areas as described in Section 6.3. Results for the ice accretion on the area further from the stagnation line for the rough and smooth surfaces are presented in Figure 6.8. The ice accretion on these areas shows very similar accumulation, although accumulation in S4 appears somewhat delayed relative to the other areas. Results for the accumulation of icing areas near the stagnation line is shown in Figure 6.9. Although there are ice growth fluctuations on rough and smooth sides in Figure 6.9, it is less significant than the

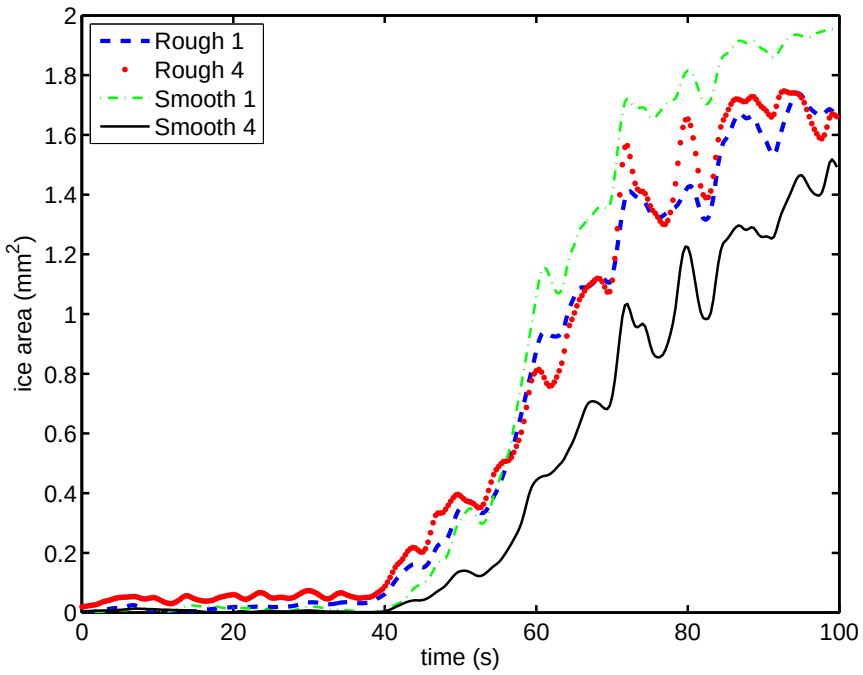

Figure 6.8: Test1. Ice accretion area within regions 1 and 4 on the cylindrical specimen at test temperature −9 °C. (Test: SM9T1HP)

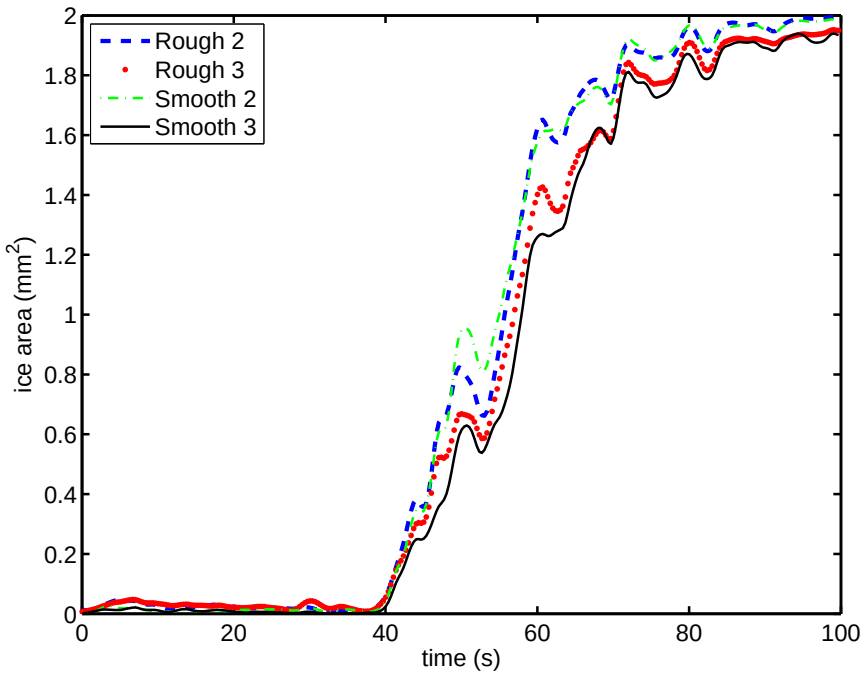

Figure 6.9: Test1. Ice accretion area within regions 2 and 3 on the cylindrical specimen at test temperature −9 °C. (Test: SM9T1HP)

fluctuations in Figure 6.8. These fluctuations can be caused by the analysis method as

well as portions of the ice being swept away due to the aerodynamic force. The code described in Section 6.3 was built to analyse each frame from the video file separately and each pixel was inspected individually. The results in region 4 and 1 do not always coincide due to the approximate nature of the viewing angle correction for the cylinder surface.

Figure 6.10 presents a montage of frames every 10 s for comparison to the results in Figures 6.8 and 6.9. Results for multiple −9 °C tests can be found in Appendix D.

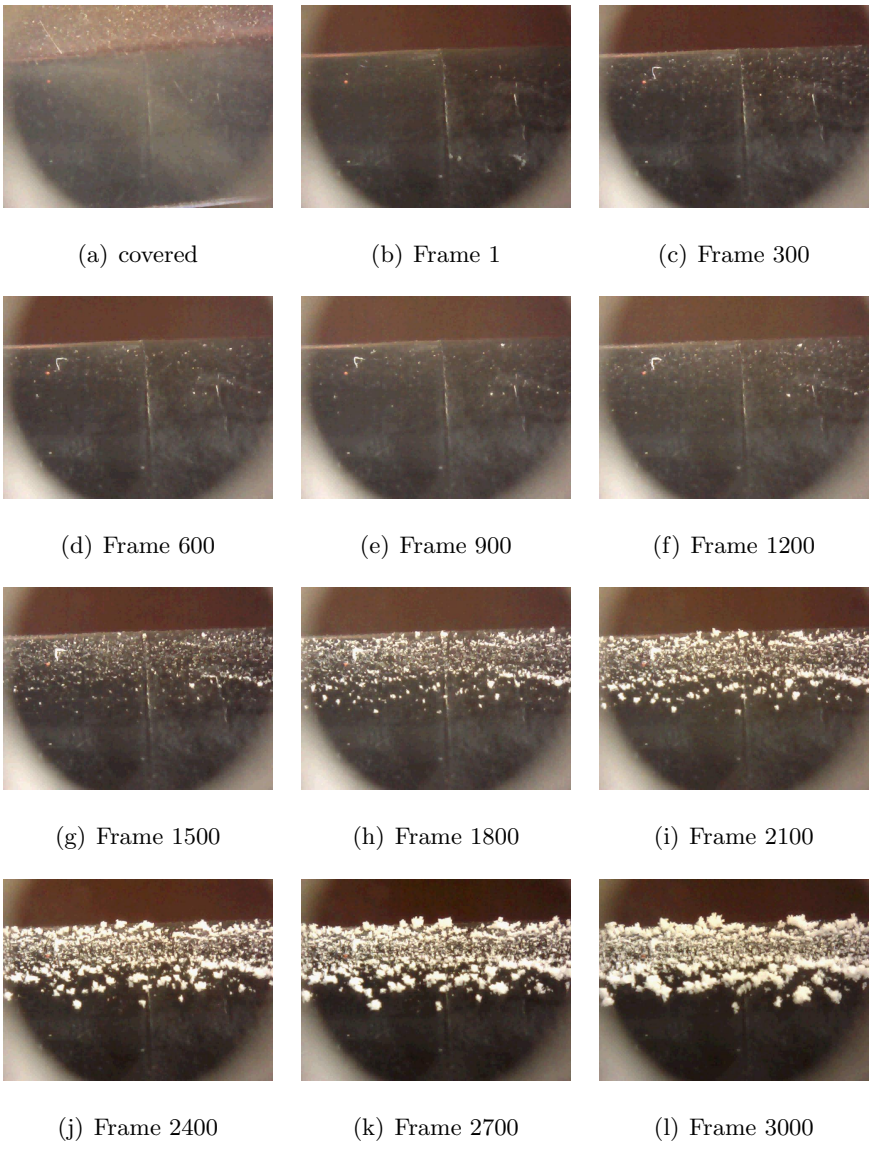

(a) covered (b) Frame 1 (c) Frame 300

(d) Frame 600 (e) Frame 900 (f) Frame 1200

(g) Frame 1500 (h) Frame 1800 (i) Frame 2100

(j) Frame 2400 (k) Frame 2700 (l) Frame 3000

Figure 6.10: Frames for ice accretion on the cylinder at −9 °C with 30 f/s recording rate from the beginning of the test. (Test: SM9T1HP)

6.5.2 Surface Temperature $-5\,^{\circ}\mathrm{C}$

For these tests the cylindrical specimen surface temperature was set to $-5\,^{\circ}\mathrm{C}$, the water tank pressure to 3.5 bar, and the flow speed to 6.5 m/s. In this case, the stream temperature varies rapidly through the liquid nitrogen duct and reaches steady temperature near the cylindrical specimen as can be seen in Figure 6.11 and Figure 6.12. Figure 6.13 and Figure 6.14 show the ice accretion on a $2\,\mathrm{mm}^2$ area on the rough and smooth surfaces. Rough and smooth sides in Figure 6.13 show similar behaviour in growth and declining of the ice. Repeated test results for the $-5\,^{\circ}\mathrm{C}$ case have been reported in Appendix D.

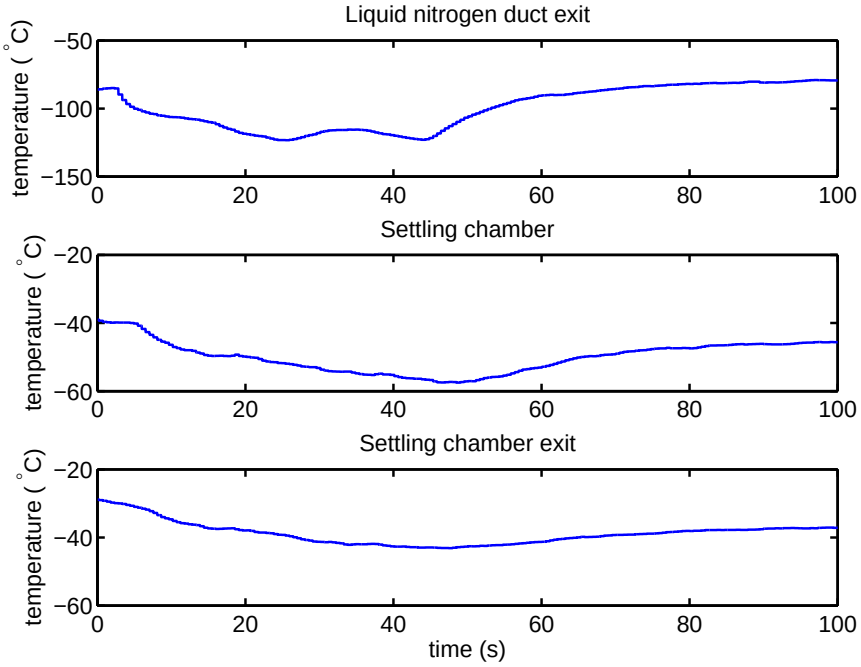

Figure 6.11: Temperatures within the facility upstream of the wind tunnel duct. Specimen temperature $-5\,^{\circ}\mathrm{C}$. (Test: SM5T2HP)

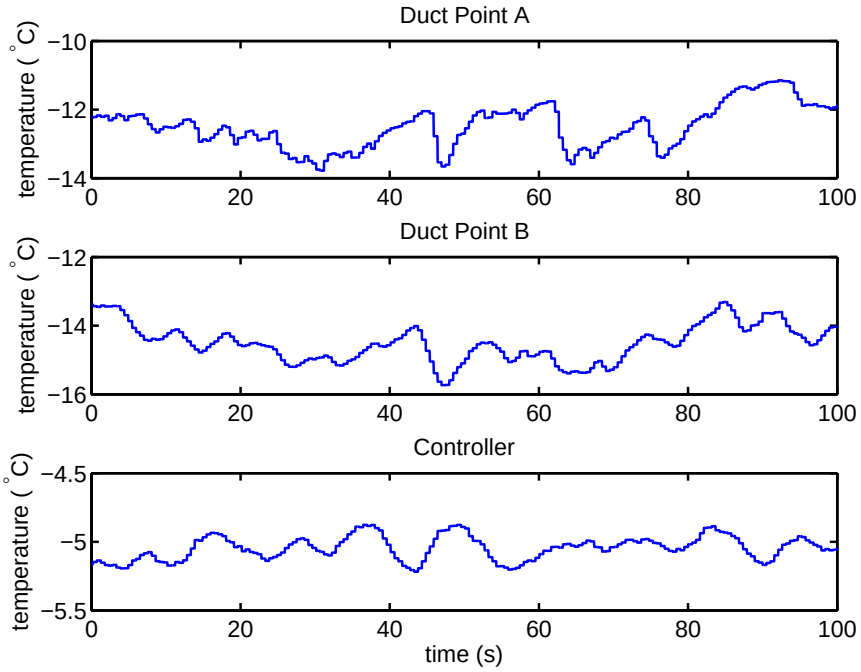

Figure 6.12: Temperatures within the wind tunnel duct for the test specimen temperature of −5 °C. (Test: SM5T2HP)

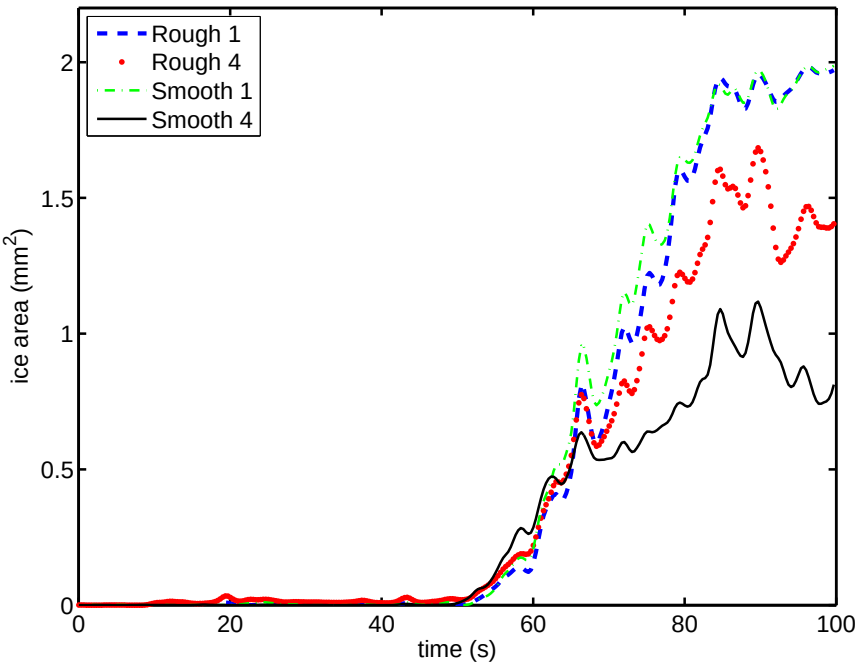

Figure 6.13: Ice accretion area within regions 1 and 4 on the cylindrical specimen at test temperature −5 °C. (Test: SM5T2HP)

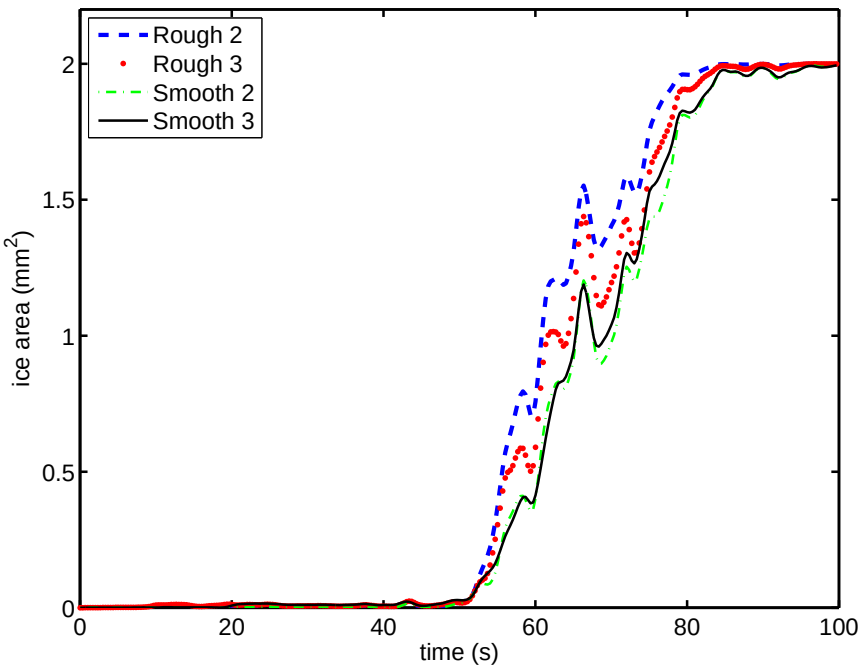

Figure 6.14: Ice accretion area within regions 2 and 3 on the cylindrical specimen at test temperature $-5\,^{\circ}$C. (Test: SM5T1HP)

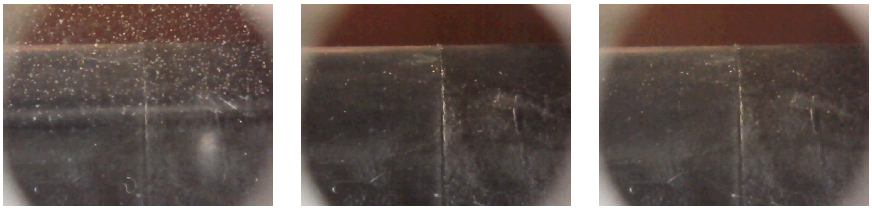

(a) covered (b) Frame 1 (c) Frame 300

(d) Frame 600 (e) Frame 900 (f) Frame 1200

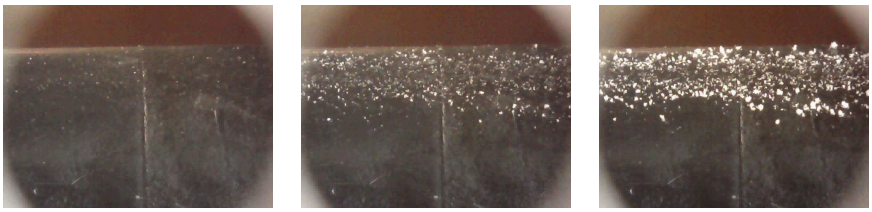

(g) Frame 1500 (h) Frame 1800 (i) Frame 2100

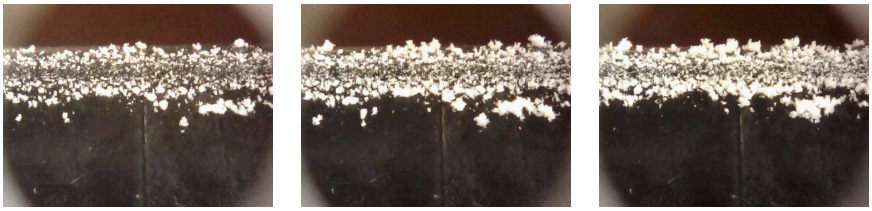

(j) Frame 2400 (k) Frame 2700 (l) Frame 3000

Figure 6.15: Frames for ice accretion on the cylinder at $-5\,^{\circ}\mathrm{C}$ with 30 f/s recording rate from the beginning of the test. (Test: SM5T2HP)

6.6 Warm Surface Temperatures

In general, the reported data for 0 °C and 5 °C specimen surface temperatures shows that the ice accretion is insignificant during the 200 s test period. In the following sections some of the results for 0 °C and 5 °C will be discussed.

6.6.1 Surface Temperature 0 °C

The ice accretion tests repeated at 0 °C specimen surface temperature, were performed nominally with the same flow conditions for −9 °C and −5 °C cases. Figure 6.16 and 6.17 show the measured flow temperatures across the entire apparatus. The surface temperature controller reading demonstrates a good performance and fluctuates only within about ±0.3 °C. In this test the time axis is 200 s, which is twice the time at −9 °C and −5 °C. The result for the whole test can be seen in Figure 6.19. The ice development on the rough and smooth sections at 0 °C are insignificant in comparison with the colder surface temperature, if the same areas are reviewed.

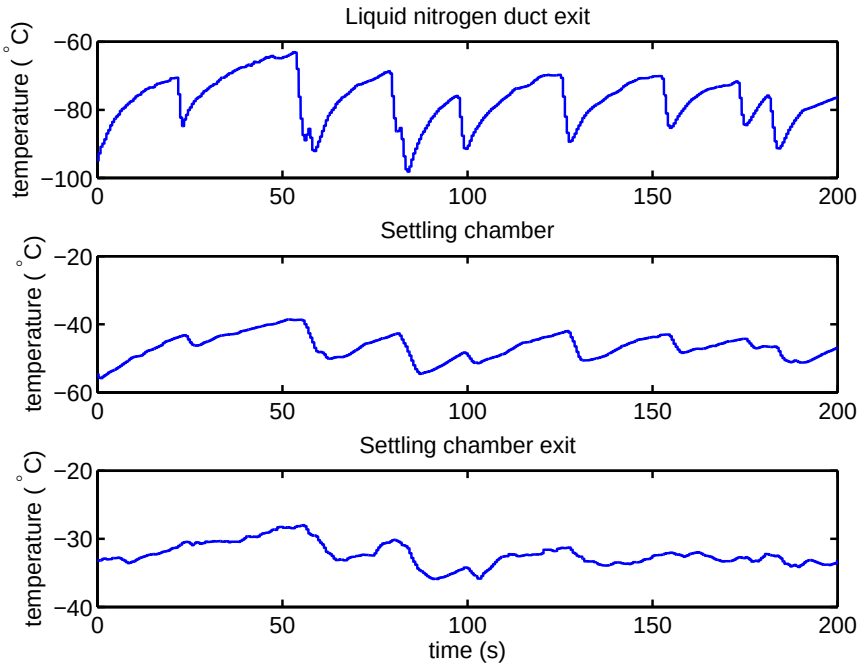

Figure 6.16: Temperatures within the facility upstream of the wind tunnel duct. Specimen temperature 0 °C. (Test: S0T5HP)

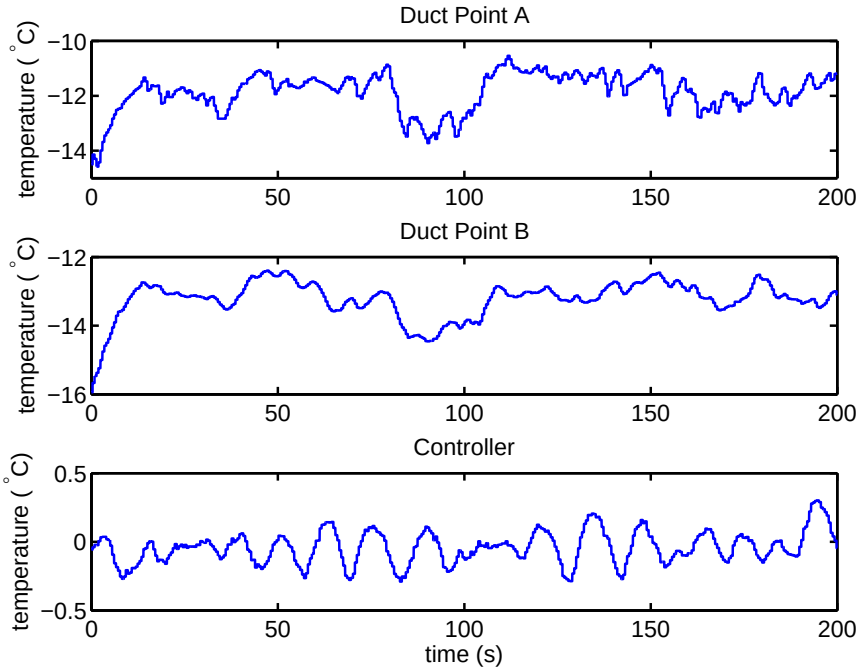

Figure 6.17: Temperatures within the wind tunnel duct for the test specimen temperature of 0 °C. (Test: S0T5HP)

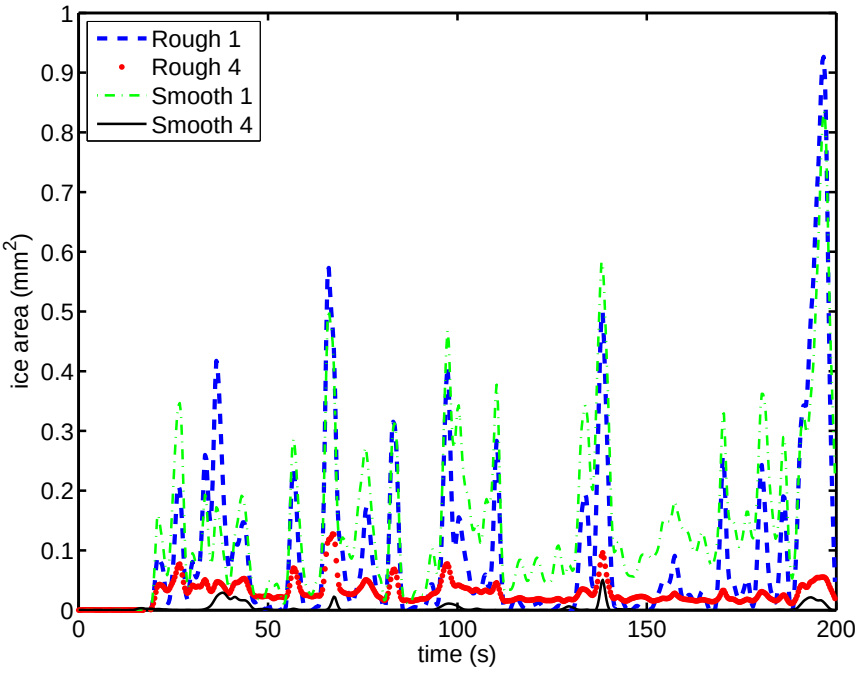

Figure 6.18: Ice accretion area within regions 1 and 4 on the cylindrical specimen at test temperature 0 °C. (Test: S0T5HP)

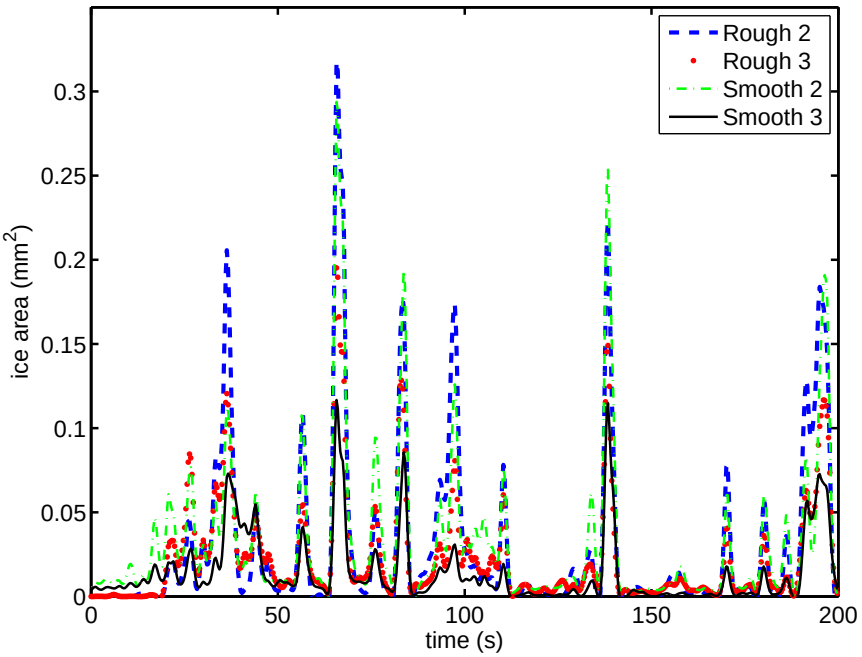

Figure 6.19: Ice accretion area within regions 2 and 3 on the cylindrical specimen at test temperature 0 °C. (Test: S0T5HP)

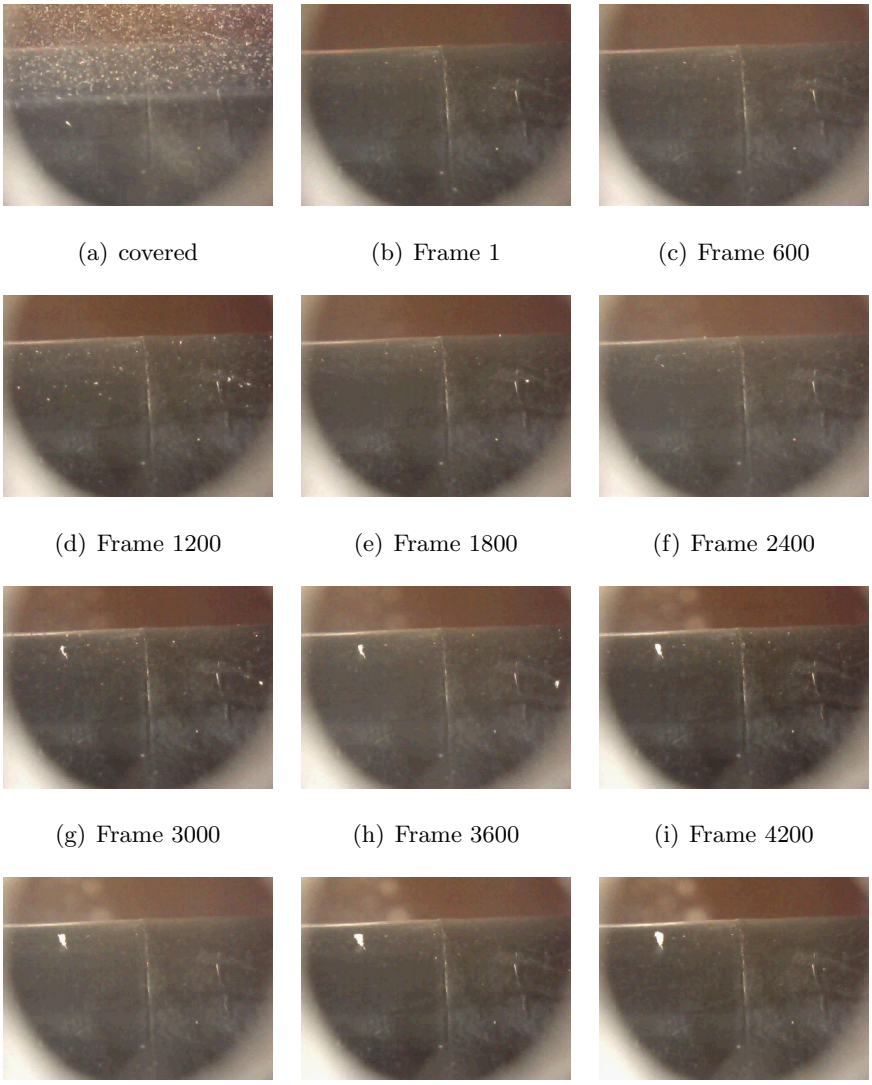

(a) covered (b) Frame 1 (c) Frame 600

(d) Frame 1200 (e) Frame 1800 (f) Frame 2400

(g) Frame 3000 (h) Frame 3600 (i) Frame 4200

(j) Frame 4800 (k) Frame 5400 (l) Frame 6000

Figure 6.20: Frames for ice accretion on the plate at 0 °C with 30 f/s recording rate from the beginning of the test. (Test: S0T5HP)

6.6.2 Surface Temperature 5 °C

Ice accretion testing was also performed with the specimen surface temperature set to 5 °C. The temperature distributions through the apparatus are shown in Figure 6.21 and Figure 6.22. The ice growth can be seen in Figure 6.23 for the rough section and Figure 6.24 for the smooth section. The usual areas relative to the stagnation line for the rough and smooth sides have been considered.

Both rough and smooth sections shown in Figure 6.23 and 6.24 demonstrate very little ice accretion even after increasing the test period to 200 s. These results are similar to the results of the 0 °C case and it can be concluded that there is no accretion above 0 °C when the ice water content is 0.42 g/m^3 or less.

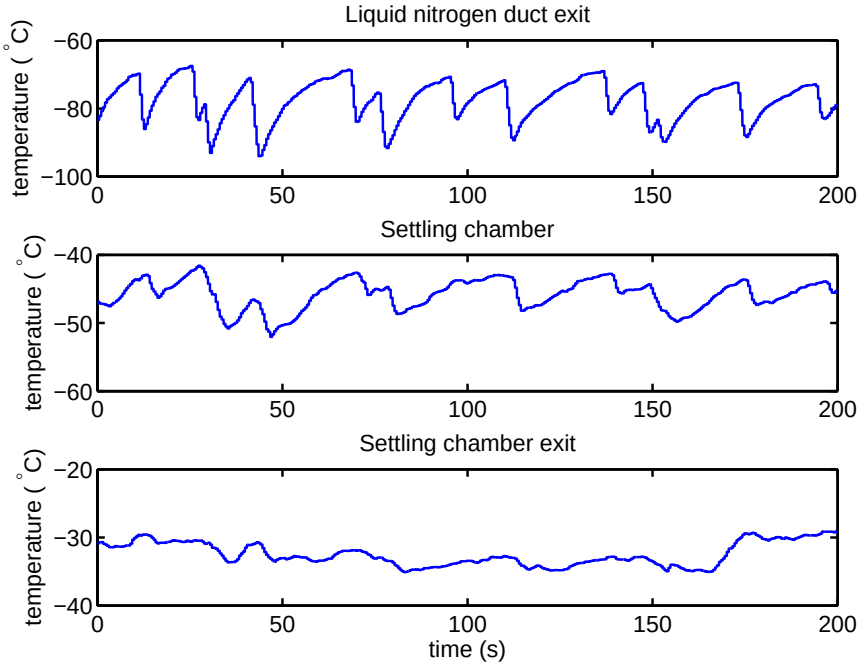

Figure 6.21: Temperatures within the facility upstream of the wind tunnel duct. Specimen temperature 5 °C. (Test: SP5T1HP)

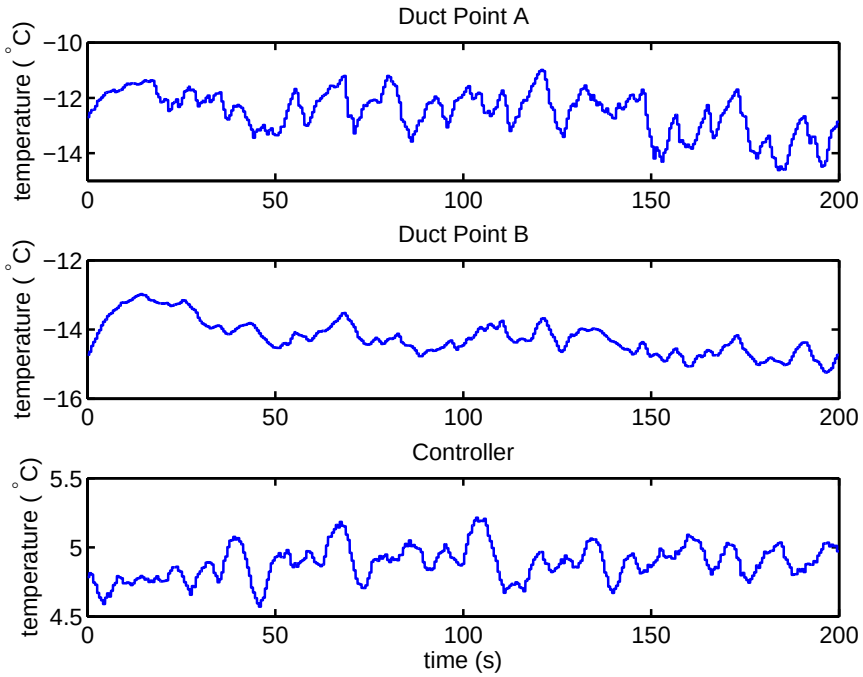

Figure 6.22: Temperatures within the wind tunnel duct for the test specimen temperature of 0 °C. (Test: SP5T1HP)

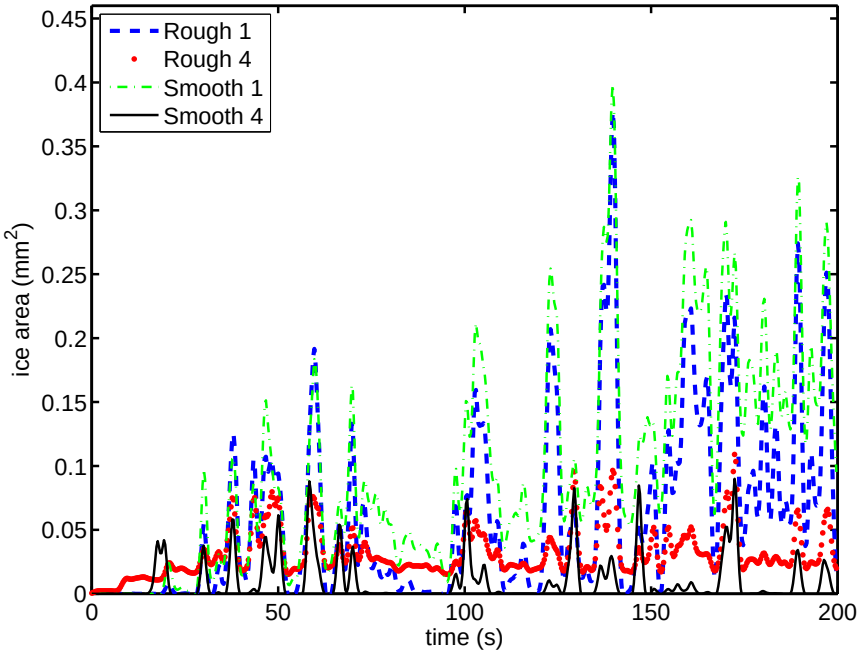

Figure 6.23: Ice accretion area within regions 1 and 4 on the cylindrical specimen at test temperature 5 °C. (Test: SP5T1HP)

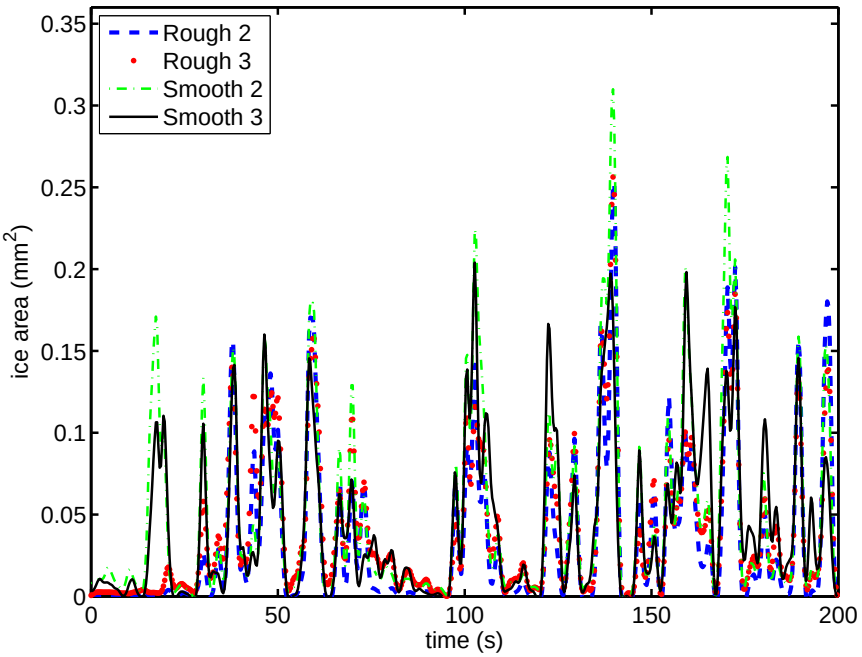

Figure 6.24: Ice accretion area within regions 2 and 3 on the cylindrical specimen at test temperature 5 °C. (Test: SP5T1HP)

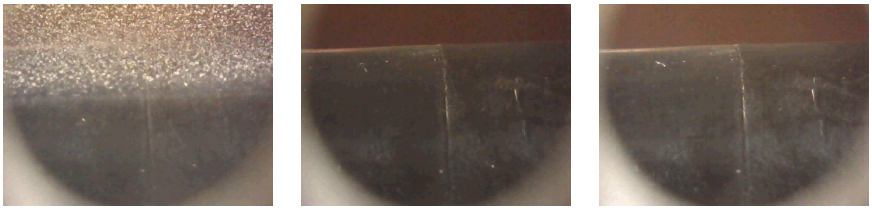

(a) covered (b) Frame 1 (c) Frame 600

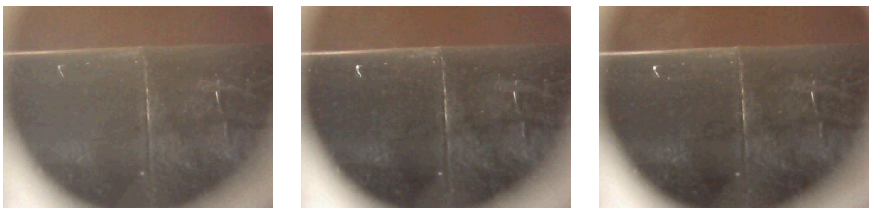

(d) Frame 1200 (e) Frame 1800 (f) Frame 2400

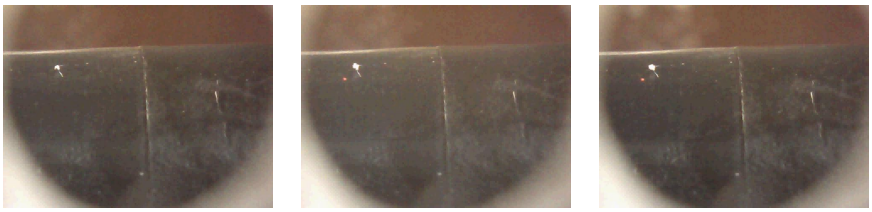

(g) Frame 3000 (h) Frame 3600 (i) Frame 4200

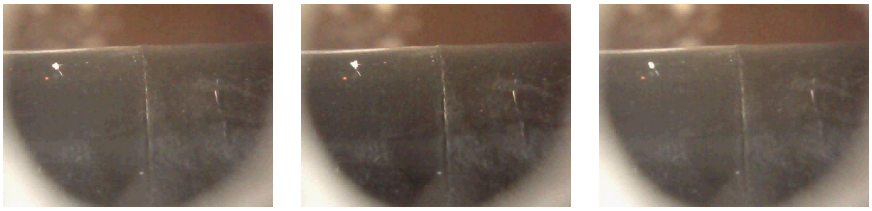

(j) Frame 4800 (k) Frame 5400 (l) Frame 6000

Figure 6.25: Frames for ice accretion on the plate at 5 °C with 30 f/s recording rate from the beginning of the test. (Test: SP5T1HP)

6.7 Test Variability

For each test on the cylindrical specimen, the variability has been defined by considering the temporal variations of the data during the test time and identifying the mean and standard deviation of the data. Results are presented in Table 6.1. The 2σ values for the temperatures at location B in the wind tunnel duct close to the test specimen vary from 0.6 to 1.8 °C. The specimen surface temperature in the whole list of tests shows small standard deviation values, due to the use of the temperature controller, which shows good performance and keeps the surface at a largely constant temperature. The maximum value of 2σ for the surface temperature was ± 0.32 °C in the SP5T2HP test at a mean surface temperature of 5 °C while the minimum was ± 0.12 °C which was recorded in SM5T4HP at a mean surface temperature of -5 °C.

6.8 Accretion Development

The development of the ice accretion in the different areas and in the different tests at nominally identical flow and surface temperature conditions was assessed by identifying the time at which ice covered 10 % and 80 % of the maximum available area (2 mm^2) in each case. Results from this analysis are presented in Figure 6.26 and Figure 6.27. The vertical axis in this figure reports the fraction of the maximum possible number of occurrence which was 24 in the case of the test results at -9 °C (8 areas $\times$ 3 experiments), 40 in the case of the test results at -5 °C (8 areas $\times$ 5 experiments), and 40 in the case of the test results at 0 °C (8 areas $\times$ 5 experiments). Results at 5 °C are not available since accretion was not registered according to the 10 % coverage criterion.

The results in Figure 6.26 and Figure 6.27 were obtained for multiple cylindrical model tests at nominally identical flow conditions, and the horizontal axis denotes the time for the sampled areas to be covered with the designated fraction of ice. Clearly, the time taken for any sampled area to reach the designated fraction of ice coverage varies dramatically. For example, up to about 60 seconds was required for all sampled areas to achieve 10 % ice coverage at surface temperature of -9 °C and even longer periods are

Table 6.1: Operating conditions for the cylindrical specimen tests, uncertainties quoted correspond to $\pm 2\sigma$ values.

Test	T_{LN_2E} (°C)	T_{SC} (°C)	T_{SCE} (°C)	T_A (°C)	T_B (°C)	IWC (g/m^3)	T_S (°C)	Figures
SM9T1HP	-91.7 ± 12.5	-49.4 ± 6.8	-42.4 ± 3.7	-13.9 ± 1.8	-15.5 ± 1.7	0.42 ± 0.26	-8.99 ± 0.20	D.1 - D.4
SM9T2HP	-86.9 ± 15.8	-46.9 ± 5.3	-40.1 ± 3.3	-15.0 ± 1.5	-15.4 ± 1.4	0.42 ± 0.26	-9.00 ± 0.14	D.5 - D.8
SM9T3HP	-81.0 ± 16.5	-45.4 ± 6.7	-39.1 ± 4.6	-13.6 ± 1.1	-15.2 ± 0.7	0.42 ± 0.26	-9.00 ± 0.16	D.9 - D.12
SM5T1HP	-73.5 ± 15.8	$-43.6.9 \pm 7.0$	-35.9 ± 4.9	-13.0 ± 1.1	-14.6 ± 1.0	0.42 ± 0.26	-5.04 ± 0.21	D.13 - D.16
SM5T2HP	-99.3 ± 30.5	-50.0 ± 9.2	-38.8 ± 6.6	-12.5 ± 1.3	-14.5 ± 1.0	0.42 ± 0.26	-5.05 ± 0.17	D.17 - D.20
SM5T3HP	-90.6 ± 20.2	-47.0 ± 10.4	-39.6 ± 7.6	-12.5 ± 1.0	-14.7 ± 1.6	0.42 ± 0.26	-5.05 ± 0.13	D.21 - D.24
SM5T4HP	-87.3 ± 13.4	-50.8 ± 6.6	-41.4 ± 4.6	-14.1 ± 0.9	-15.9 ± 1.0	0.42 ± 0.26	-5.05 ± 0.12	D.25 - D.28
SM5T5LP	-77.8 ± 20.1	-44.2 ± 8.3	-36.9 ± 5.6	-13.3 ± 1.2	-14.7 ± 0.6	0.3 ± 0.15	-4.99 ± 0.21	D.29 - D.32
S0T1HP	-71.4 ± 13.3	-41.0 ± 5.5	-33.7 ± 2.9	-12.8 ± 1.0	-14.4 ± 0.8	0.42 ± 0.26	-0.06 ± 0.17	D.33 - D.36
S0T2HP	-71.4 ± 17.7	-40.5 ± 7.4	-32.6 ± 4.3	-9.7 ± 1.2	-11.4 ± 1.0	0.42 ± 0.26	-0.01 ± 0.22	D.37 - D.40
S0T3HP	-75.6 ± 12.8	-44.7 ± 4.6	-33.2 ± 6.6	-15.1 ± 3.2	-16.2 ± 1.3	0.42 ± 0.26	-0.06 ± 0.19	D.41 - D.44
S0T4HP	-79.8 ± 12.6	-45.7 ± 4.8	-36.8 ± 2.9	-11.1 ± 1.5	-12.8 ± 1.0	0.42 ± 0.26	-0.05 ± 0.22	D.45 - D.48
S0T5HP	-77.1 ± 14.2	-46.7 ± 7.3	-32.3 ± 3.4	-11.9 ± 1.4	-13.2 ± 1.1	0.42 ± 0.26	-0.04 ± 0.24	D.49 - D.52
SP5T1HP	-77.6 ± 11.4	-45.8 ± 4.4	-32.5 ± 3.4	-12.5 ± 1.6	-14.2 ± 1.0	0.42 ± 0.26	4.89 ± 0.24	D.53 - D.56
SP5T2HP	-78.9 ± 13.4	-46.0 ± 6.0	-31.5 ± 3.5	-13.9 ± 2.2	-15.4 ± 1.8	0.42 ± 0.26	4.85 ± 0.32	D.57 - D.60
SP5T3HP	-79.4 ± 16.0	-46.1 ± 6.9	-28.6 ± 2.6	-13.1 ± 1.9	-14.6 ± 1.3	0.42 ± 0.26	4.89 ± 0.25	D.61 - D.64
SP5T4HP	-79.4 ± 14.9	-45.2 ± 8.8	-23.9 ± 11.9	-13.3 ± 2.2	-14.6 ± 1.8	0.42 ± 0.26	4.90 ± 0.23	D.65 - D.68
SP5T5HP	-39.2 ± 30.0	-28.3 ± 13.8	-18.8 ± 5.7	-8.9 ± 0.8	-10.6 ± 1.5	0.42 ± 0.26	4.94 ± 0.29	D.69 - D.72

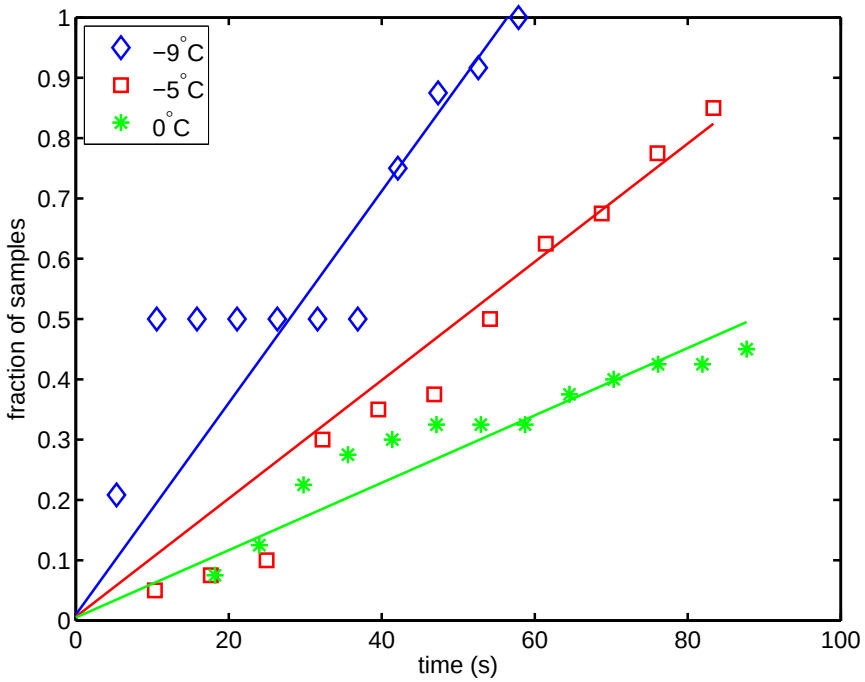

Figure 6.26: Number of samples with at least 10 % ice coverage as a function of time. Lines of the best fit (forced to pass through the origin) are also presented for three surface temperatures: −9 °C, −5 °C, and 0 °C.

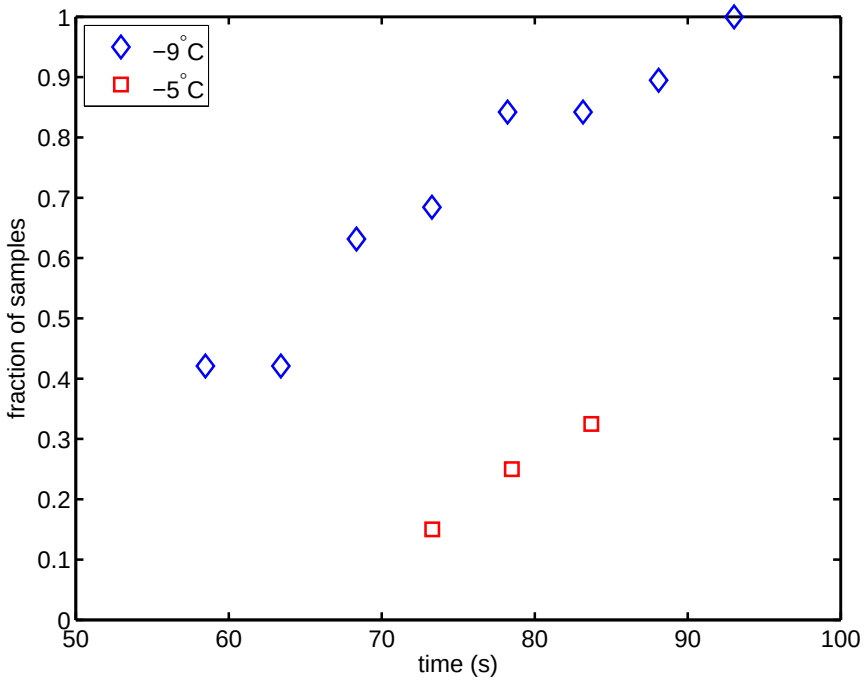

Figure 6.27: Number of samples with at least 80 % ice coverage as a function of time.

required at higher surface temperatures (Figure 6.26). Given the apparent stochastic nature of the ice accretion development at the present conditions, it is possible to interpret these figures in terms of the probabilities. Both figures effectively describe the likelihood that a particular sampled area will be covered with the designated fraction of ice as a function of time.

Figure 6.26 shows that the likelihood of 10 % ice coverage at −9 °C increases with time and by 50 s, about 85 % of the total number of samples had 10 % ice coverage. The results for 80 % ice coverage of the sampled areas is presented in Figure 6.27 and it shows substantial delay in achieving 80 % coverage relative to the 10 % case. For the −9 °C surface temperature, 80 % coverage of the sampled area starts to appear after 50 s and by 100 s, all of the sampled areas show 80 % coverage.

At −5 °C surface temperature, Figure 6.26 shows that the likelihood of achieving 10 % coverage at any given time is lower than −9 °C for the surface temperature tests. Less than half of the total number of samples at −5 °C achieved 10 % coverage in the first 50 s. The fraction of the number of samples covered by ice continued to increase with time and by 100 s around 85 % of the samples have an ice coverage of at least 10 %. For the case of achieving 80 % coverage by ice (Figure 6.27), a clear delay can be seen relative to the 10 % coverage case for the −5 °C surface temperature.

Although the number of samples achieving 10 % coverage at the 0 °C surface temperature initially increase with time at rate similar to that of −5 °C surface temperature case (Figure 6.27), 80 % coverage of the sampled area is not achieved in any cases within the first 100 seconds (Figure 6.27).

The experimental results reveal that at the cold surface temperatures (−9 °C and −5 °C), the ice accumulated to completely fill all of the areas within about 100 s. While at the warmer temperatures (0 °C and 5 °C), there is insignificant ice accretion on the sampled areas (for both the rough and smooth sections).

6.9 Discussion

6.9.1 Subzero Ice Accretion

The results from the mathematical model and the experimental tests of the ice accretion on the cylindrical specimen were presented for the free stream speed of 6.5 m/s. The low Reynolds number achieved in the present tests means the results are not directly relevant to typical turbofan icing conditions, but they do provide the opportunity for model validation at low speeds. The experiments were performed using entirely solid phase water particles to investigate the possibility of ice particle accretion in the vicinity of the stagnation point at subfreezing conditions as suggested by the model. Previous observation suggested that solid ice particles bounce off aircraft structures at subfreezing conditions and do not results in any accretion (Mason et al., 2006).

Mason et al. (2011) tested mixed ice-water droplet accretion using an apparatus which generated test conditions directly relevant to the engine icing hypothesis. Ambient flow and surface temperatures where above $-1\,^{\circ}\mathrm{C}$, the flow speed was 90 m/s, and the particle diameter was larger than 115 μm. The work by Mason et al. (2011) focuses on the mixed phase ice conditions and differs from the present study in terms of the surface temperature, particle size, and the free stream speed.

The experimental results in the present study verify that accretion of ice particles is possible at subfreezing surface temperatures in the vicinity of the stagnation region. Struk et al. (2012) also found that ice accretion can occur on the leading edge but the experimental work of Struk et al. (2012) was performed for crystal and mixed crystal-water droplets concentration above $1.1\,\mathrm{g/m^3}$, at different total flow temperature between $5\,^{\circ}\mathrm{C}$ and $15\,^{\circ}\mathrm{C}$. Although Struk et al. (2012) tested the accretion of ice particles, the air flow temperature above $0\,^{\circ}\mathrm{C}$ is likely to partially melt the crystals and cause mixed ice $-$ liquid conditions. The Struk et al. (2012) work also differs from the present work in that a lower ice content of around $0.42\,\mathrm{g/m^3}$ was used for short test period of less than 200 s.

The model in Chapter 3 for the cylindrical specimen can be used to explain the present

results. The ice accretion can occur because the friction force is higher than the aerodynamic drag force in the boundary layer, as shown in Figure 6.1. At the low free stream speeds, the thickness of the stagnation region boundary layer is relatively large, and this reduces the magnitude of the aerodynamic drag force relative to the higher speed case. Larger ice particles can remain stationary in the vicinity of the stagnation point at lower free stream speeds. The model also shows that with a decrease of the friction coefficient, ice particles are less likely to remain stationary on the surface since the maximum particle size for which the friction exceeds the aerodynamic drag shifts to smaller values.

In the initial stage of ice accretion at subfreezing temperatures there is no detectable difference between the rough and the smooth surfaces used in these tests. Dotan et al. (2009) reported that the roughness of the surface may affect the ice growth on the surface but no limits for the roughness were specified. In the present work the maximum roughness of the average peak to valley height was around 4.6 μm, whereas ice particle sizes were around 50 μm, and the boundary layer thickness was around 70 μm. It is currently speculated that the surface roughness will have to approach either the particle size or the boundary layer thickness in order to affect the accretion initiation process.

6.9.2 Role of Surface Temperature

The role of the surface temperature on the initiation of the ice accretion was tested by performing the experiments at different surface temperatures (-9, -5, 0, and 5 °C). The experimental results demonstrate that the ice accretion can initiate at surface temperatures less than 0 °C and does not occur for temperatures above 0 °C. The role of the surface temperature on the ice accretion initiation can be seen in Figure 6.26 and Figure 6.27. At a fix free stream speed, the model of Chapter 3 indicates that at lower particle and surface temperatures, the friction coefficient will be higher, allowing larger particles to adhere to the surface and this will lead to a faster rate of ice accretion.

From Figure 6.9 and Figure 6.14, the ice coverage of the areas S3 and R3 can be compared at two different temperatures -9 °C and -5 °C. The ice growth in these

cases shows a clear delay in the $-5\,^{\circ}\mathrm{C}$ test with accretion starts occurring at around 50 s, while at $-9\,^{\circ}\mathrm{C}$, the accretion started earlier at 40 s. The fluctuation of the ice growth area in $-5\,^{\circ}\mathrm{C}$ test was higher than the fluctuation in the $-9\,^{\circ}\mathrm{C}$. These two features can be explained due to increase of the adhesive force of the ice particles with decreasing of the surface temperature.

The results of the ice accretion for $-9\,^{\circ}\mathrm{C}$ and $-5\,^{\circ}\mathrm{C}$ cases show that the growth of ice coverage on the areas close to stagnation region occurs faster than in the areas further away from the stagnation region. The stagnation region has higher friction force according to the model in Chapter 3, and the aerodynamic drag force is smaller than the friction force in this region. The friction force is also affected the surface temperature and increases with temperature decreases, so the friction force is likely to be responsible for this effect.

6.10 Conclusion

In this chapter, two matters have been addressed: (1) the possibility of the ice accretion in the vicinity of the stagnation region at subfreezing temperatures; and (2) the role of the surface temperature in the ice accretion process. The experimental data and mathematical model demonstrate that ice initiation can occur in the vicinity of the stagnation point at the present conditions for temperatures below $0\,^{\circ}\mathrm{C}$. It is also found that the rate of accretion is highly dependant on the surface temperature: there is virtually no accretion at a surface temperature of $0\,^{\circ}\mathrm{C}$ or above. For the surface roughness test, there was no detected influence on the accretion process.

Chapter 7

Ice Accretion on Flat Plate Specimen

7.1 Introduction

Ice accretion initiation experiments on a flat plate specimen are presented in this chapter. The motivation for the flat plate work and the methodology used to obtain the experimental results as well as the data analysis methods are also presented. The ice accretion results on cold and warm surfaces with nominally identical external flow conditions are reported. The specimen was divided into two areas having different roughness. No accretion on the surface aligned with the flow direction was registered, but icing near the leading edge stagnation region was observed. The initiation of the ice accretion on the leading edge is similar to the results obtained in Chapter 6 and depends strongly on the surface temperature.

7.2 Motivation and Experiment Design

Ice accretion in the stagnation region of the cylinder at subfreezing conditions and absence of accretion at melting conditions were both demonstrated in Chapter 6, consistent with the stagnation region accretion model introduced in Chapter 3. A model

for accretion initiation in the boundary layer of a flat plate was also introduced in Chapter 3, and this model similarly indicated the possibility of ice accretion. An experimental arrangement that could test the applicability of the model in the flat plate arrangement was therefore investigated.

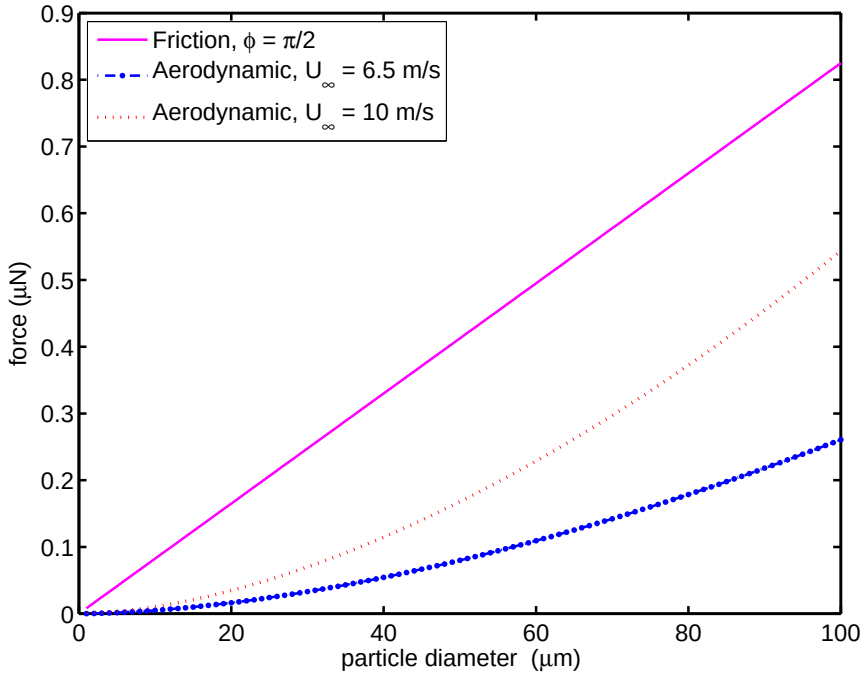

Figure 7.1: Aerodynamic drag force and the friction force variation with particle diameter for $\mu = 0.07$, $x = d_p$, $u_p = 0$, volume fraction of 0.05, $\phi = \pi/2$, and different free stream speeds.

Results from the model (Chapter 3) for the relatively low flow speeds that can be achieved in the present facility are presented in Figure 7.1 for the case of a laminar boundary layer on a flat plat. The results show that the friction forces are higher than the drag force even at the very high contact angle of $\pi/2$ and low friction coefficient of $\mu = 0.07$ at the low speed of 6.5 m/s. At the slightly higher free stream flow speed of 10 m/s which can also be achieved in the present facility, the aerodynamic force is also less than the friction force. Figure 7.1 was produced for the case where the distance from the leading edge is equal to the particle diameter, while Figure 7.2 was generated for the case of particles at a distance of 1 mm from the leading edge. As the distance from the leading edge increases, larger ice particles can remain stationary on the surface.

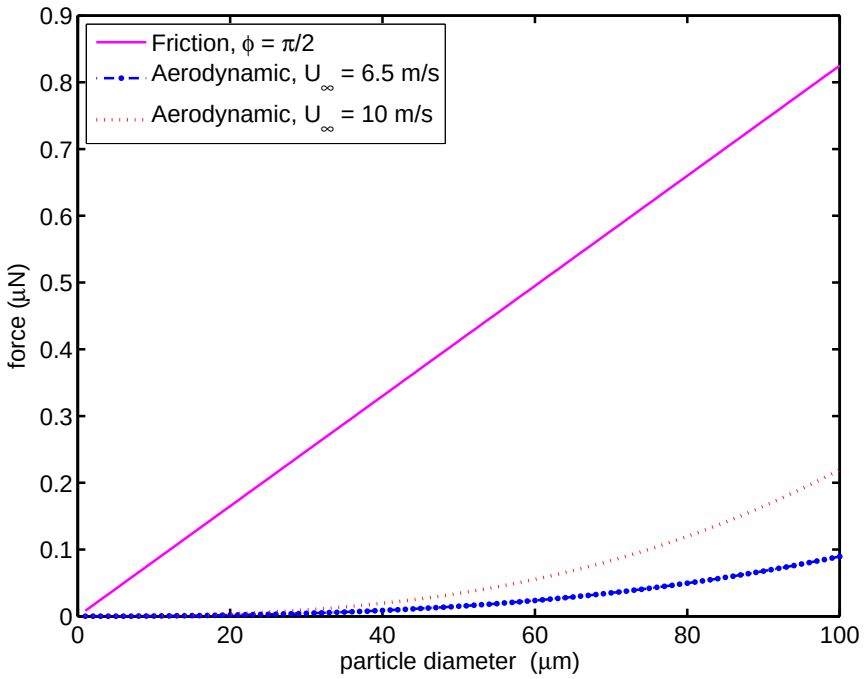

Figure 7.2: Aerodynamic drag force and the friction force variation with particle diameter for $\mu = 0.07$, $x = 1\,\text{mm}$, $u_p = 0$, volume fraction of 0.05, $\phi = \pi/2$, and different free stream speeds.

If an ice particle moving in the flow at 6.5 m/s makes the contact with the surface of the flat plate, some distance will be required to decelerate to zero, depending on the ice particle diameter. The deceleration of particles in the flat plate case will occur due to the combined effect of the friction and aerodynamic drag force on the particle in the boundary layer. While in the case of the stagnation region of a cylinder, the deceleration primarily happens via the collision of the ice particle with the surface.

Figure 7.3 shows results from the calculation of the deceleration distance of different size ice particles for different coefficients of friction based on an integration of Newton's law $\ddot{x} = F/m_p$ where F is the instantaneous net force acting on the particle due to combined effect of aerodynamic and friction forces. As the ice friction coefficient increases the deceleration distance decreases. In Figure 7.3 two extreme friction coefficients and two moderate coefficient values were considered, these values are: 0.05, 0.07, 0.1 and 0.6. For particles with $d_p = 100\,\mu\text{m}$, the deceleration distance varies from 32 mm at the lowest friction coefficient to less than 5 mm at the highest friction coefficient. Figure 7.3 demonstrates that according to the model (Chapter 3), ice accretion initiation can

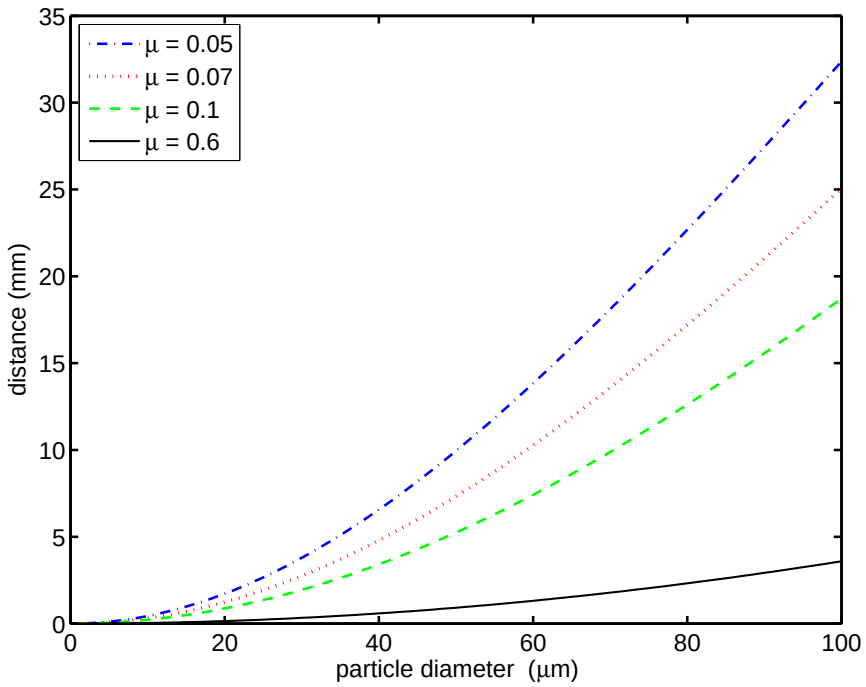

Figure 7.3: Particle distance variation to stop with particle diameter for different friction coefficient μ, and at initial conditions of $u_p = 6.5$, volume fraction of 0.05, $\phi = \pi/2$, and free stream speeds 6.5 m/s.

occur with a relatively short distance of the leading edge for the conditions which can be generated using the present facility.

Therefore a flat plate experiment was established with the goal of further examining the validity of the model introduced in Chapter 3. Unfortunately the leading edge of the flat plate specimen used in this work was relatively blunt and this had a profound effect on the experiment. Ice accretion on the flat plate surface was not observed, although movement of ice deposits along the flat plat surface was recorded when ice particles were no longer present in the flow. Therefore, in the following presentation, the analysis of the results is focused on the stagnation region of the blunt leading edge, in a manner similar to that presented in Chapter 6.

7.3 Testing Methods

Prior to an ice accretion test, reference images were obtained using a reference specimen to relate physical locations on the actual flat plate test specimen to pixels in the video record. The reference flat plate specimen was divided spatially into a grid made up of $1 \times 1\,\mathrm{mm}^2$ areas marked on the plate surface, and these regions were analysed to assess the spatial differences in ice accretion on the specimen. The marked reference plate was the same dimensions as the test plate and it was placed in the position of the actual test plate as shown in Figure 7.4. The centre line of the wind tunnel and the stagnation line of the plate edge were marked as broken lines on the reference plate. The area of interest corresponds to one millimetre on either side of the centre line.

On the actual plate specimen, the left hand side of the centre line was a rough area, where it has been painted black only. The right hand side of the specimen was the smooth surface, which was painted black and polished using a fine-grade sandpaper. So for each test, ice accretion data for two different roughnesses on either side of the centre of the tunnel and specimen were recorded.

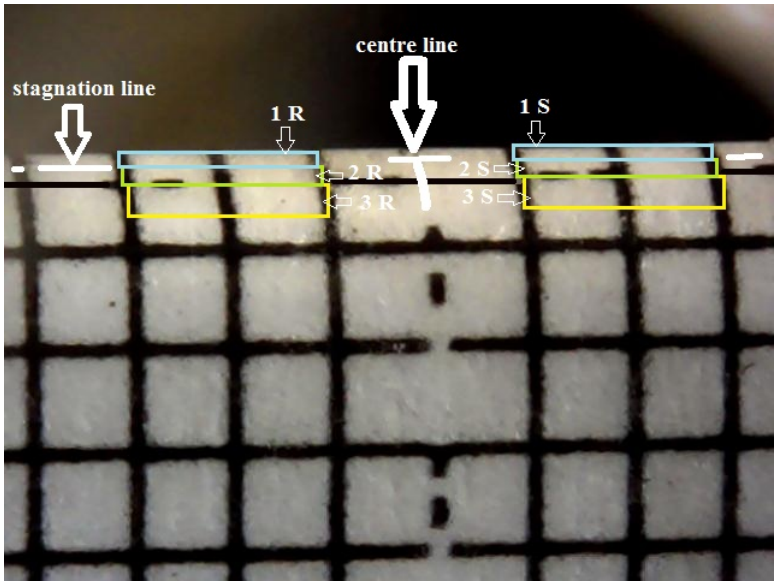

Figure 7.4: Annotated photograph of the flat plate reference model with a $1 \times 1\,\mathrm{mm}$ grid.

To analyse the accretion results, both sides (rough and smooth) were treated separately and each side was divided into three areas. These three areas were designated: 1 Smooth (1S), 2 Smooth (2S), and 3 Smooth (3S), for the smooth side and for the

rough side as 1 Rough (1R), 2 Rough (2R), and 3 Rough (3R) as indicated in Figure 7.4. For the flat plate model the 1mm area corresponds to: 162×13 pixels for 1R and 1S, 162×15 pixels for 2R and 2S, and 162×24 pixels for area 3R and 3S. The equivalent area of each pixel was identified and the particle diameter having the same cross-section area was calculated. Pixels in 1R are equivalent to a particle size of 24 μm, and the pixels in 3S or 3R are equivalent to a particle size of 18 μm. After recording the reference image, the reference model was replaced by the actual plate, which is shown in Figure 7.5.

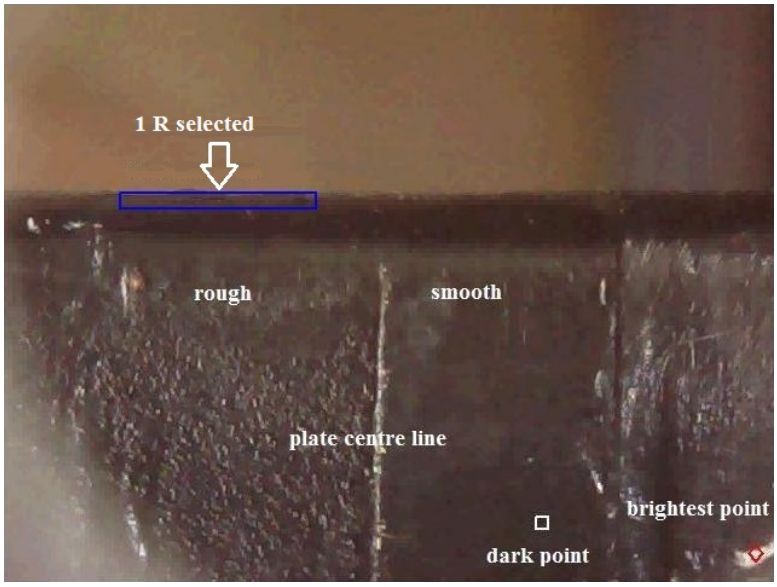

Figure 7.5: Annotated photograph of the flat plate model after removing the plastic protector.

The ice accretion tests followed the procedure mentioned in Section 6.3.

The surface roughness of both smooth and rough sides for the plate specimen were measured using a MITATOYO Surftest-4 surface roughness stylus. The average roughness for the smooth side was found to be $R_a = 3\,\mu$m, and the average peak to valley height R_z was 5.5 μm. For the rough region the R_a was 4.5 μm and R_z was 14.5 μm.

7.4 Analysis Methods

To find the ice accretion area on the surface, a code was built using Matlab. The method used by the code is described in Section 6.4.

7.5 Cold Surface Temperatures

Complete tests results are presented in Appendix E. Each test was repeated three times or more and in general, the reported data for $-9\,^{\circ}\mathrm{C}$ in this chapter shows that the ice accretion happened faster close to the stagnation line, and in all cases a complete coverage of the area is achieved between 20 s to 40 s. Ice accretion occurs more slowly further away from the stagnation line and it can take up to 100 s to achieve a complete coverage of the local area. At $-5\,^{\circ}\mathrm{C}$, although the results show some delay in the accretion process, they demonstrate identical behaviour of the accumulation to $-9\,^{\circ}\mathrm{C}$ case. In the following sections the results for the $-9\,^{\circ}\mathrm{C}$ and $-5\,^{\circ}\mathrm{C}$ will be discussed in more detail.

7.5.1 Surface Temperature $-9\,^{\circ}\mathrm{C}$

The cold room temperature was set to $-10\,^{\circ}\mathrm{C}$, flow speed was set to 6.5 m/s, and the water tank pressure was set to 3.5 bar, the test specimen temperature was set to $-9\,^{\circ}\mathrm{C}$. Figure 7.6 and Figure 7.7 show the typical temperatures of the flow through the wind tunnel duct at different locations. The combination of duct temperatures, flow speed, and thermal modelling indicates that the droplets are most likely to be in solid state as discussed in Section 4.3.

In Figure 7.6 the liquid nitrogen duct exit temperature shows a variation in temperature between $-100\,^{\circ}\mathrm{C}$ and $-75\,^{\circ}\mathrm{C}$, and this arises due to the decrease in the liquid nitrogen level and the duct refilling process. Although corresponding temperature fluctuations are also observed in the settling chamber and at the exit of the chamber, the variation in amplitude decreases from $\pm 10\,^{\circ}\mathrm{C}$ in the liquid nitrogen duct down to $\pm 5\,^{\circ}\mathrm{C}$ at the settling chamber exit, see Figure 7.6. The flow temperatures rise through

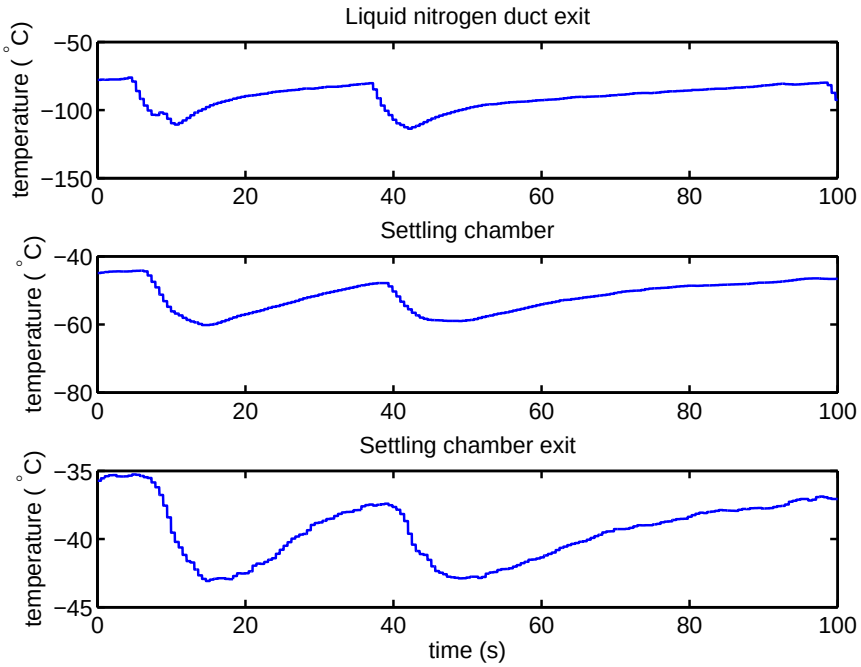

Figure 7.6: Temperatures within the facility upstream of the wind duct. Specimen temperature −9 °C. (Test: FM9T4HP)

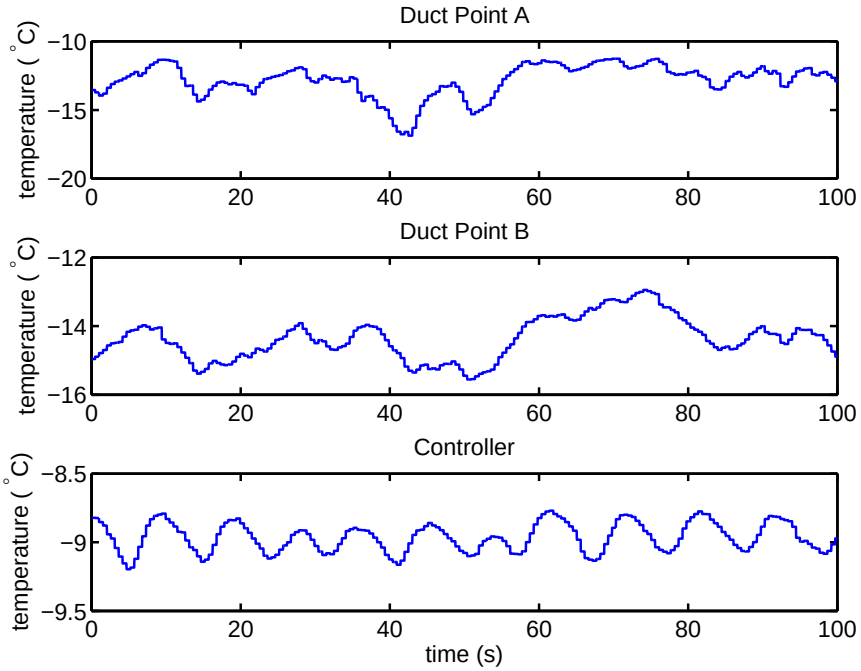

Figure 7.7: Temperatures within the wind tunnel duct for the test specimen temperature of −9 °C. (Test: FM9T4HP)

out the facility from the liquid nitrogen duct onwards due to heat transfer from the relatively warm cold room environment at −10 °C. At the inlet of the wind tunnel duct

and near the test specimen, an additional temperature increase is observed in Figure 7.7 due to mixing between the particle laden flow and the cold room air. Within the duct at point A and B, the temperature is constant with time to about $\pm 2\,^{\circ}\mathrm{C}$ and a variation of about $\pm 0.2\,^{\circ}\mathrm{C}$ is recorded on the surface of the test specimen as shown in Figure 7.7.

The area of ice accretion was determined for each of the $1\,\mathrm{mm}^2$ area as described in Section 7.3. Results for the ice accumulation on areas near the stagnation line are shown in Figure 7.8 and Figure 7.9 and the ice accretion in Figure 7.10 shows the accumulation on the area further from the stagnation line. The ice accretion on these areas shows very similar accumulation, although the accumulation on the Smooth 3 and Rough 3 areas appear somewhat delayed relative to the other areas. The delay in the ice accretion on Rough 3 is due to the distance from the stagnation line, and the earlier accretion on region 2 can change the flow field effect on any particle landed on this area later on. Figure 7.11 presents a montage of frames every 10 s for comparison to the results in Figures 7.8, 7.9, and 7.8. Results for multiple $-9\,^{\circ}\mathrm{C}$ tests can be found in Appendix E, which, in general, show similar ice area growth behaviour.

In this test, the ice growth rate was not calculated because the initiation of the ice accretion is main concern of this study; the growth processes have to be studied in the future work.

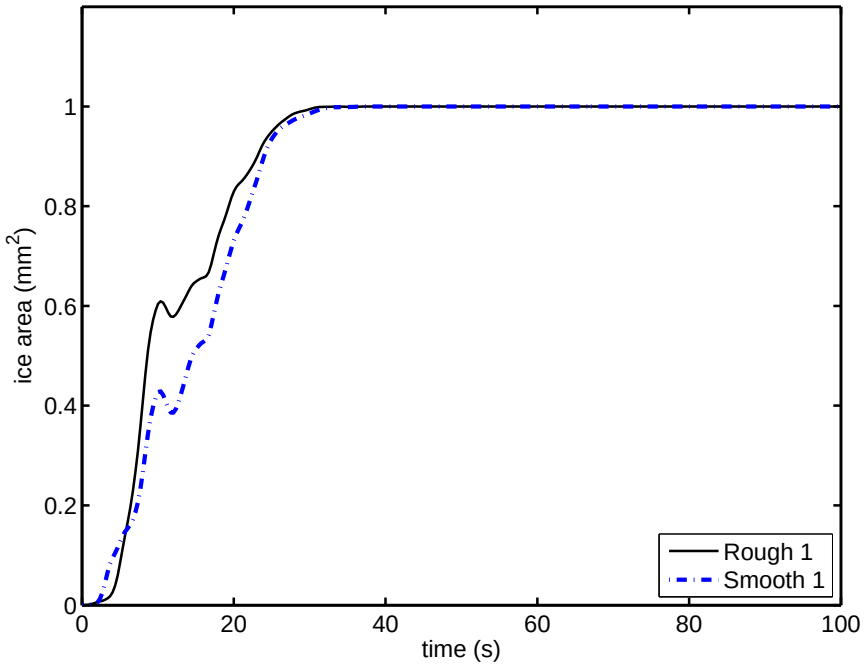

Figure 7.8: Ice accretion area within region 1 on the flat plate specimen at test temperature −9 °C. (Test: FM9T4HP)

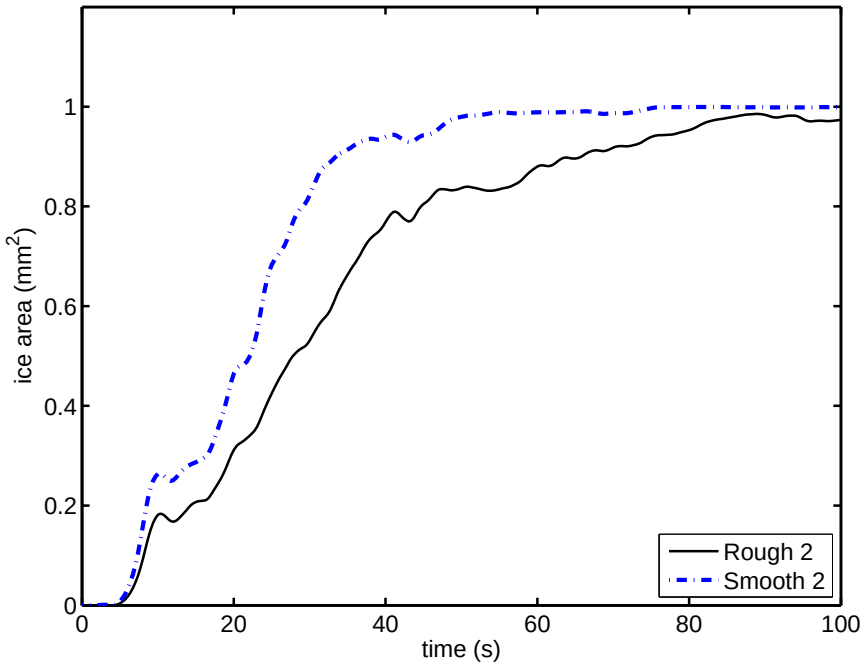

Figure 7.9: Ice accretion area within region 2 on the flat plate specimen at test temperature −9 °C. (Test: FM9T4HP)

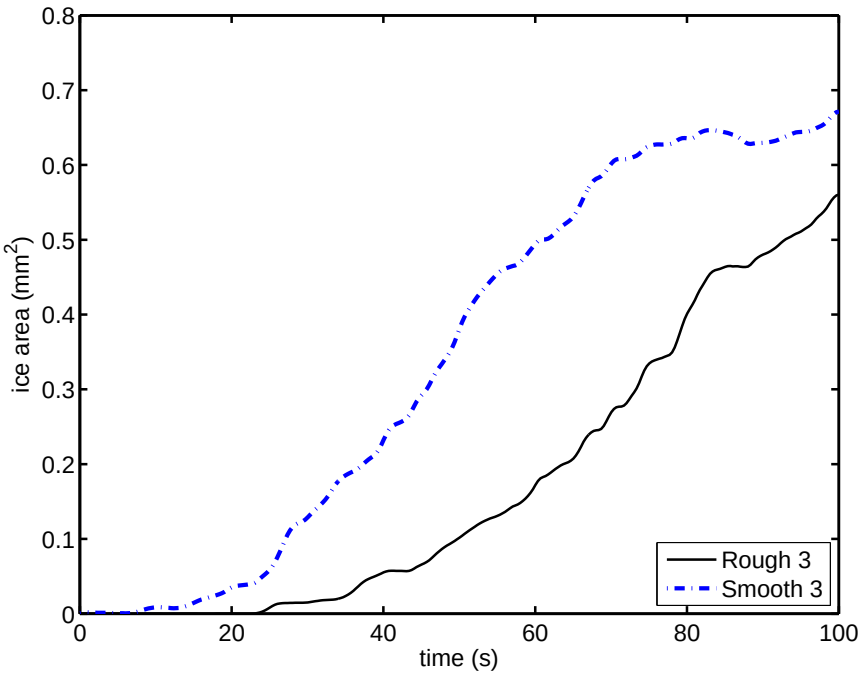

Figure 7.10: Ice accretion area within region 3 on the flat plate specimen at test temperature −9 °C. (Test: FM9T4HP)

(a) covered (b) Frame 1 (c) Frame 300

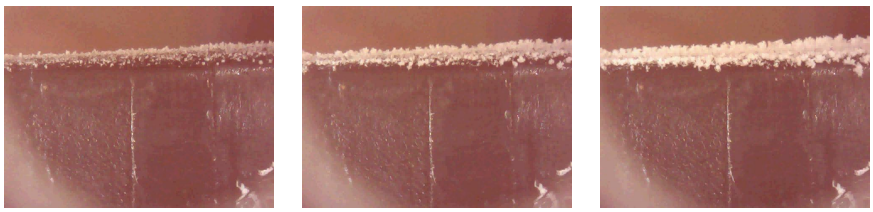

(d) Frame 600 (e) Frame 900 (f) Frame 1200

(g) Frame 1500 (h) Frame 1800 (i) Frame 2100

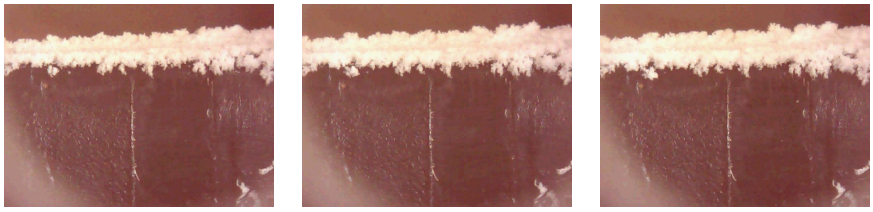

(j) Frame 2400 (k) Frame 2700 (l) Frame 3000

Figure 7.11: Frames for ice accretion on the plate at $-9\,^{\circ}\mathrm{C}$ with $30\,\mathrm{f/s}$ recording rate from the beginning of the test. (Test: FM9T4HP)

7.5.2 Surface Temperature −5 °C

For these tests the specimen surface temperature was set to −5 °C, the water tank pressure to 3.5 bar, and the flow speed to 6.5 m/s. In this case, the stream temperature varies rapidly through the liquid nitrogen duct and reaches a steady temperature near the flat plate specimen as can be seen in Figure 7.12 and Figure 7.13. Figures 7.14, 7.15, and 7.16 show the ice accretion on a 1 mm^2 area on the rough and smooth surfaces. Rough and smooth sides in Figure 7.14 show similar behaviour of ice growth. Repeated test results for the −5 °C case have been reported in Appendix E.

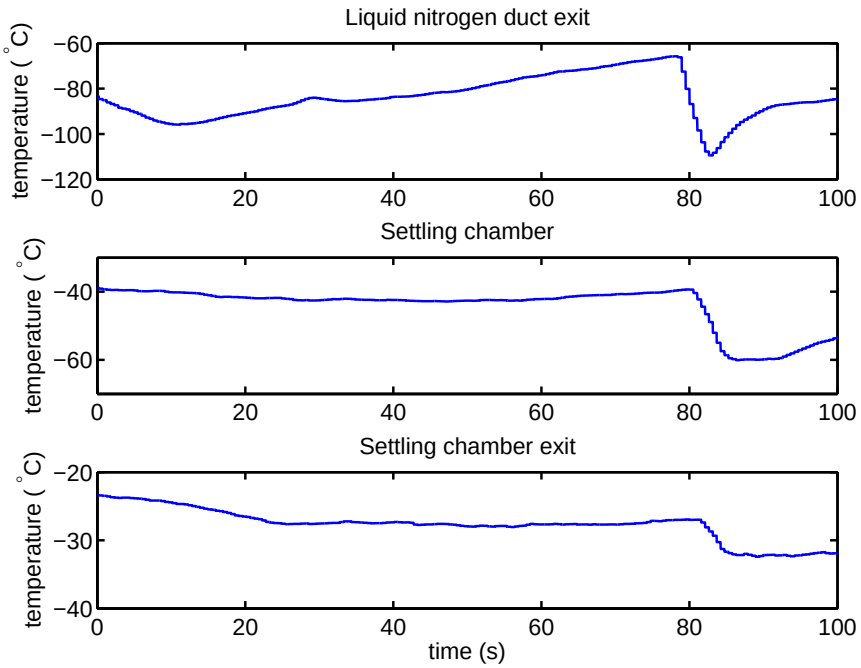

Figure 7.12: Temperatures within the facility upstream of the wind duct. Specimen temperature −5 °C.(Test: FM5T1HP)

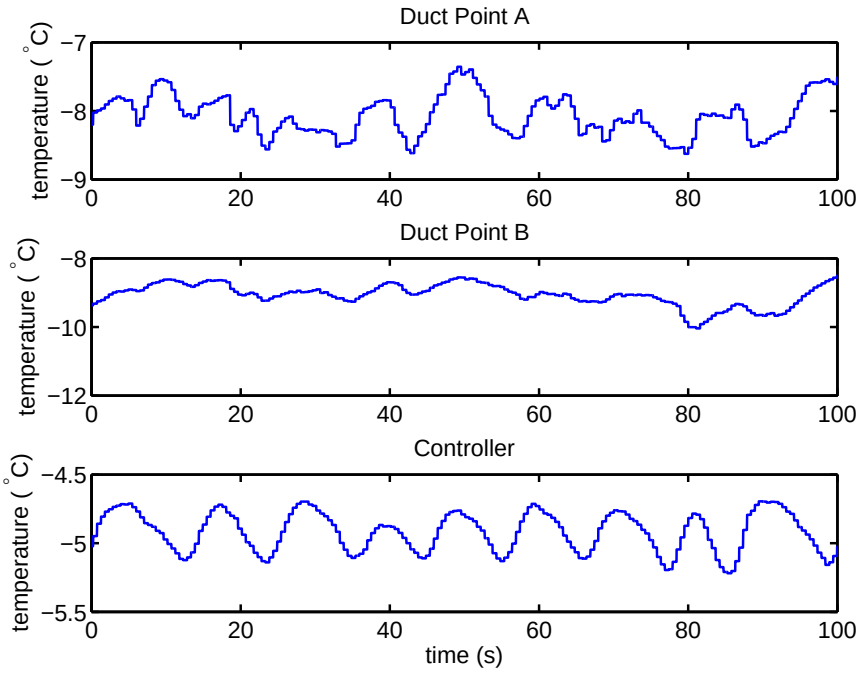

Figure 7.13: Temperatures within the wind tunnel duct for the test specimen temperature of −5 °C. (Test: FM5T1HP)

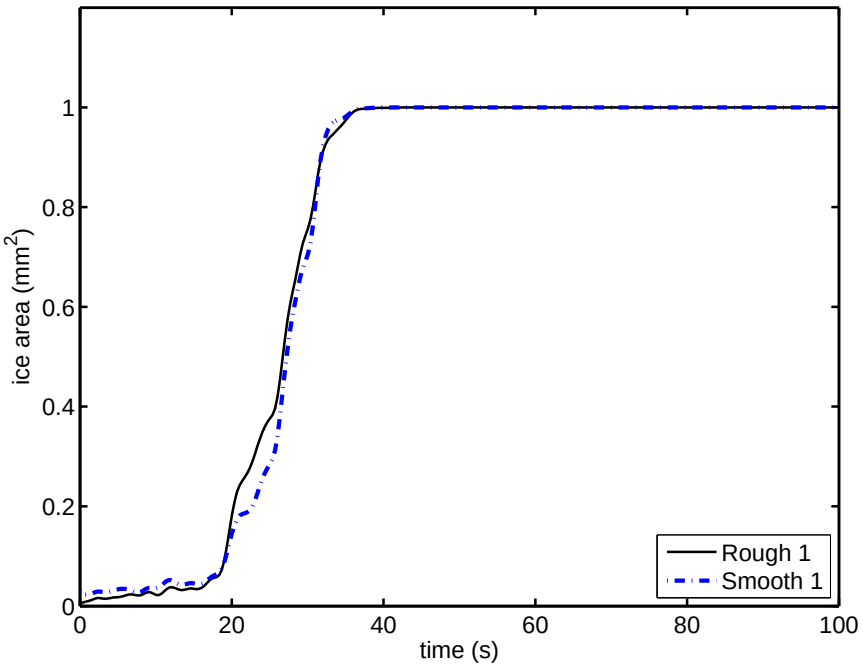

Figure 7.14: Ice accretion area within region 1 on the flat plate specimen at test temperature −5 °C. (Test: FM5T1HP)

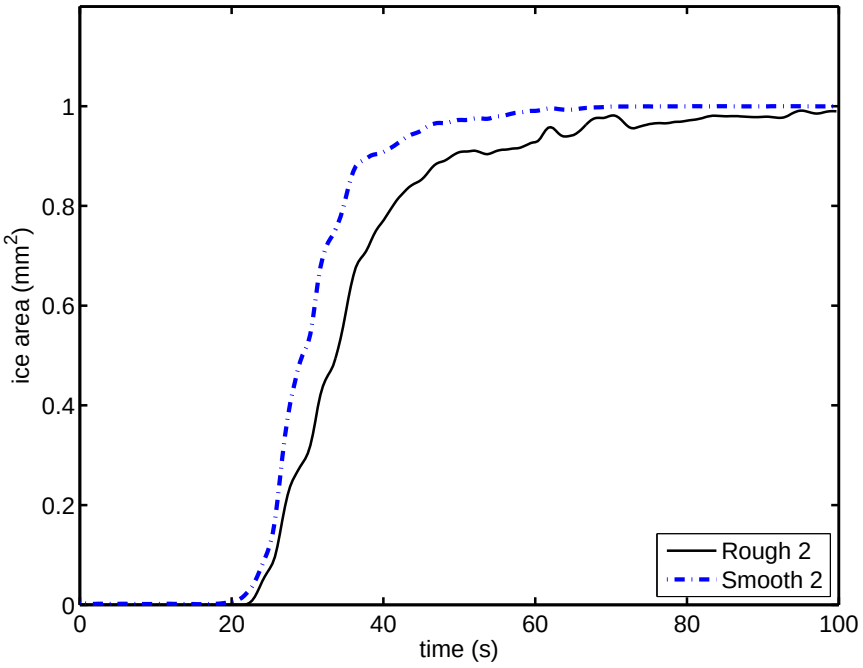

Figure 7.15: Ice accretion area within region 2 on the flat plate specimen at test temperature −5 °C. (Test: FM5T1HP)

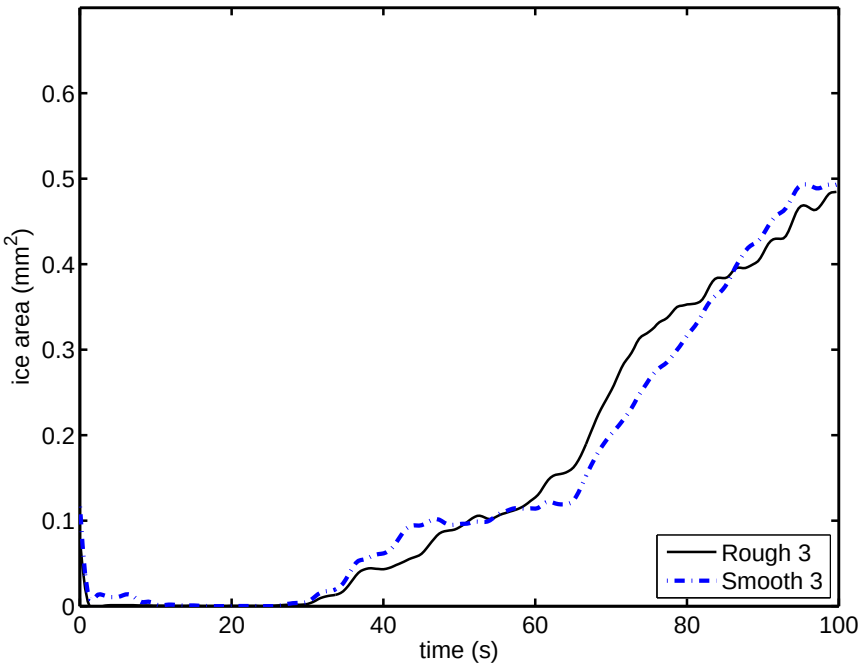

Figure 7.16: Ice accretion area within region 3 on the flat plate specimen at test temperature −5 °C. (Test: FM5T1HP)

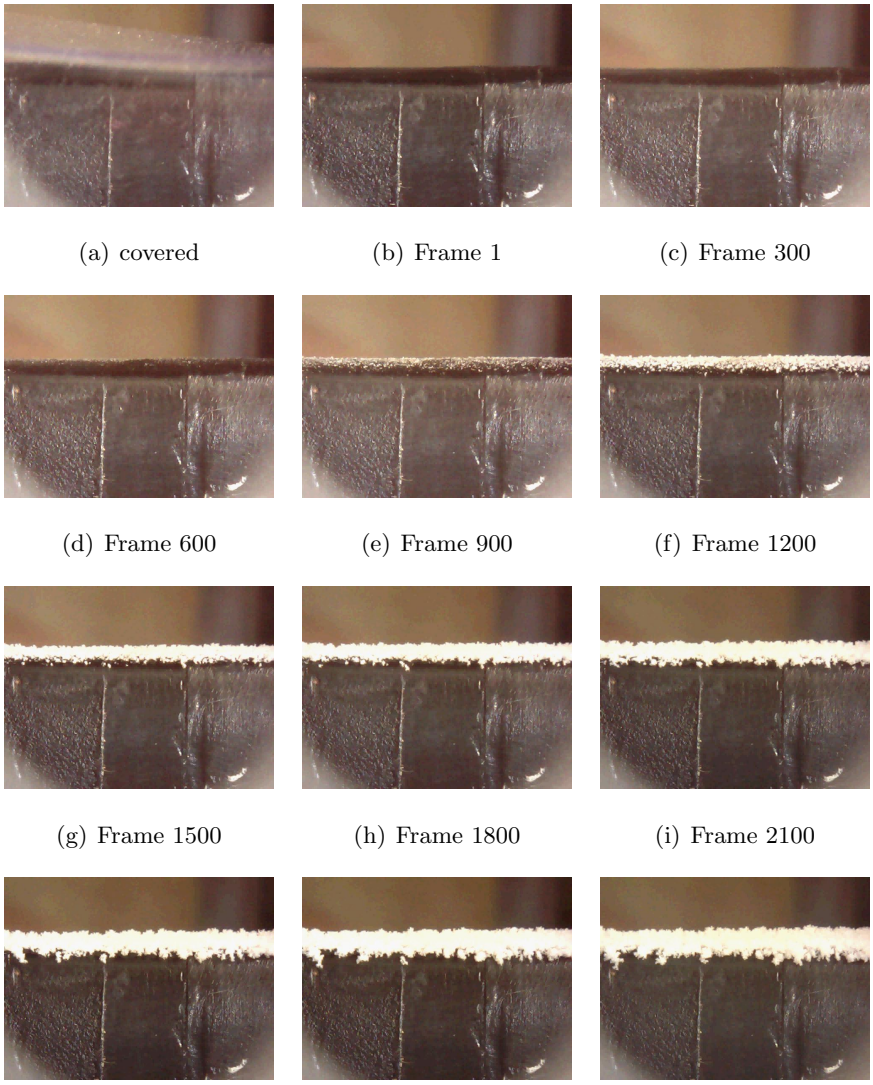

(a) covered (b) Frame 1 (c) Frame 300

(d) Frame 600 (e) Frame 900 (f) Frame 1200

(g) Frame 1500 (h) Frame 1800 (i) Frame 2100

(j) Frame 2400 (k) Frame 2700 (l) Frame 3000

Figure 7.17: Frames for ice accretion on the plate at −5 °C with 30 f/s recording rate from the beginning of the test. (Test: FM5T1HP)

7.6 Warm Surface Temperatures

In general, the reported data for 0 °C and 5 °C specimen surface temperatures shows that ice accretion is insignificant during the 200 s test period. In the following sections some of the results for 0 °C and 5 °C will be discussed.

7.6.1 Surface Temperature 0 °C

The ice accretion tests at 0 °C specimen surface temperature were performed with nominally the same flow conditions as the −9 °C and −5 °C cases. Figure 7.18 and Figure 7.19 show the measured flow temperatures across the entire apparatus. The surface temperature controller reading demonstrates a good performance and fluctuates only within about ±0.3 °C.

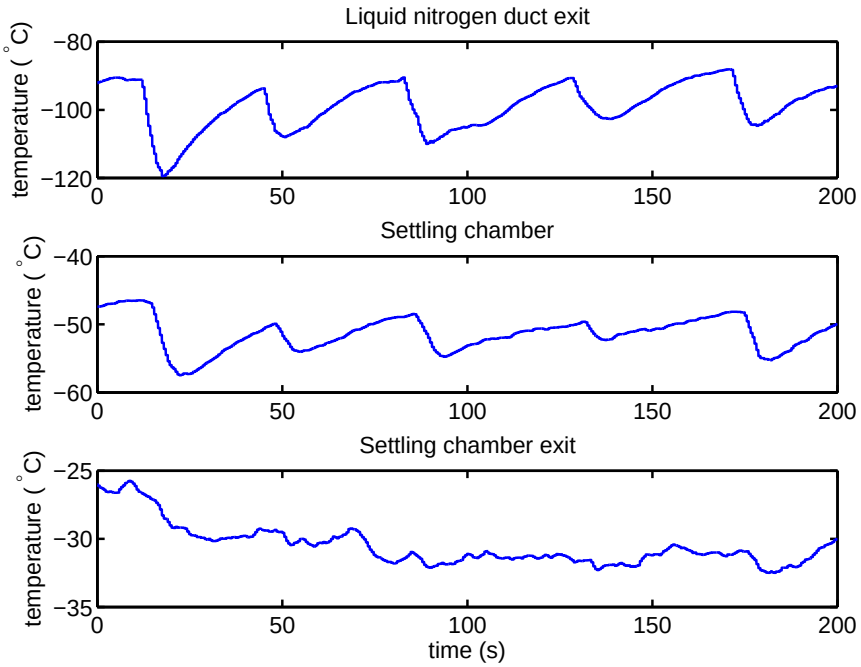

Figure 7.18: Temperatures within the facility upstream of the wind duct. Specimen temperature 0 °C. (Test: F0T1HP)

In this test the time axis is 200 s, which is twice the time of the −9 °C and −5 °C. The ice development on the rough and smooth sections at 0 °C are insignificant in comparison with the colder surface temperature, if the same areas are reviewed.

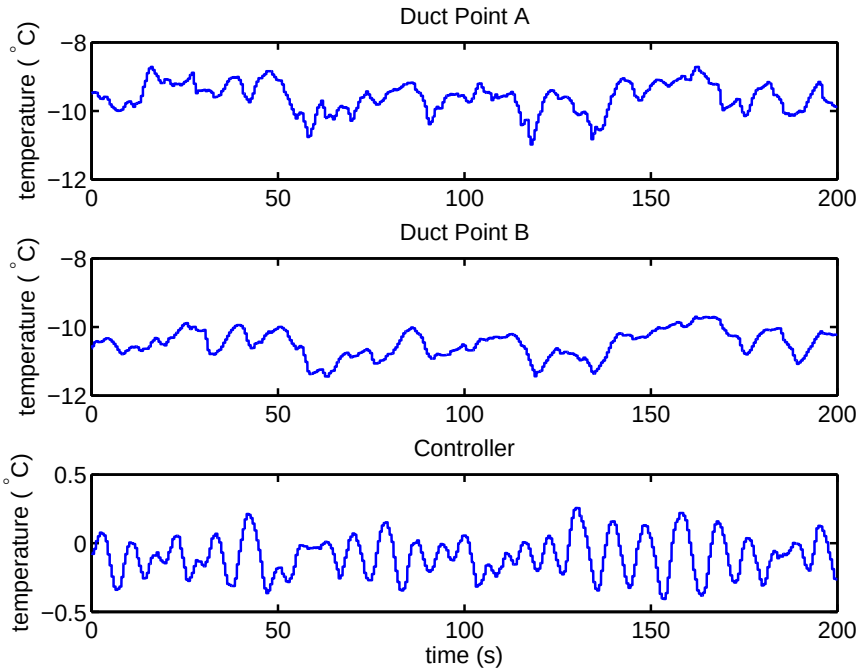

Figure 7.19: Temperatures within the wind tunnel duct for the test specimen temperature of 0 °C. (Test: F0T1HP)

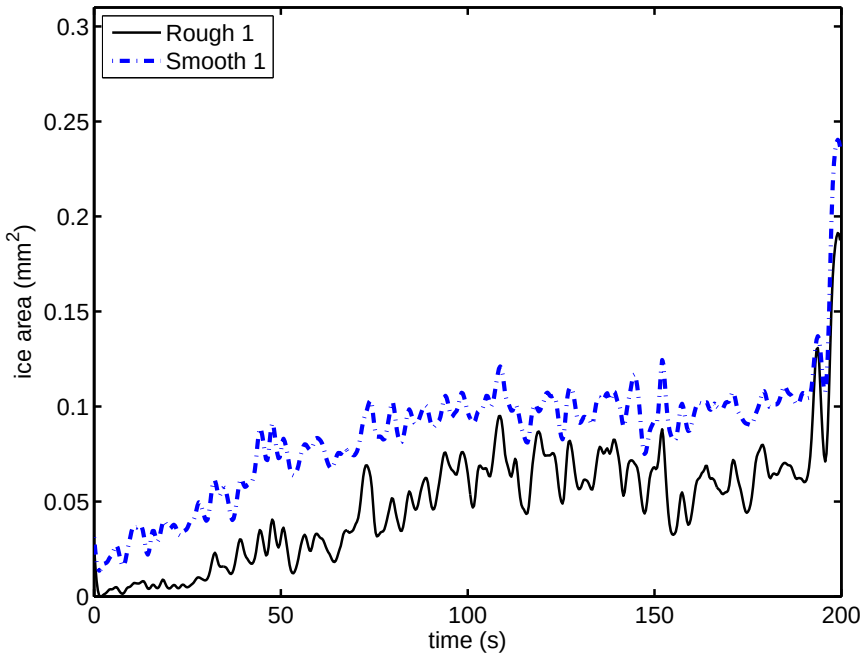

Figure 7.20: Ice accretion area within region 1 on the flat plate specimen at test temperature 0 °C. (Test: F0T1HP)

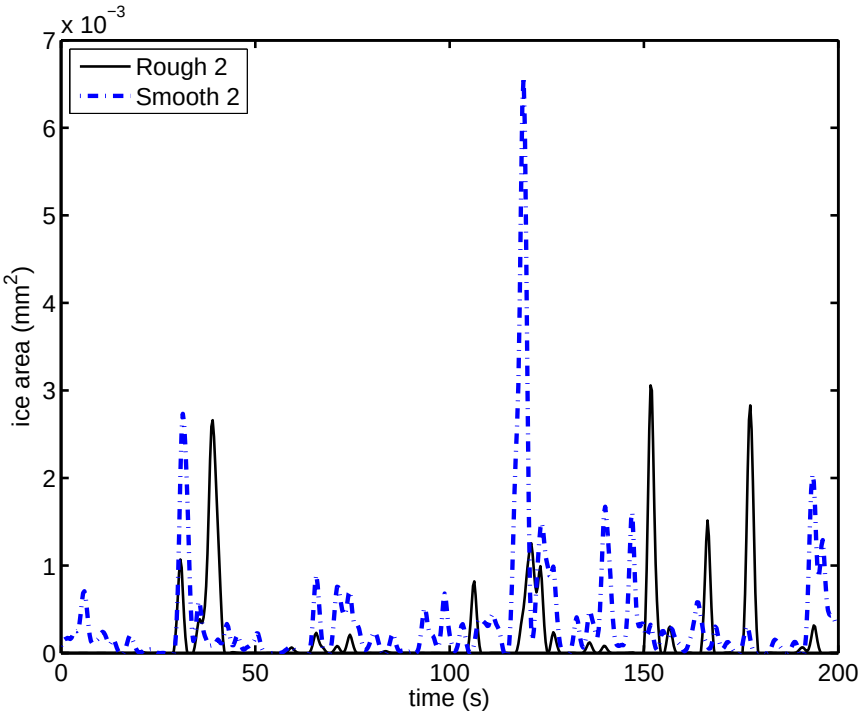

Figure 7.21: Ice accretion area within region 2 on the flat plate specimen at test temperature 0 °C. (Test: F0T1HP)

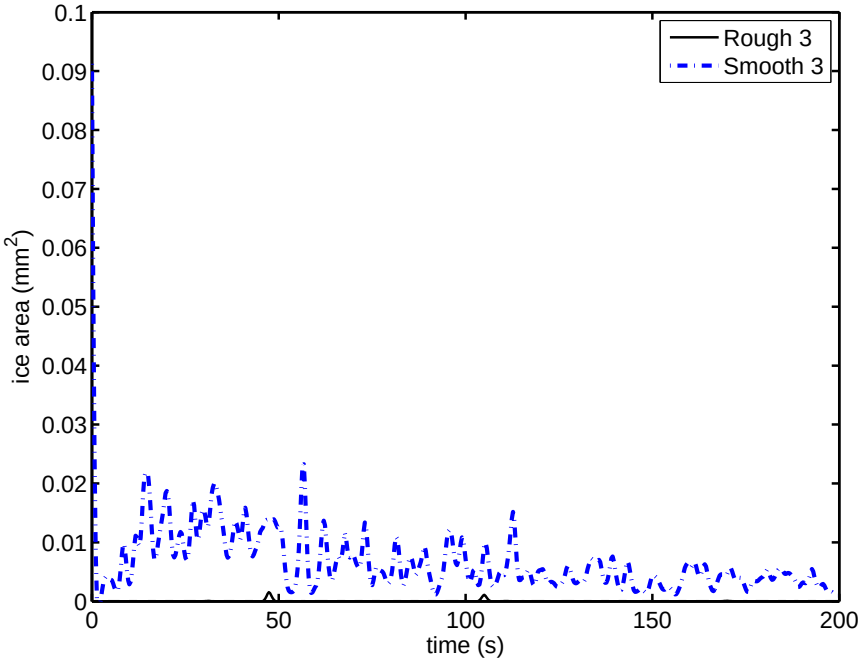

Figure 7.22: Ice accretion area within region 3 on the flat plate specimen at test temperature 0 °C. (Test: F0T1HP)

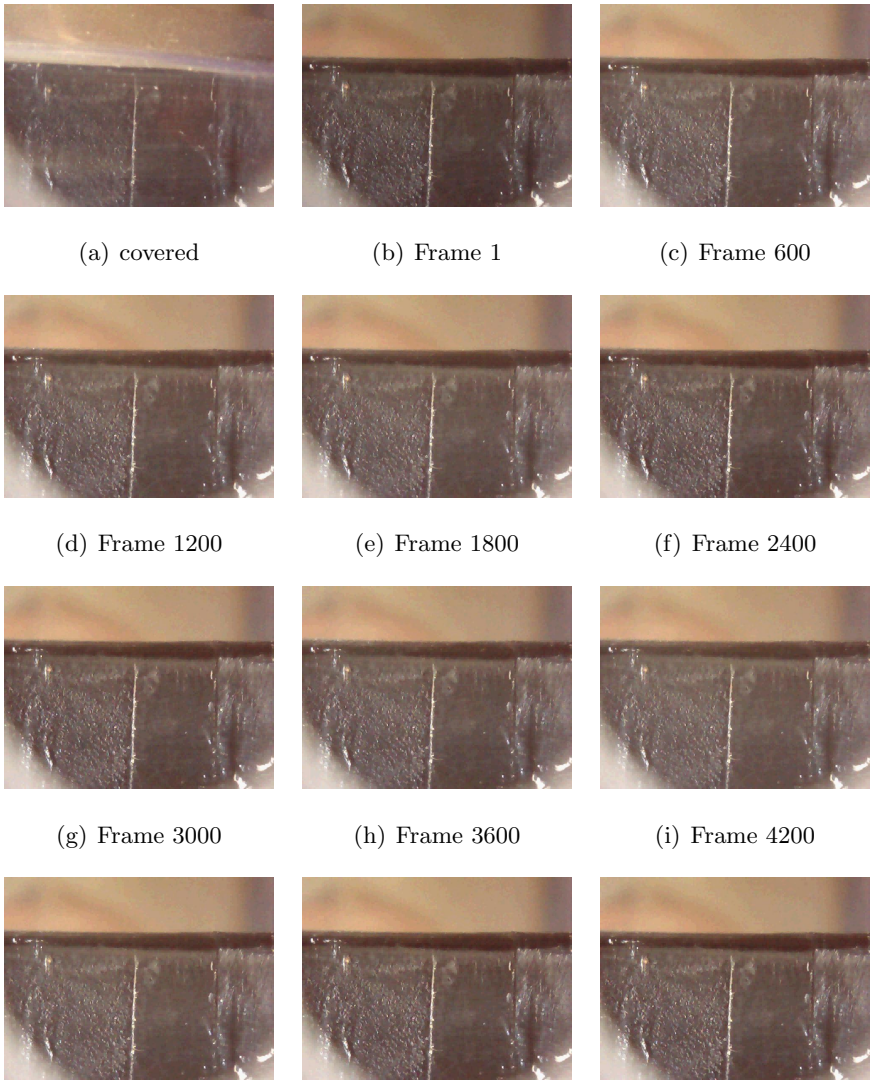

(a) covered (b) Frame 1 (c) Frame 600

(d) Frame 1200 (e) Frame 1800 (f) Frame 2400

(g) Frame 3000 (h) Frame 3600 (i) Frame 4200

(j) Frame 4800 (k) Frame 5400 (l) Frame 6000

Figure 7.23: Frames for ice accretion on the plate at 0 °C with 30 f/s recording rate from the beginning of the test. (Test: F0T1HP)

7.6.2 Surface Temperature 5 °C

Ice accretion testing was also performed with the specimen surface temperature set to 5 °C. The temperature distributions through the apparatus are shown in Figures 7.24 and 7.25. The ice growth can be seen in Figures 7.26, 7.27, and 7.28 for the rough and smooth sides. The usual areas relative to the stagnation line for the rough and smooth sides have been considered.

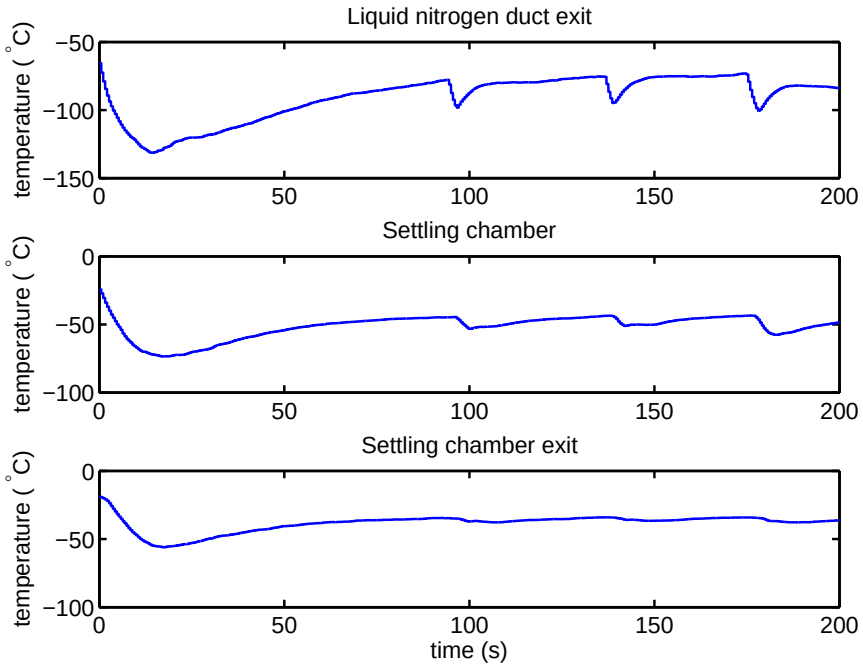

Figure 7.24: Temperatures within the facility upstream of the wind duct. Specimen temperature 5 °C. (Test: FP5T2HP)

Both rough and smooth sides shown in Figures 7.26, 7.27, and 7.28 demonstrate very little amounts of ice accretion even after increasing the test period to 200 s. These results are similar to the results of the 0 °C case and it can be concluded that there is no accretion above 0 °C, when the ice water content is 0.42 g/m^3 or less.

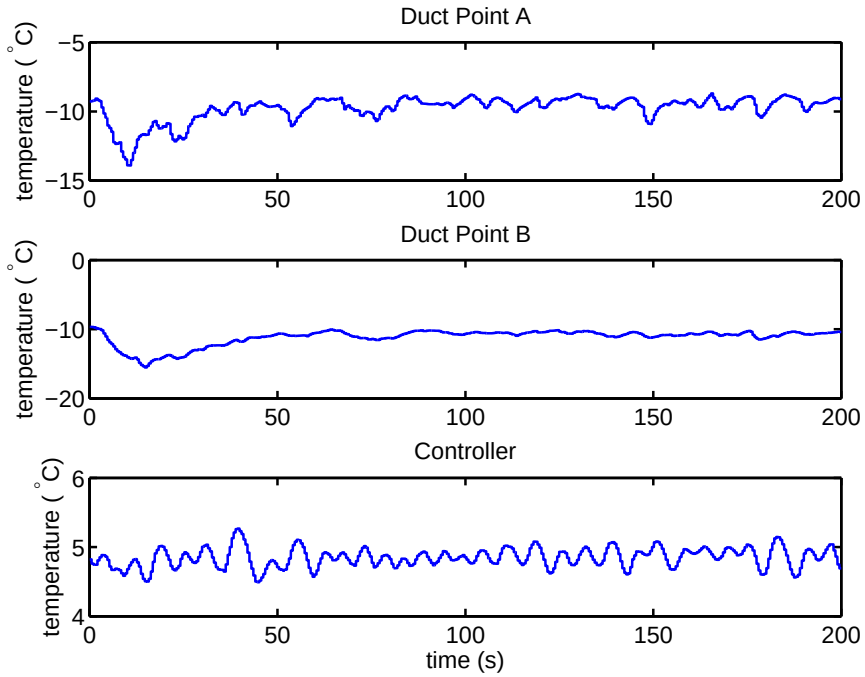

Figure 7.25: Temperatures within the wind tunnel duct for the test specimen temperature of 5 °C. (Test: FP5T2HP)

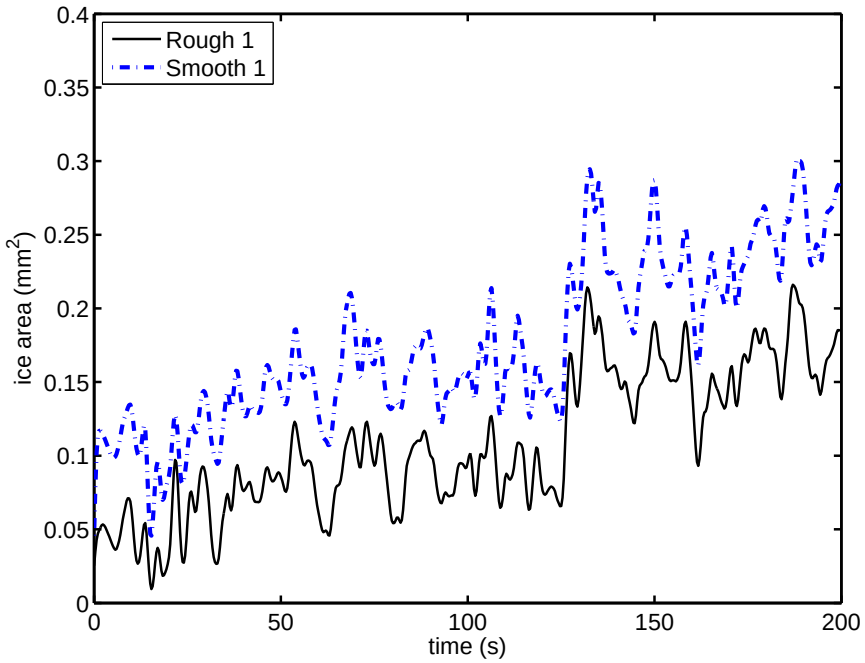

Figure 7.26: Ice accretion area within region 1 on the flat plate specimen at test temperature 5 °C. (Test: FP5T2HP)

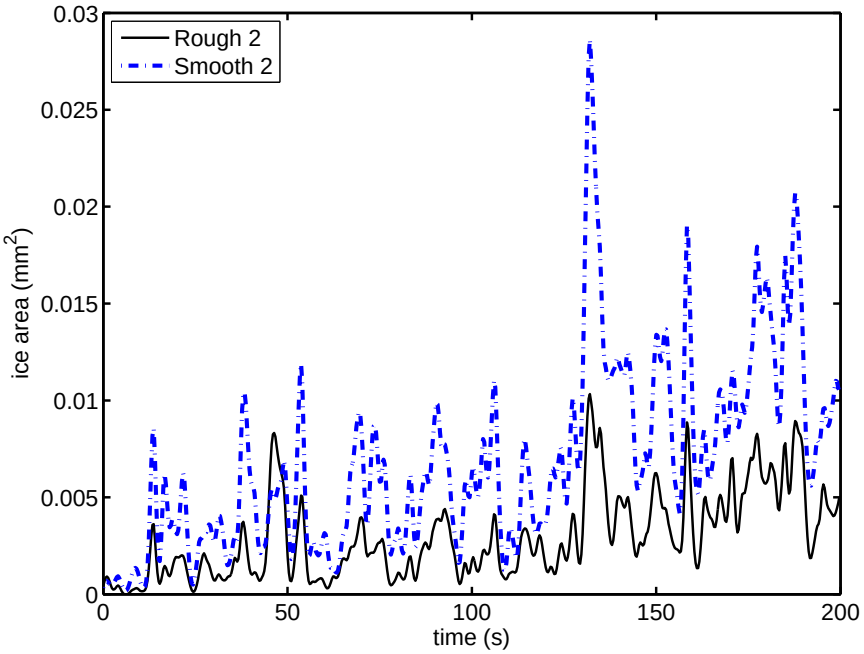

Figure 7.27: Ice accretion area within region 2 on the flat plate specimen at test temperature 5 °C. (Test: FP5T2HP)

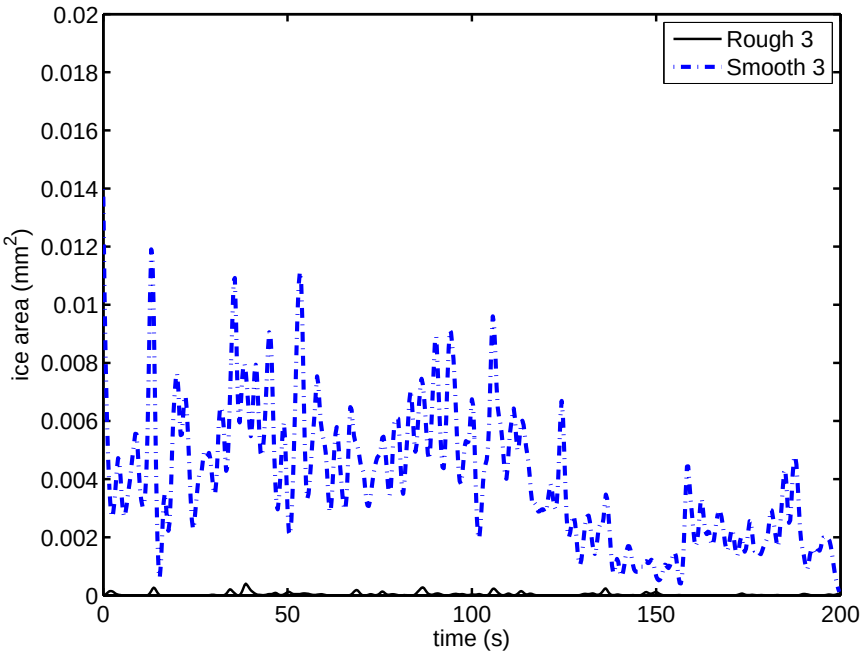

Figure 7.28: Ice accretion area within region 3 on the flat plate specimen at test temperature 5 °C. (Test: FP5T2HP)

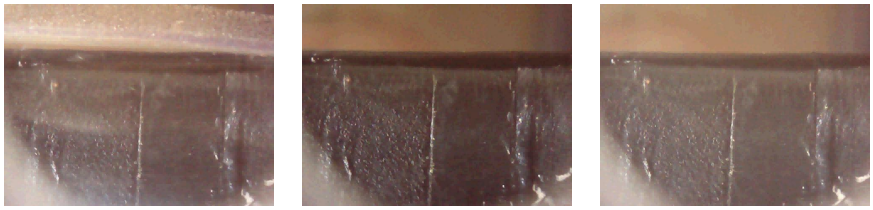

(a) covered (b) Frame 1 (c) Frame 600

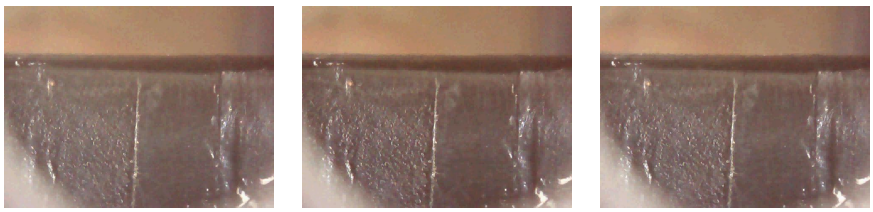

(d) Frame 1200 (e) Frame 1800 (f) Frame 2400

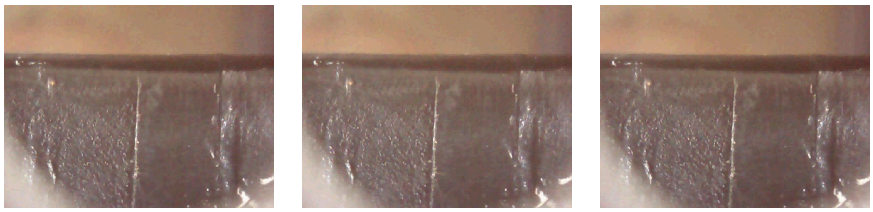

(g) Frame 3000 (h) Frame 3600 (i) Frame 4200

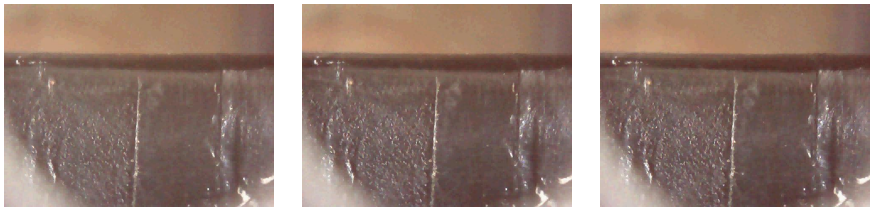

(j) Frame 4800 (k) Frame 5400 (l) Frame 6000

Figure 7.29: Frames for ice accretion on the plate at 5 °C with 30 f/s recording rate from the beginning of the test. (Test: FP5T2HP)

7.7 Post-Test Ice Removal

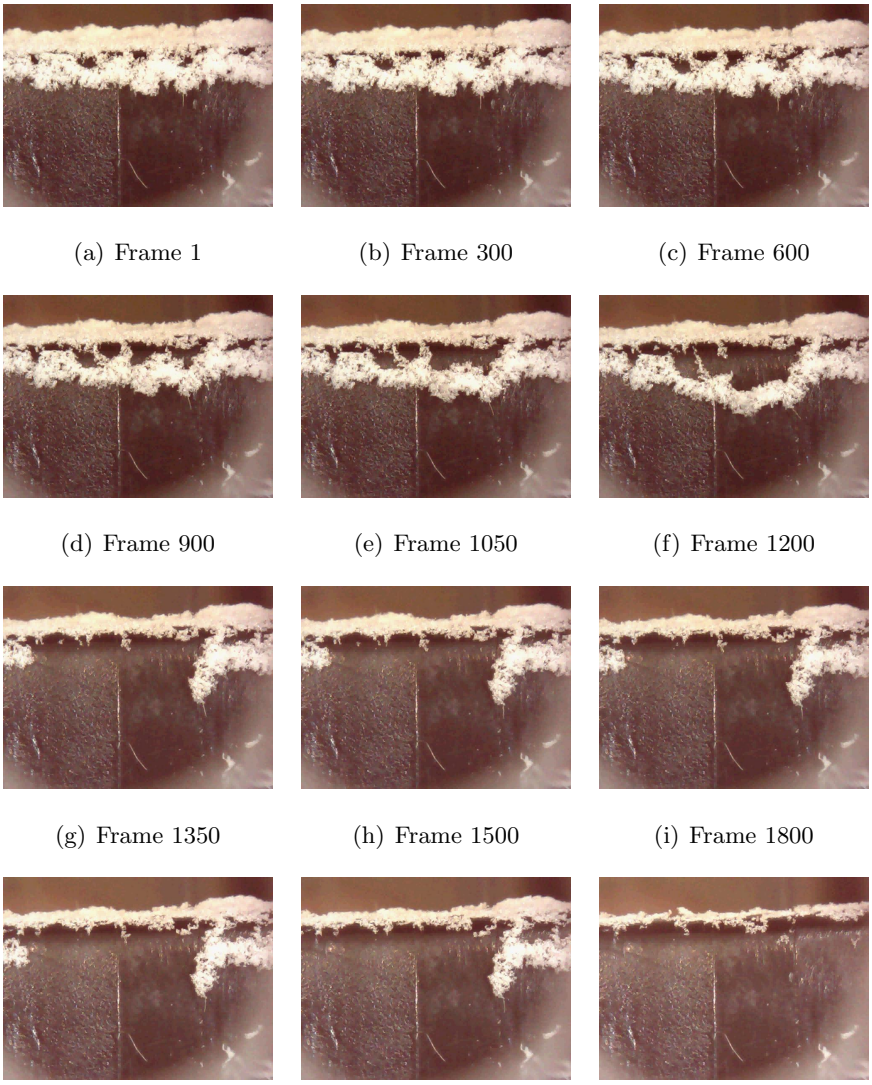

(a) Frame 1 (b) Frame 300 (c) Frame 600

(d) Frame 900 (e) Frame 1050 (f) Frame 1200

(g) Frame 1350 (h) Frame 1500 (i) Frame 1800

(j) Frame 1950 (k) Frame 2100 (l) Frame 2800

Figure 7.30: Frames for the aerodynamic effect on the accumulated ice on the plate at −9 °C with 30 f/s recording rate from the end of the test. (Test: FM9T1HP)

The accumulated ice on the cold surface can be swept away due to the effect of the aerodynamic force and the weak bond of the ice with the surface for both smooth and rough regions. After testing the ice accretion on a surface temperature of −9 °C and stoping the water injection, video recording was continued to record the ice removal process. Figure 7.30(a) shows the first frame after the test. During the sequence of photos in Figure 7.30(b) to Figure 7.30(l), the movement of a large portion of the ice

can be clearly seen moving away from the stagnation region.

7.8 Test Variability

For each test on the flat plate, the variability has been defined by considering the temporal variations of the data during the test time and identifying the mean and standard deviation of the data. Results are presented in Table 7.1. The 2σ values for the temperatures at location B in the wind tunnel duct close to the test specimen vary from 0.6 to 2.3 °C. The specimen surface temperature in the whole list of tests shows small standard deviation values, due to the use of the temperature controller, which shows good performance and keeps the surface at a largely constant temperature. The maximum value of 2σ for the surface temperature was ± 0.36 °C in FP5T1HP test at a mean surface temperature of 5 °C while the minimum was ± 0.2 °C which was recorded in FM9T2HP and in FP5T3HP at temperature of -9 °C and 5 °C respectively.

7.9 Accretion Development

Ice accretion on the flat plate surface aligned with the flow was not achieved in the present experiments. Therefore the analysis of the experiments focuses on the stagnation region area − the leading edge of the plate.

The development of the ice accretion in the different stagnation region areas and in the different tests at nominally identical flow and surface temperature conditions was assessed by identifying the time at which ice covered 10 % and 80 % of the maximum available area (1 mm^2) in each case. Results from this analysis are presented in Figure 7.31 and Figure 7.32. The vertical axis in these figures reports the fraction of the maximum possible number of occurrences which was 24 in the case of the tests results of -9 °C (6 areas× 4 experiments), 18 in the case of the tests results at -5 °C (6 areas × 3 experiments), and 24 in the case of the tests results at 0 °C (6 areas× 4 experiments). Results at 5 °C are not available since ice accretion was not registered according to the 10 % coverage criterion.

Table 7.1: Operating conditions for the flat plate specimen tests, uncertainties quoted correspond to $\pm 2\sigma$ values.

Test	T_{LN_2E} (°C)	T_{SC} (°C)	T_{SCE} (°C)	T_A (°C)	T_B (°C)	IWC (g/m^3)	T_S (°C)	Figures
FM9T1HP	-87.5 ± 12.8	-49.8 ± 8.3	-32.2 ± 2.9	-11.6 ± 1.0	-13.3 ± 1.0	0.42 ± 0.26	-8.96 ± 0.23	E.1- E.5
FM9T2HP	-71.5 ± 15.0	-41.8 ± 4.3	-30.8 ± 1.8	-12.6 ± 1.0	-13.7 ± 0.6	0.42 ± 0.26	-8.99 ± 0.20	E.6 - E.10
FM9T3HP	-87.4 ± 10.5	-49.3 ± 5.3	-32.5 ± 2.2	-10.9 ± 0.8	-12.6 ± 1.0	0.42 ± 0.26	-8.94 ± 0.23	E.11 - E.15
FM9T4HP	-90.9 ± 17.9	-51.9 ± 9.1	-39.4 ± 4.4	-12.8 ± 2.4	-14.4 ± 1.2	0.42 ± 0.26	-8.96 ± 0.21	E.16 - E.20
FM5T1HP	-84.0 ± 18.8	-44.2 ± 12.5	-27.7 ± 4.5	-8.0 ± 0.5	-9.0 ± 0.6	0.42 ± 0.26	-4.90 ± 0.29	E.21 - E.25
FM5T2HP	-91.1 ± 10.2	-43.8 ± 2.0	-24.2 ± 2.9	-9.1 ± 0.8	-10.3 ± 1.1	0.42 ± 0.26	-4.94 ± 0.33	E.26 - E.30
FM5T3HP	-97.2 ± 15.7	-49.3 ± 8.8	-25.9 ± 2.8	-9.2 ± 1.2	-10.8 ± 1.6	0.42 ± 0.26	-4.95 ± 0.26	E.31 - E.35
F0T1HP	-98.8 ± 13.6	-51.4 ± 4.9	-30.5 ± 3.0	-9.6 ± 0.9	-10.5 ± 0.8	0.42 ± 0.26	-0.09 ± 0.28	E.36 - E.40
F0T2HP	-96.3 ± 16.7	-54.1 ± 6.2	-31.9 ± 7.4	-10.1 ± 1.6	-11.6 ± 0.9	0.42 ± 0.26	-0.10 ± 0.27	E.41 - E.45
F0T3HP	-93.6 ± 14.1	-51.2 ± 5.6	-32.2 ± 2.2	-11.0 ± 0.8	-12.2 ± 0.8	0.42 ± 0.26	-0.13 ± 0.23	E.46 - E.50
F0T4HP	-90.4 ± 19.5	-50.5 ± 9.0	-32.5 ± 2.4	-10.3 ± 0.9	-11.4 ± 1.0	0.42 ± 0.26	-0.13 ± 0.30	E.52 - E.55
FP5T1HP	-85.6 ± 15.0	-51.6 ± 8.9	-38.2 ± 3.2	-11.4 ± 1.5	-13.3 ± 1.3	0.42 ± 0.26	4.87 ± 0.36	E.56 - E.60
FP5T2HP	-90.6 ± 32.2	-51.6 ± 17.0	-38.5 ± 12.5	-9.7 ± 1.8	-11.2 ± 2.3	0.42 ± 0.26	4.85 ± 0.29	E.61 - E.65
FP5T3HP	-89.0 ± 14.5	-52.2 ± 6.1	-39.6 ± 3.2	-11.8 ± 1.1	-13.4 ± 0.9	0.42 ± 0.26	4.82 ± 0.20	E.66 - E.70

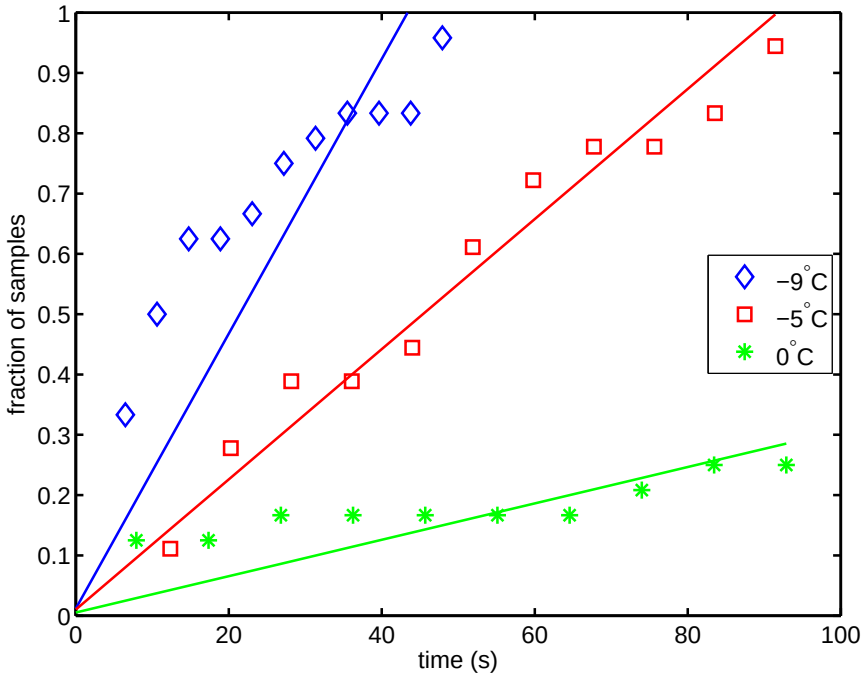

Figure 7.31: Number of samples with at least 10 % ice coverage in the stagnation region of the flat plate specimen as a function of time. Lines of the best fit (forced to pass through the origin) are also presented for three surface temperatures: −9 °C, −5 °C, and 0 °C.

For the −9 °C case, 10 % ice coverage of all samples was achieved in less than 50 s, while the 80 % coverage was achieved for about two thirds of the total number of tests in the first 50 s. The number of samples achieving 80 % coverage continued to increase in a regular manner until the end of the test period.

The 10 % ice coverage at −5 °C occurs slower than in the −9 °C case and within the first 50 s only about half of the total number of samples were covered with this fraction of ice. For the 80 % ice coverage case, the number of samples achieving this level continued to grow throughout the whole test period of 100 s. Although 10 % coverage can be achieved at 0 °C during the test period, 80 % coverage was not achieved in the 0 °C surface temperature case. Neither 10 % nor 80 % coverage was achieved for a surface temperature of 5 °C.

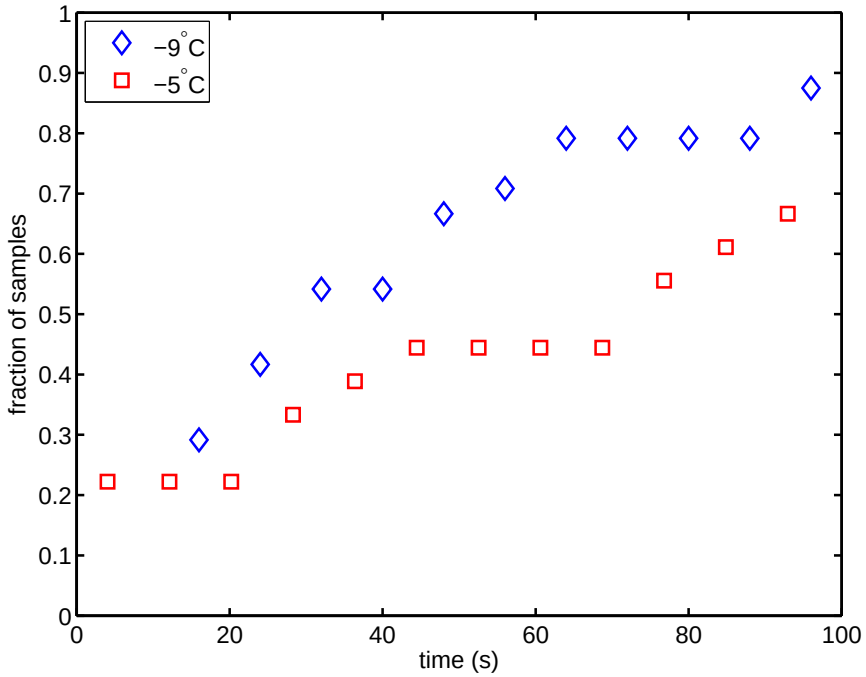

Figure 7.32: Number of samples with at least 80 % ice coverage in the stagnation region of the flat plate specimen as a function of time.

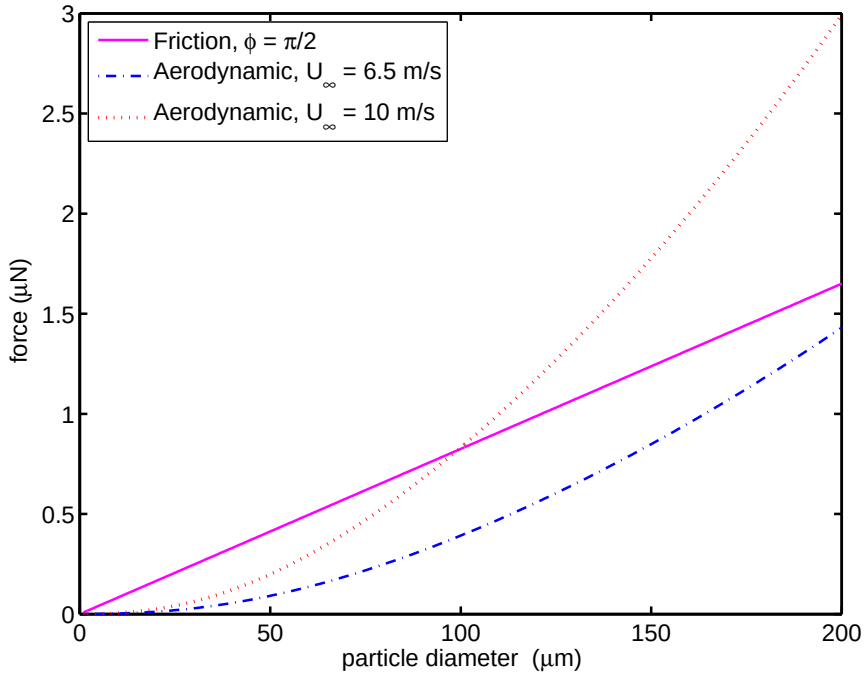

Figure 7.33: Stagnation region aerodynamic drag force and the friction force variation with particle diameter for $\mu = 0.07$, $x = 1\,\text{mm}$, $u_p = 0$, volume fraction of 0.05, $\phi = \pi/2$, cylinder diameter of 3 mm, and different free stream speeds.

7.10 Flat Plate Stagnation Region

The experimental results show that there was no accumulation at any conditions beyond the leading edge of the flat plate. However, accretion was registered near the stagnation point in a manner similar to that observed in Chapter 6 for a 10 mm diameter cylinder. In the work of this chapter, however, the leading edge had a diameter of 3 mm. Results from the mathematical model for a leading edge diameter of 3 mm are presented in Figure 7.33. At a speed of 6.5 m/s, which is the experiment test speed, and for the particles smaller than 200 μm, the aerodynamic force is less than the friction force. Therefore, ice accretion is expected to initiate for the distances of 1 mm or less from the leading edge of the flat plate.

7.11 Discussion

Although, the mathematical model for the flat plate boundary layer shows it is possible for the ice particles to remain stationary on the surface at locations downstream from the leading edge, the experimental results only demonstrate accretion initiation in the stagnation region of the flat plate leading edge. The expected reason for the lack of ice accretion initiation on the flat plate surface away from the leading edge is the deflection of the ice particles away from the flat plate boundary layer by the leading edge and associated flow field. The vertical momentum imparted to the particles by the leading edge and associated flow field means virtually no particles will enter the flat plate boundary layer downstream of the leading edge. To test this hypothesis, it is recommended for future studies to have a sharp leading edge to mitigate the deflection and to study the probability of particles in the flow reaching the surface beyond the edge.

Figure 7.34 was generated by combining the 10 % ice coverage results for the cylinder and the flat plate specimens based on the lines of best fit for Figure 6.26 and Figure 7.31. The accretion on the cylindrical model (10 mm diameter) shows a slower rate of coverage than for the leading edge of the flat plate (3 mm diameter) for the 10 % ice coverage in the -9 and -5 °C cases. In the 0 °C case, the ice coverage rate of the plate

is slower than the cylinder.

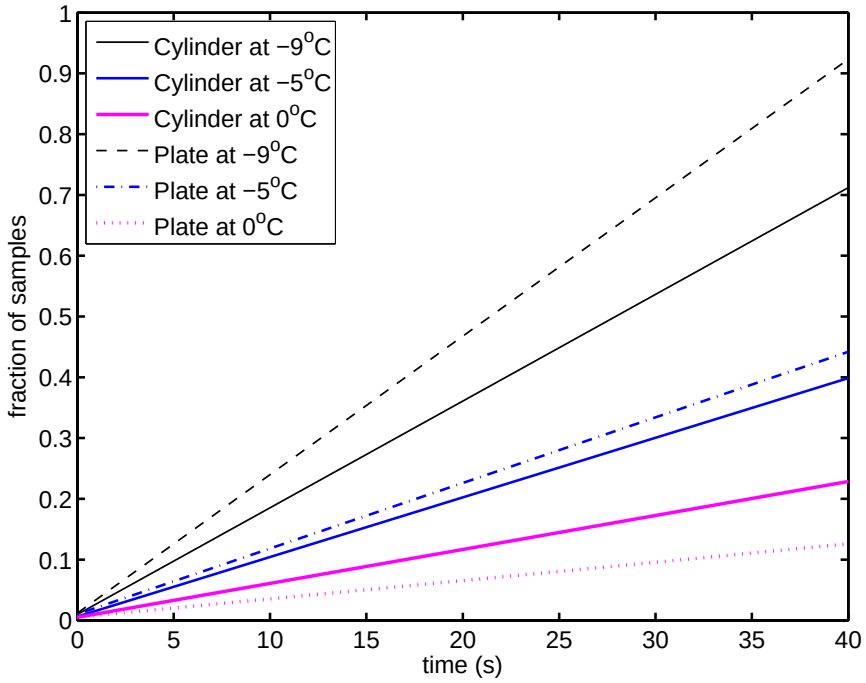

Figure 7.34: Lines of best fit for the number of samples with at least 10 % ice coverage of the cylinder (10 mm diameter) and the leading edge of the flat plate (3 mm diameter) at different surface temperatures.

For the 80 % ice coverage, the flat plate specimen leading edge results at −9 and −5 °C show the ice coverage started before 20 s and continued during the whole 100 s test period, Figure 7.32. However, the cylindrical specimen did not shown any coverage for both −9 and −5 °C before the first 50 s has passed. The mathematical model for the stagnation region ice accretion initiation indicates that at a given distance from the stagnation point, the aerodynamic drag on the ice particles will increases with decreasing diameter. Hence, the model suggests accretion initiation should be less likely for the smaller diameter leading edge. The flat plate leading edge (3 mm diameter) actually shows faster ice coverage than the cylinder model (10 mm diameter) and this may arise because the flat plate leading edge was not subjected to temperature control and its temperature may have decreased significantly below the controller value, and the friction forces generally increase with the surface temperature decreases causing a high accumulation rate. The flat plate temperature measurement was taken in the middle of the plate as shown in Figure 4.10 (b) and the leading edge temperature will be lower by 1 °C to 2.5 °C according to the results in Figure 4.11.

7.12 Conclusion

The experimental results reveal that the solid ice accretion occurs in the stagnation region of the flat plate leading edge and there is no accretion recorded on the surface of the plate downstream. This is a similar case to that of the cylindrical specimen. Although the mathematical model suggested that the cylinder model with a diameter of 10 mm will generate lower aerodynamic drag forces on particles than the leading edge of the flat plate with a diameter of 3 mm, the leading edge of the flat plate generally shows a faster ice coverage than the cylinder. It is suggested that this effect arises due to lower temperatures on the flat plate leading edge because the plate temperature was not controlled in this region.

Chapter 8

Conclusion

8.1 Motivation

Aircraft icing has been studied for many years and significant contributions continue to be made in areas of both experiments and simulation. The icing problem was studied with the aim of understanding the properties that affect the glaze and rime ice accretion process. Important properties include: the free stream velocity, angle of attack, environment temperature, surface roughness, shape and temperature of the surface, liquid water content, and the droplet size distribution within the cloud. Many simulation codes have been developed to predict the effective shape of the aircraft wings due to the accretion and the power penalty associated with the geometry changes. Such codes are typically validated for low Mach number conditions and do not entirely explain the fundamental physics of the accretion process. Experimentally, a few expensive, large scale icing wind tunnels have been used in conjunction with sophisticated measurement equipment to validate the ice simulation codes.

Although most of the icing research has focused on the accretion on aircraft structures, the type of aircraft icing which has motivated the present study has been identified only relatively recently−ice accumulation in aero-engine compressors. This icing problem occurs due to the presence of solid phase ice particles in the deep convection clouds. The hypothesis of the aero-engine compressor ice accretion considers that the solid

ice particles ingested by the engine will enter the first stages of the compressor and due to the elevated air and surface temperatures, the ice particles melt, forming a layer of water on the compressor surfaces. Subsequent impingement of ice particles on compressor surfaces reduces the surface temperature until it reaches the freezing temperature which then initiates the period of rapid ice accumulation. Although water in the solid phase enters the engine, the generation of the liquid phase through heat transfer within the compressor is considered to play a critical role in the accretion process.

The aero-engine ice accretion problem is not fully understood and a limited number of experimental and simulation studies have been performed in this field. The experimental studies mostly focus on the mixed ice-liquid condition and ice accretion events are reported in some of the tests. These wind-tunnel-simulated accretion events are also challenging to interpret because of the various complexities, including the fact that ice is injected into a wind tunnel air stream which is at a higher temperature than the freezing temperature, which causes melting of the ice particles and increases the uncertainty in the liquid water content of the mixture. Furthermore, in these previous experiments, ice shavers have been used to generate the ice particles. Ice shavers produce a large range of particle sizes and random shapes. In the field of computational simulation, studies are still in progress in an effort to predict the location of the ice accretion within the compressor, and understand the conditions which are conducive to rapid accretion, and such simulations are yet to be validated.

The physical process leading to the initiation and initial development of ice accretion in aero-engines are not well understood, so contributions in this area are needed.

8.2 Approach

In this study, a mathematical model was introduced and an experimental apparatus was developed to study the initiation of solid ice accretion with solid ice particle sizes and surface temperatures relevant to the case of aircraft engine icing.

The mathematical model in this study considers the aerodynamic drag force on a

spherical ice particle within the boundary layer on the surface. The model also considers the friction force as arising due to the adhesion force between the surface and the ice particle associated with a liquid film. The balance between the friction force and the aerodynamic drag force establishes the limiting conditions for the initiation of ice accretion. In this model, thermal effects enter through the friction coefficient dependence on the temperature; heat transfer effects are not explicitly considered. Two types of boundary layers have been considered: the stagnation region boundary layer on a cylinder, and the laminar boundary layer on a flat plate.

A small wind tunnel apparatus was developed to generate solid ice particles and operate test specimens at thermal conditions relevant to engine icing event conditions, and to validate the mathematical model. This facility is an open loop tunnel system which retains the water droplets in a liquid nitrogen section for a sufficient time to ensure ice particles are produced. Although this facility cannot duplicate all the relevant aero-engine conditions encountered at flight altitude, including the high Reynolds number and the kinetic energy of the ice particles, it can simulate the thermal conditions of the air, the ice, and the surface. Principal features and characteristics of the new facility are listed below:

- The facility has relatively low operating costs.
- The flow speed in the wind tunnel duct is relatively low and was measured using a pitot tube and hot wire anemometer. Flow speeds of around 10 m/s with a spatial uniformity in the core flow region of 6 % are achieved.
- The main wind tunnel duct is a 70 mm diameter tube.
- The small test section allows easy access to visualise the initiation of ice accretion.
- An inexpensive microscope camera was used to visualise the accretion process.
- The ice water content and ice particle distribution were measured using a sampling technique. The IWC was found to be $0.42\,\mathrm{g/m^2}$ with uncertainty of $\pm 0.26\,\mathrm{g/m^2}$, and the particle size distribution was centred around $50\,\mu$m.

Two different aerodynamic models were used in this study: cylindrical and flat plate

specimens. The surface temperature was controlled and held constant within $\pm 0.3\,^{\circ}\mathrm{C}$ during any particular test, to study the effect of the surface temperature on the ice accretion process. The spatial temperature distribution for both of the specimens was found to be uniform within 14 % of the mean temperature difference between the surface and the flow air. Each specimen was divided into a rough and a smooth section and the roughness of each section was found to be $R_a = 0.5\,\mu$m and $R_z = 2.5\,\mu$m for the smooth side of the cylindrical specimen, while for the rough side $R_a = 1.0\,\mu$m and $R_z = 4.6\,\mu$m. In the flat plate case, $R_a = 3\,\mu$m and $R_z = 5.5\,\mu$m for the smooth side and for the rough side $R_a = 4.5\,\mu$m and $R_z = 14.5\,\mu$m.

The initiation of ice accretion due to solid ice particles only was considered; no mixed phase condition was investigated in the present study. Although, the liquid phase is expected to play a significant role in the aero-engine compressor ice accretion due to the elevated air and surface temperature within the compressor, the simplified problem considered in the present work provides an opportunity to potentially discover some of the important features.

The accretion process depends on the engine surface temperature and as the temperature decreases, the chance of the accumulation increases. Although the actual engine surfaces temperatures decrease as the ice particles impact the engine surfaces, this study focuses on the case constant surface temperatures as a simplified approach to study the ice crystal accretion and introduces the hardware and modelling of icing which may facilitate the discovery of some important aero-engine ice crystal icing features.

8.3 Model Outcomes and Questions Arising

The mathematical model indicates that the accumulation of ice particles can occur for certain combinations of particle sizes, temperatures, and air speeds. The drag force is exceeded by the friction force near the stagnation point of the cylinder model and sufficiently for downstream from the leading edge of the flat plate and these are the locations where icing will initiate. In the cylinder stagnation point boundary layer

case, small coefficients of friction and large contact angles for the liquid film were sufficient to show the possibility of accretion. While in the flat plate boundary layer case, even using the assumption of a high friction coefficient and a small contact angle for the liquid film, only small sized particles can remain stationary on the surface near the leading edge. In the model, uncertainty of the results arises because of unknown values of the contact angle for the liquid film, the volume of the liquid assumed to exist between the particle and the surface, and the distance between the particle and the surface.

The model suggests ice accretion dependencies that have not commonly been observed in prior experimental studies. Therefore, the experiments performed in this work have addressed the following questions. (1) Can ice accretion initiate in the stagnation region at subfreezing conditions? (2) Do elevated surface temperature reduce accretion initiation prospects? (3) Can ice accretion initiate within the presence of the flat plate boundary layer?

8.4 Experiments Performed and Knowledge Generated

The experiments were performed at four surface temperatures: $-9\,^{\circ}\mathrm{C}$, $-5\,^{\circ}\mathrm{C}$, $0\,^{\circ}\mathrm{C}$, and $5\,^{\circ}\mathrm{C}$, and the wind tunnel flow speed was set at 6.5 ± 0.2 m/s. The ice water content was fixed to be $0.42\,\mathrm{g/m^2}$ with uncertainty of $\pm 0.26\,\mathrm{g\ m^2}$ based on $\pm 2\sigma$. The particles have a size of approximately $50\,\mu$m and have a spherical shape. The surface roughness of the cylindrical specimen is $R_a = 0.5\,\mu$m and $R_z = 2.5\,\mu$m for the smooth side, while for the rough side $R_a = 1.0\,\mu$m and $R_z = 4.6\,\mu$m. In the flat plate case, $R_a = 3\,\mu$m and $R_z = 5.5\,\mu$m for the smooth side, and for the rough side $R_a = 4.5\,\mu$m and $R_z = 14.5\,\mu$m.

The results of the cylinder and flat plate model tests show that ice accretion can occur at subfreezing temperatures in the vicinity of the stagnation point on both the cylinder and the leading edge of the flat plate. The cylinder model had a diameter of 10 mm and the leading edge of the flat plate had a diameter of 3 mm. Accretion in these stagnation regions occurred more rapidly with reductions in the surface temperatures;

the ice accretion area in the −9 °C case increased more rapidly than the −5 °C case, consistent with the results from the mathematical model. Consistent ice coverage above the about 10 % of the surface area in the vicinity of the stagnation point was not recorded at a surface temperature of 0 °C in either case, and no accretion was identified at a surface temperature of 5 °C.

The flat plate specimen tests showed accretion in the vicinity of the leading edge, but there was no occasion when the ice accumulated on the surface downstream from the leading edge. The lack of accretion recorded on the flat plate surface was likely to be because of the transverse momentum imparted to the particles by the leading edge and associated flow field which resulted in very few, if any particles entering the flat plate boundary layer downstream of the leading edge.

Due to the large diameter of the cylinder in comparison with the flat plate leading edge, the cylinder model generates lower aerodynamic drag forces on particles than the flat plate leading edge. Hence, the cylinder is expected to have higher accretion rate than the flat plate leading edge. However, the flat plate leading edge shows slightly faster ice growth than the cylinder, and this is attributed to lower temperatures at the leading edge which can arise because this region of the plate was not thermally controlled.

8.5 Limitations and Further Work

This work has established new hardware and a body knowledge which can be extended to provide a more complete understanding of the initiation of the icing process. Limitations of this study are listed below.

- The Reynolds number is low and the experimental flow conditions do not replicate the engine compressor conditions during flight.
- The study focused on the ice crystal accretion at sub-freezing temperatures and low Mach number.
- The air flow contained only ice particles which simplifies the problem analyses but is not representative of compressor conditions.

- The distance between the particle and the surface in the mathematical model (H) was assumed to be zero.
- The ice particle was assumed to have a spherical shape due to the atomiser use.
- The impinging ice particles coefficient of restitution is assumed to be zero.
- The viewing angle of the cylindrical model is controlled by the curvature of the surface which may effect the result accuracies.

Further studies in this area may seek to address the limitations described above, and could also undertake work as described below.

- The wind tunnel Reynolds and Mach number can be increased by adding more powerful fan.
- The cylinder surface heat load can be kept constant to find the time required for the ice crystal to accumulate at a specific starting temperature.
- The duration of the test can be increased by increasing the size of the water tank and air reservoir, and by adding more nozzles to the spray system, the ice water content can be increased to assess the accretion process at higher ice water content conditions.
- The experiment can be performed at 1 and $-1\,^{\circ}\mathrm{C}$ to reduce the fluctuation effect of the controller temperature ($\pm 0.3\,^{\circ}\mathrm{C}$) around the freezing temperature at the atmospheric pressure.
- With relative minor modifications to the facility and its operation, the mixed phase icing test which is more representative condition for the engine icing, can be performed.
- A stereo vision microscope video system could be implemented to study the ice accretion thickness on the surface.
- Improved ice water content measurement methods should be adopted.
- The mathematical model does not explicitly treat heat and mass transfer, and phase change effects.

- If accretion initiation in a flat plate boundary layer is to be investigated, the plate should have a sharp leading edge and should be inclined at a slight angle to the flow. The aerodynamic flow associated with this arrangement in the confined wind tunnel duct will need to be investigated.

- It is recommended that a sharp leading edge be used for the flat plate to mitigate the flow field deflection and to test the ice accretion beyond the leading edge area.

- The probability of the ice particle bouncing and shedding can be studied at range of particle sizes and surface temperature.

- A prediction of the accumulation time history can be developed by combining the CFD simulation, the developed mathematical model and the experimental results.

References

AI-Khalil, K. and Salamon, L. 1998, Development of the cox icing research facility, *in* '36th Aerospace Science Meeting & Exhibit, AIAA - 98-0097', AIAA, Reno, NV.

Akkok, M., Ettles, C. M. M. and Calabrese, S. J. 1987, 'Parameters affecting the kinetic friction of ice', *Journal of Tribology* **109**(3), 552–559.

Al-Khalil, K. 2003, Assessment of effects of mixed-phase icing conditions on thermal ice protection systems, Technical report.

Antonini, C., Carmona, F. J., Pierce, E., Marengo, M. and Amirfazli, A. 2009, 'General methodology for evaluating the adhesion force of drops and bubbles on solid surfaces', *Langmuir* **25**(11), 6143–6154.

Bellucci, M. 2007, Cloud characterization in CIRA icing wind tunnel, PhD thesis, Università degli Studi di Napoli Federico II.

Bengtsson, L., Hodges, K. I. and Roeckner, E. 2006, 'Storm tracks and climate change', *Journal of Climate* **19**(15), 3518–3543.

Bowden, F. P. 1953, 'Friction on snow and ice', *Proceedings of the Royal Society of London. Series A. Mathematical and Physical Sciences* **217**(1131), 462–478.

Brennen, C. E. 2005, *Fundamentals of multiphase flow*, Cambridge University Press.

Casassa, G., Narita, H. and Maeno, N. 1991, 'Shear cell experiments of snow and ice friction', *Journal of Applied Physics* **69**(6), 3745–3756.

Cebeci, T. and Kafyeke, F. 2003, 'Aircraft icing', *Annual Review of Fluid Mechanics* **35**(1), 11–21.

Chintamani, S., Delcarpio, D. and Langmeyer, G. 1997, Development of Boeing research aerodynamic icing tunnel circuit, *in* 'AGARD conference proceedings', AGARD, pp. 8–1.

Colbeck, S. C. 1988, 'The kinetic friction of snow', *Journal of Glaciology* **34**, 1–9.

Currie, T. C., Struk, P. M., Tsao, J., Fuleki, D. and Knezevici, D. C. 2012, Fundamental study of mixed-phase icing, with application to ice crystal accretion in aircraft jet engines, *in* '4th AIAA Atmospheric and Space Environments Conference, American Institute of Aeronautics and Astronautics, Reston, VA (submitted for publication)'.

Das, K., Hamed, A. and Basu, D. 2006, 'Ice shape prediction for turbofan rotating blades', *AIAA Paper* **209**, 2006.

De Gregorio, F., Esposito, B., Mingione, G., Vicini, A. and Aerospaziali, C. 1997, 'Experimental and computational aerodynamics applications for an icing wind tunnel design', *Italian Aerospace Research Center, Aerodynamics of Wind Tunnel Circuits and their Components (97-27840 01-09)* .

de Lazzer, A., Dreyer, M. and Rath, H. J. 1999, 'Particle surface capillary forces', *Langmuir* **15**(13), 4551–4559.

Döppenschmidt, A., Kappl, M. and Butt, J. B. 1998, 'Surface properties of ice studied by atomic force microscopy', *The Journal of Physical Chemistry B* **102**(40), 7813–7819.

Dotan, A., Dodiuk, H., Laforte, C. and Kenig, S. 2009, 'The relationship between water wetting and ice adhesion', *Journal of Adhesion Science and Technology* **23**(15), 1907–1915.

Evans, D. C. B., Nye, J. F. and Cheeseman, K. J. 1976, The kinetic friction of ice, *in* 'the Royal Society of London. Series A, Mathematical and Physical Sciences', Vol. 347, The Royal Society, pp. 493–512.

Fan, X., Ten, P., Clarke, C., Bramley, A. and Zhang, Z. 2003, 'Direct measurement of the adhesive force between ice particles by micromanipulation', *Powder Technology* **131**(2-3), 105–110.

Frederking, R. and Barker, A. 2002, Friction of sea ice on steel for condition of varying speeds, *in* 'Proc. 12th International Offshore and Polar Engineering Conference', pp. 26–31.

Fu, R., Del Genio, A. D. and Rossow, W. B. 1990, 'Behavior of deep convective clouds in the tropical pacific deduced from isccp radiances', *Journal of climate* **3**(10), 1129–1152.

Gent, R. W., Dart, N. P. and Cansdale, J. T. 2000, 'Aircraft icing', *Philosophical Transactions of the Royal Society of London. Series A: Mathematical, Physical and Engineering Sciences* **358**(1776), 2873–2911.

Griffiths, R. C. and Korkan, K. D. 1992, Study of theoretical and wind tunnel results on flight degradation due to leading edge rime ice accretion, Technical report, Presented at the 30th Aerospace Sciences Meeting, Reno, NV, 6-9 Jan. 1992; sponsored by AIAA.

Grzych, M. L. and Mason, J. G. 2010, 6.8 weather conditions associated with jet engine power loss and damage due to ingestion of ice particles: What we′ve learned through 2009, *in* '14th Conference on Aviation, Range, and Aerospace Meteorology'.

Hamed, A., Das, K. and Basu, D. 2005, 'Numerical simulations of ice droplet trajectories and collection efficiency on aero-engine rotating machinery', *AIAA Paper* **1248**, 2005.

Hays, D. A. 1995, 'Adhesion of charged particles', *Journal of adhesion science and technology* **9**(8), 1063–1073.

Heinrich, A. 1991, Aircraft icing handbook, Technical report.

Heymsfield, A. and Miloshevich, L. 1993, 'Homogeneous ice nucleation and supercooled liquid water in orographic wave clouds', *Journal of the atmospheric sciences* **50**(15), 2335–2353.

Hwang, K., German, R. and Lenel, F. 1987, 'Capillary forces between spheres during agglomeration and liquid phase sintering', *Metallurgical and Materials Transactions A* **18A**(1), 11–17.

Irvine, T., Kevdzija, S., Sheldon, D. and Spera, D. 2001, *Overview of the Icing and Flow Quality Improvements Program for the NASA Glenn Icing Research Tunnel*, National Aeronautics and Space Administration, Glenn Research Center.

Israelachvili, J. N. 2011, *Intermolecular and surface forces: revised third edition*, Academic press.

Jellinek, H. H. G. 1960, Adhesive properties of ice, part II, Technical Report Res. Rep. 62, U. S. Army Snow Ice and Permafrost Res. Estab.

Jin, Z. and Hu, H. 2010, 'Icing process of small water droplets impinging onto a frozen cold plate', *Journal of Thermophysics and Heat Transfer* **24**(4), 841–845.

Jorgensen, D. and Lemone, M. 1989, 'Vertically velocity characteristics of oceanic convection.', *Journal of Atmospheric Sciences* **46**, 621–640.

Jorgenson, P., Veres, J., Wright, W., May, R. and Jorgenson-NASA, P. 2011, 'Engine icing modeling and simulation (part I): Ice crystal accretion on compression system components and modeling its effects on engine performance', *SAE Technical Paper* pp. 38–0025.

Kennedy, F. E., Schulson, E. M. and Jones, D. E. 2000, 'The friction of ice on ice at low sliding velocities', *Philosophical Magazine A* **80**(5), 1093 – 1110.

Kietzig, A.-M. 2010, Microscopic ice friction, PhD thesis, The University of British Columbia.

Kietzig, A.-M., Hatzikiriakos, S. G. and Englezos, P. 2009, 'Ice friction: The effects of surface roughness, structure, and hydrophobicity', *Journal of Applied Physics* **106**(2), 024303–024303–7.

Kind, R. J., Potapczuk, M. G., Feo, A., Golia, C. and Shah, A. D. 1998, 'Experimental and computational simulation of in-flight icing phenomena', *Progress in Aerospace Sciences* **34**(5-6), 257–345.

Knezevici, D. C., Fuleki, D., Currie, T. C., Galeote, B., Chalmers, J. and MacLeod, J. 2013, Particle size effects on ice crystal accretion–part II, *in* '5th Atmospheric and Space Environments Conference', AIAA.

Knezevici, D. C., Fuleki, D., Currie, T. C. and MacLeod, J. D. 2012, Particle size effects on ice crystal accretion, *in* '4th AIAA Atmospheric and Space Environments Conference', AIAA.

Knollenberg, R., Kelly, K. and Wilson, J. 1993, 'Measurements of high number densities of ice crystals in the tops of tropical cumulonimbus', *Journal of geophysical research* **98**, 8639–8664.

Kreith, F. and Bohn, M. S. 2001, *Principles of heat transfer*, 6th edn, Brooks/Cole Pub, Australia.

Kuhns, I., Mason, B., Kuhns, I. and Mason, B. 1968, 'The supercooling and freezing of small water droplets falling in air and other gases', *Proceedings of the Royal Society of London. Series A. Mathematical and Physical Sciences* **302**(1471), 437–452.

Kuroiwa, D. 1977, 'The kinetic friction on snow and ice', *Journal of Glaciology* **19**(81), 141–152.

Langham, E. and Mason, B. 1958, 'The heterogeneous and homogeneous nucleation of supercooled water', *Proceedings of the Royal Society of London. Series A. Mathematical and Physical Sciences* **247**(1251), 493–504.

Lawson, R. P., Angus, L. J. and Heymsfield, A. J. 1998, 'Cloud particle measurements in thunderstorm anvils and possible weather threat to aviation', *Journal of Aircraft* **35**(1), 113–121.

Lee, S. and Loth, E. 2008, 'Simulation of icing on a cascade of stator blades', *Journal of Propulsion and Power* **24**(6), 1309–1316.

Liang, H., Martin, J. M. and Mogne, T. L. 2003, 'Experimental investigation of friction on low-temperature ice', *Acta Materialia* **51**(9), 2639–2646.

Liao, S., Liu, X. and Feulner, M. 2011, 'An analysis of turbofan inlet water and ice concentration effects in icing conditions', *SAE Technical Paper* pp. 38–0050.

Lozowski, E. P., Szilder, K. and Makkonen, L. 2000, 'Computer simulation of marine ice accretion', *Philosophical Transactions of the Royal Society of London. Series A: Mathematical, Physical and Engineering Sciences* **358**(1776), 2811–2845.

Maeno, N., Arakawa, M., Yasutome, A., Mizukami, N. and Kanazawa, S. 2003, 'Ice ice friction measurements, and water lubrication and adhesion-shear mechanisms', *Canadian Journal of Physics* **81**, 241–249.

Makkonen, L. 2000, 'Models for the growth of rime, glaze, icicles and wet snow on structures', *Philosophical Transactions of the Royal Society of London. Series A: Mathematical, Physical and Engineering Sciences* **358**(1776), 2913–2939.

Mason, J. G., Chow, P. and Fuleki, D. M. 2011, 'Understanding ice crystal accretion and shedding phenomenon in jet engines using a rig test', *Journal of engineering for gas turbines and power* **133**(4).

Mason, J., Strapp, J. and Chow, P. 2006, The ice particle threat to engines in flight, *in* '44th AIAA Aerospace Sciences meeting and Exhibit', pp. AIAA Paper 2006–206.

May, R., Guo, T., Veres, J., Jorgenson, P. and Ryan, D. 2011, 'Engine icing modeling and simulation (part 2): Performance simulation of engine rollback phenomena', *SAE Technical Paper* pp. 38–0026.

Messinger, B. 1953, 'Equilibrium temperature of an unheated icing surface as a function of air speed', *Journal of the Aeronautical Sciences* pp. 29–42.

Minoya, T., Hiramoto, R., Otsuka, H. and Hosokawa, K. 2010, Observation of ice accretion phenomena to axial fan, *in* '13th Asian Congress of Fluid Mechanics 17-21 December', Dhaka, Bangladesh, pp. 663–666.

Mollinger, A. and Nieuwstadt, F. 1996, 'Measurement of the lift force on a particle fixed to the wall in the viscous sublayer of a fully developed turbulent boundary layer', *Journal of Fluid Mechanics* **316**, 285–306.

Mossop, S. C. 1955, 'The freezing of supercooled water', *Proceedings of the Physical Society. Section B* **68**(4), 193.

Mu, F. and Su, X. 2007, 'Analysis of liquid bridge between spherical particles', *China Particuology* **5**(6), 420–424.

Oksanen, P. and Keinonen, J. 1982, 'The mechanism of friction of ice', *Wear* **78**(3), 315–324.

Orr, F. M., Scriven, L. E. and Rivas, A. P. 1975, 'Pendular rings between solids: meniscus properties and capillary force', *Journal of Fluid Mechanics* **67**(04), 723–742.

Pan, D., Liu, L.-M., Slater, B., Michaelides, A. and Wang, E. 2011, 'Melting the ice: On the relation between melting temperature and size for nanoscale ice crystals', *ACS Nano* **5**(6), 4562–4569.

Poots, G. I. 1996, *Ice and snow accretion on structures*, Research Studies Press, Tauton, Somerset, England.

Poots, G. I. 2000, 'Introductory remarks', *Philosophical Transactions of the Royal Society of London. Series A: Mathematical, Physical and Engineering Sciences* **358**(1776), 2803–2810.

Pruppacher, H. R. and Neiburger, M. 1968, Design and performance of the UCLA cloud tunnel, *in* 'International Conference on Cloud Physics', pp. 389–392.

Rabinovich, Y. I., Esayanur, M. S. and Moudgil, B. M. 2005, 'Capillary forces between two spheres with a fixed volume liquid bridge: theory and experiment', *Langmuir* **21**(24), 10992–10997.

Raraty, L. E. and Tabor, D. 1958, 'The adhesion and strength properties of ice', *Proceedings of the Royal Society of London. Series A. Mathematical and Physical Sciences* **245**(1241), 184–201.

Ríos, M. and Cho, Y. 2008, *Analysis of ice crystal ingestion as a source of ice accretion inside turbofans*, Fluid Dynamics and Co-located Conferences, American Institute of Aeronautics and Astronautics. doi:10.2514/6.2008-4165.

Ríos, P. M. 2012, Ice crystal ingestion by turbofans, PhD thesis, Drexel University.

Rosenfeld, D. and Lensky, I. M. 1998, 'Satellite-based insights into precipitation formation processes in continental and maritime convective clouds', *Bulletin of the American Meteorological Society* **79**(11), 2457–2476.

Rosenfeld, D. and Woodley, W. L. 2000, 'Deep convective clouds with sustained supercooled liquid water down to-37.5 c', *Nature* **405**(6785), 440–442.

Ryerson, C. C. and Gow, A. J. 2000, 'Crystalline structure and physical properties of ship superstructure spray ice', *Philosophical Transactions of the Royal Society of London. Series A: Mathematical, Physical and Engineering Sciences* **358**(1776), 2847–2871.

Schlichting, H. 1979, *Boundary-layer theory*, McGraw-Hill series in mechanical engineering, 7th edn, McGraw-Hill, New York.

Scholten, J. and Murray, D. 1998, 'Unsteady heat transfer and velocity of a cylinder in cross flow i. low freestream turbulence', *International Journal of Heat and Mass Transfer* **41**(10), 1139 – 1148.

Sprakel, J., Besseling, N. A. M., Cohen Stuart, M. A. and Leermakers, F. A. M. 2008, 'Capillary adhesion in the limit of saturation: Thermodynamics, self-consistent field modeling and experiment', *Langmuir* **24**(4), 1308–1317.

Stith, J., Dye, J., Bansemer, A., Heymsfield, A., Grainger, C., Petersen, W. and Cifelli, R. 2002, 'Microphysical observations of tropical clouds', *Journal of Applied Meteorology* **41**(2), 97–117.

Struk, P., Broeren, A., Tsao, J., Vargas, M., Wright, W., Currie, T., Knezevici, D. and Fuleki, D. 2012, Fundamental ice crystal accretion physics studies, Technical Report NASA/TM-2012-217429.

Taghavi, R. R. and Jin, W. 2008, 'Effects of ice formation on the flowfield of an aircraft engine inlet', *ASME Conference Proceedings* **2008**(48418), 117–128.

Takeuchi, M. 2006, 'Adhesion forces of charged particles', *Chemical Engineering Science* **61**(7), 2279 – 2289. ¡ce:title¿Papers Presented at the Eleventh and Twelfth Nisshin Engineering Particle Technology International Symposium¡/ce:title¿ ¡xocs:full-name¿Papers Presented at the Eleventh and Twelfth Nisshin Engineering Particle Technology International Symposium¡/xocs:full-name¿.

Tarantola, A. 2013, 'Monster machines: if a jet engine can survive GE′s wind tunnel, it can survive anything', *GIZMODO, Austrlia* .

Thomas, S. K., Cassoni, R. P. and MacArthur, C. D. 1996, 'Aircraft anti-icing and de-icing techniques and modeling', *Journal of Aircraft* **33**(5), 841–854.

Tusima, K. and Tabata, T. 1979, Friction measurements of sea ice on flat plates of metals, plastics and coatings, *in* '5th International Conference oil Port and Ocean Engineering under Arc tic Conditions', Trondheim, Norway, pp. 741–755.

Vargaftik, N., Volkov, B. and Voljak, L. 1983, *International tables of the surface tension of water*, American Chemical Society and the American Institute of Physics for the National Bureau of Standards Washington, DC.

Walton, O. R. 2008, 'Review of adhesion fundamentals for micron-scale particles', *KONA Powder and Particle Journal* **26**, 129–141.

White, F. M. 1991, *Viscous fluid flow*, New York.

Willett, C. D., Adams, M. J., Johnson, S. A. and Seville, J. P. K. 2000, 'Capillary bridges between two spherical bodies', *Langmuir* **16**(24), 9396–9405.

Wright, W., Jorgenson, P. and Veres, J. 2010, Mixed phase modeling in GlennICE with application to engine icing, *in* 'Atmospheric and Space Envirnments Coference', AIAA - 2010 - 7674, Toronto, Canada.

Yang, S.-o., Kleehammer, D. M., Huo, Z., Sloan, E. D. and Miller, K. T. 2004, 'Temperature dependence of particle-particle adherence forces in ice and clathrate hydrates', *Journal of Colloid and Interface Science* **277**(2), 335–341.

Appendix A

First Experimental Apparatus Arrangement

A.1 Introduction

The original design of the vertical wind tunnel to study the ice accretion and preliminary results will be presented. Because of the low residence time and mild thermal conditions for the water droplet inside the cold stream, this arrangement was not used. For the primary experiments reported in this dissertation.

A.2 Arrangement

The original experimental rig for producing ice particles and injecting them into a wind tunnel flow was arranged as illustrated in Figure A.1. The apparatus operated in a cold room which has a set point temperature of between -20 °C and 0 °C. Air temperatures within this range are encountered in the early stages of aero-engine compressors exposed to the potential high altitude solid phase ice accretion conditions.

Cold room air is driven through a heat exchanger designed to reduce the air stream temperature to around $-50\,^{\circ}\mathrm{C}$. The initial heat exchanger arrangement used in these

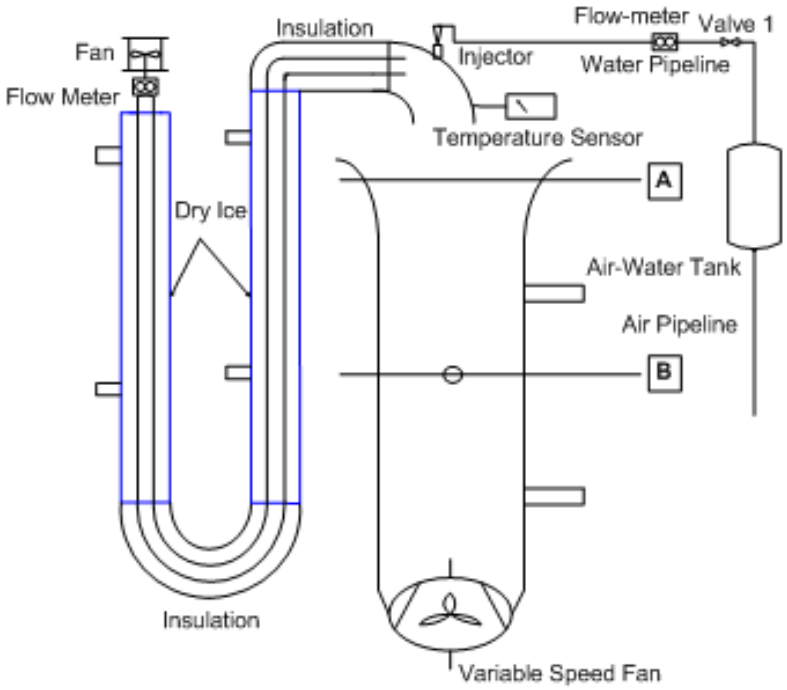

Figure A.1: Schematic diagram for the experimental apparatus with dry ice tube heat exchanger.

experiments consisted of two 12.5 mm diameter vertical copper tubes each with a length of approximately 1.1 m. These copper tubes were each housed within a larger PVC pipe (40 mm) containing dry ice. In the arrangement used for subsequent experiments, the heat exchanger consisted of a 12 mm diameter copper tube with a length of approximately 2 m which was enclosed by an ice box containing dry ice. The temperature of the air leaving the heat exchanger was measured in the 40 mm diameter PVC 90° elbow as illustrated in Figure A.2.

A water injection nozzle (UniJet model TX with an orifice of 0.36 mm) delivers water droplets through an elbow at the exit of the heat exchanger. The injection nozzle was not directly inserted into the cold air stream at −50 °C but was aligned with a hole in the outer radius of the elbow so that most of the droplet spray penetrated into the cold air stream. Water was delivered to the injection nozzle from a water tank containing purified water which can be pressurised to between 2 to 5 bar.

The water was injected into the cold air flow from the heat exchanger and the tempera-

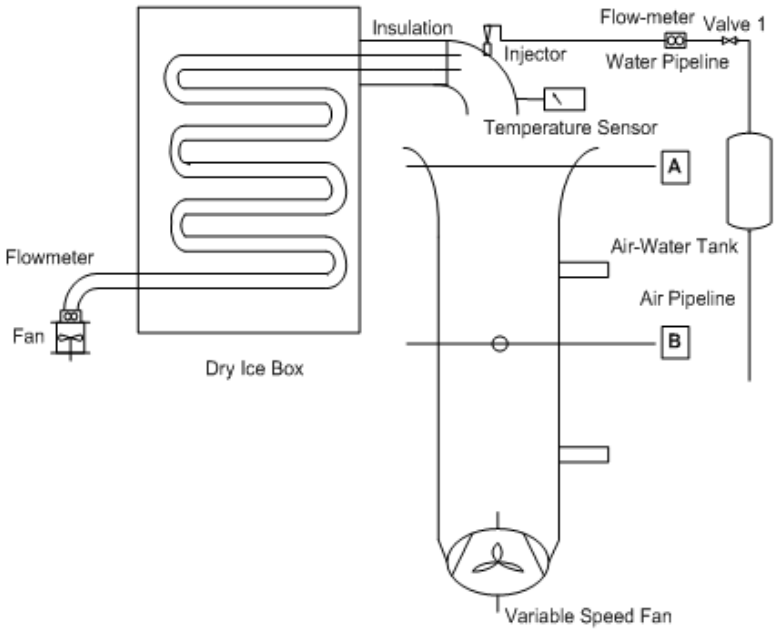

Figure A.2: Schematic diagram for the experimental apparatus with dry ice box heat exchanger.

ture of the droplets decreases through heat exchange with the surrounding air. The ice particles produced in this manner will be near spherical in shape. Mason et al. (2006) indicate that producing ice particles to simulate cloud ice conditions in ground-based test facilities is a challenging task because in the high altitude atmospheric environment, numerous different shapes can occur. In fact, cloud ice particles are likely to exist in a greater range of shapes and sizes relative to super cooled droplets. The particle shape will affect the particle trajectories and the collection efficiency of aerodynamic objects. However, for current purposes - the initial testing and refining of accretion initiation simulation methods - the use of near spherical particles is appropriate.

After producing the ice particles, the cold, ice-laden air stream is blended with air from the cold room environment. Mixing between the cold ice-laden air flow and the warmer air from the cold room environment occurs as the streams approach the inlet to small wind tunnel. The wind tunnel is a Perspex tube with an internal diameter of 70 mm and a variable speed fan at the downstream end of the tunnel. A variety of test objects can be positioned within the Perspex tube as required to examine the influence of geometric effect on the initiation of accretion. However, for the experiments reported herein, a 9.6 mm diameter copper tube fitted with an internal heater was used as the

test object.

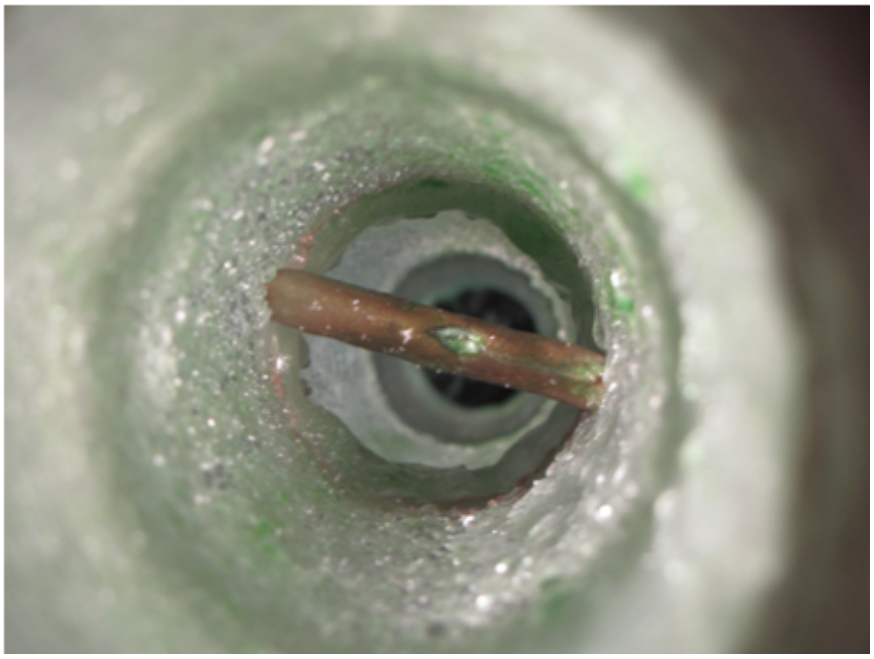

Figure A.3: Photograph of the glaze ice accretion on the wind tunnel duct and test specimen viewed from the wind tunnel inlet. Configuration using the dry ice heat exchanger.

The dry ice heat exchanger configuration did not provide sufficient residence time or sufficiently low temperature conditions to ensure droplet phase change. As can be seen from results in Figure A.3 and Figure A.4 glaze ice dominated the accretion, which confirms that the water droplets have not become ice.

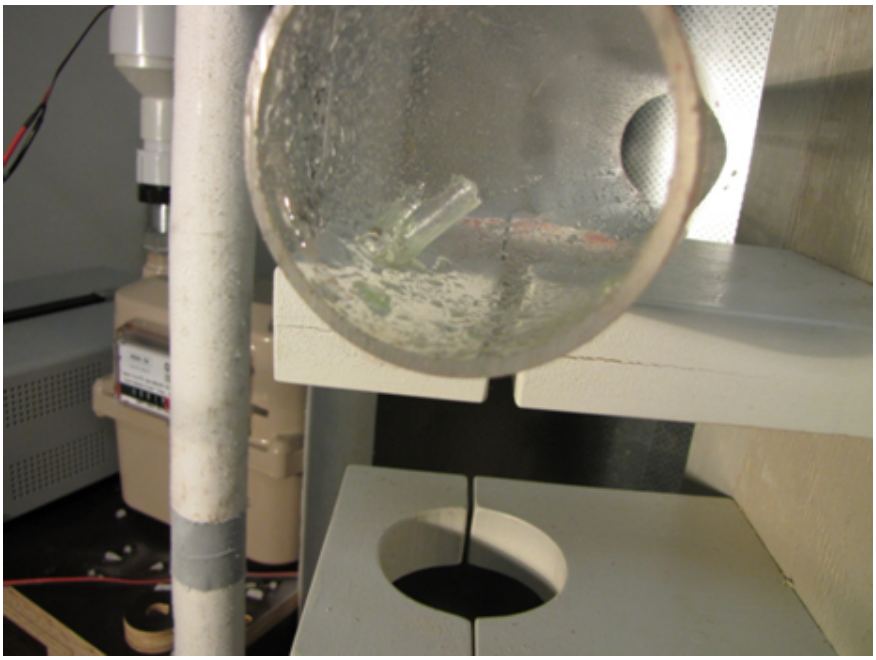

Figure A.4: Photograph shows the glaze ice accretion around the test specimen remaining in the place of after the test specimen is removed. Wind tunnel configuration using the dry ice heat exchanger.

A.3 Nozzles Droplet Size Distribution

A water injection nozzle, UniJet model TX with an orifice of 0.36 mm was operated at a range of different working pressures and samples of the droplets were collected on microscope slides. A representative photograph of water droplets is presented in Figure A.5. Droplet sizing was achieved using a reference image of a known scale and image analysis software applied to the microscope photographs of the droplets. Results from the image analysis of the droplets at different nozzle working pressures between 2.1 and 3.6 bar are presented in Figure A.6. For the 2.1 and 2.3 bar tests, the droplet sizes varied from 0.2 to 0.8 mm in mean volume diameter. With an increase in the working pressure, a decrease of the droplet size was observed. In the case of 3.6 bar, the observed droplet size distribution was limited to between 0.1 and 0.4 mm. The droplet sizes produced with the UniJet nozzle were substantially larger than the particle size anticipated in high altitude clouds (values between 1 and 50 μm are expected).

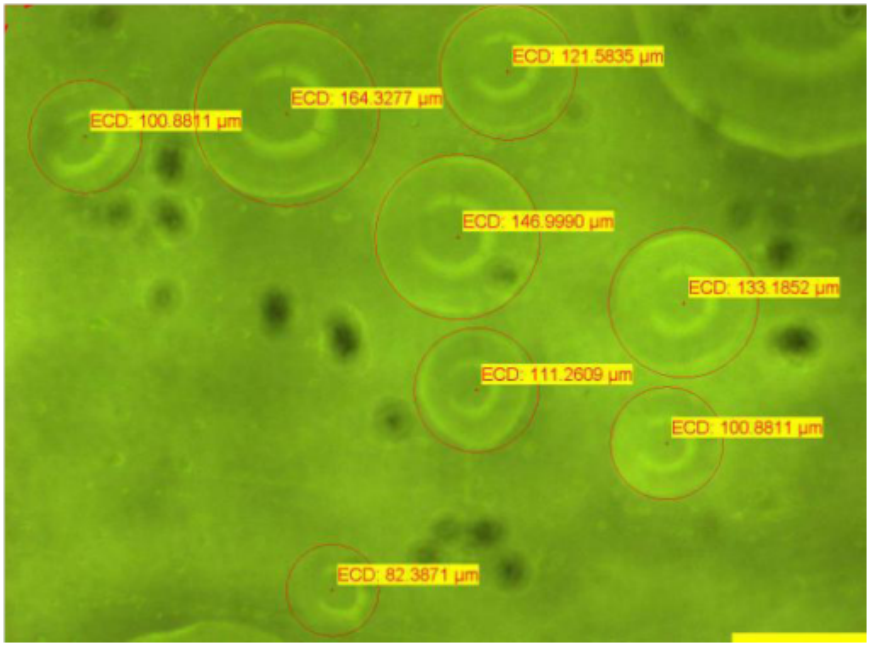

Figure A.5: Photograph of water droplets on a microscope slide with identification of droplet diameters

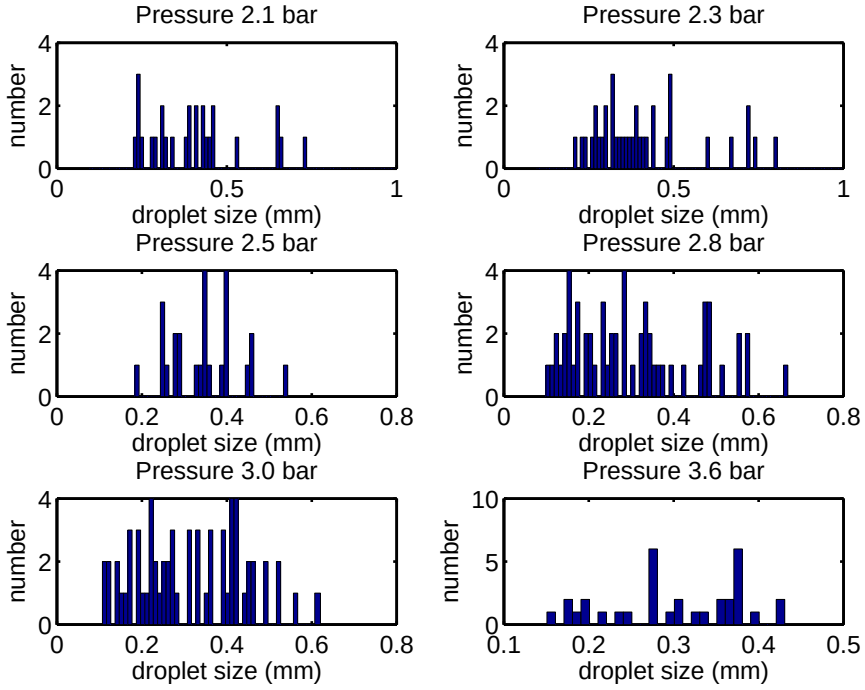

Figure A.6: Droplets size distribution histograms for different nozzle operating pressures, Nozzle type UniJet model TX.

Appendix B

Particle Image Velocimetry

B.1 Introduction

A Photron SA3 with frame rate of 500 frame/second in conjunction with a laser light source (Novalasers X125 Compact Portable) to create a particle image velocimetry (PIV) system for the study of the impact of the solid ice particles on the surface. Figure B.1 shows some particle paths around the cylindrical specimen visualised by using the high speed camera and a laser light. Figure B.2 shows a sequence of frames to illustrate the particle trajectories around the cylindrical specimen.

Figure B.1: Air flow streamline at 500 f/s recording rate and flow speed 6.5 m/s.

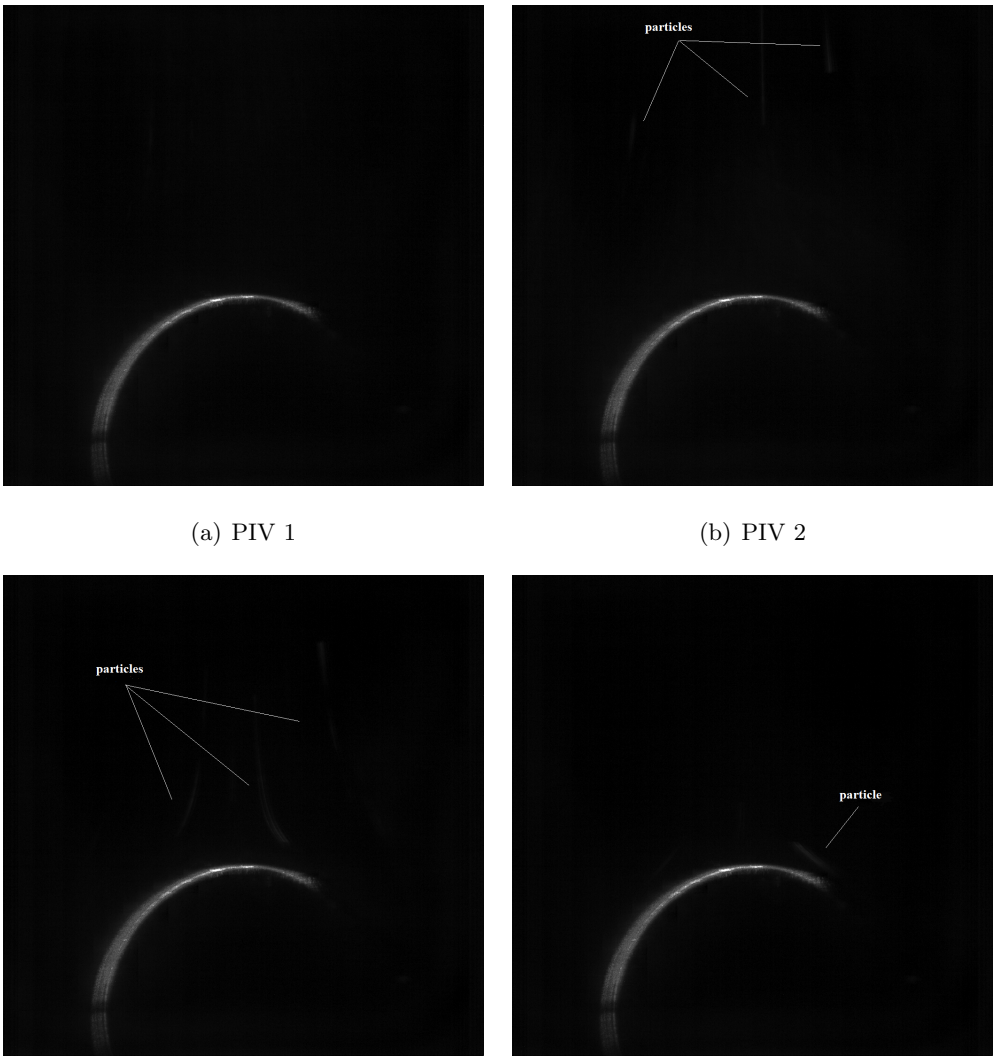

(a) PIV 1

(b) PIV 2

(c) PIV 3

(d) PIV 4

Figure B.2: Frames for flow stream and particles around the cylinder at 500 f/s recording rate and flow speed 6.5 m/s.

Appendix C

Hardware and Software Specification

C.1 LabView System

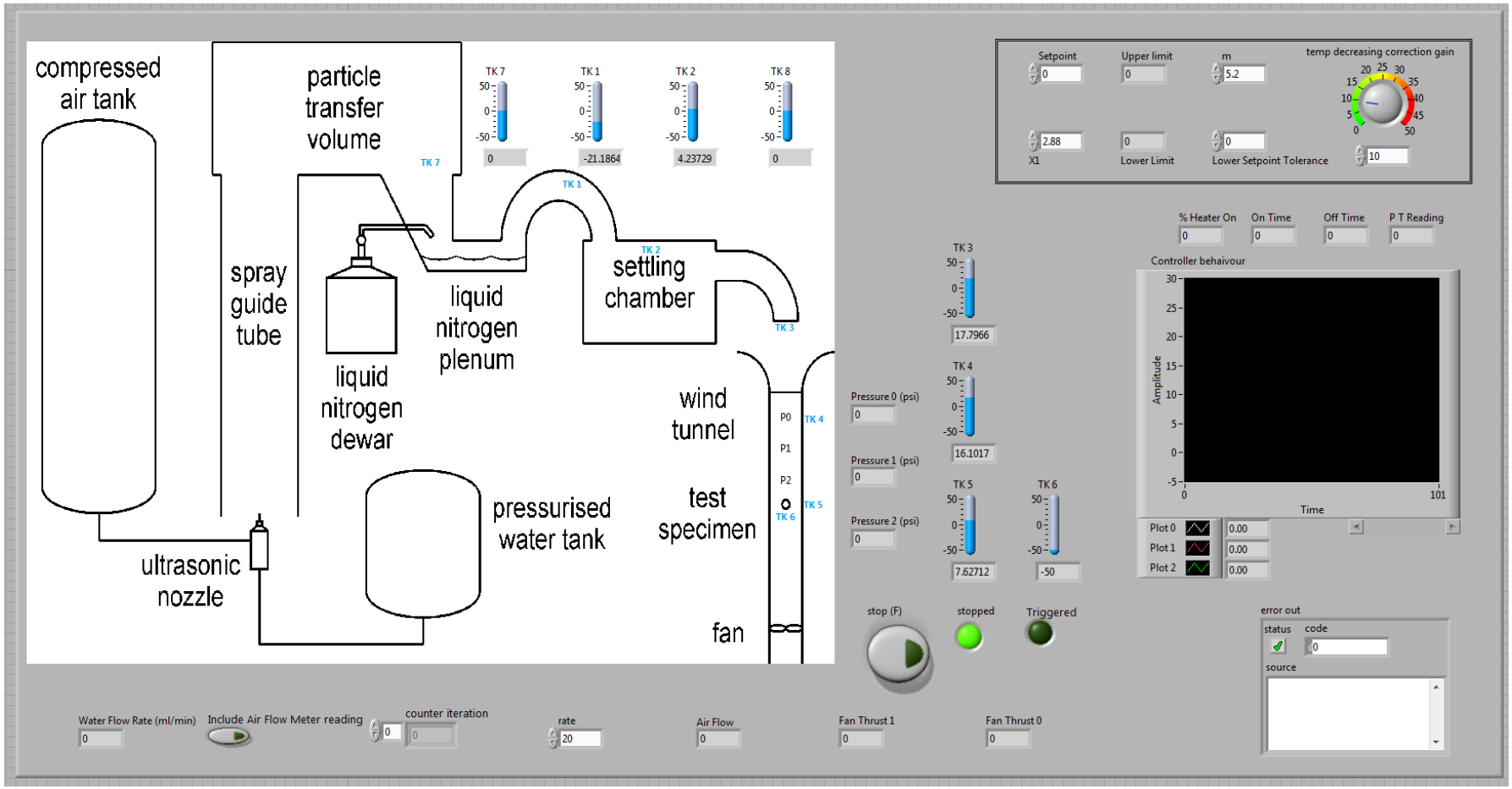

Figure C.1: LabView data acquisition interface screen shot.

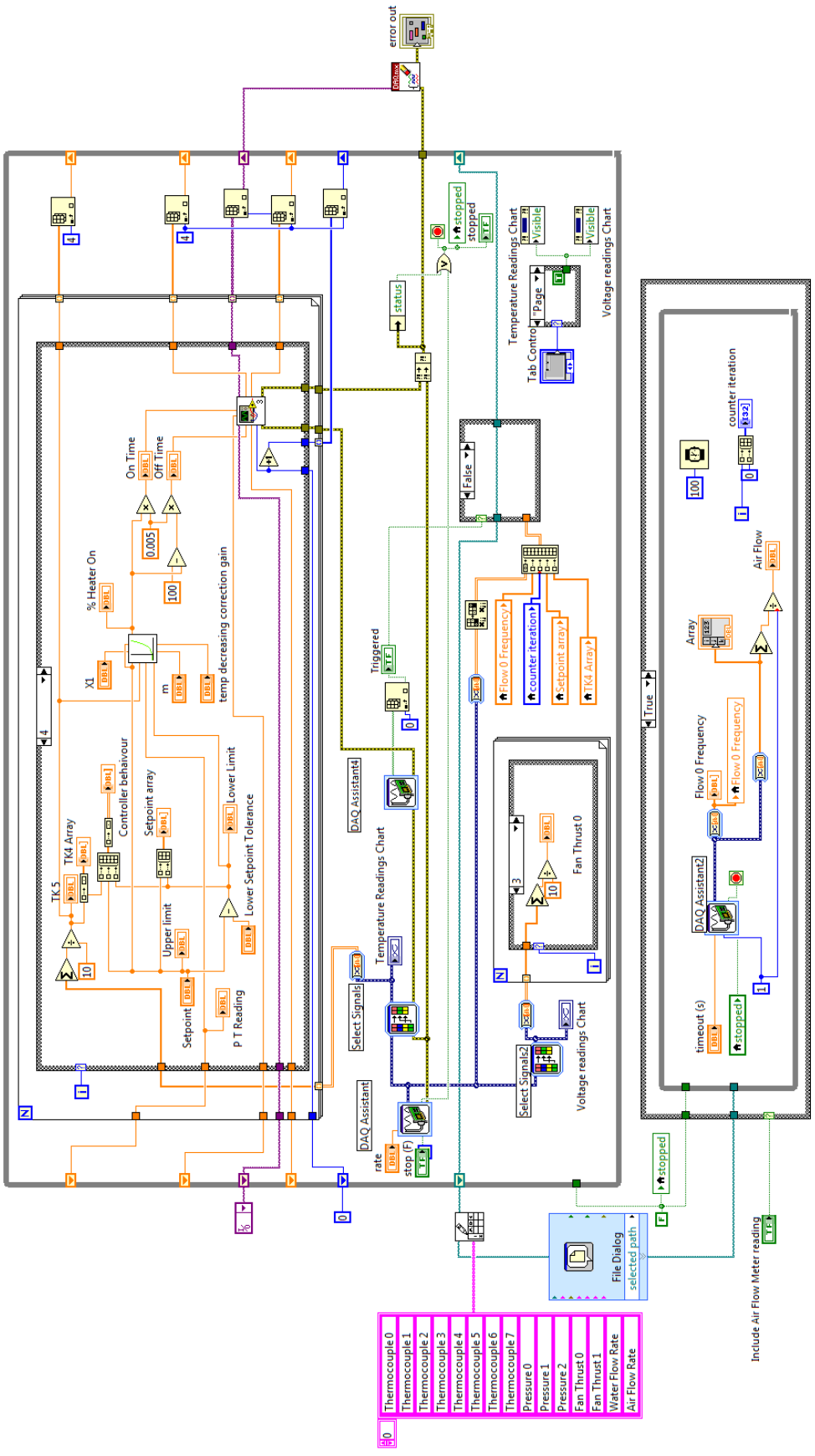

Figure C.2: LabView data acquisition system diagram.

C.2 Ultrasonic Nozzle Data sheet

www.pnr-nozzles.com

ULTRASONIC ATOMIZERS

ATOMIZERS AND FITTINGS

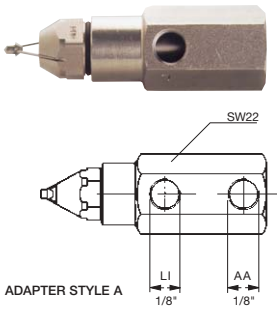

ADAPTER STYLE A

Ultrasonic atomizers produce the finest sprays available with air assistance for industrial processes, with a narrow angle full cone jet.
Water and air do not mix in a confined volume before leaving the nozzle and therefore their feed pressures can be adjusted independently without influencing each other: this allows for a very wide regulation range on the liquid capacity and makes it easier to reach the desired operating conditions.

Please note that the code given in the table only refers to the atomizing head and must be completed with the identification for one of the four connection adapters available, as shown below in the page.
The drawing beside shows an atomizing head assembled onto one A type adapter.

Materials	Atomizing head	B1 AISI 303 Stainless steel
	Adapter	B1 AISI 303 Stainless steel
		T1 Brass

WM = Water capacity (l/min)
AH = Air capacity (Ncm/h)

IDENTIFICATION CODES

ATOMIZING HEAD
The codes given in the table refer to the atomizing head only, and can be used to order the head as a separate part.

ADAPTERS
Can be ordered separately using the codes below, please replace
XX = B1 for AISI 303
XX = T1 for brass

COMPLETE ATOMIZERS
To identify a complete atomizer, please add to the head code the three suffix letters describing the adapter material and the adapter style according to the information below.

MAD 0801 B1 **X Y Z**

Adapter Material
A = T1 Brass
B = B1 AISI 303

Adapter style
A = XMA 0103 xx
B = XMA 0101 xx
C = XMA 0102 xx
D = XMA 0100 xx

Connection
B = BSP F
N = NPT F

	Set-up Code		Air pressure (bar) 0,5 WM	AH	0,7 WM	AH	1,0 WM	AH	2,0 WM	AH	3,0 WM	AH
25°	MAD 0331 B1	2	0,10	3,1	0,12	3,0	0,15	3,1	0,27	2,7	-	-
		3	0,05	3,7	0,10	3,1	0,12	3,6	0,20	3,7	0,32	2,9
		4	0,02	4,7	0,05	4,8	0,08	4,4	0,18	4,4	0,25	4,2
		5	-	-	0,02	5,3	0,05	5,3	0,13	5,5	0,22	5,2
		6	-	-	-	-	0,02	6,1	0,12	6,0	0,18	5,8
	MAD 0801 B1	2	0,23	2,7	0,28	2,9	0,37	2,7	0,72	2,2	-	-
		3	0,22	3,6	0,27	3,6	0,32	3,5	0,52	3,2	0,82	2,7
		4	0,18	4,5	0,22	4,4	0,28	4,6	0,45	4,6	0,62	4,7
		5	0,12	5,4	0,18	5,3	0,25	5,6	0,40	5,4	0,53	5,4
		6	0,07	6,2	0,13	6,3	0,22	6,2	0,35	6,3	0,50	6,2
	MAD 1131 B1	2	0,50	7,3	0,60	6,6	0,73	6,9	1,15	5,6	-	-
		3	0,40	9,7	0,50	9,5	0,65	9,4	0,96	9,3	1,35	7,9
		4	0,27	11,6	0,37	11,9	0,55	11,8	0,93	12,1	1,20	11,5
		5	0,13	13,9	0,23	13,8	0,38	14,0	0,87	14,1	1,15	13,8
		6	0,07	18,6	0,13	18,7	0,27	8,7	0,72	18,9	1,10	19,0
40°	MAL 0800 B1	2	0,18	2,7	0,23	2,7	0,32	2,9	0,73	2,1	-	-
		3	0,15	3,7	0,18	3,9	0,25	3,5	0,50	3,7	0,85	2,6
		4	0,10	4,5	0,17	4,6	0,22	4,9	0,33	4,8	0,53	4,4
		5	0,03	5,4	0,10	5,6	0,18	5,4	0,30	5,4	0,45	5,3
		6	-	-	0,03	6,2	0,12	6,3	0,27	6,2	0,38	6,3
	MAL 1130 B1	2	0,46	7,3	0,52	7,2	0,68	6,8	1,13	5,7	-	-
		3	0,38	9,5	0,47	9,7	0,65	10,2	0,95	9,4	1,27	7,7
		4	0,23	11,8	0,35	11,8	0,50	11,9	0,88	12,1	1,15	11,8
		5	0,13	13,5	0,23	13,9	0,37	14,0	0,82	14,1	1,10	14,2
		6	0,07	16,0	0,13	16,2	0,27	16,2	0,63	16,2	1,03	16,3
	MAL 1300 B1	2	0,95	14,6	1,12	16,5	1,40	16,3	2,42	10,4	-	-
		3	0,80	19,3	1,00	20,0	1,26	22,2	1,90	19,2	2,87	14,5
		4	0,60	24,7	0,80	24,7	1,08	25,0	1,80	25,0	2,40	23,2
		5	0,42	29,9	0,60	30,3	0,90	30,4	1,70	30,5	2,27	29,9
		6	0,23	35,6	0,40	36,0	0,67	35,6	1,55	36,2	2,15	35,2

Liquid pressure (bar)

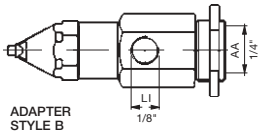

ADAPTER STYLE B

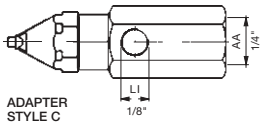

ADAPTER STYLE C

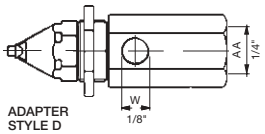

ADAPTER STYLE D

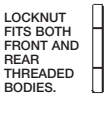

B and D adapter style allow for mounting the atomizer through a wall or the side of a duct.
In this case do not forget to order the VAC 0021 B1 locknut, which fits both, to hold the adapter in place.

Figure C.3: Data sheet for the ultrasonic nozzle used in primary experiments.

Appendix D

Cylindrical Specimen Tests Results

D.1 Introduction

The results of the ice accretion experiments with the cylindrical specimen are presented. The experiments were performed with constant air and water pressure delivered to the water spray nozzle yielding constant ice water content conditions across four different specimen surface temperatures and two different surface roughnesses.

Table D.1: Operating conditions for the cylindrical specimen tests, uncertainties quoted correspond to $\pm 2\sigma$ values.

Test	T_{LN_2E} (°C)	T_{SC} (°C)	T_{SCE} (°C)	T_A (°C)	T_B (°C)	IWC (g/m^3)	T_S (°C)	Figures
SM9T1HP	-91.7 ± 12.5	-49.4 ± 6.8	-42.4 ± 3.7	-13.9 ± 1.8	-15.5 ± 1.7	0.42 ± 0.26	-8.99 ± 0.20	D.1 - D.4
SM9T2HP	-86.9 ± 15.8	-46.9 ± 5.3	-40.1 ± 3.3	-15.0 ± 1.5	-15.4 ± 1.4	0.42 ± 0.26	-9.00 ± 0.14	D.5 - D.8
SM9T3HP	-81.0 ± 16.5	-45.4 ± 6.7	-39.1 ± 4.6	-13.6 ± 1.1	-15.2 ± 0.7	0.42 ± 0.26	-9.00 ± 0.16	D.9 - D.12
SM5T1HP	-73.5 ± 15.8	$-43.6.9 \pm 7.0$	-35.9 ± 4.9	-13.0 ± 1.1	-14.6 ± 1.0	0.42 ± 0.26	-5.04 ± 0.21	D.13 - D.16
SM5T2HP	-99.3 ± 30.5	-50.0 ± 9.2	-38.8 ± 6.6	-12.5 ± 1.3	-14.5 ± 1.0	0.42 ± 0.26	-5.05 ± 0.17	D.17 - D.20
SM5T3HP	-90.6 ± 20.2	-47.0 ± 10.4	-39.6 ± 7.6	-12.5 ± 1.0	-14.7 ± 1.6	0.42 ± 0.26	-5.05 ± 0.13	D.21 - D.24
SM5T4HP	-87.3 ± 13.4	-50.8 ± 6.6	-41.4 ± 4.6	-14.1 ± 0.9	-15.9 ± 1.0	0.42 ± 0.26	-5.05 ± 0.12	D.25 - D.28
SM5T5LP	-77.8 ± 20.1	-44.2 ± 8.3	-36.9 ± 5.6	-13.3 ± 1.2	-14.7 ± 0.6	0.3 ± 0.15	-4.99 ± 0.21	D.29 - D.32
S0T1HP	-71.4 ± 13.3	-41.0 ± 5.5	-33.7 ± 2.9	-12.8 ± 1.0	-14.4 ± 0.8	0.42 ± 0.26	-0.06 ± 0.17	D.33 - D.36
S0T2HP	-71.4 ± 17.7	-40.5 ± 7.4	-32.6 ± 4.3	-9.7 ± 1.2	-11.4 ± 1.0	0.42 ± 0.26	-0.01 ± 0.22	D.37 - D.40
S0T3HP	-75.6 ± 12.8	-44.7 ± 4.6	-33.2 ± 6.6	-15.1 ± 3.2	-16.2 ± 1.3	0.42 ± 0.26	-0.06 ± 0.19	D.41 - D.44
S0T4HP	-79.8 ± 12.6	-45.7 ± 4.8	-36.8 ± 2.9	-11.1 ± 1.5	-12.8 ± 1.0	0.42 ± 0.26	-0.05 ± 0.22	D.45 - D.48
S0T5HP	-77.1 ± 14.2	-46.7 ± 7.3	-32.3 ± 3.4	-11.9 ± 1.4	-13.2 ± 1.1	0.42 ± 0.26	-0.04 ± 0.24	D.49 - D.52
SP5T1HP	-77.6 ± 11.4	-45.8 ± 4.4	-32.5 ± 3.4	-12.5 ± 1.6	-14.2 ± 1.0	0.42 ± 0.26	4.89 ± 0.24	D.53 - D.56
SP5T2HP	-78.9 ± 13.4	-46.0 ± 6.0	-31.5 ± 3.5	-13.9 ± 2.2	-15.4 ± 1.8	0.42 ± 0.26	4.85 ± 0.32	D.57 - D.60
SP5T3HP	-79.4 ± 16.0	-46.1 ± 6.9	-28.6 ± 2.6	-13.1 ± 1.9	-14.6 ± 1.3	0.42 ± 0.26	4.89 ± 0.25	D.61 - D.64
SP5T4HP	-79.4 ± 14.9	-45.2 ± 8.8	-23.9 ± 11.9	-13.3 ± 2.2	-14.6 ± 1.8	0.42 ± 0.26	4.90 ± 0.23	D.65 - D.68
SP5T5HP	-39.2 ± 30.0	-28.3 ± 13.8	-18.8 ± 5.7	-8.9 ± 0.8	-10.6 ± 1.5	0.42 ± 0.26	4.94 ± 0.29	D.69 - D.72

D.2 Surface Temperature −9 °C

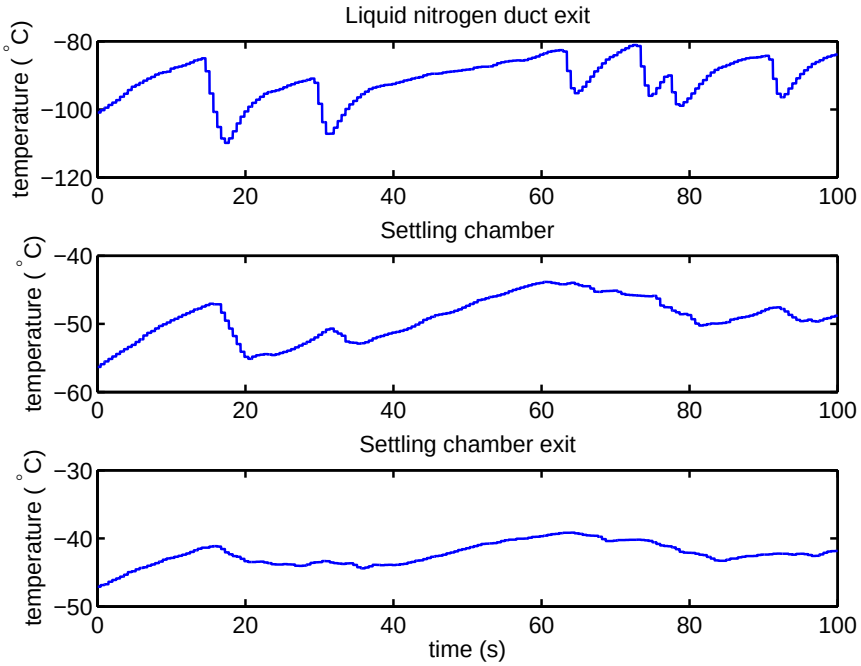

Figure D.1: Test SM9T1HP. Temperatures within the facility upstream of the wind duct. Specimen temperature −9 °C.

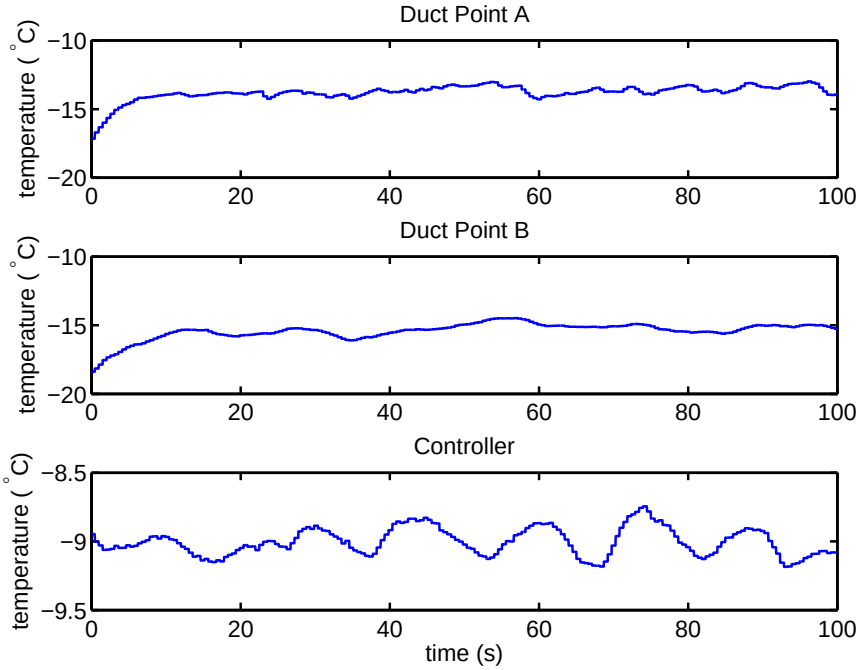

Figure D.2: Test SM9T1HP. Temperatures within the wind tunnel duct for the test specimen temperature of −9 °C.

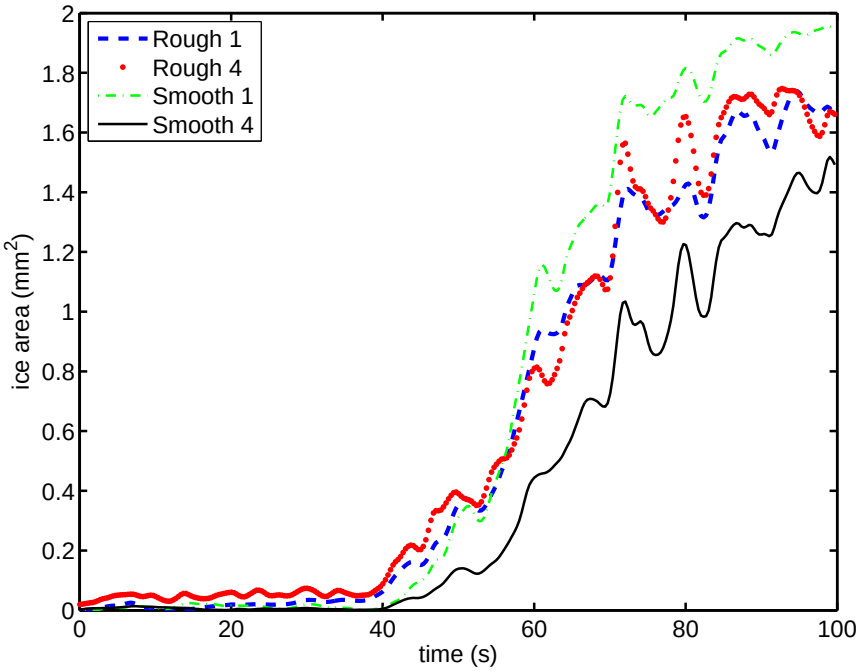

Figure D.3: Test SM9T1HP. Ice accretion area within regions 1 and 4 on the cylindrical specimen at test temperature −9 °C.

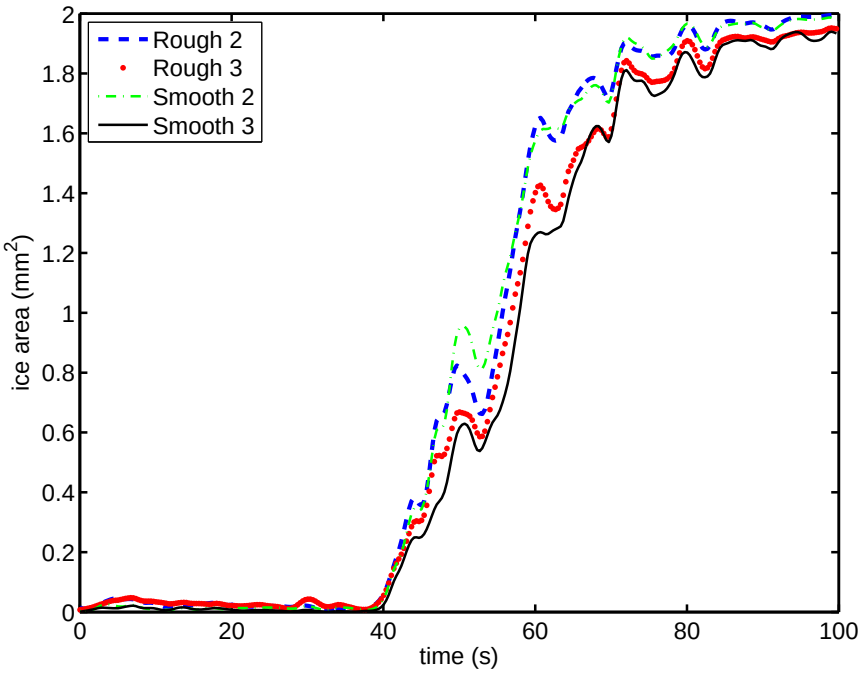

Figure D.4: Test SM9T1HP. Ice accretion area within regions 2 and 3 on the cylindrical specimen at test temperature −9 °C.

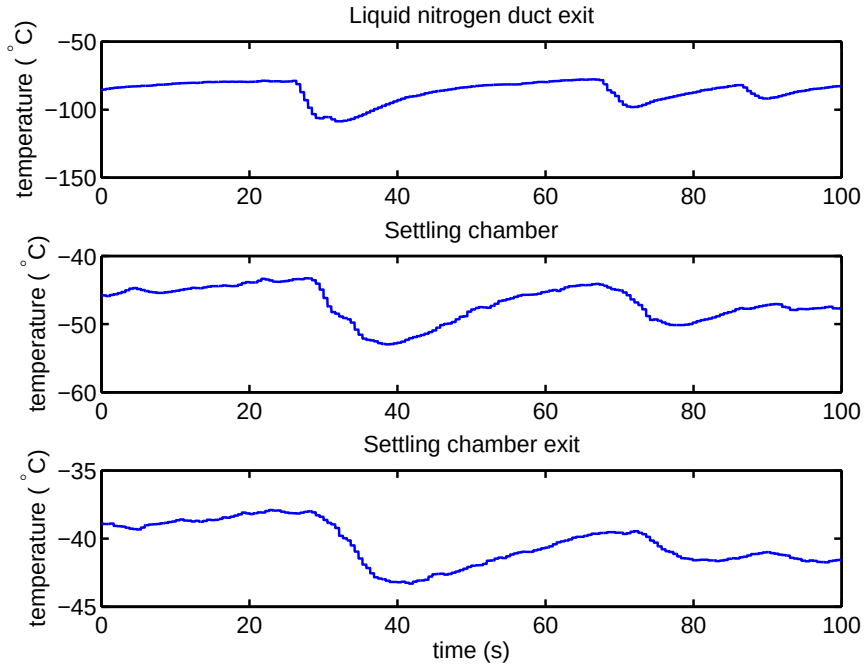

Figure D.5: Test SM9T2HP. Temperatures within the facility upstream of the wind duct. Specimen temperature −9 °C.

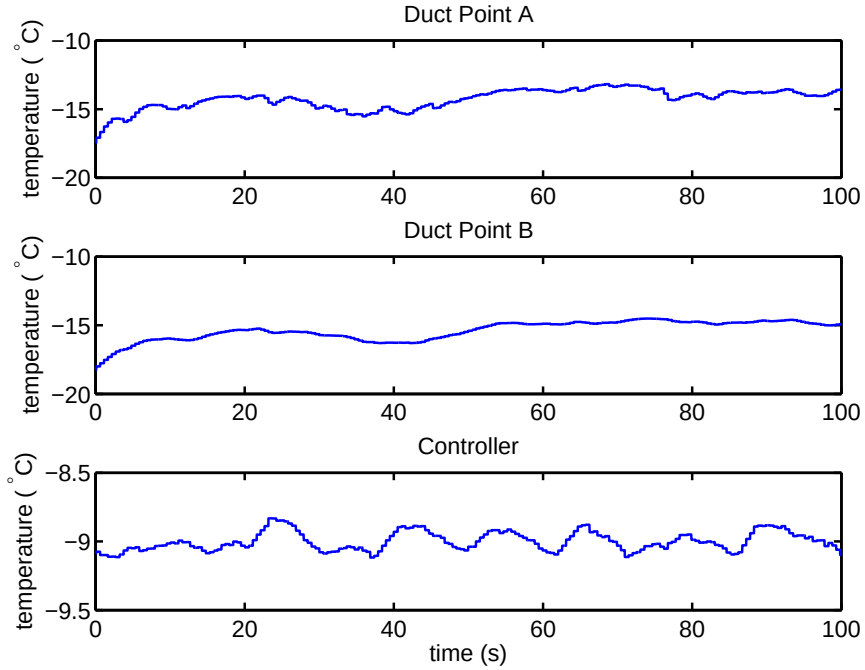

Figure D.6: Test SM9T2HP. Temperatures within the wind tunnel duct for the test specimen temperature of −9 °C.

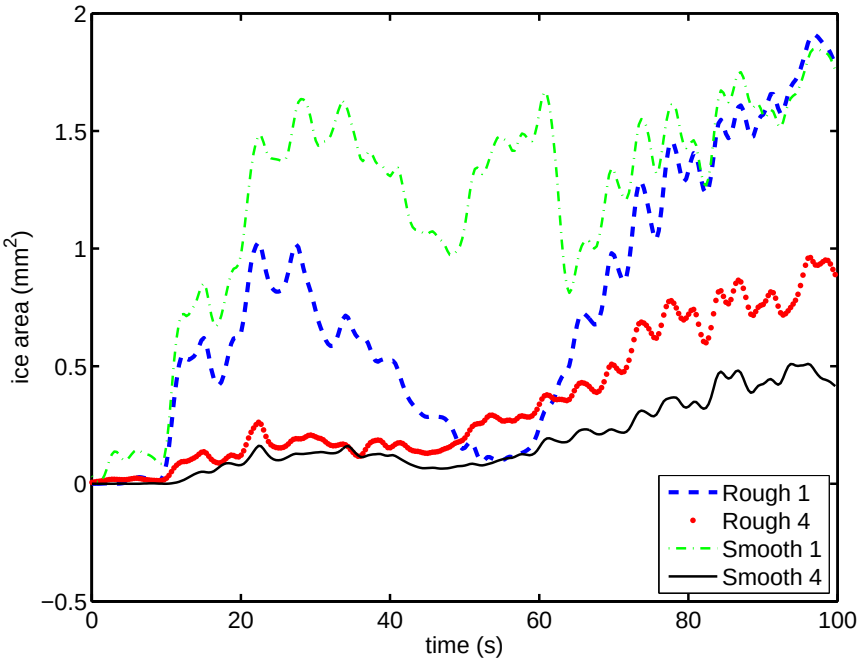

Figure D.7: Test SM9T2HP. Ice accretion area within regions 1 and 4 on the cylindrical specimen at test temperature −9 °C.

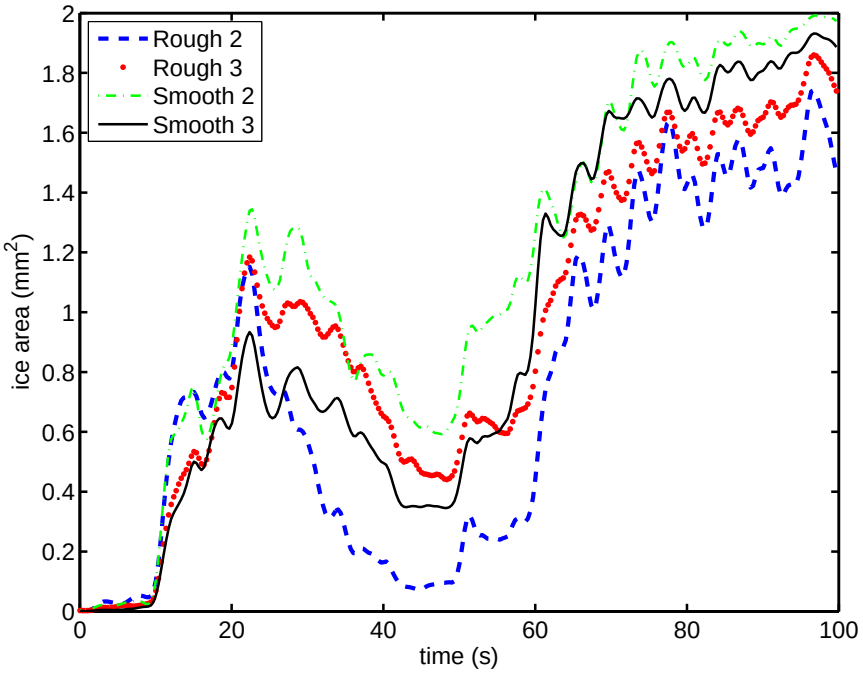

Figure D.8: Test SM9T2HP. Ice accretion area within regions 2 and 3 on the cylindrical specimen at test temperature −9 °C.

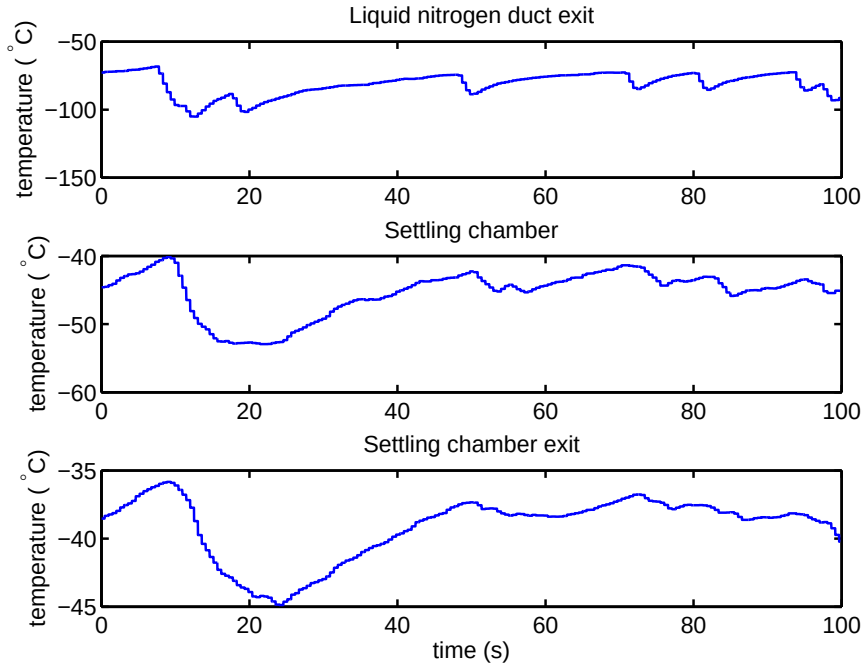

Figure D.9: Test SM9T3HP. Temperatures within the facility upstream of the wind duct. Specimen temperature −9 °C.

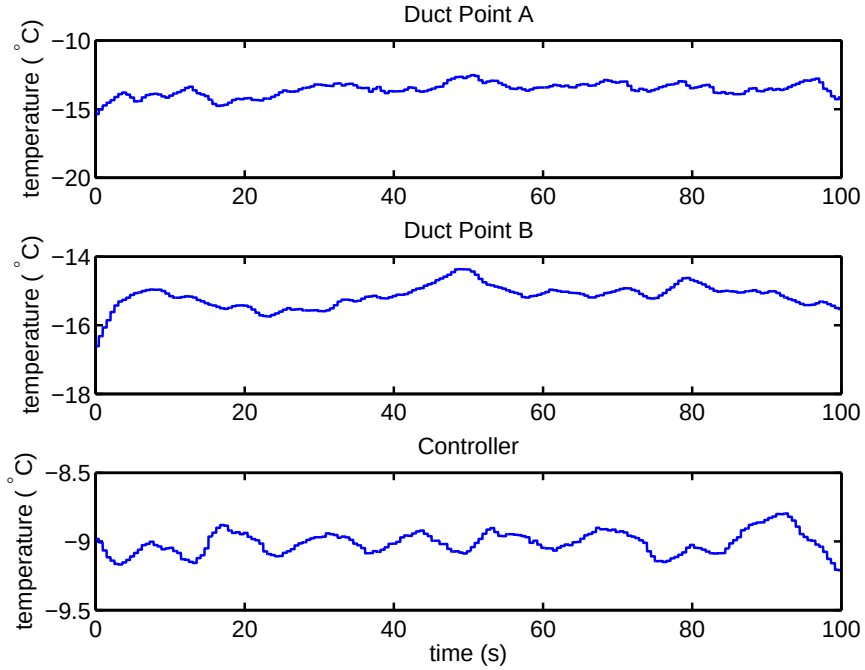

Figure D.10: Test SM9T3HP. Temperatures within the wind tunnel duct for the test specimen temperature of −9 °C

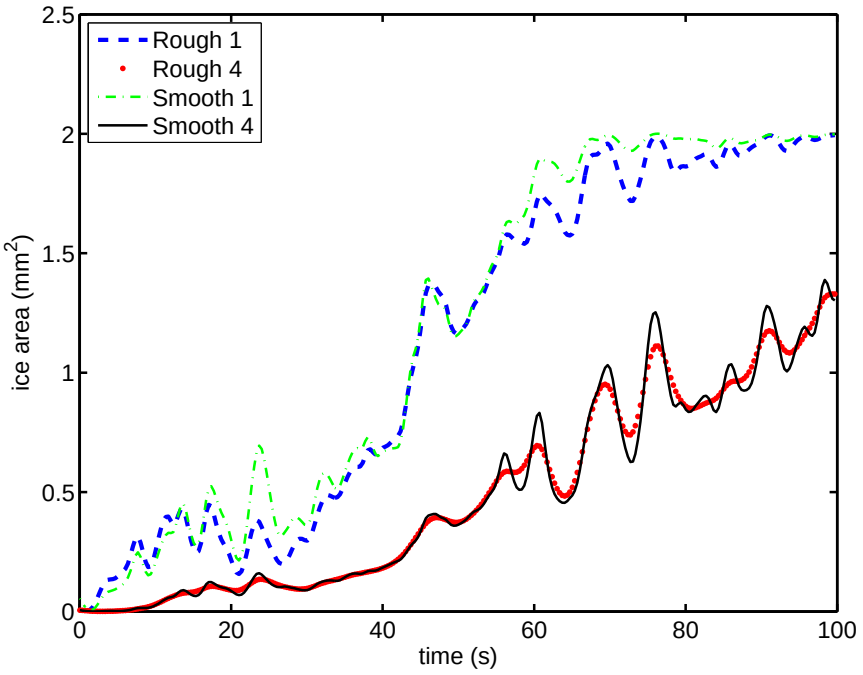

Figure D.11: Test SM9T3HP. Ice accretion area within regions 1 and 4 on the cylindrical specimen at test temperature −9 °C.

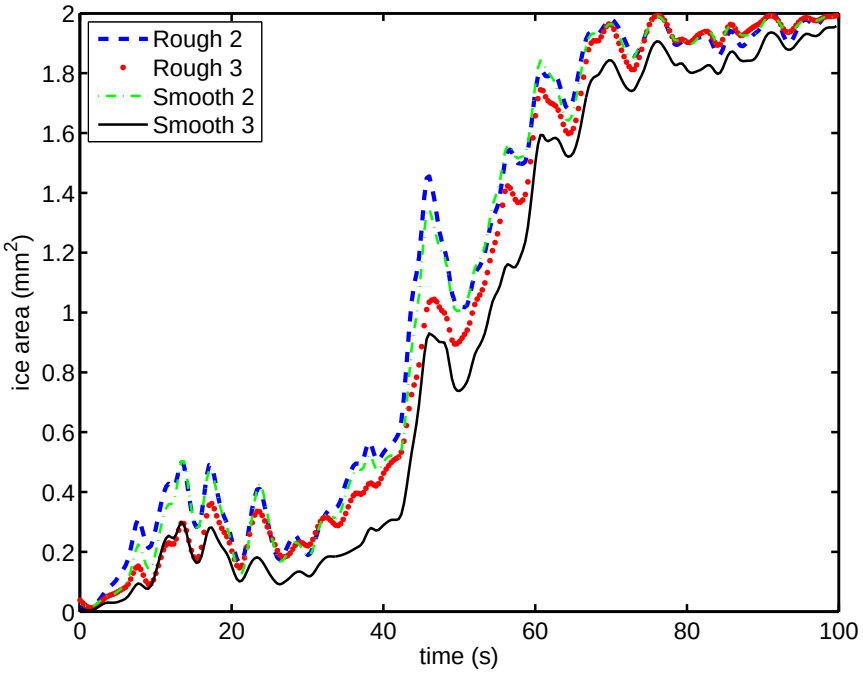

Figure D.12: Test SM9T3HP. Ice accretion area within regions 2 and 3 on the cylindrical specimen at test temperature −9 °C.

D.3 Surface Temperature −5 °C

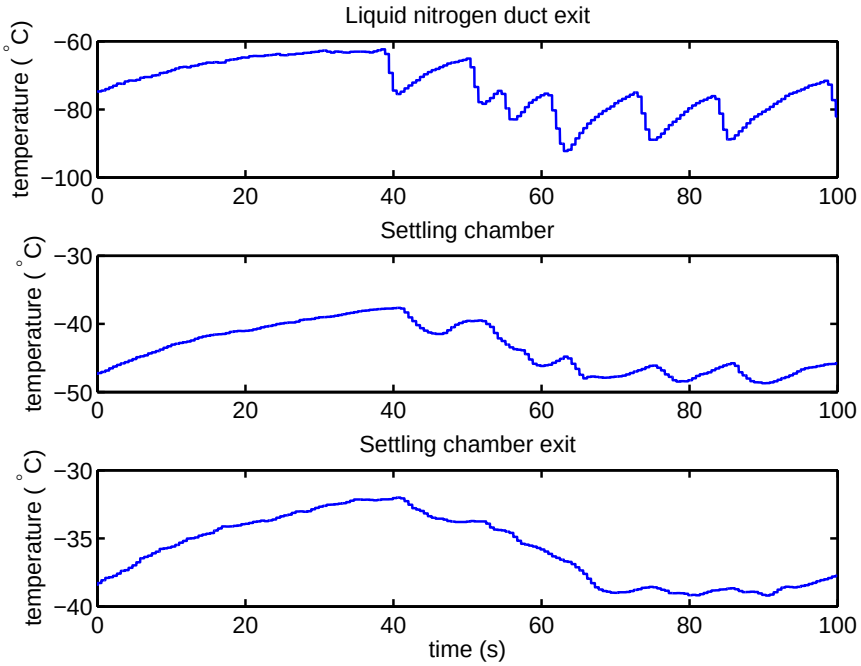

Figure D.13: Test SM5T1HP. Temperatures within the facility upstream of the wind duct. Specimen temperature −5 °C.

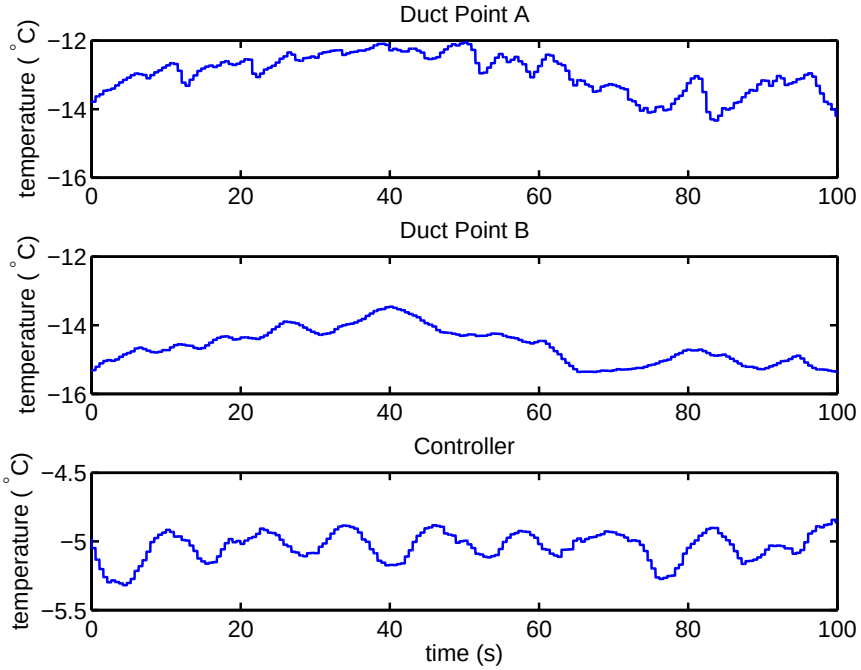

Figure D.14: Test SM5T1HP. Temperatures within the wind tunnel duct for the test specimen temperature of −5 °C.

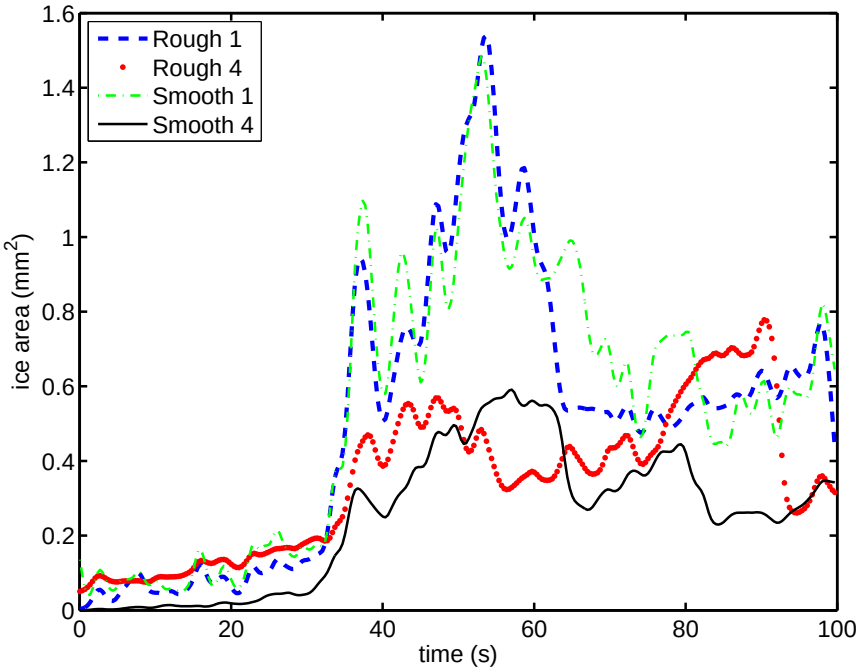

Figure D.15: Test SM5T1HP. Ice accretion area within regions 1 and 4 on the cylindrical specimen at test temperature −5 °C.

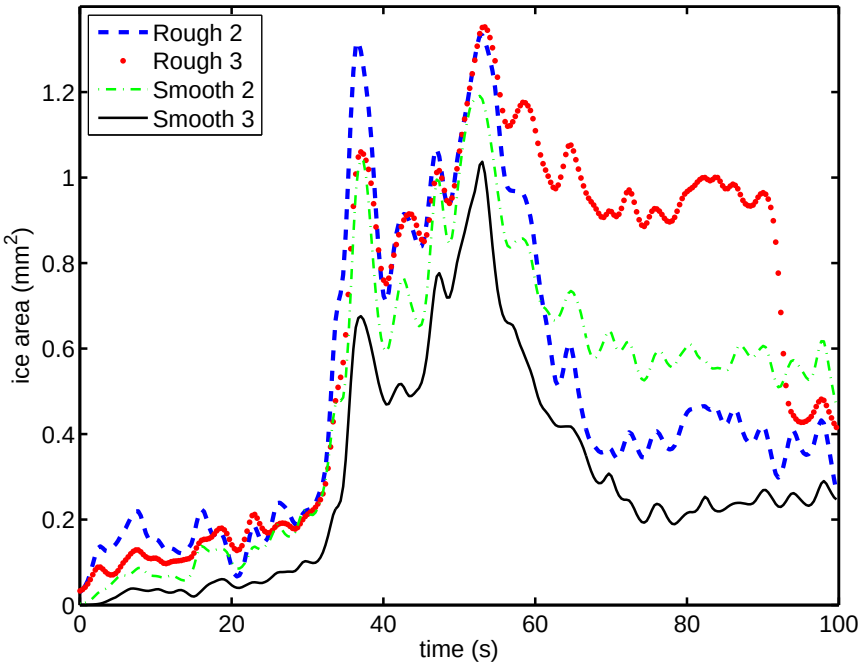

Figure D.16: Test SM5T1HP. Ice accretion area within regions 2 and 3 on the cylindrical specimen at test temperature −5 °C.

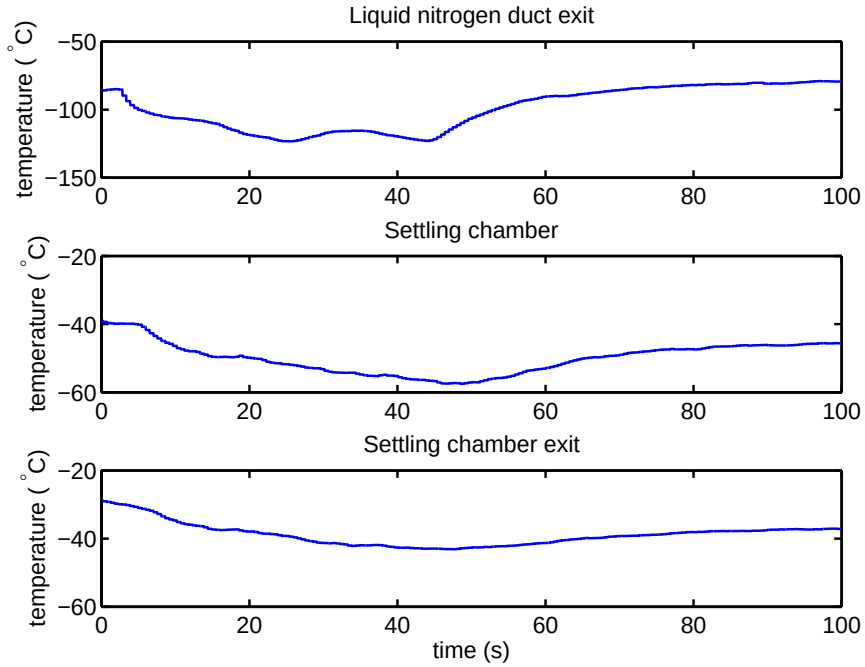

Figure D.17: Test SM5T2HP. Temperatures within the facility upstream of the wind duct. Specimen temperature −5 °C.

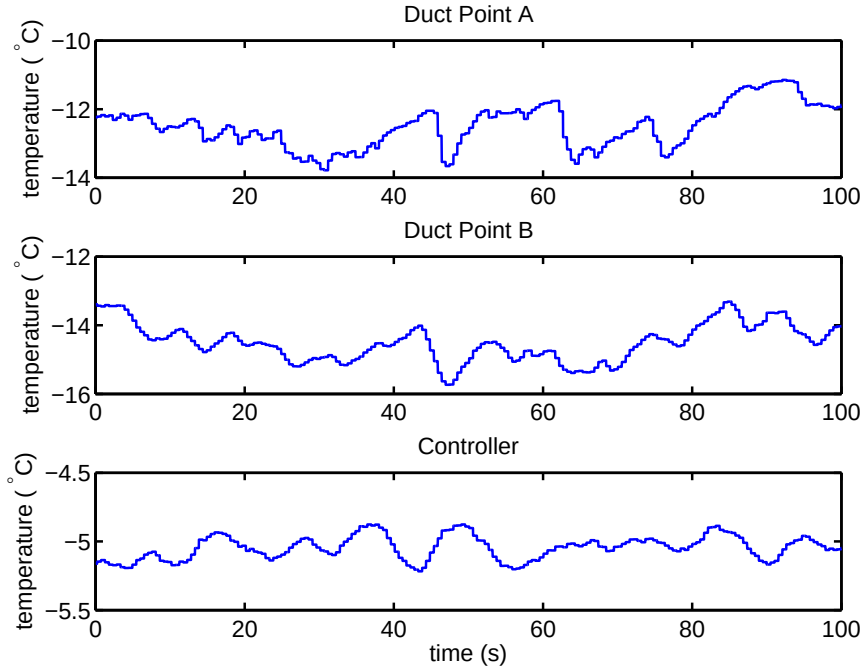

Figure D.18: Test SM5T2HP. Temperatures within the wind tunnel duct for the test specimen temperature of −5 °C.

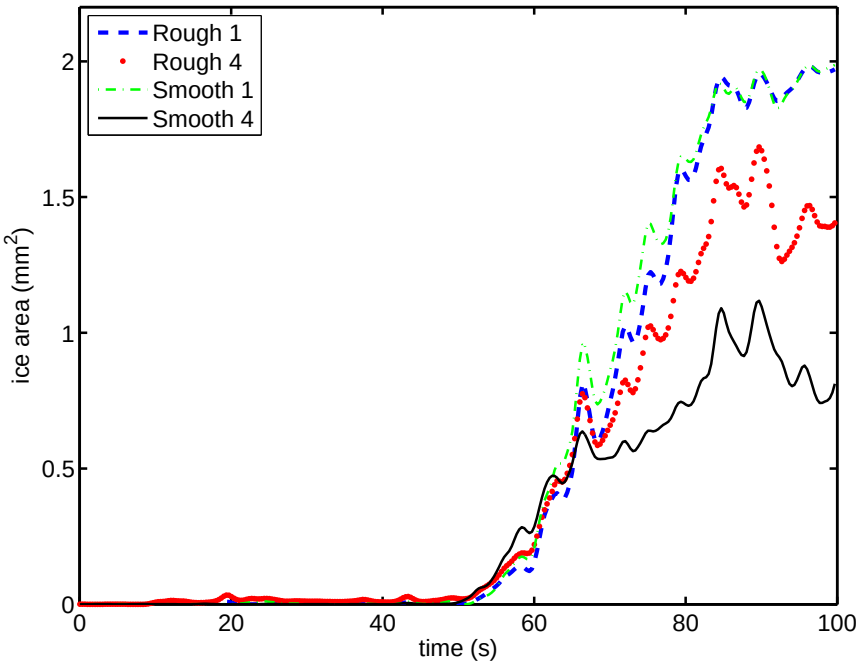

Figure D.19: Test SM5T2HP. Ice accretion area within regions 1 and 4 on the cylindrical specimen at test temperature −5 °C.

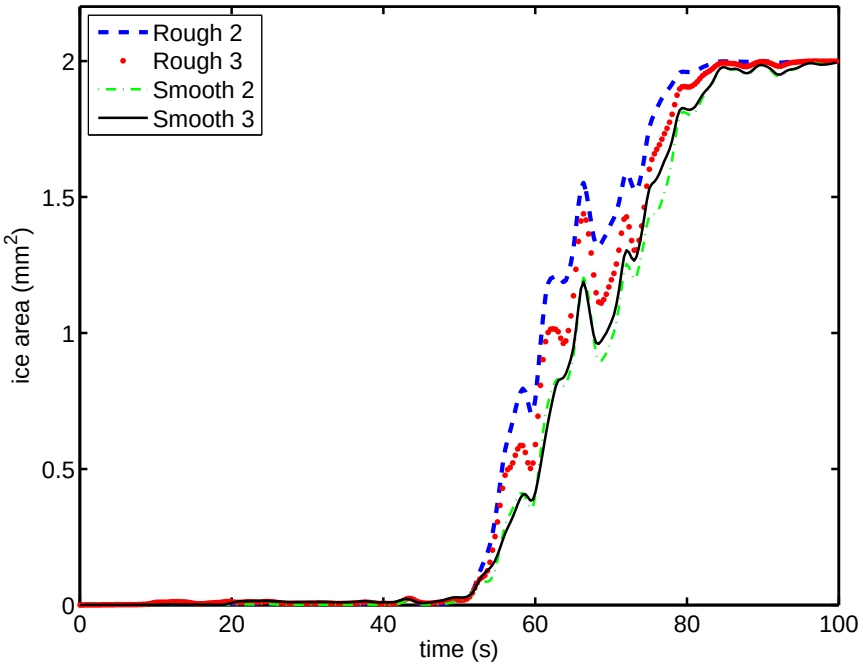

Figure D.20: Test SM5T2HP. Ice accretion area within regions 2 and 3 on the cylindrical specimen at test temperature −5 °C.

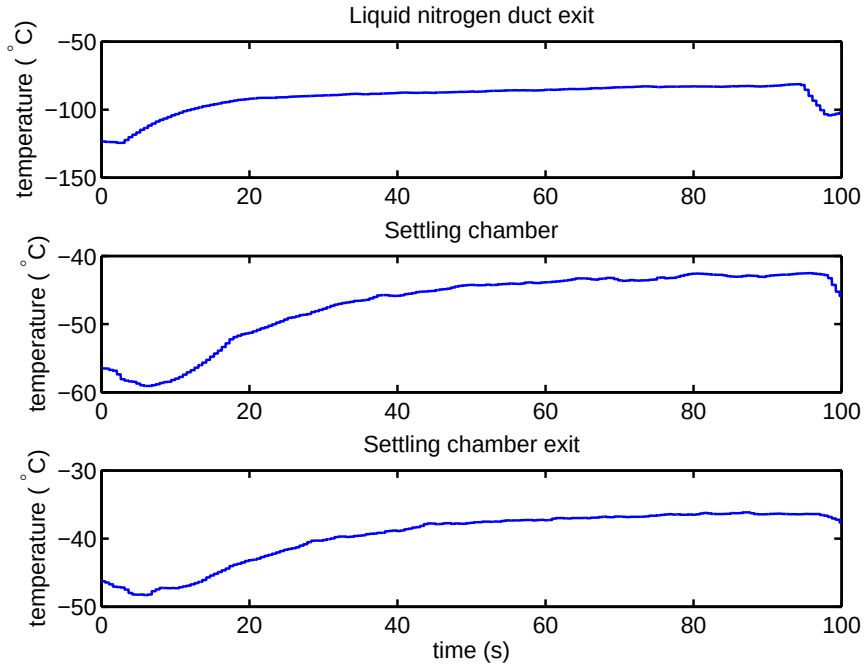

Figure D.21: Test SM5T3HP. Temperatures within the facility upstream of the wind duct. Specimen temperature −5 °C.

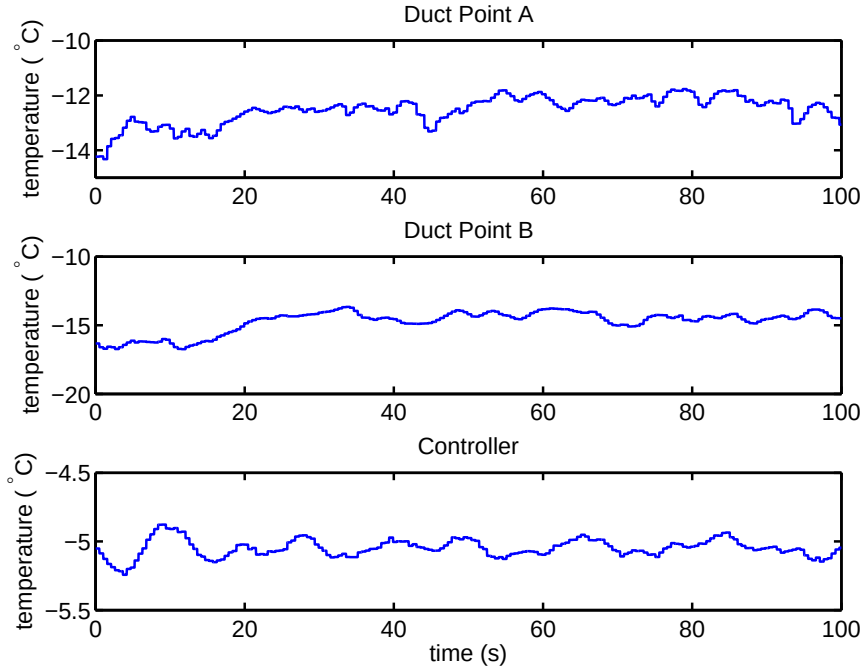

Figure D.22: Test SM5T3HP. Temperatures within the wind tunnel duct for the test specimen temperature of −5 °C.

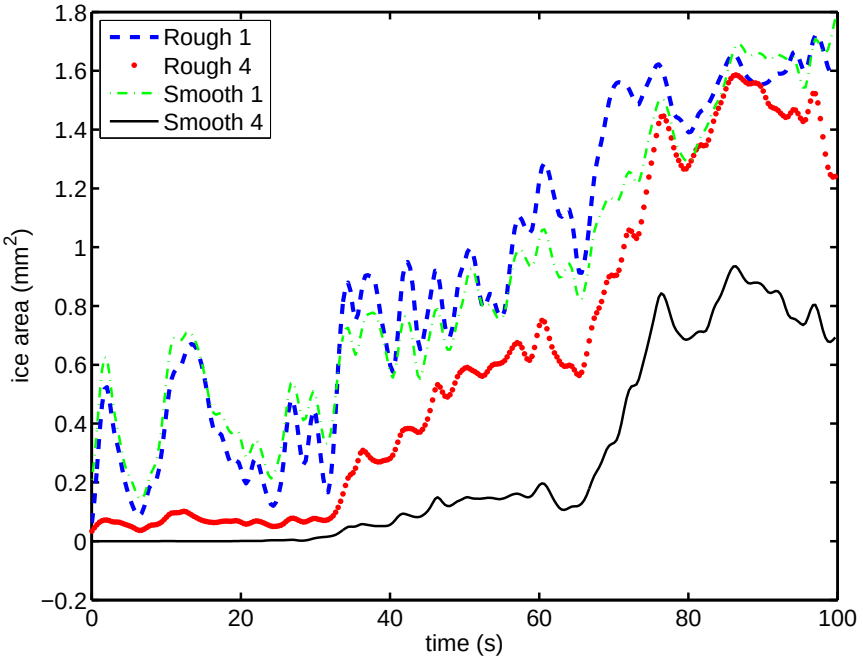

Figure D.23: Test SM5T3HP. Ice accretion area within regions 1 and 4 on the cylindrical specimen at test temperature −5 °C.

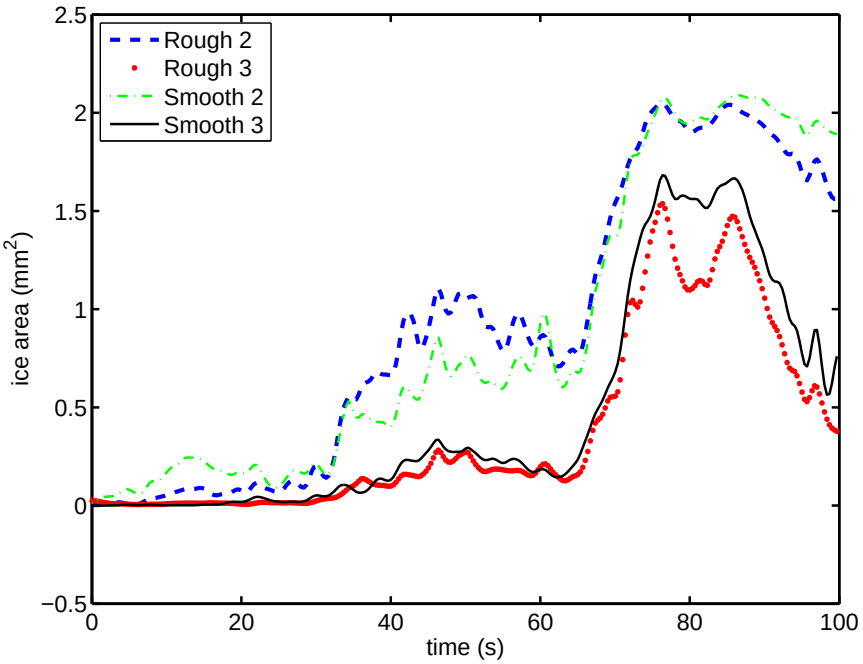

Figure D.24: Test SM5T3HP. Ice accretion area within regions 2 and 3 on the cylindrical specimen at test temperature −5 °C.

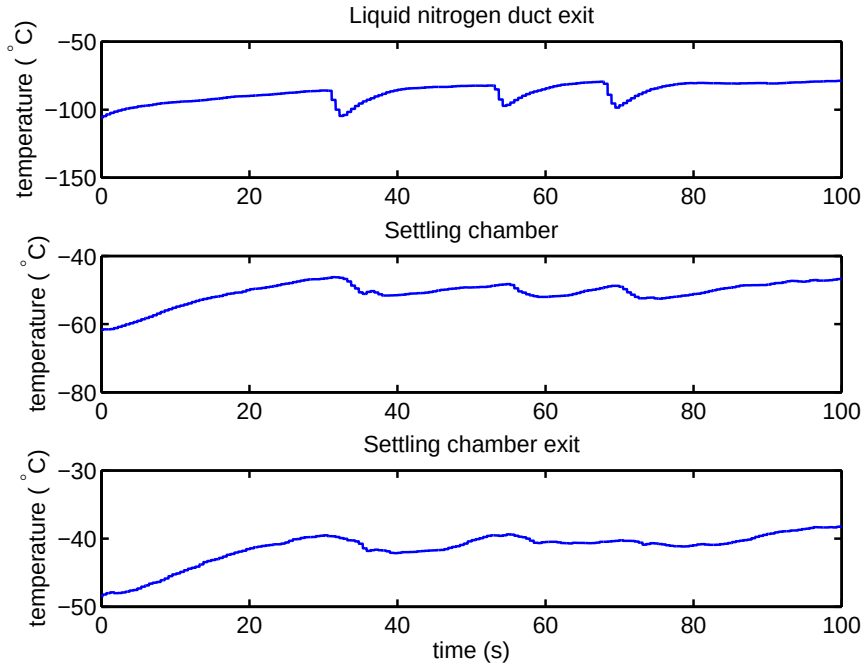

Figure D.25: Test SM5T4HP. Temperatures within the facility upstream of the wind duct. Specimen temperature −5 °C.

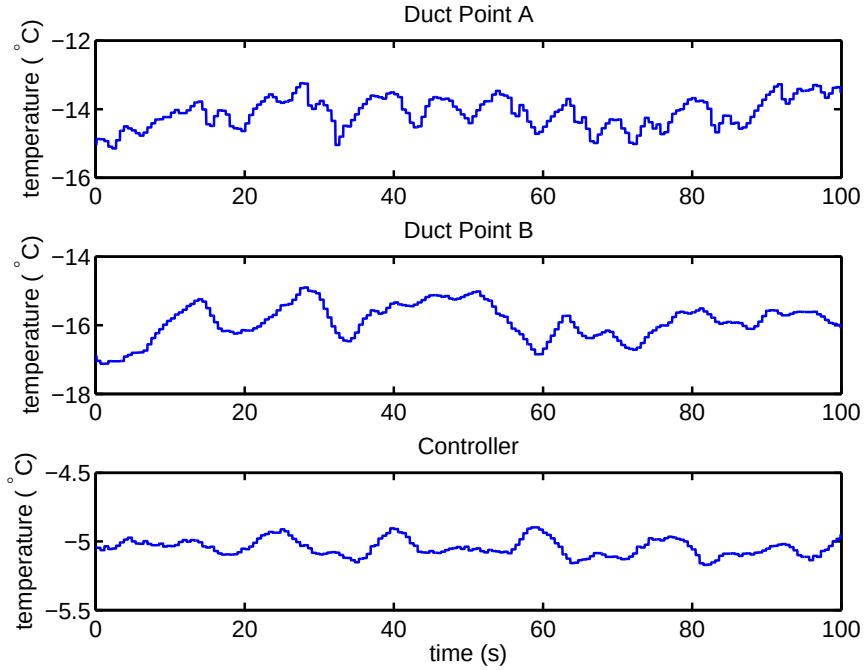

Figure D.26: Test SM5T4HP. Temperatures within the wind tunnel duct for the test specimen temperature of −5 °C.

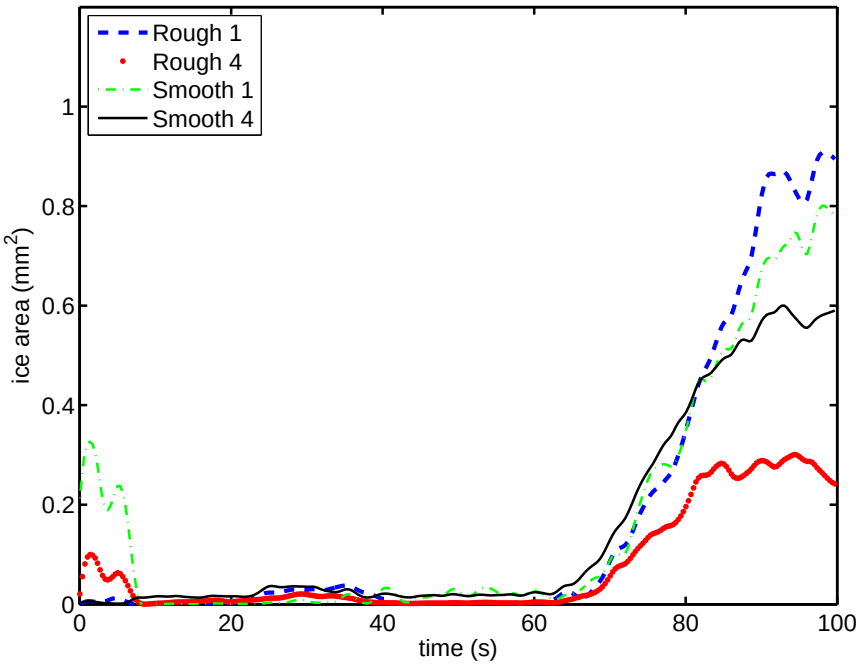

Figure D.27: Test SM5T4HP. Ice accretion area within regions 1 and 4 on the cylindrical specimen at test temperature −5 °C.

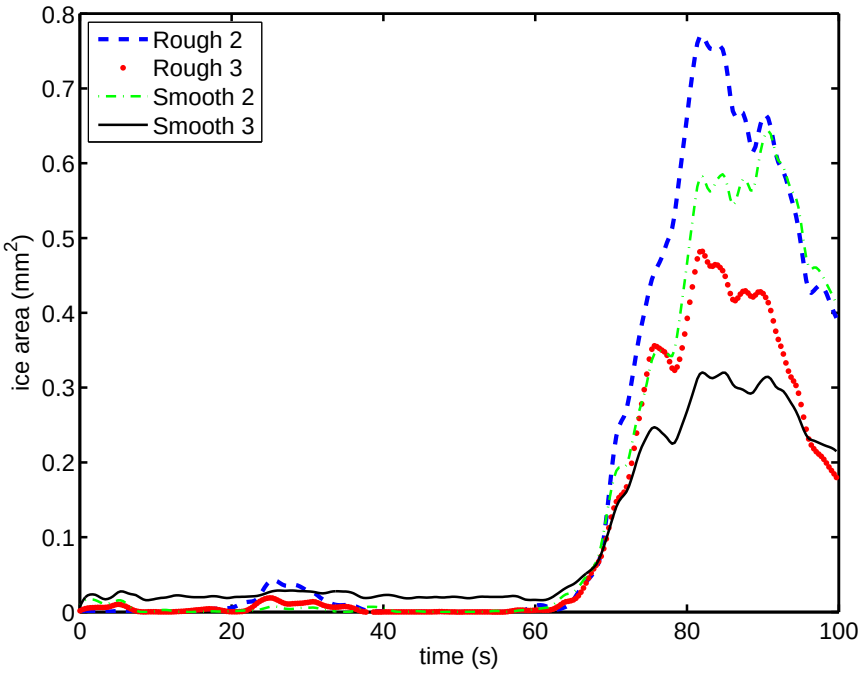

Figure D.28: Test SM5T4HP. Ice accretion area within regions 2 and 3 on the cylindrical specimen at test temperature −5 °C.

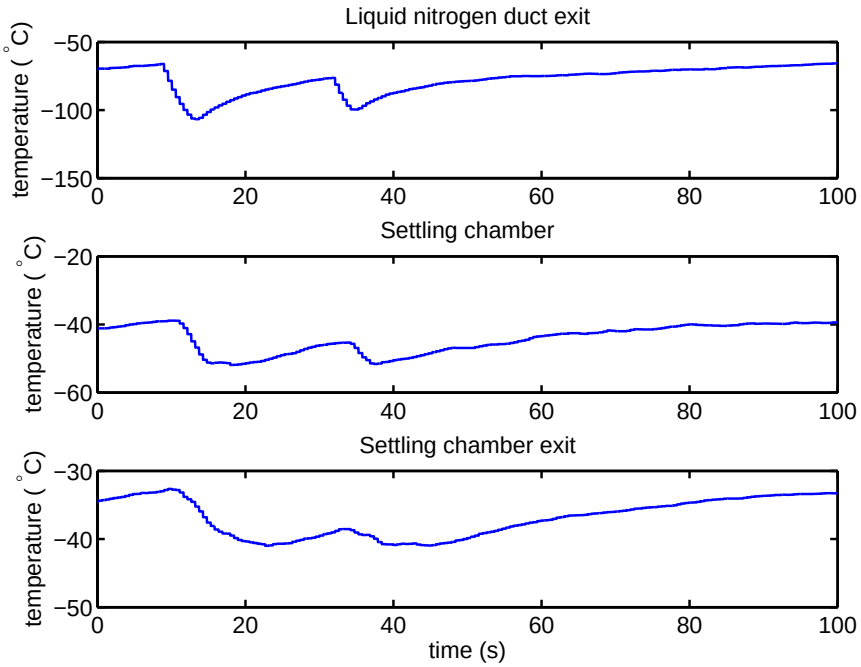

Figure D.29: Test SM5T5LP. Temperatures within the facility upstream of the wind duct. Specimen temperature −5 °C.

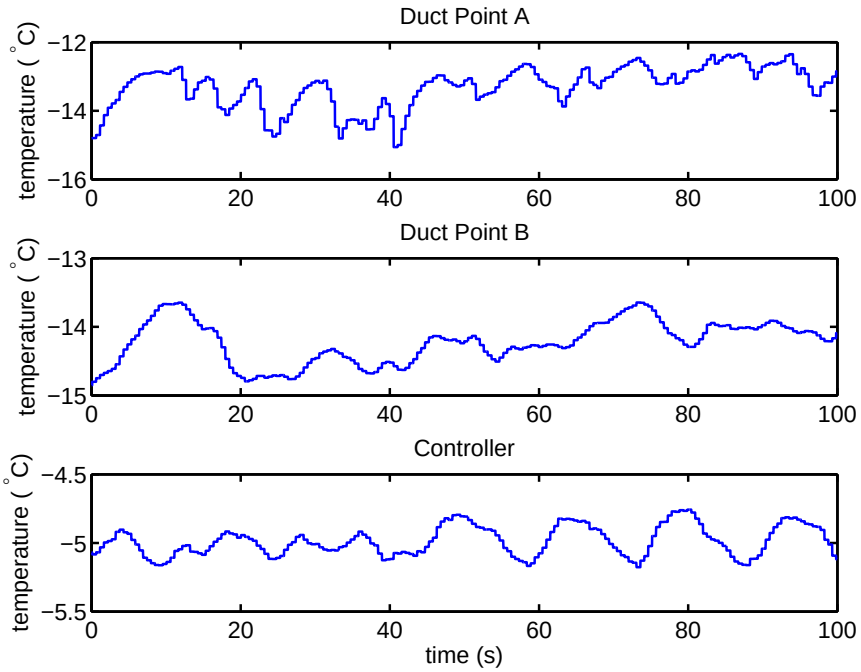

Figure D.30: Test SM5T5LP. Temperatures within the wind tunnel duct for the test specimen temperature of −5 °C.

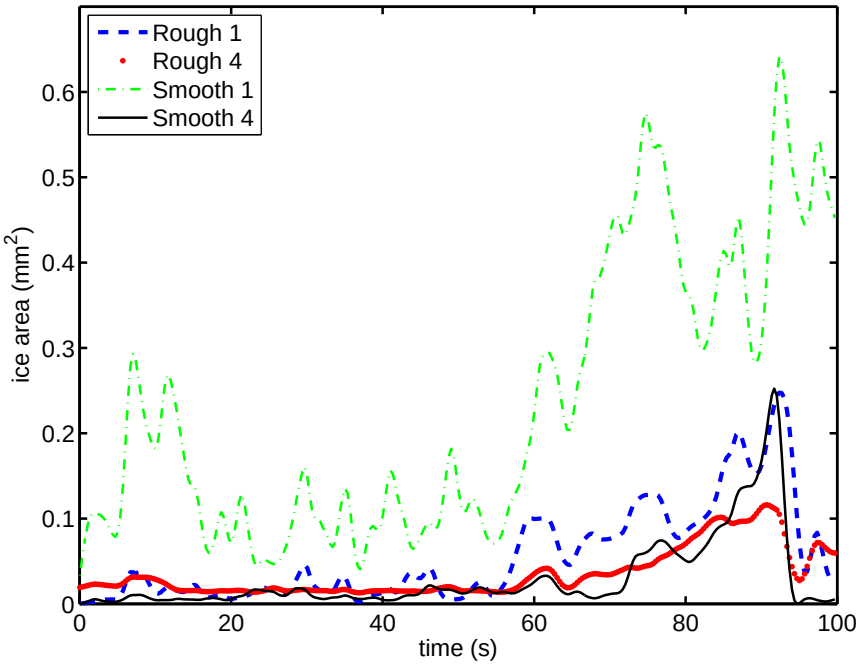

Figure D.31: Test SM5T5LP. Ice accretion area within regions 1 and 4 on the cylindrical specimen at test temperature −5 °C and at lower IWC.

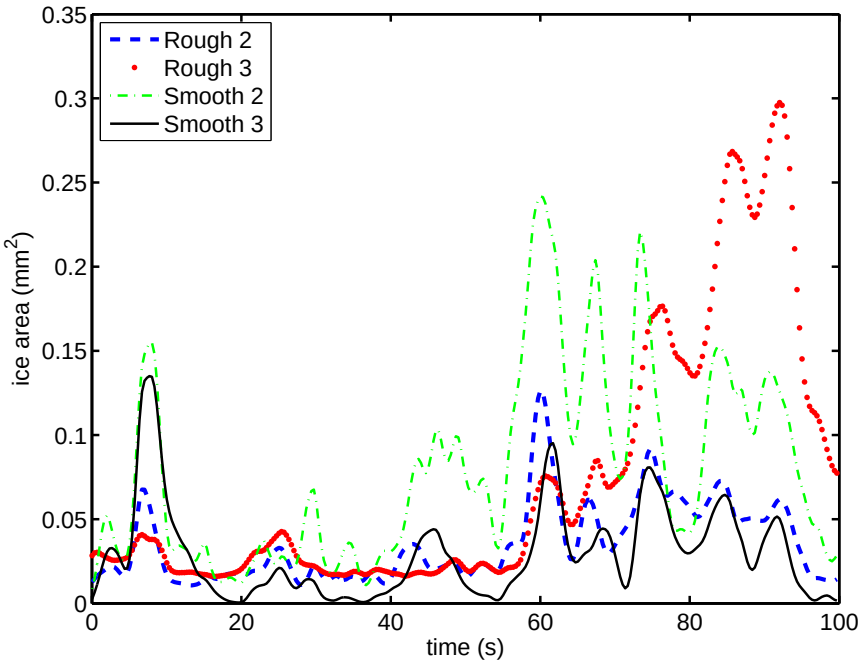

Figure D.32: Test SM5T5LP. Ice accretion area within regions 2 and 3 on the cylindrical specimen at test temperature −5 °C and at lower IWC.

D.4 Surface Temperature 0 °C

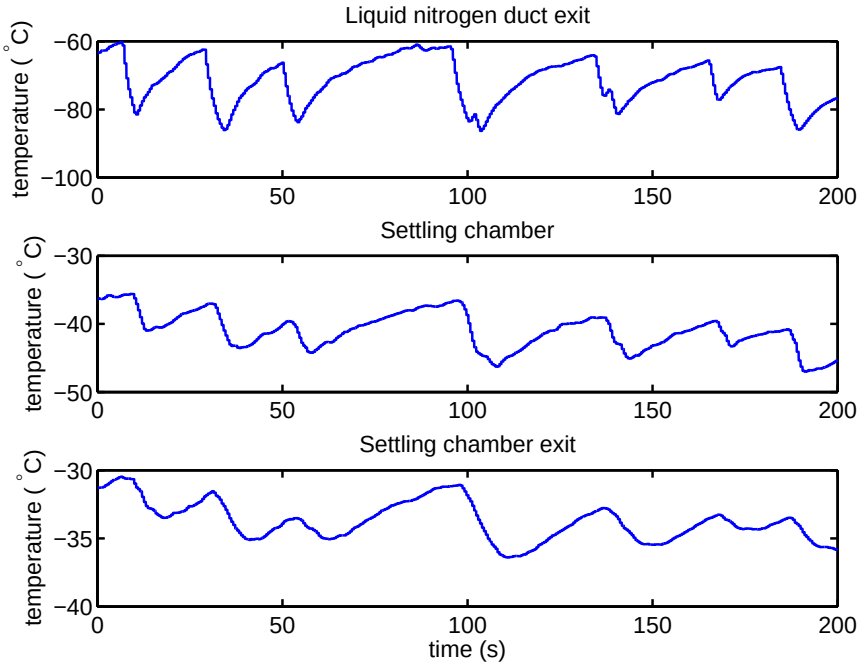

Figure D.33: Test S0T1HP. Temperatures within the facility upstream of the wind duct. Specimen temperature 0 °C.

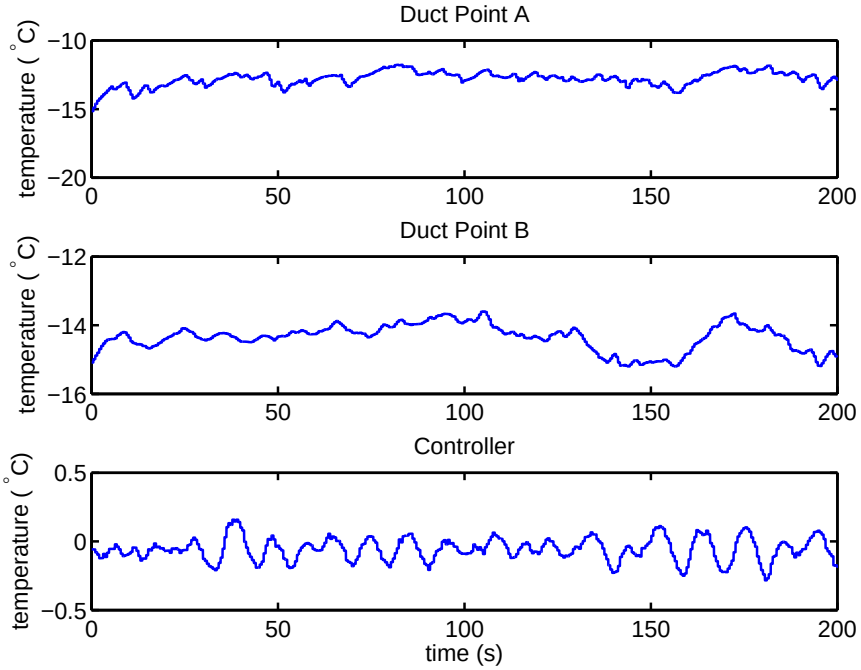

Figure D.34: Test S0T1HP. Temperatures within the wind tunnel duct for the test specimen temperature of 0 °C.

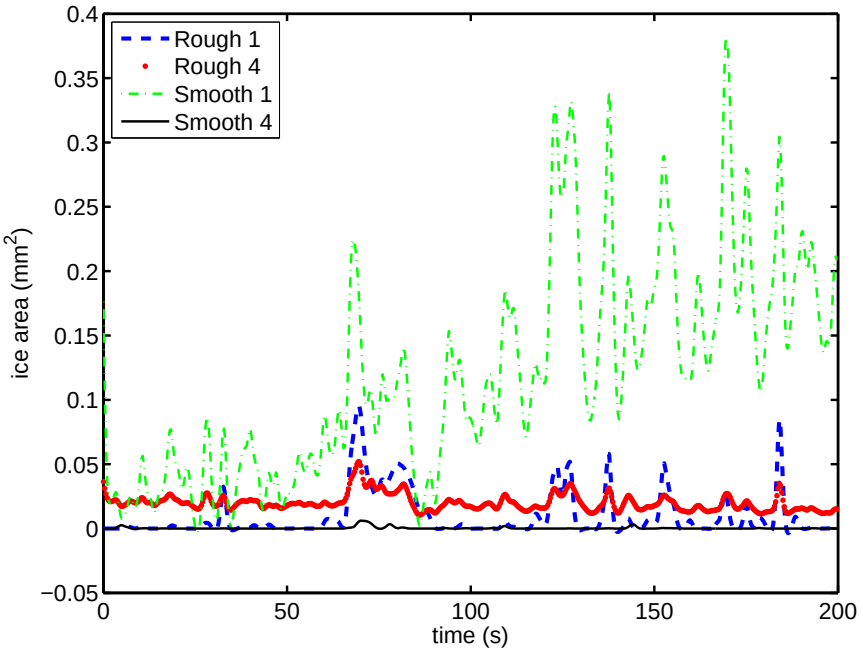

Figure D.35: Test S0T1HP. Ice accretion area within regions 1 and 4 on the cylindrical specimen at test temperature 0 °C.

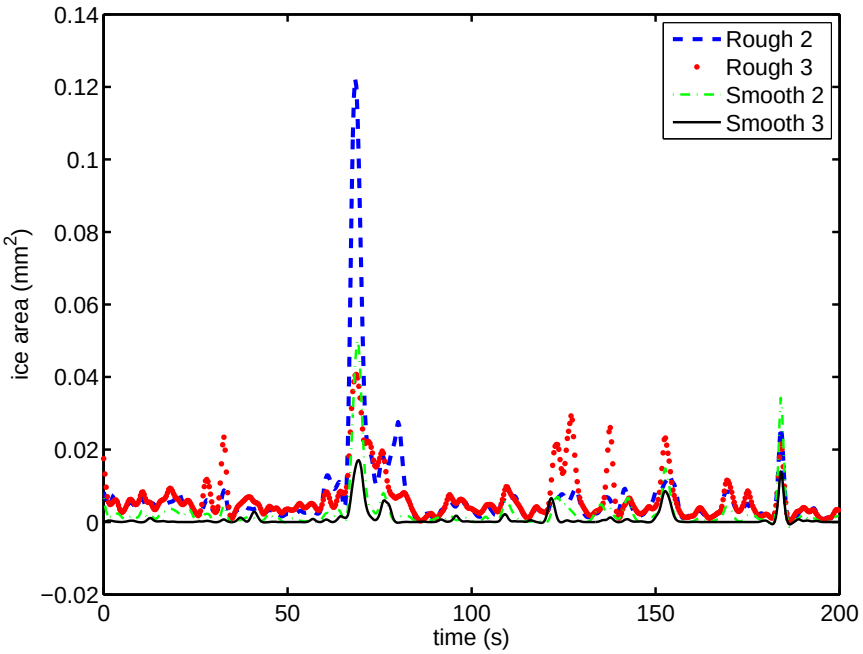

Figure D.36: Test S0T1HP. Ice accretion area within regions 2 and 3 on the cylindrical specimen at test temperature 0 °C.

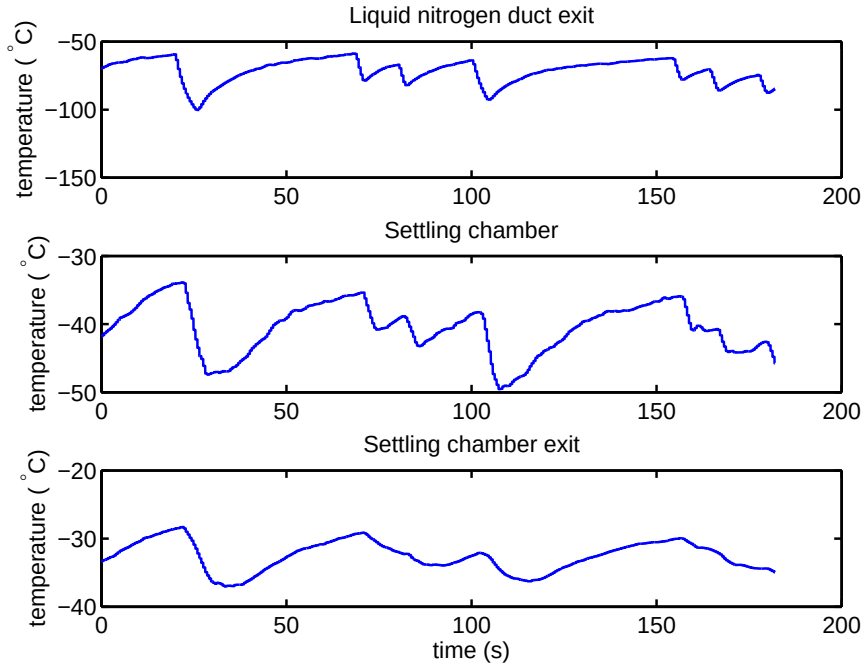

Figure D.37: Test S0T2HP. Temperatures within the facility upstream of the wind duct. Specimen temperature 0 °C.

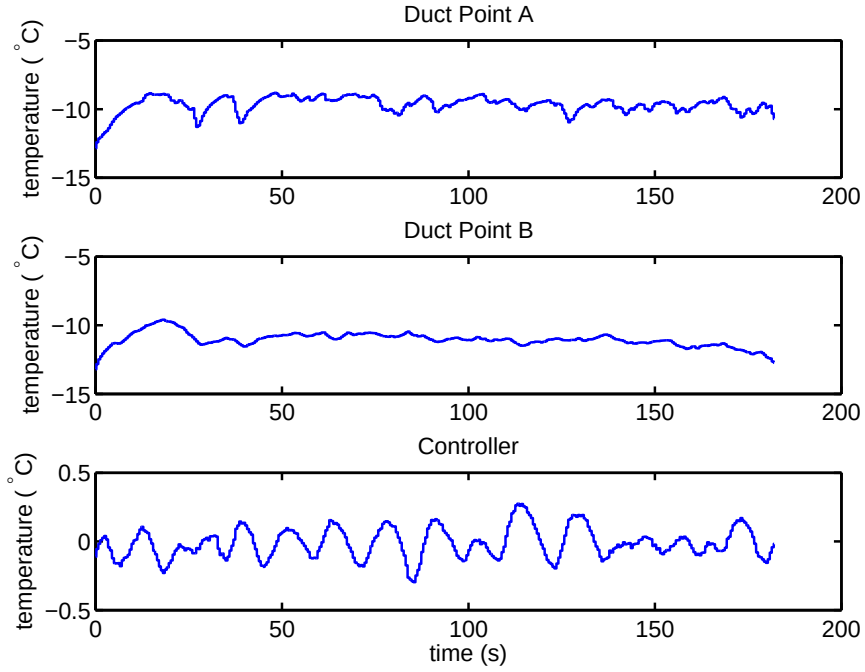

Figure D.38: Test S0T2HP. Temperatures within the wind tunnel duct for the test specimen temperature of 0 °C.

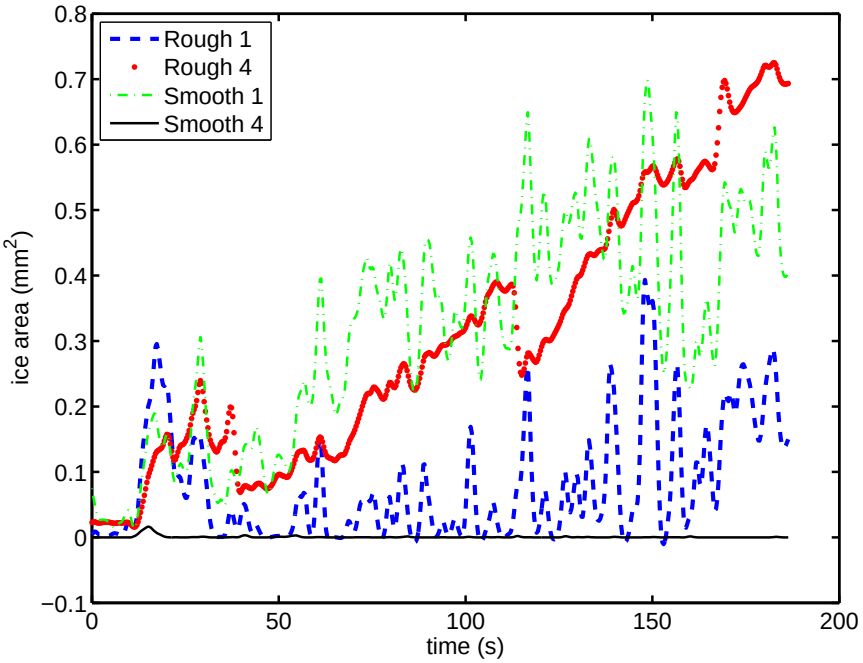

Figure D.39: Test S0T2HP. Ice accretion area within regions 1 and 4 on the cylindrical specimen at test temperature 0 °C.

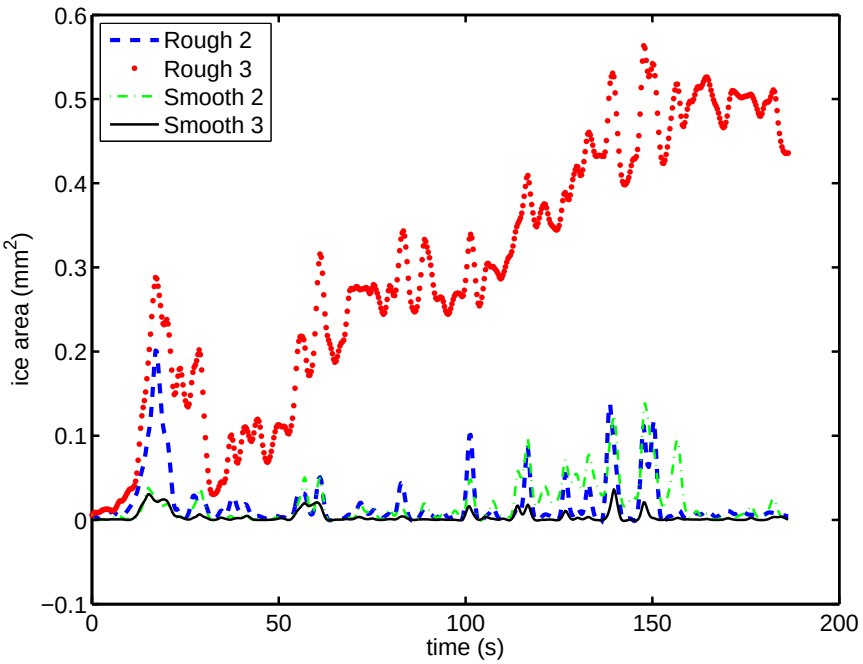

Figure D.40: Test S0T2HP. Ice accretion area within regions 2 and 3 on the cylindrical specimen at test temperature 0 °C.

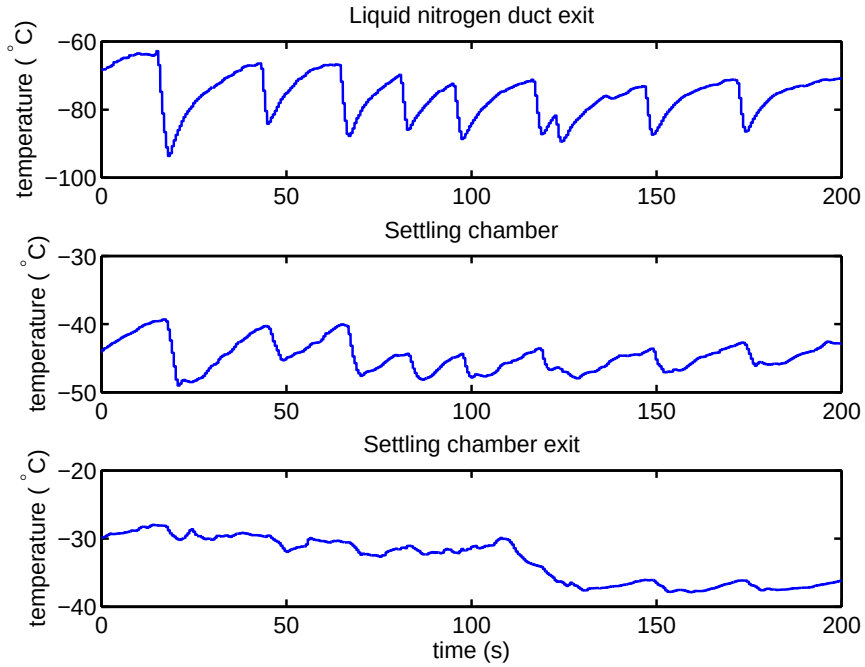

Figure D.41: Test S0T3HP. Temperatures within the facility upstream of the wind duct. Specimen temperature 0 °C.

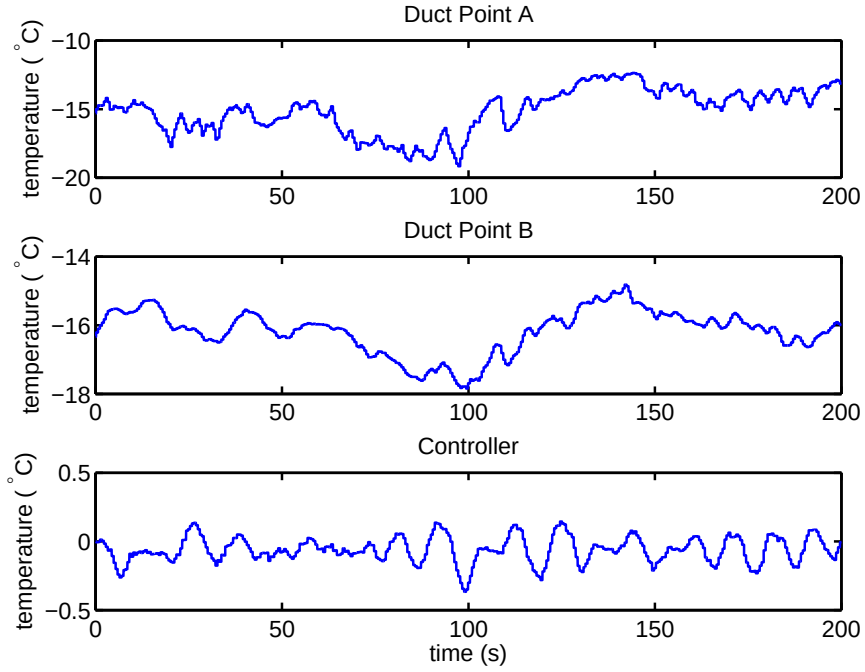

Figure D.42: Test S0T3HP. Temperatures within the wind tunnel duct for the test specimen temperature of 0 °C.

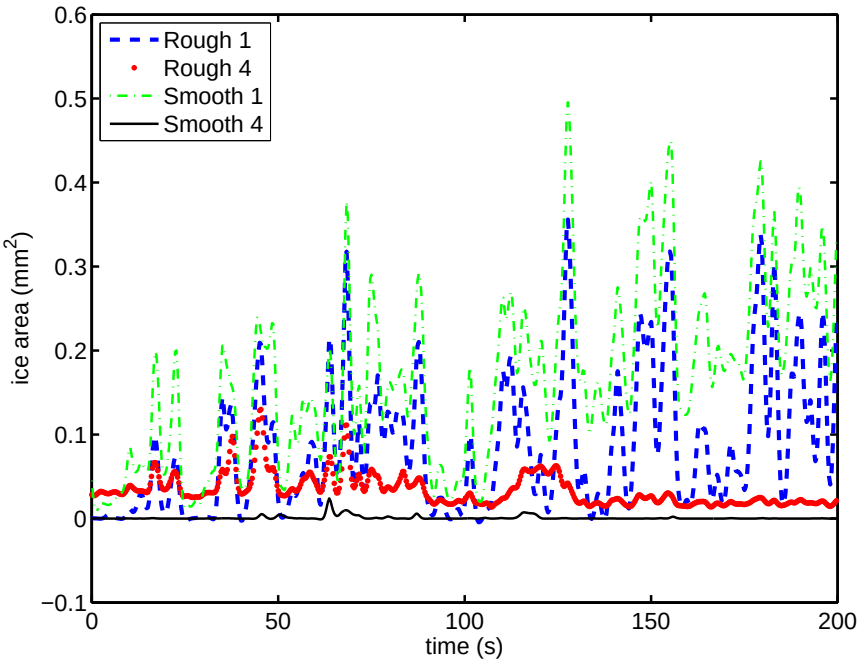

Figure D.43: Test S0T3HP. Ice accretion area within regions 1 and 4 on the cylindrical specimen at test temperature 0 °C.

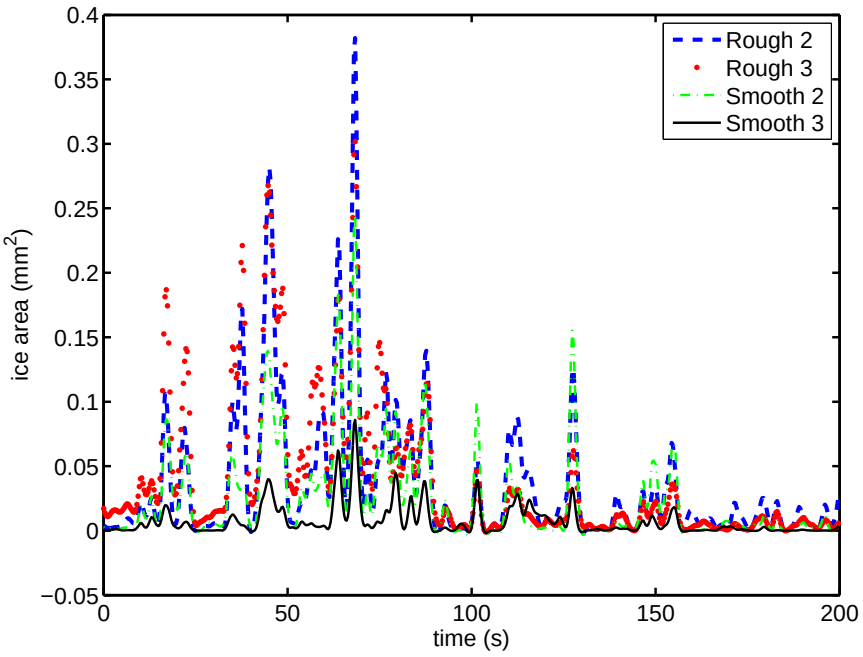

Figure D.44: Test S0T3HP. Ice accretion area within regions 2 and 3 on the cylindrical specimen at test temperature 0 °C.

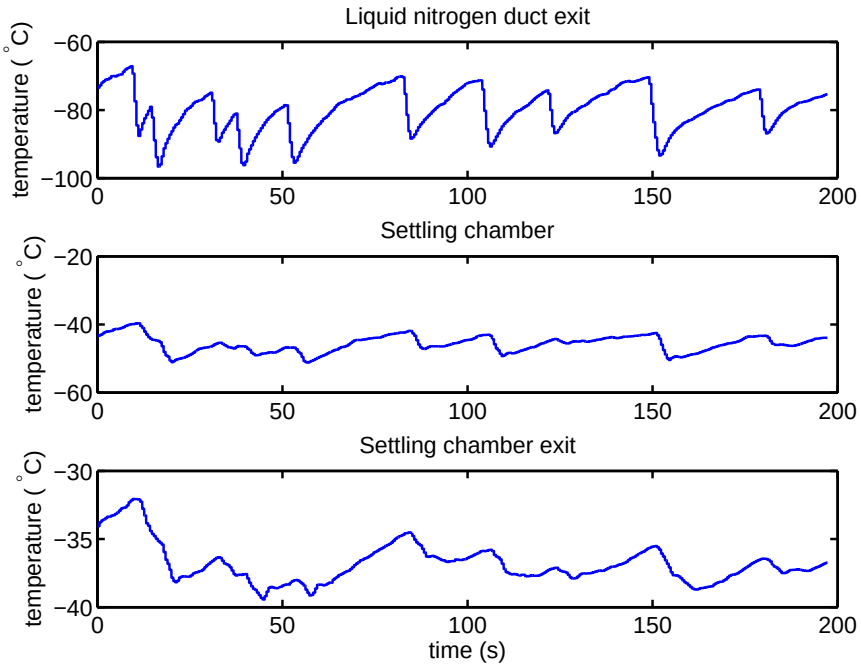

Figure D.45: Test S0T4HP. Temperatures within the facility upstream of the wind duct. Specimen temperature 0 °C.

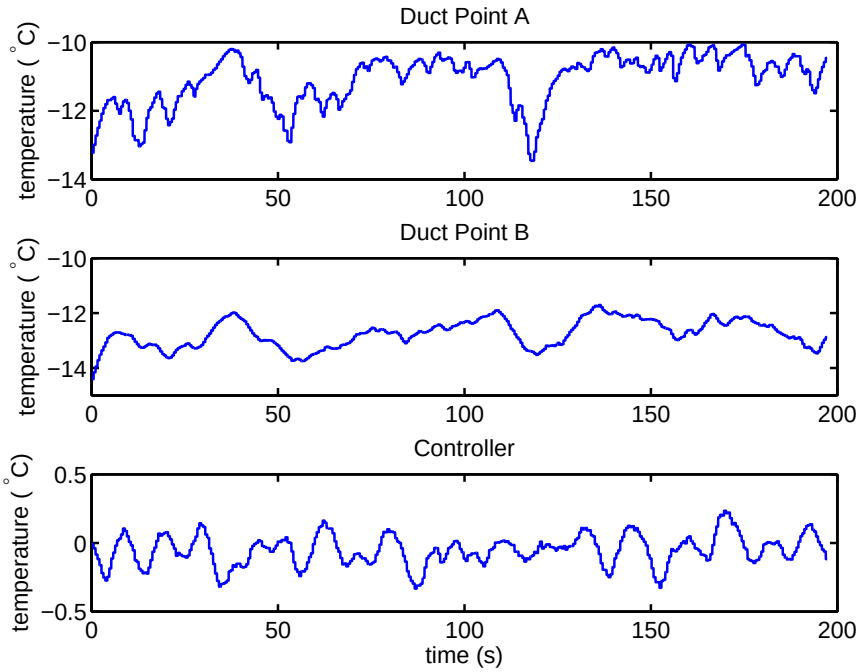

Figure D.46: Test S0T4HP. Temperatures within the wind tunnel duct for the test specimen temperature of 0 °C.

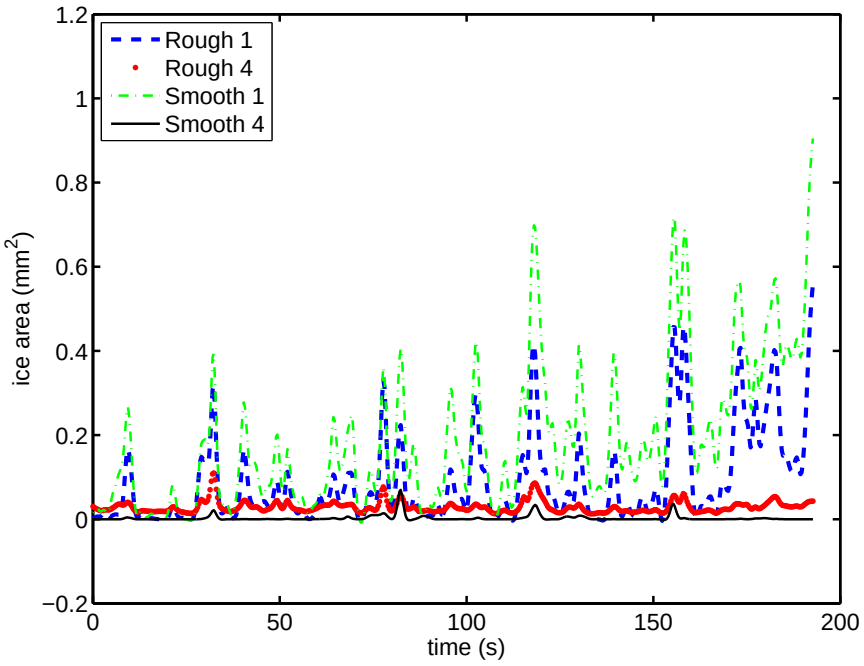

Figure D.47: Test S0T4HP. Ice accretion area within regions 1 and 4 on the cylindrical specimen at test temperature 0 °C.

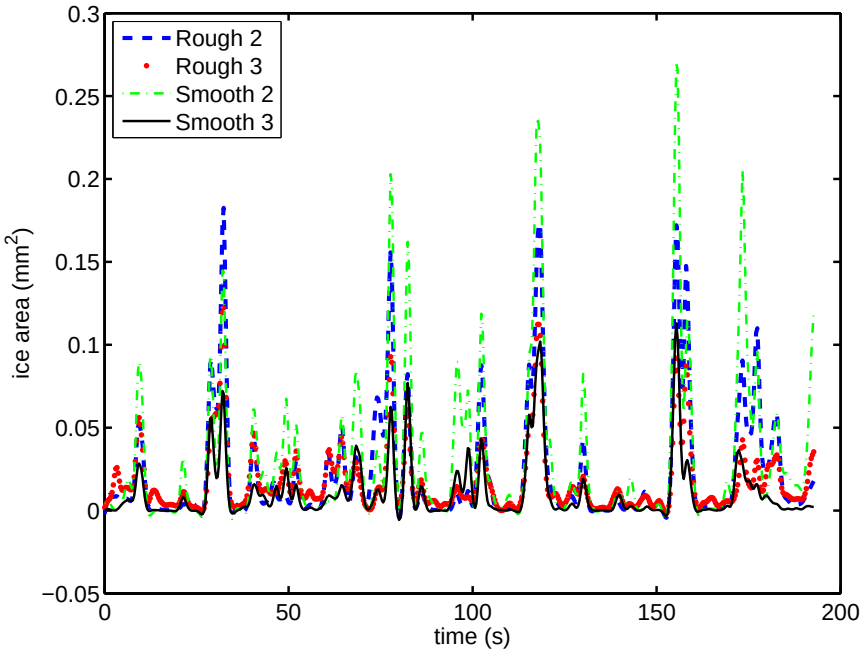

Figure D.48: Test S0T4HP. Ice accretion area within regions 2 and 3 on the cylindrical specimen at test temperature 0 °C.

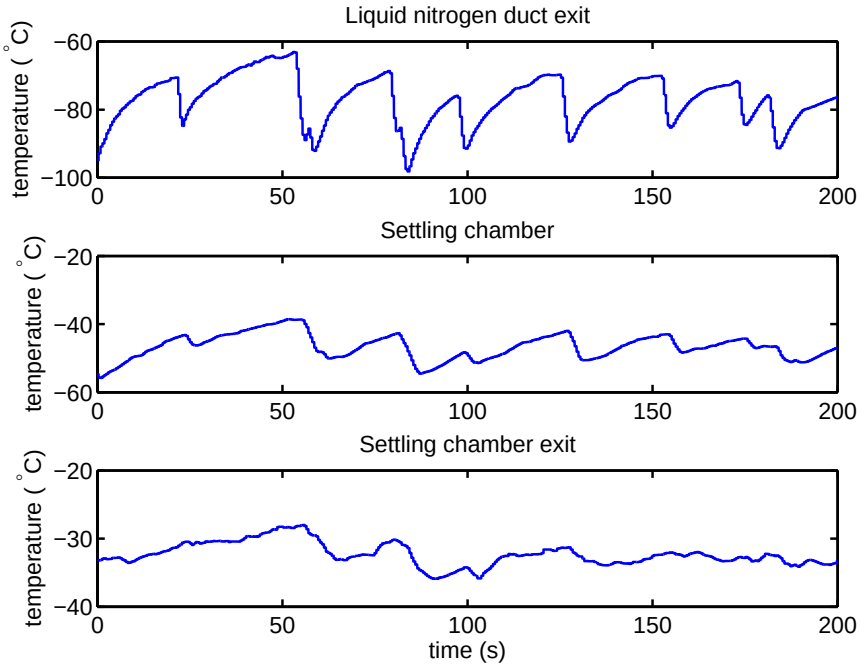

Figure D.49: Test S0T5HP. Temperatures within the facility upstream of the wind duct. Specimen temperature 0 °C.

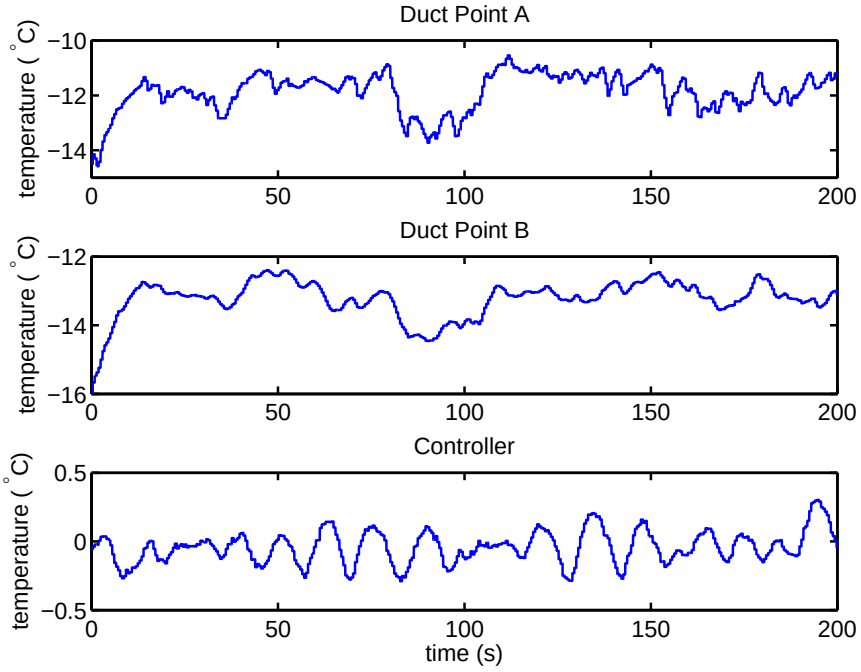

Figure D.50: Test S0T5HP. Temperatures within the wind tunnel duct for the test specimen temperature of 0 °C.

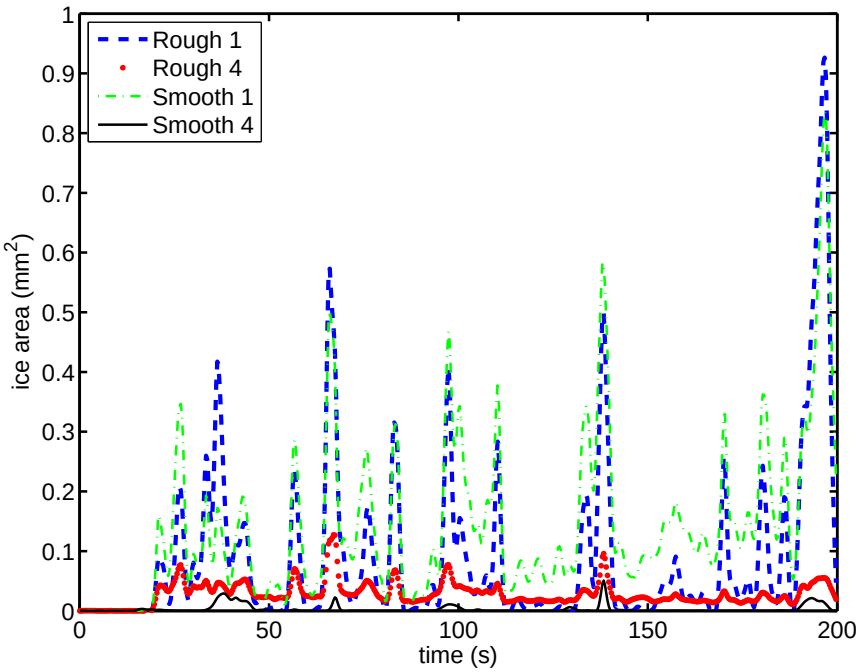

Figure D.51: Test S0T5HP. Ice accretion area within regions 1 and 4 on the cylindrical specimen at test temperature 0 °C.

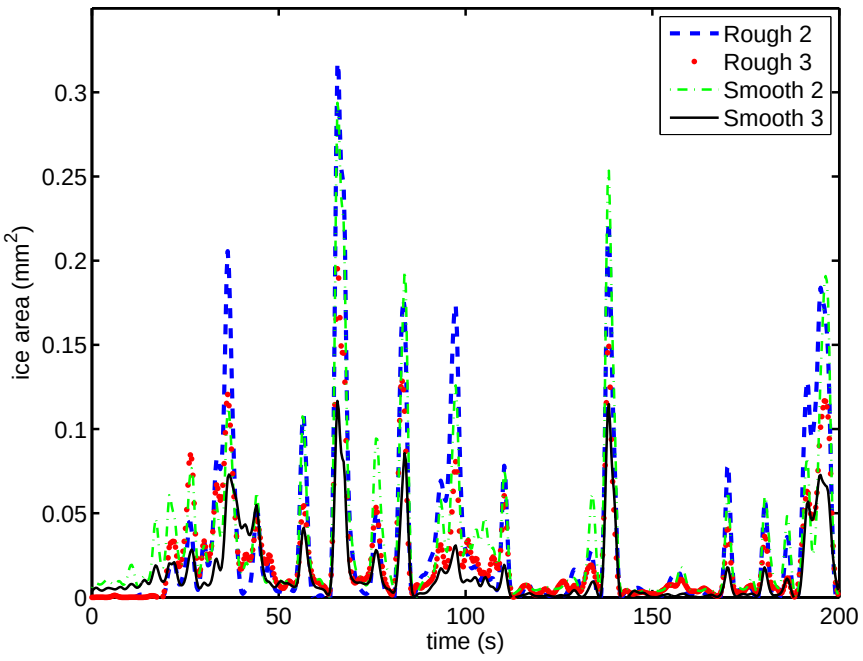

Figure D.52: Test S0T5HP. Ice accretion area within regions 2 and 3 on the cylindrical specimen at test temperature 0 °C.

D.5 Surface Temperature 5 °C

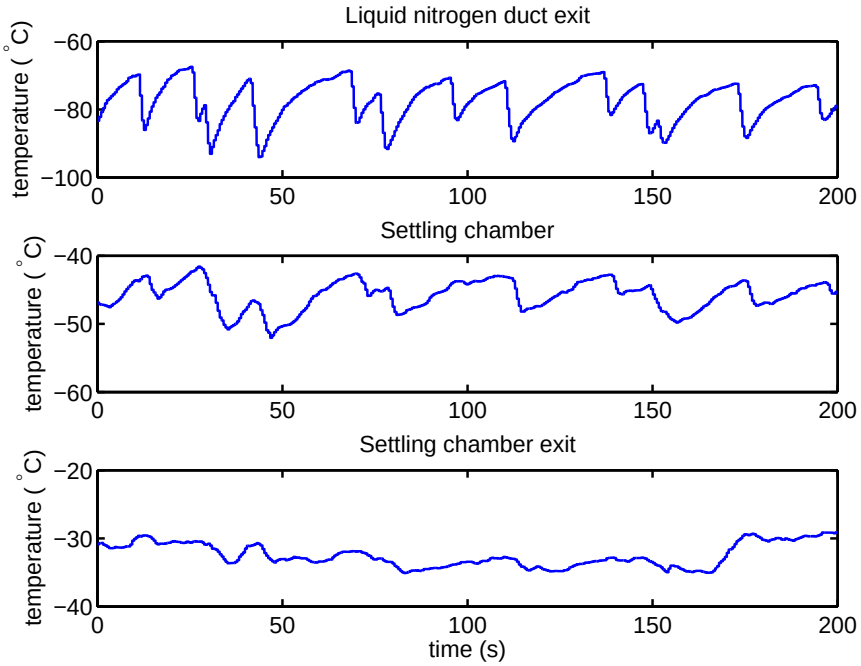

Figure D.53: Test SP5T1HP. Temperatures within the facility upstream of the wind duct. Specimen temperature 5 °C.

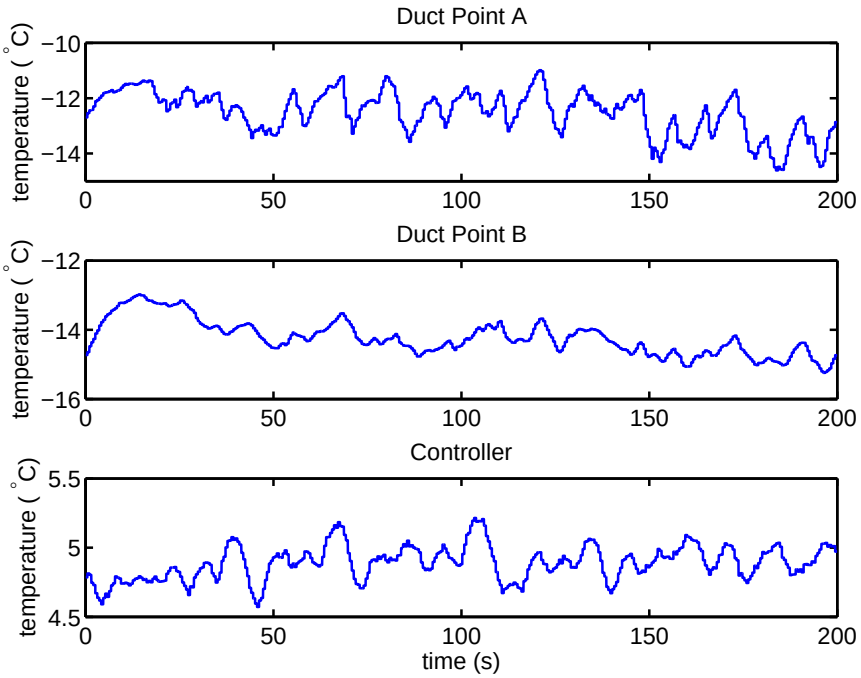

Figure D.54: Test SP5T1HP. Temperatures within the wind tunnel duct for the test specimen temperature of 5 °C.

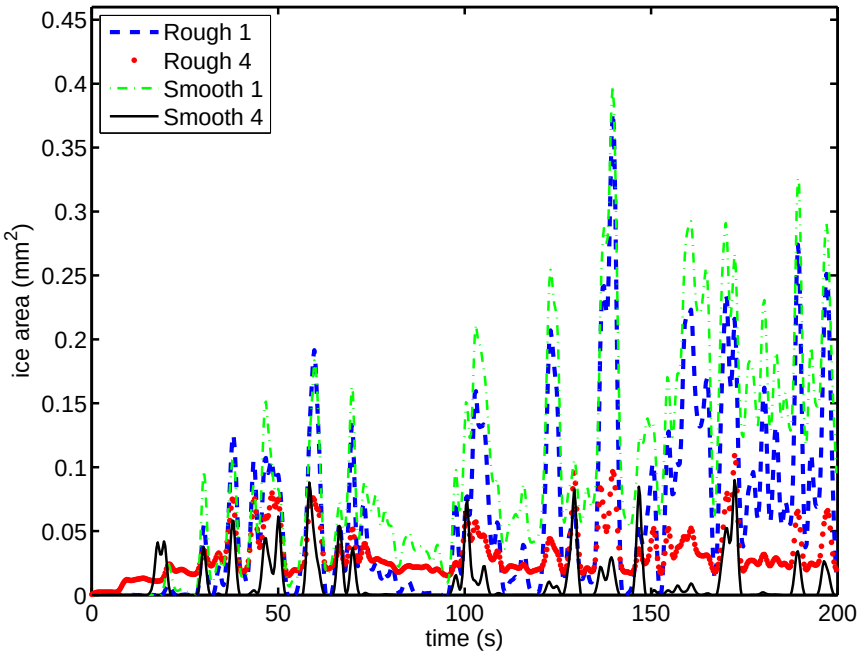

Figure D.55: Test SP5T1HP. Ice accretion area within regions 1 and 4 on the cylindrical specimen at test temperature 5 °C.

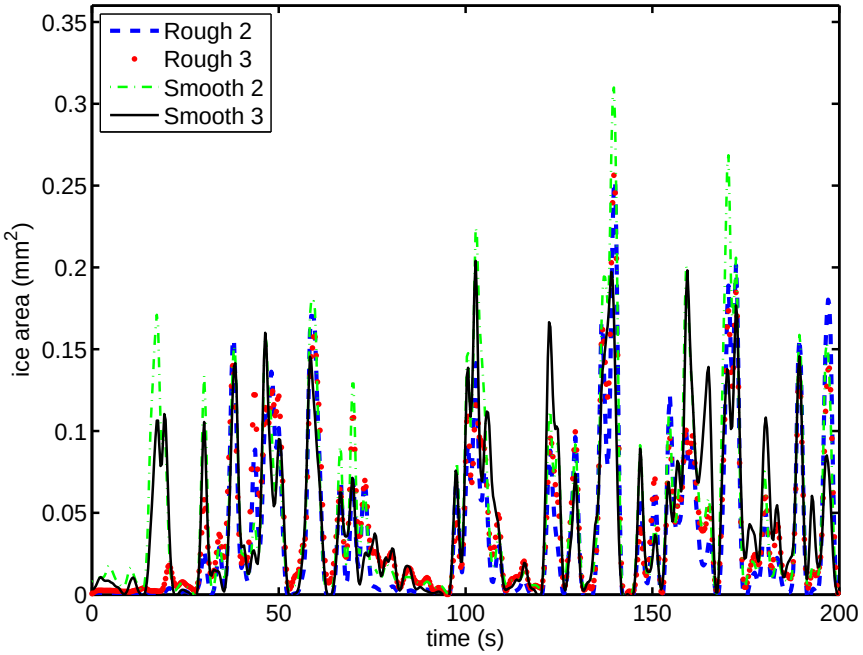

Figure D.56: Test SP5T1HP. Ice accretion area within regions 2 and 3 on the cylindrical specimen at test temperature 5 °C.

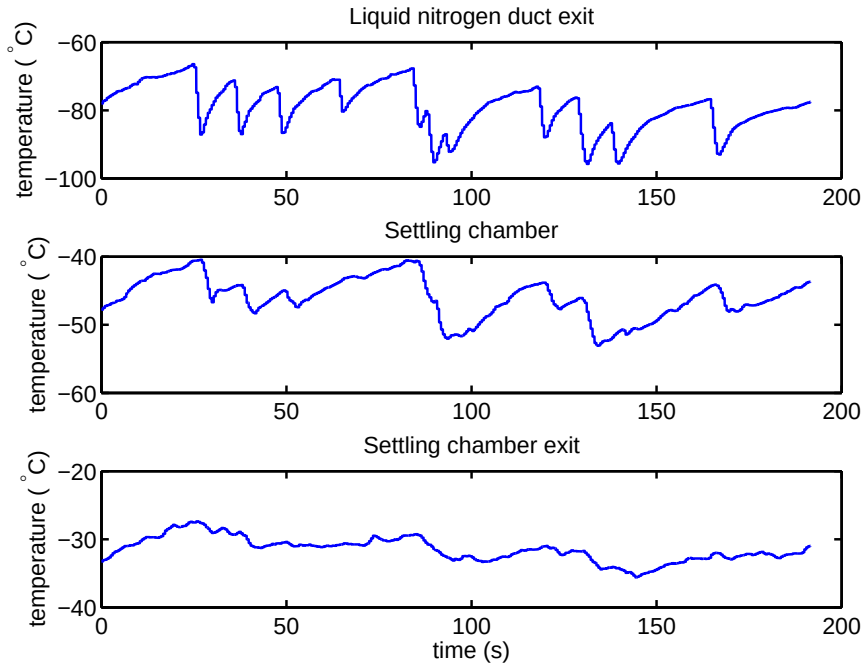

Figure D.57: Test SP5T2HP. Temperatures within the facility upstream of the wind duct. Specimen temperature 5 °C.

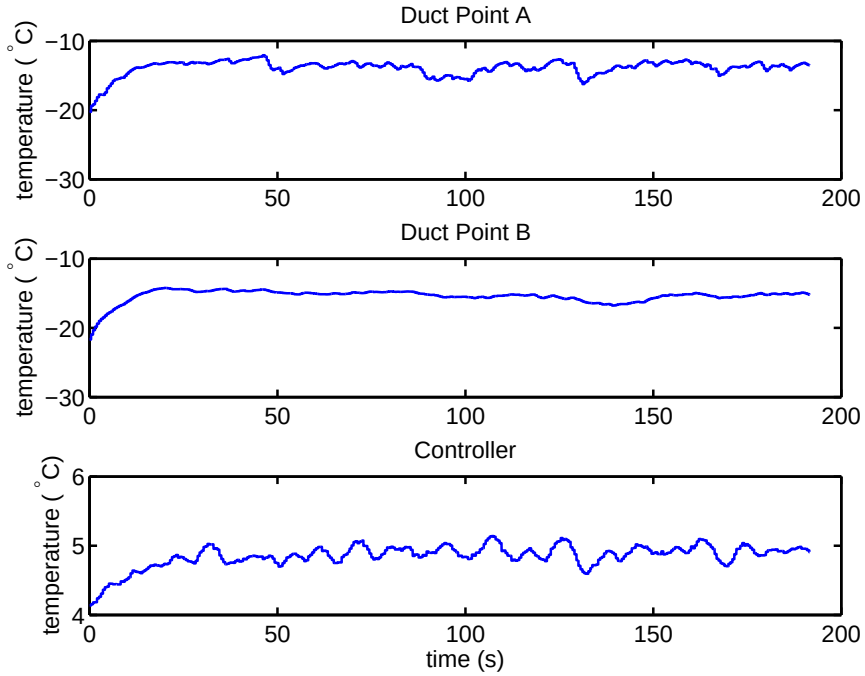

Figure D.58: Test SP5T2HP. Temperatures within the wind tunnel duct for the test specimen temperature of 5 °C.

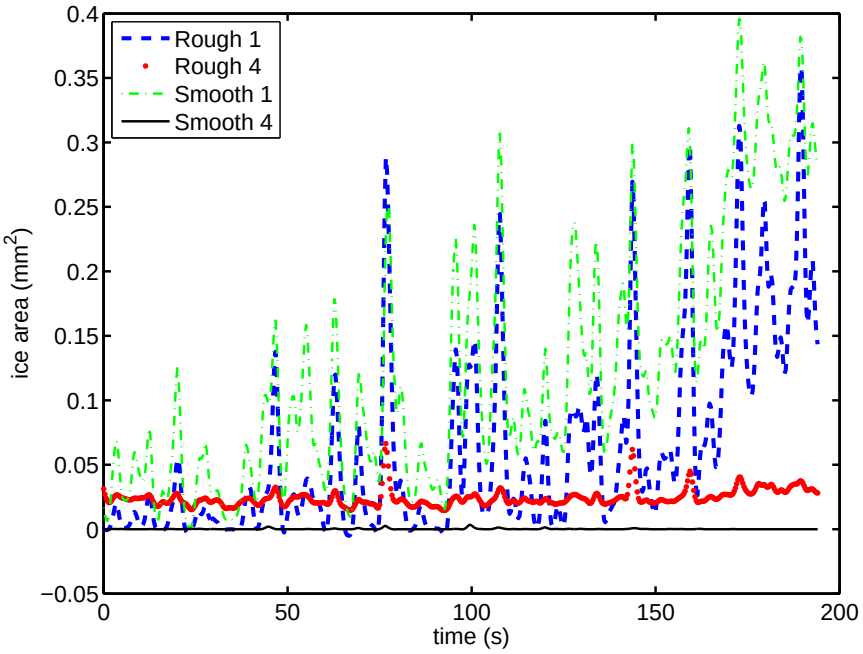

Figure D.59: Test SP5T2HP. Ice accretion area within regions 1 and 4 on the cylindrical specimen at test temperature 5 °C.

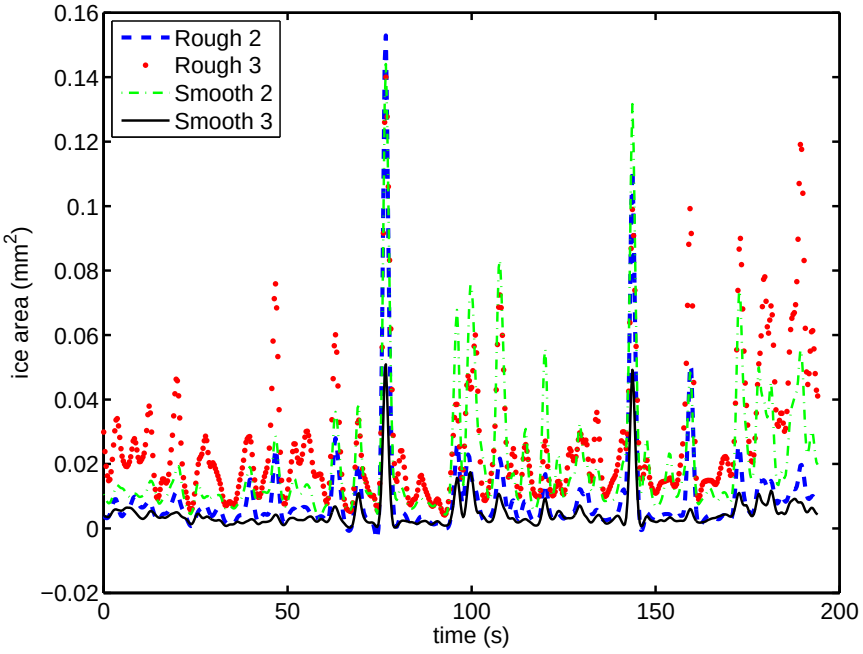

Figure D.60: Test SP5T2HP. Ice accretion area within regions 2 and 3 on the cylindrical specimen at test temperature 5 °C.

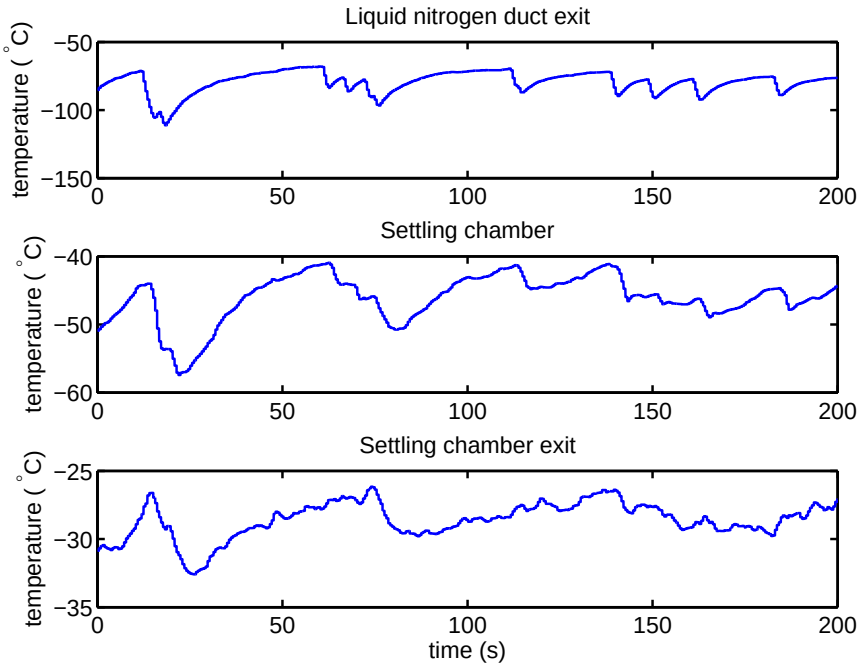

Figure D.61: Test SP5T3HP. Temperatures within the facility upstream of the wind duct. Specimen temperature 5 °C.

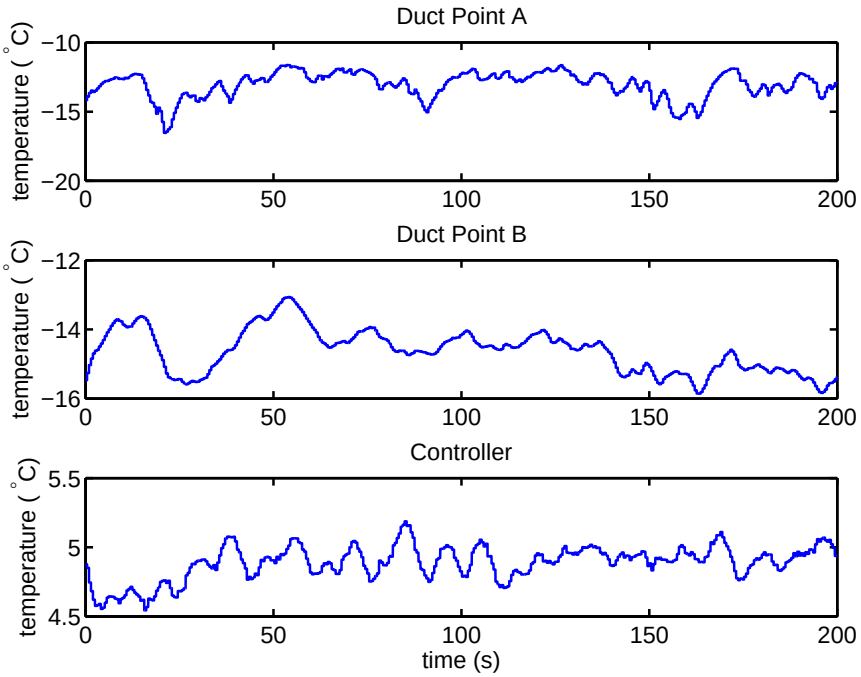

Figure D.62: Test SP5T3HP. Temperatures within the wind tunnel duct for the test specimen temperature of 5 °C.

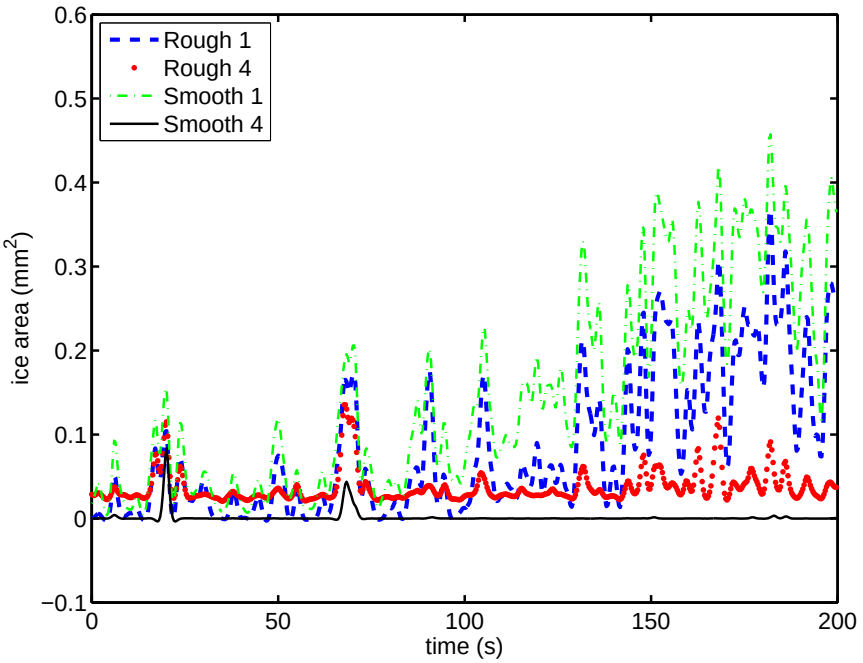

Figure D.63: Test SP5T3HP. Ice accretion area within regions 1 and 4 on the cylindrical specimen at test temperature 5 °C.

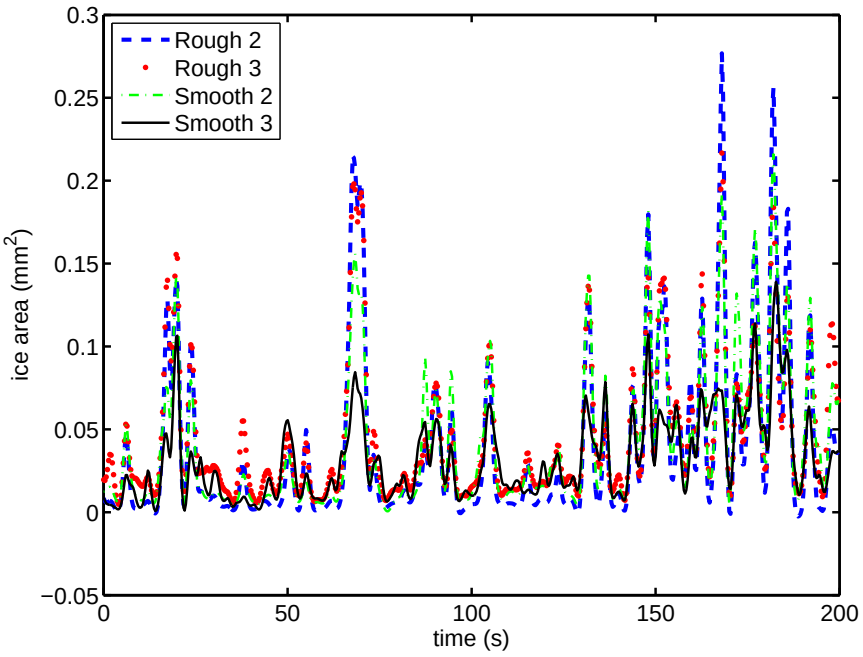

Figure D.64: Test SP5T3HP. Ice accretion area within regions 2 and 3 on the cylindrical specimen at test temperature 5 °C.

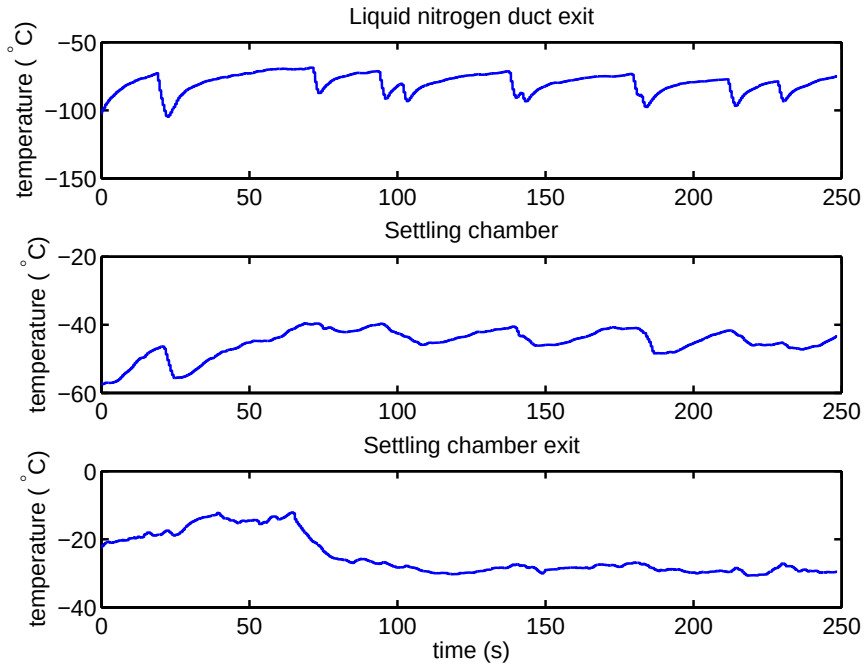

Figure D.65: Test SP5T4HP. Temperatures within the facility upstream of the wind duct. Specimen temperature 5 °C.

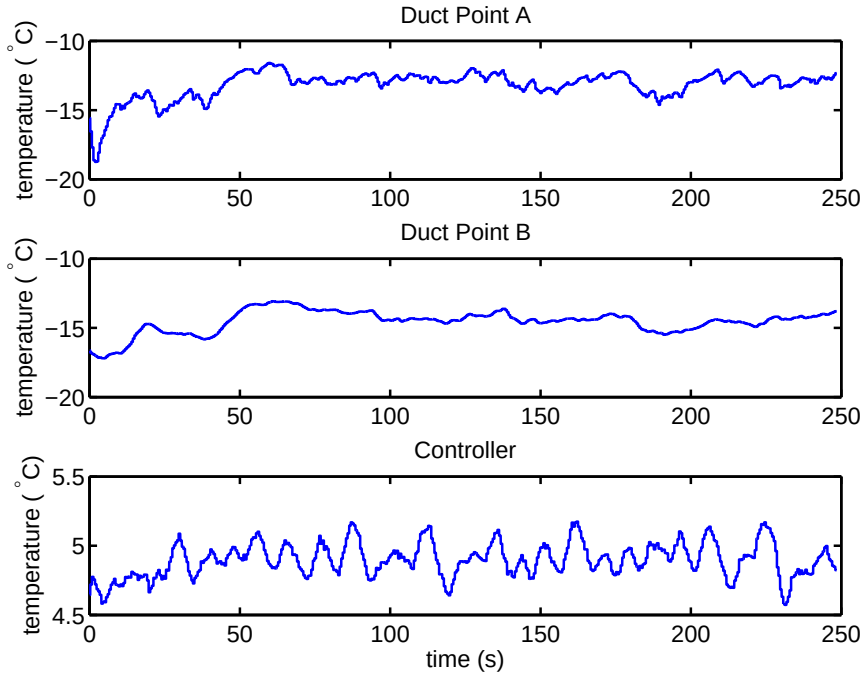

Figure D.66: Test SP5T4HP. Temperatures within the wind tunnel duct for the test specimen temperature of 5 °C.

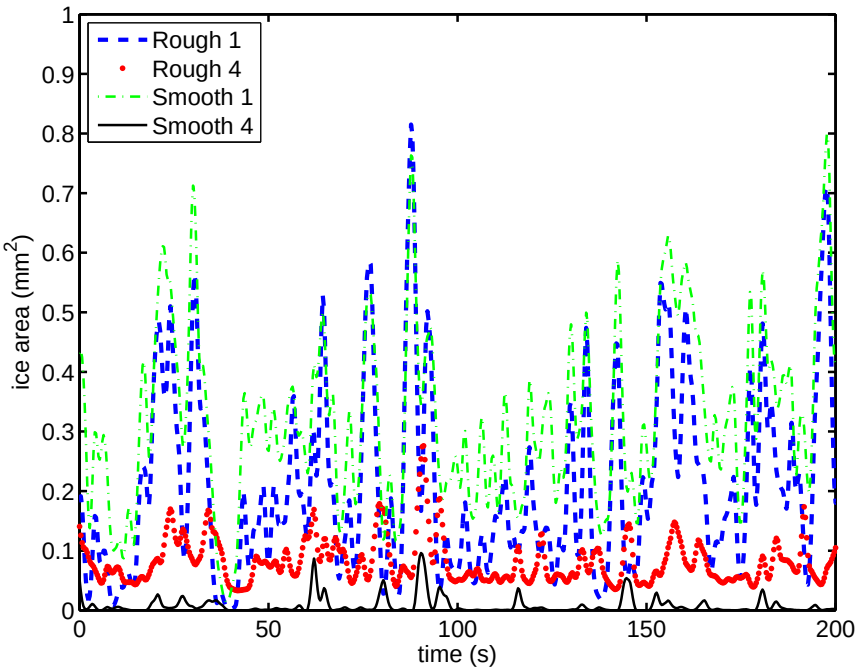

Figure D.67: Test SP5T4HP. Ice accretion area within regions 1 and 4 on the cylindrical specimen at test temperature 5 °C.

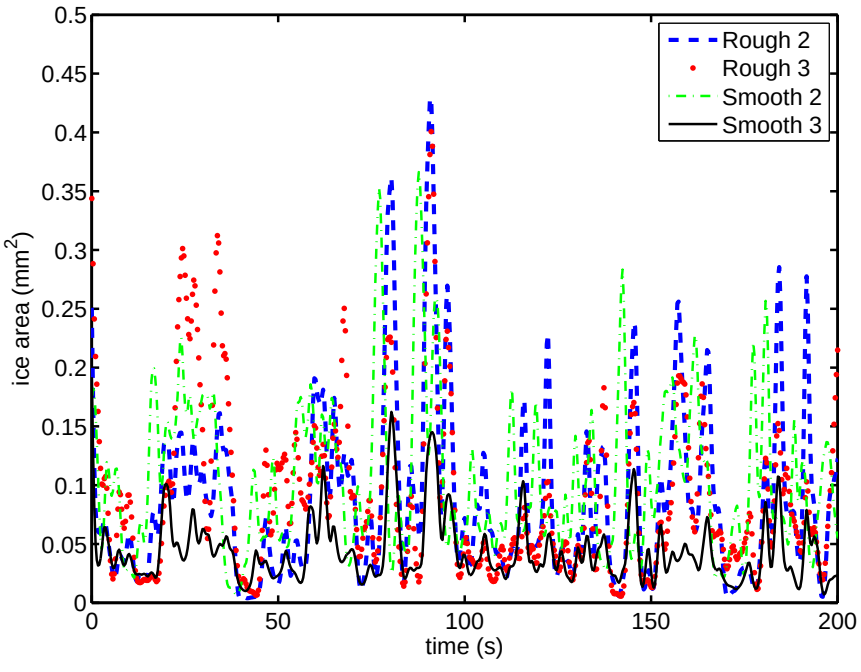

Figure D.68: Test SP5T4HP. Ice accretion area within regions 2 and 3 on the cylindrical specimen at test temperature 5 °C.

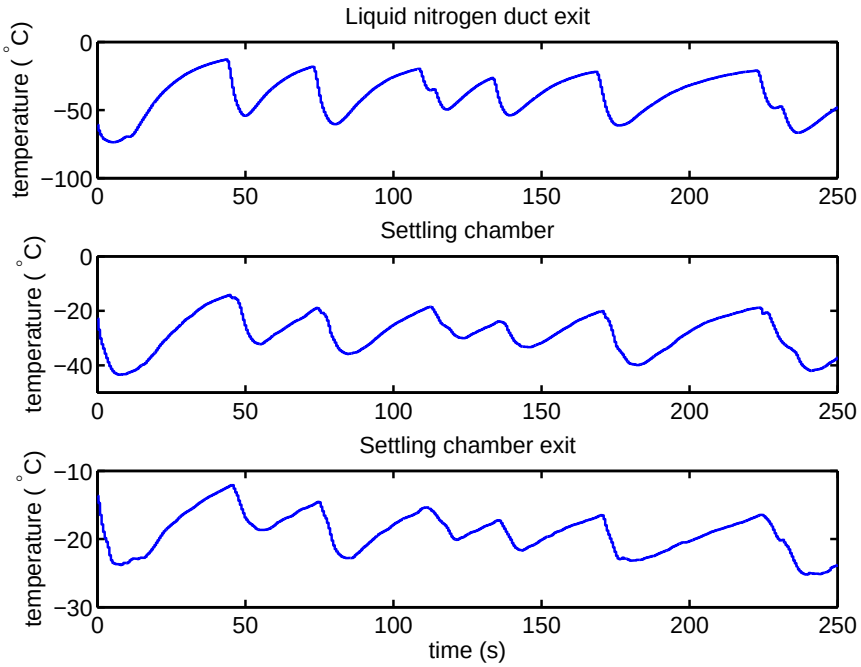

Figure D.69: Test SP5T5HP. Temperatures within the facility upstream of the wind duct. Specimen temperature 5 °C.

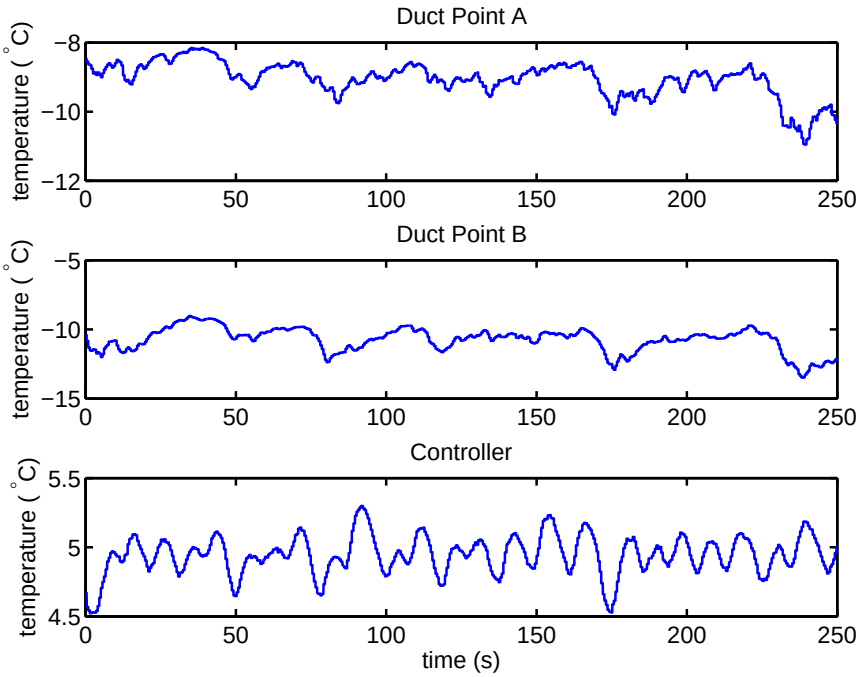

Figure D.70: Test SP5T5HP. Temperatures within the wind tunnel duct for the test specimen temperature of 5 °C.

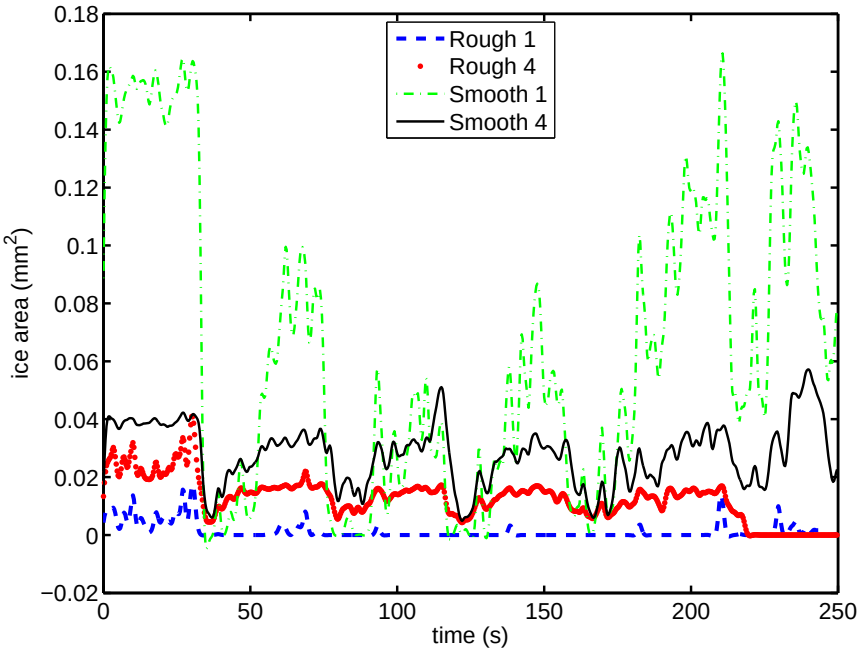

Figure D.71: Test SP5T5HP. Ice accretion area within regions 1 and 4 on the cylindrical specimen at test temperature 5 °C.

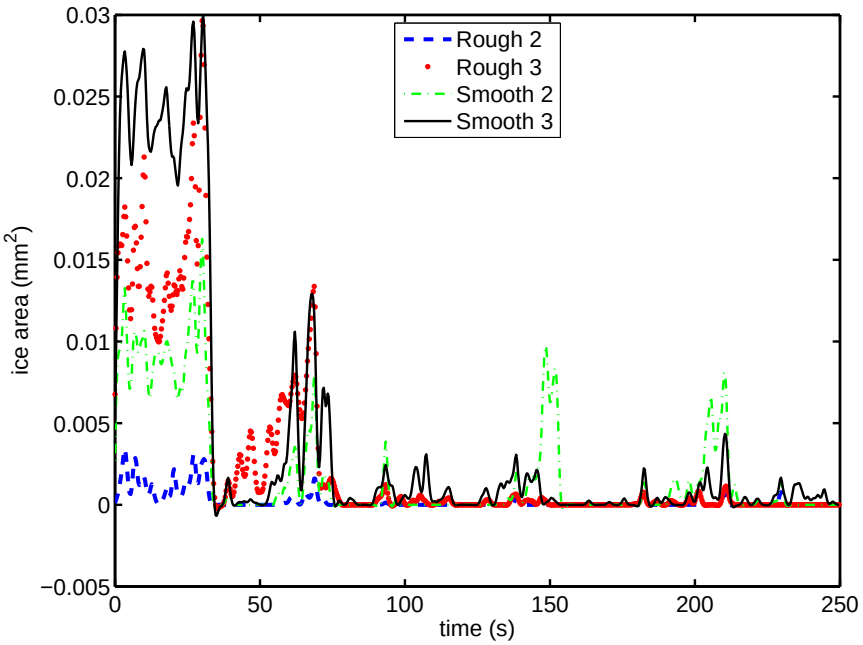

Figure D.72: Test SP5T5HP. Ice accretion area within regions 2 and 3 on the cylindrical specimen at test temperature 5 °C.

Appendix E

Flat Plate Specimen Tests Results

E.1 Introduction

The results of the ice accretion experiments with the flat plate specimen are presented. The experiments were performed with constant air and water pressure delivered to the water spray nozzle yielding constant ice water content conditions across four different specimen surface temperatures and two different surface roughnesses.

Table E.1: Operating conditions for the flat plate specimen tests, uncertainties quoted correspond to $\pm 2\sigma$ values.

Test	T_{LN_2E} (°C)	T_{SC} (°C)	T_{SCE} (°C)	T_A (°C)	T_B (°C)	IWC (g/m^3)	T_S (°C)	Figures
FM9T1HP	-87.5 ± 12.8	-49.8 ± 8.3	-32.2 ± 2.9	-11.6 ± 1.0	-13.3 ± 1.0	0.42 ± 0.26	-8.96 ± 0.23	E.1- E.5
FM9T2HP	-71.5 ± 15.0	-41.8 ± 4.3	-30.8 ± 1.8	-12.6 ± 1.0	-13.7 ± 0.6	0.42 ± 0.26	-8.99 ± 0.20	E.6 - E.10
FM9T3HP	-87.4 ± 10.5	-49.3 ± 5.3	-32.5 ± 2.2	-10.9 ± 0.8	-12.6 ± 1.0	0.42 ± 0.26	-8.94 ± 0.23	E.11 - E.15
FM9T4HP	-90.9 ± 17.9	-51.9 ± 9.1	-39.4 ± 4.4	-12.8 ± 2.4	-14.4 ± 1.2	0.42 ± 0.26	-8.96 ± 0.21	E.16 - E.20
FM5T1HP	-84.0 ± 18.8	-44.2 ± 12.5	-27.7 ± 4.5	-8.0 ± 0.5	-9.0 ± 0.6	0.42 ± 0.26	-4.90 ± 0.29	E.21 - E.25
FM5T2HP	-91.1 ± 10.2	-43.8 ± 2.0	-24.2 ± 2.9	-9.1 ± 0.8	-10.3 ± 1.1	0.42 ± 0.26	-4.94 ± 0.33	E.26 - E.30
FM5T3HP	-97.2 ± 15.7	-49.3 ± 8.8	-25.9 ± 2.8	-9.2 ± 1.2	-10.8 ± 1.6	0.42 ± 0.26	-4.95 ± 0.26	E.31 - E.35
F0T1HP	-98.8 ± 13.6	-51.4 ± 4.9	-30.5 ± 3.0	-9.6 ± 0.9	-10.5 ± 0.8	0.42 ± 0.26	-0.09 ± 0.28	E.36 - E.40
F0T2HP	-96.3 ± 16.7	-54.1 ± 6.2	-31.9 ± 7.4	-10.1 ± 1.6	-11.6 ± 0.9	0.42 ± 0.26	-0.10 ± 0.27	E.41 - E.45
F0T3HP	-93.6 ± 14.1	-51.2 ± 5.6	-32.2 ± 2.2	-11.0 ± 0.8	-12.2 ± 0.8	0.42 ± 0.26	-0.13 ± 0.23	E.46 - E.50
F0T4HP	-90.4 ± 19.5	-50.5 ± 9.0	-32.5 ± 2.4	-10.3 ± 0.9	-11.4 ± 1.0	0.42 ± 0.26	-0.13 ± 0.30	E.52 - E.55
FP5T1HP	-85.6 ± 15.0	-51.6 ± 8.9	-38.2 ± 3.2	-11.4 ± 1.5	-13.3 ± 1.3	0.42 ± 0.26	4.87 ± 0.36	E.56 - E.60
FP5T2HP	-90.6 ± 32.2	-51.6 ± 17.0	-38.5 ± 12.5	-9.7 ± 1.8	-11.2 ± 2.3	0.42 ± 0.26	4.85 ± 0.29	E.61 - E.65
FP5T3HP	-89.0 ± 14.5	-52.2 ± 6.1	-39.6 ± 3.2	-11.8 ± 1.1	-13.4 ± 0.9	0.42 ± 0.26	4.82 ± 0.20	E.66 - E.70

E.2 Surface Temperature −9 °C

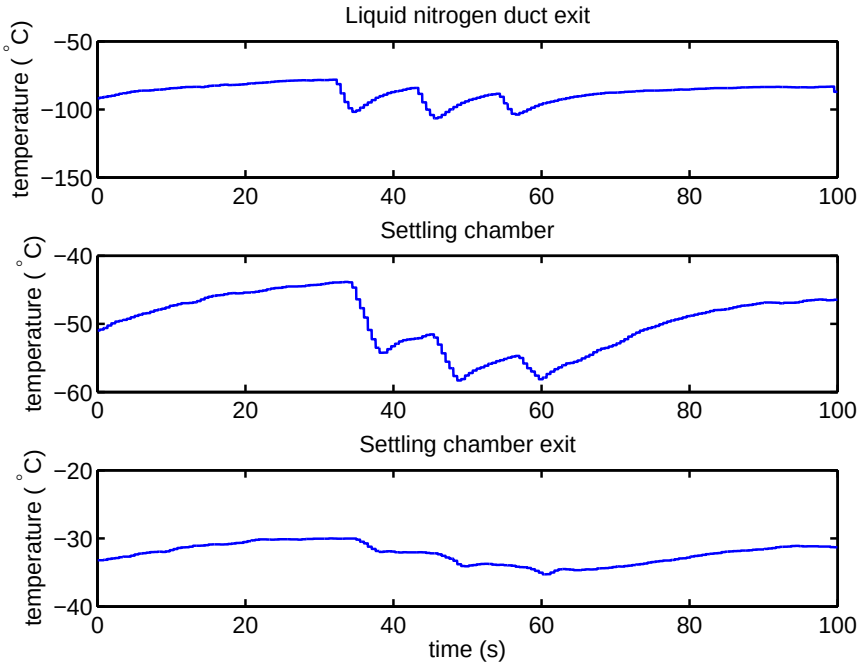

Figure E.1: Test FM9T1HP. Temperatures within the facility upstream of the wind tunnel duct. Specimen temperature −9 °C.

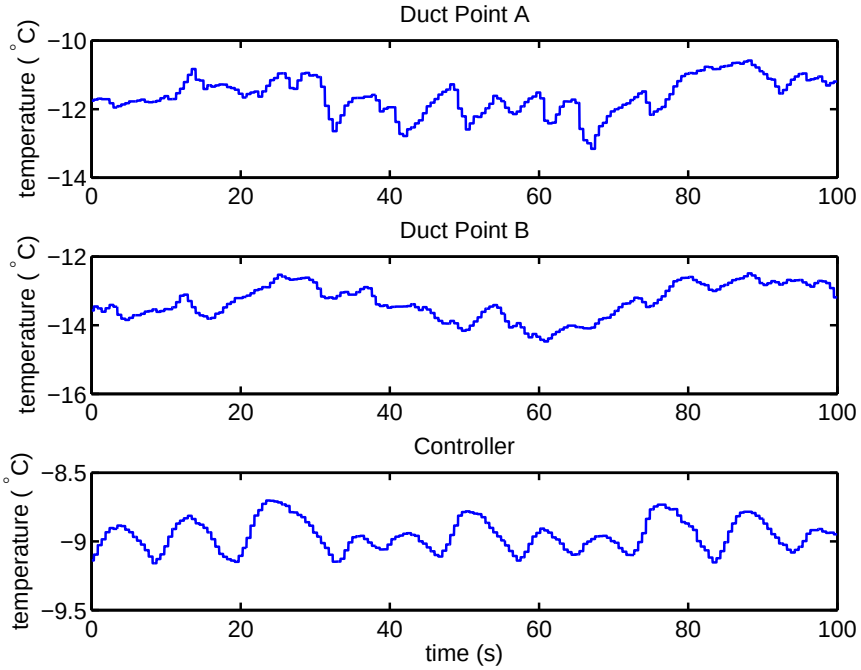

Figure E.2: Test FM9T1HP. Temperatures within the wind tunnel duct for the test specimen temperature of −9 °C.

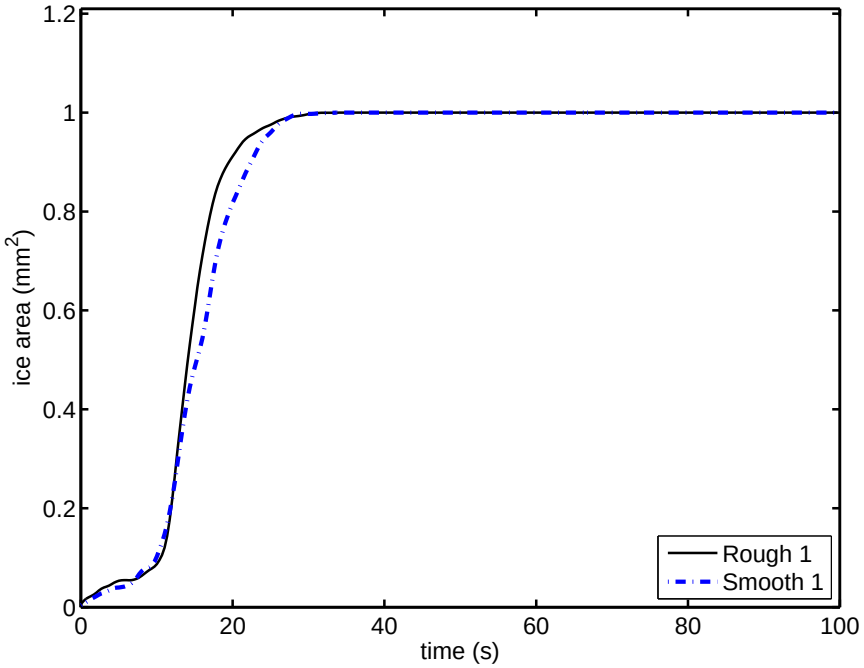

Figure E.3: Test FM9T1HP. Ice accretion area within region 1 on the flat plate specimen at test temperature −9 °C.

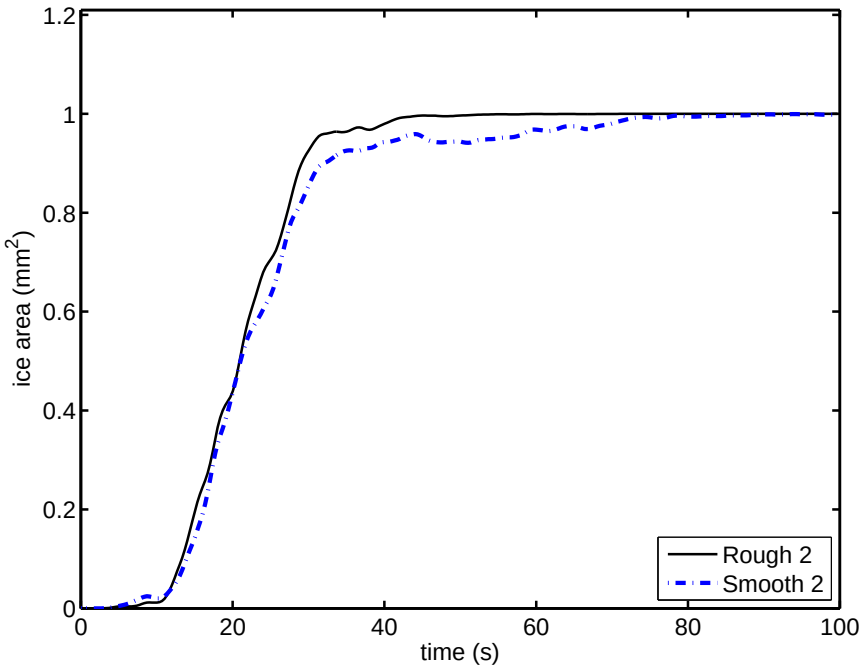

Figure E.4: Test FM9T1HP. Ice accretion area within region 2 on the flat plate specimen at test temperature −9 °C.

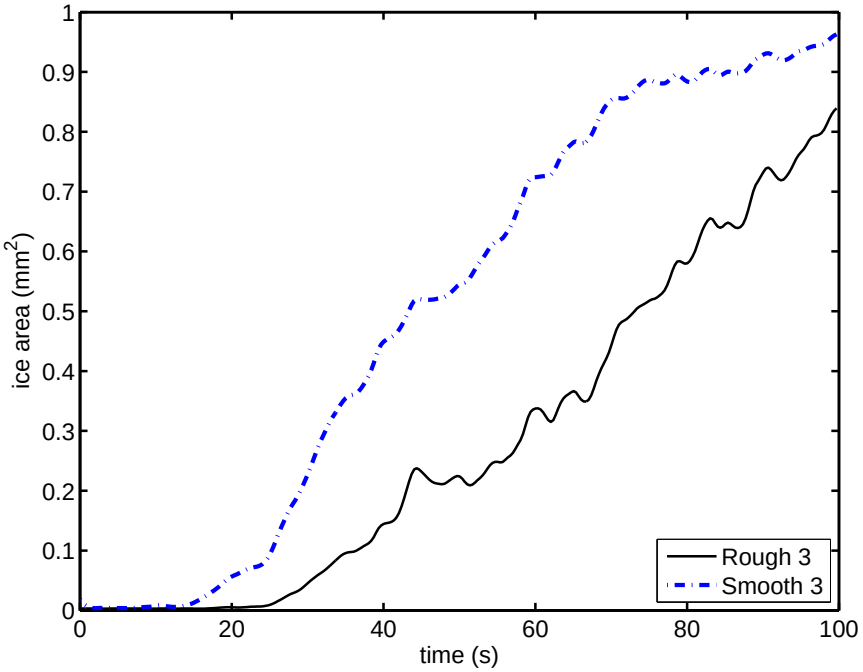

Figure E.5: Test FM9T1HP. Ice accretion area within region 3 on the flat plate specimen at test temperature −9 °C.

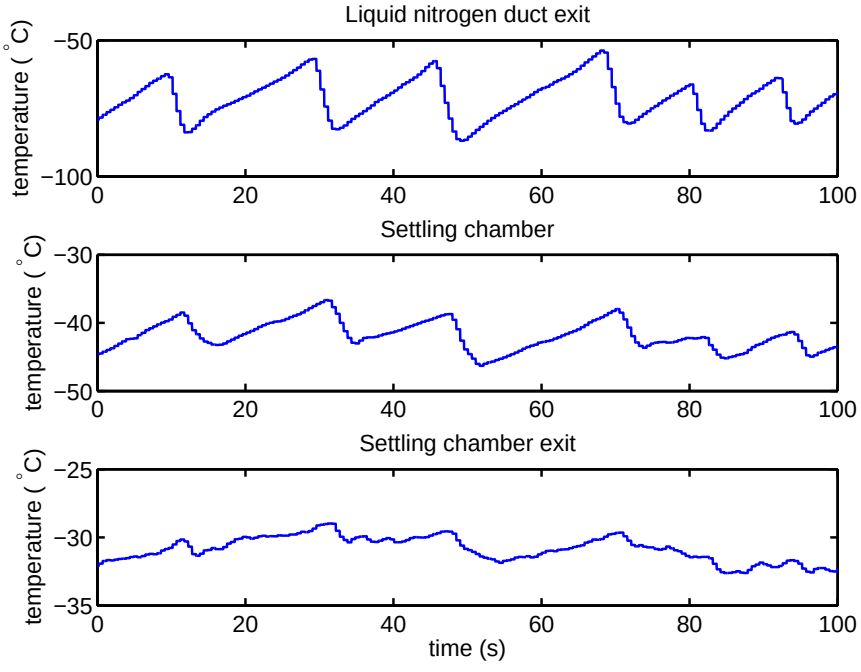

Figure E.6: Test FM9T2HP. Temperatures within the facility upstream of the wind tunnel duct. Specimen temperature −9 °C.

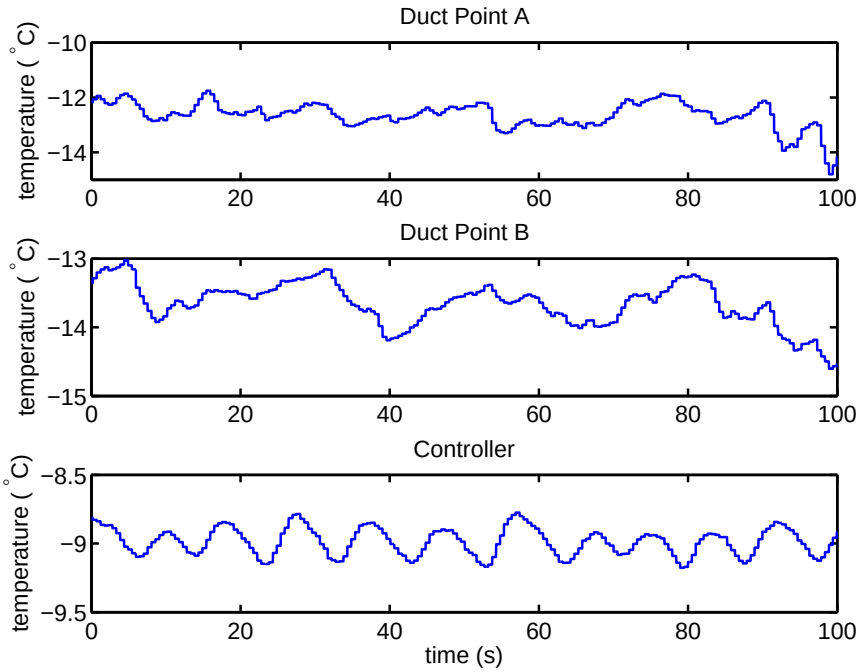

Figure E.7: Test FM9T2HP. Temperatures within the wind tunnel duct for the test specimen temperature of −9 °C.

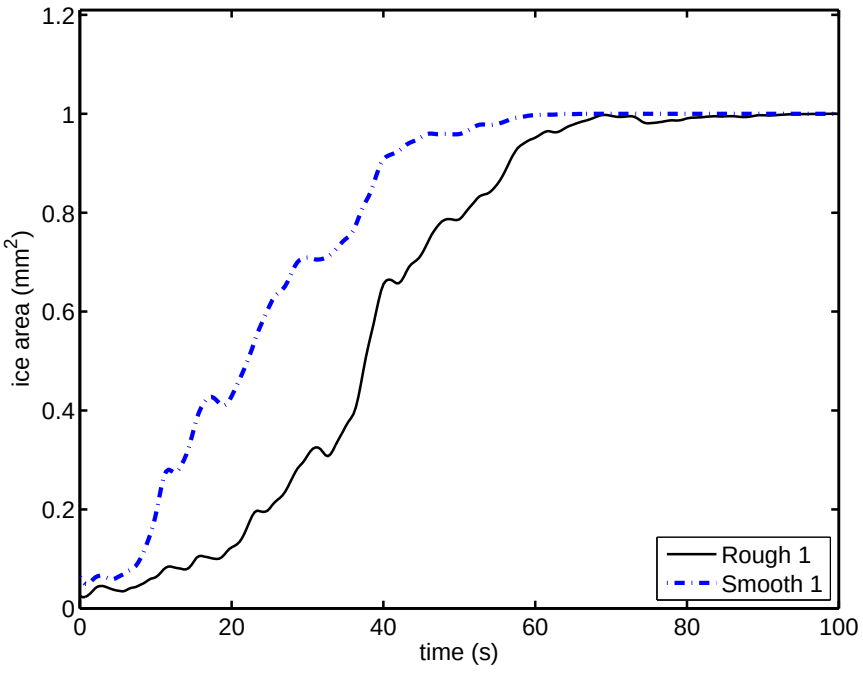

Figure E.8: Test FM9T2HP. Ice accretion area within region 1 on the flat plate specimen at test temperature −9 °C.

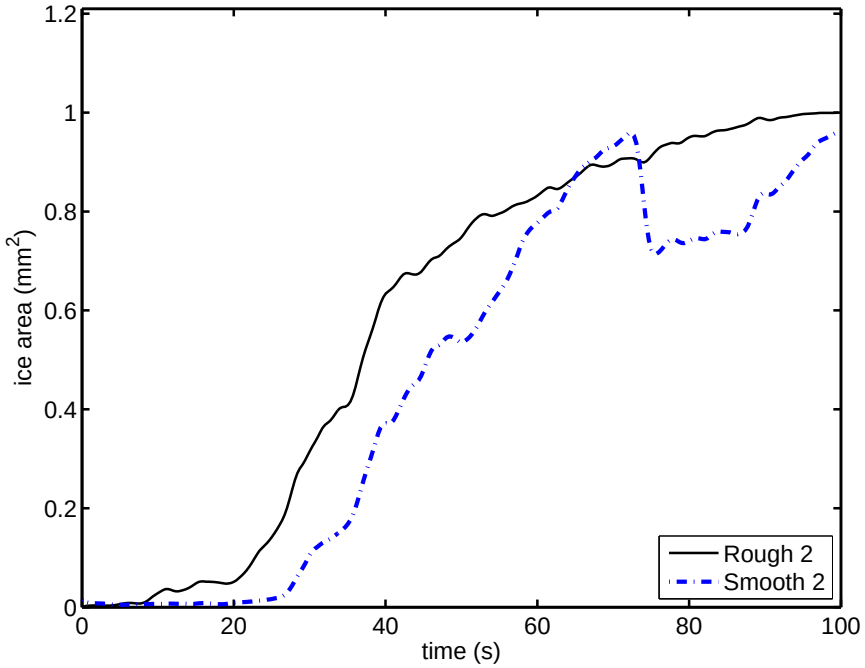

Figure E.9: Test FM9T2HP. Ice accretion area within region 2 on the flat plate specimen at test temperature −9 °C.

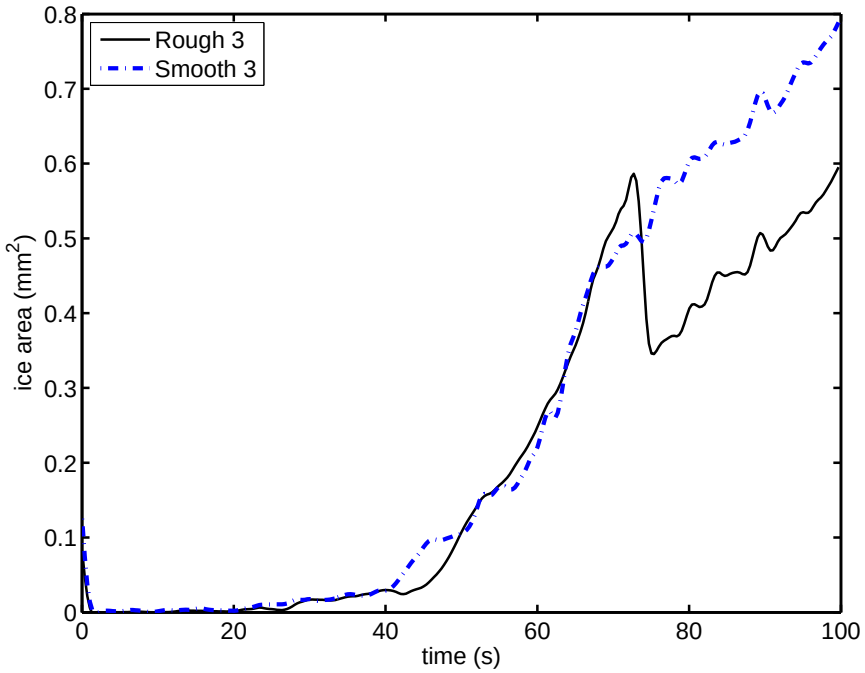

Figure E.10: Test FM9T2HP. Ice accretion area within region 3 on the flat plate specimen at test temperature −9 °C.

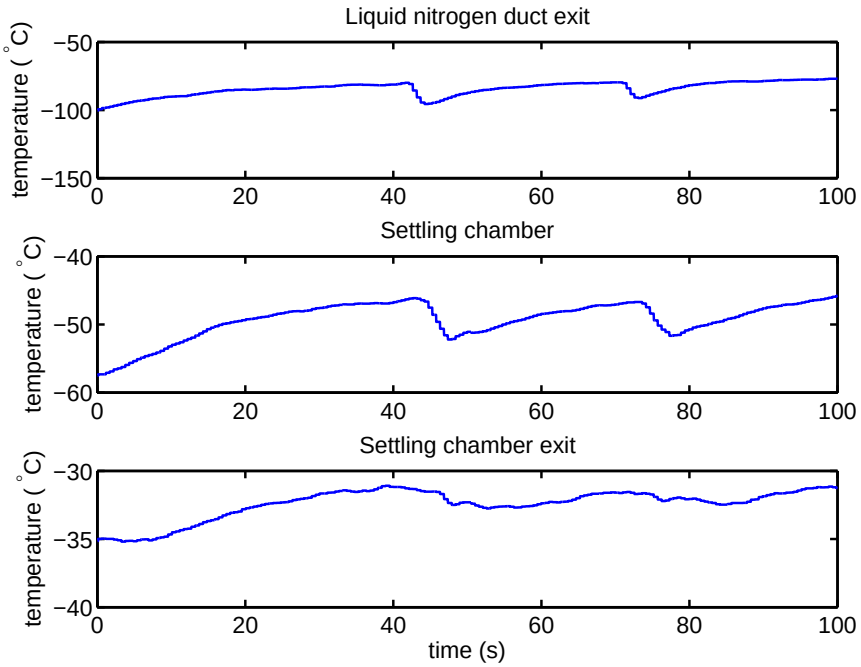

Figure E.11: Test FM9T3HP. Temperatures within the facility upstream of the wind tunnel duct. Specimen temperature −9 °C.

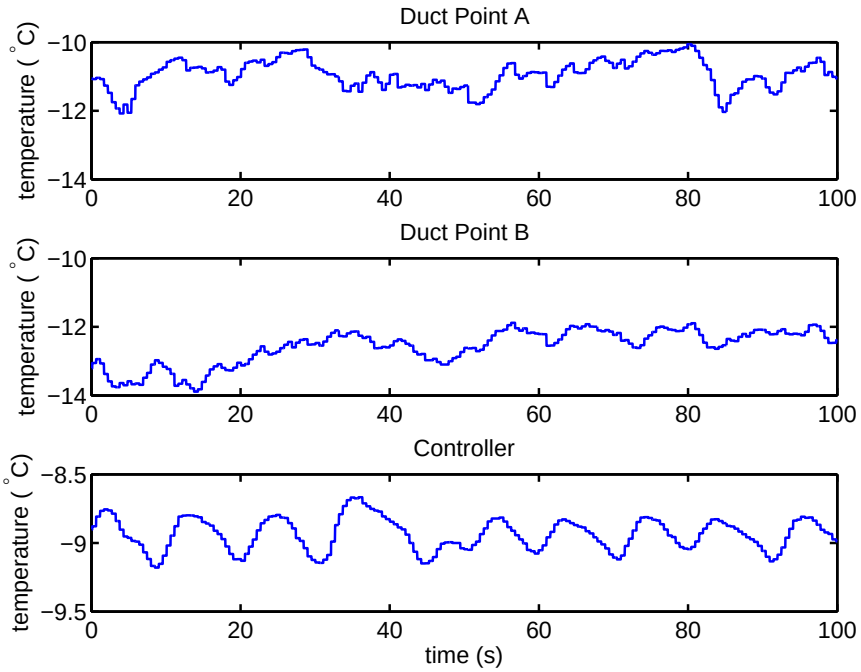

Figure E.12: Test FM9T3HP. Temperatures within the wind tunnel duct for the test specimen temperature of −9 °C.

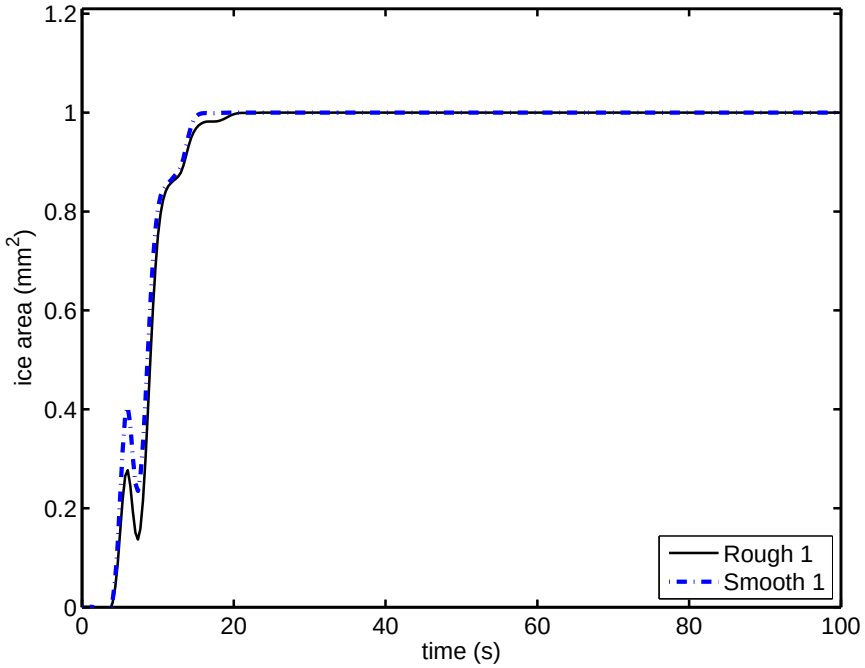

Figure E.13: Test FM9T3HP. Ice accretion area within region 1 on the flat plate specimen at test temperature −9 °C.

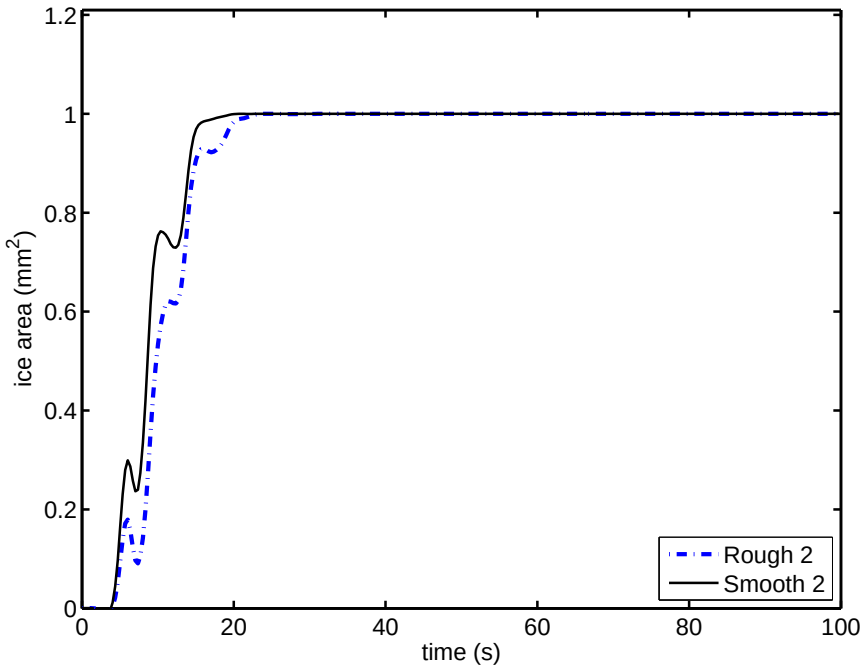

Figure E.14: Test FM9T3HP. Ice accretion area within region 2 on the flat plate specimen at test temperature −9 °C.

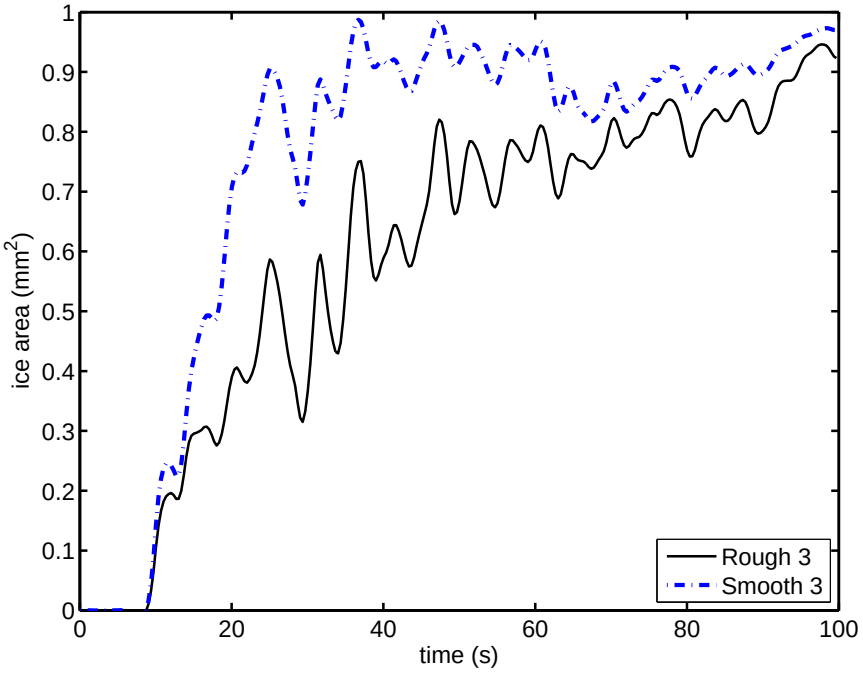

Figure E.15: Test FM9T3HP. Ice accretion area within region 3 on the flat plate specimen at test temperature −9 °C.

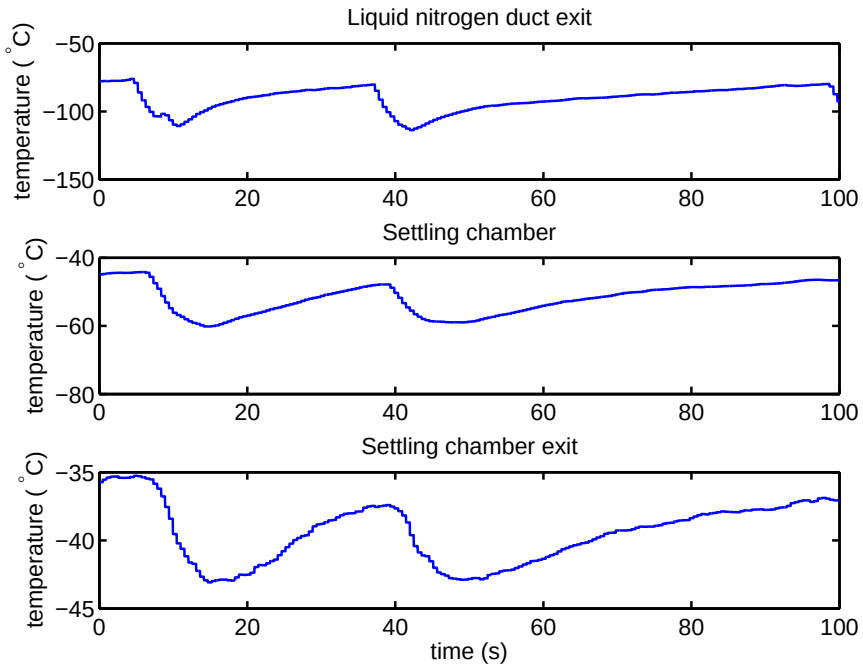

Figure E.16: Test SM9T4HP. Temperatures within the facility upstream of the wind tunnel duct. Specimen temperature −9 °C.

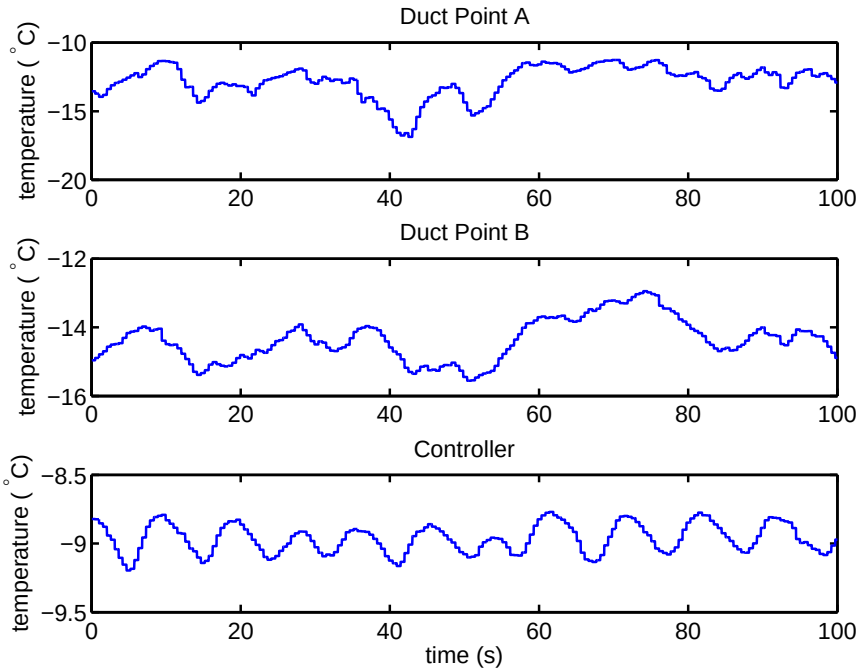

Figure E.17: Test SM9T4HP. Temperatures within the wind tunnel duct for the test specimen temperature of −9 °C

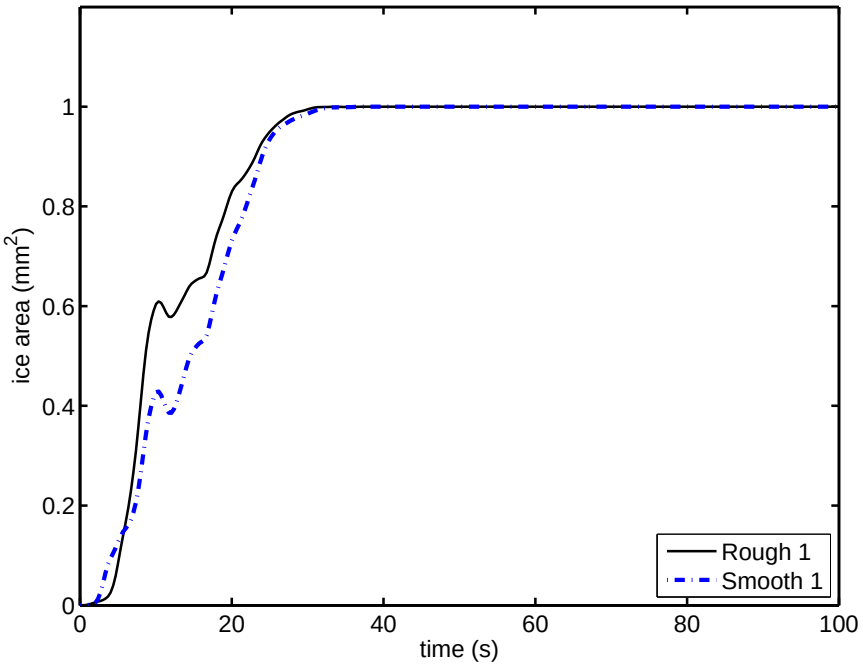

Figure E.18: Test SM9T4HP. Ice accretion area within region 1 on the flat plate specimen at test temperature −9 °C.

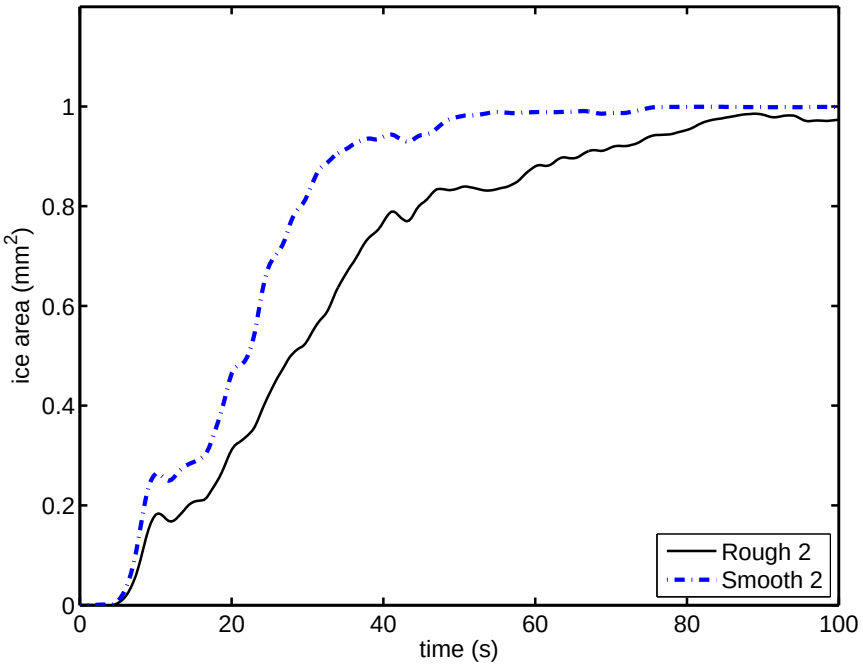

Figure E.19: Test SM9T4HP. Ice accretion area within region 2 on the flat plate specimen at test temperature −9 °C.

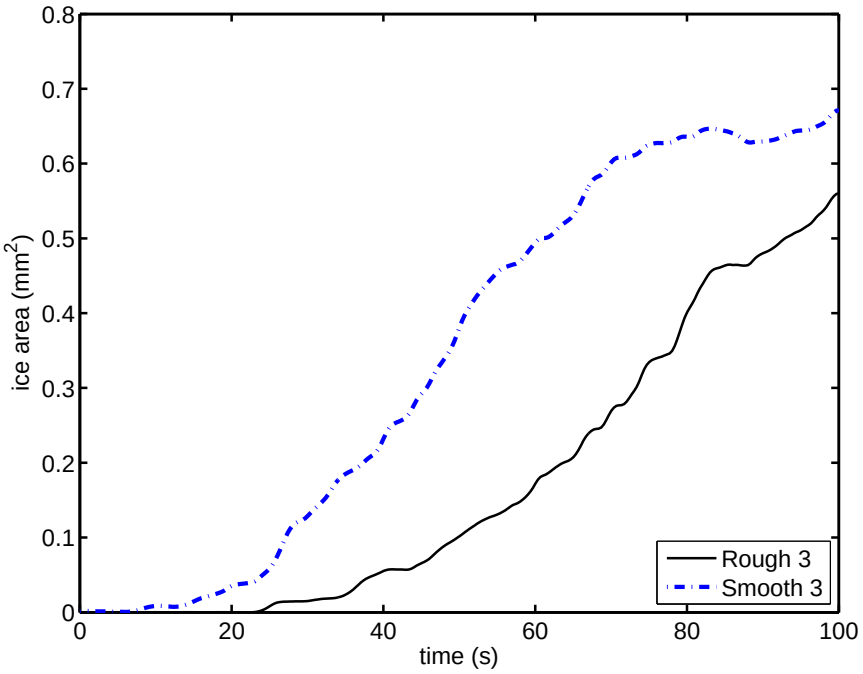

Figure E.20: Test SM9T4HP. Ice accretion area within region 3 on the flat plate specimen at test temperature −9 °C.

E.3 Surface Temperature −5 °C

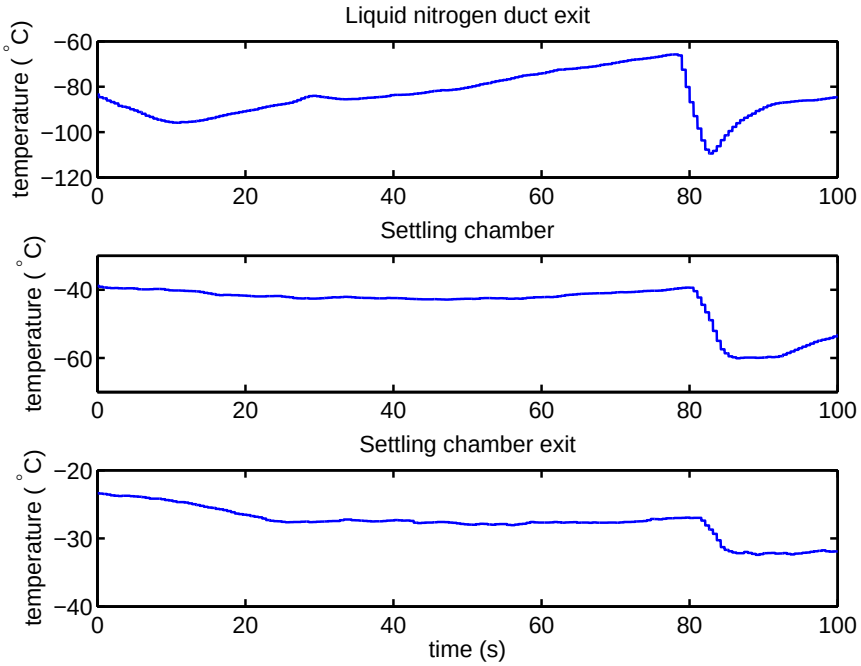

Figure E.21: Test FM5T1HP. Temperatures within the facility upstream of the wind tunnel duct. Specimen temperature −5 °C.

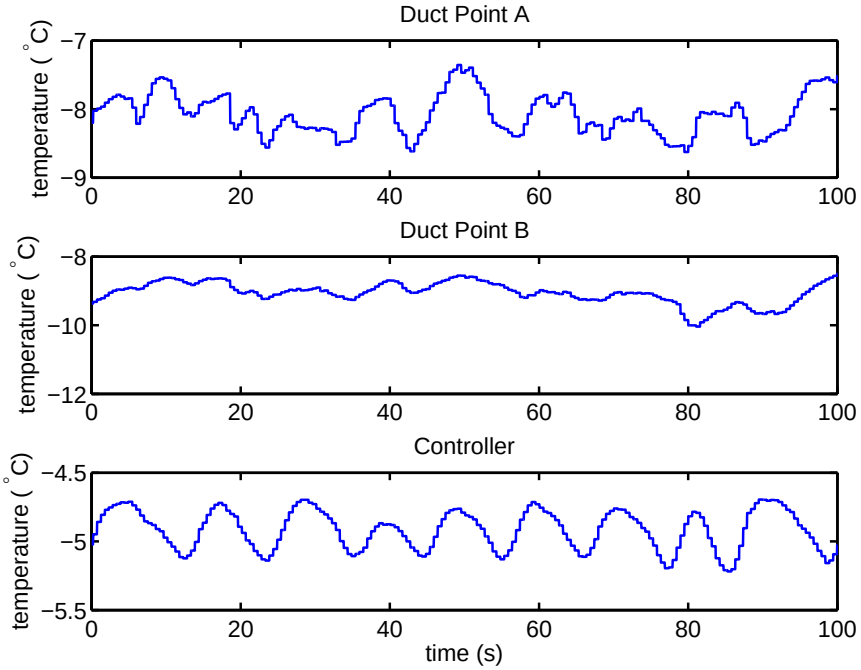

Figure E.22: Test FM5T1HP. Temperatures within the wind tunnel duct for the test specimen temperature of −5 °C.

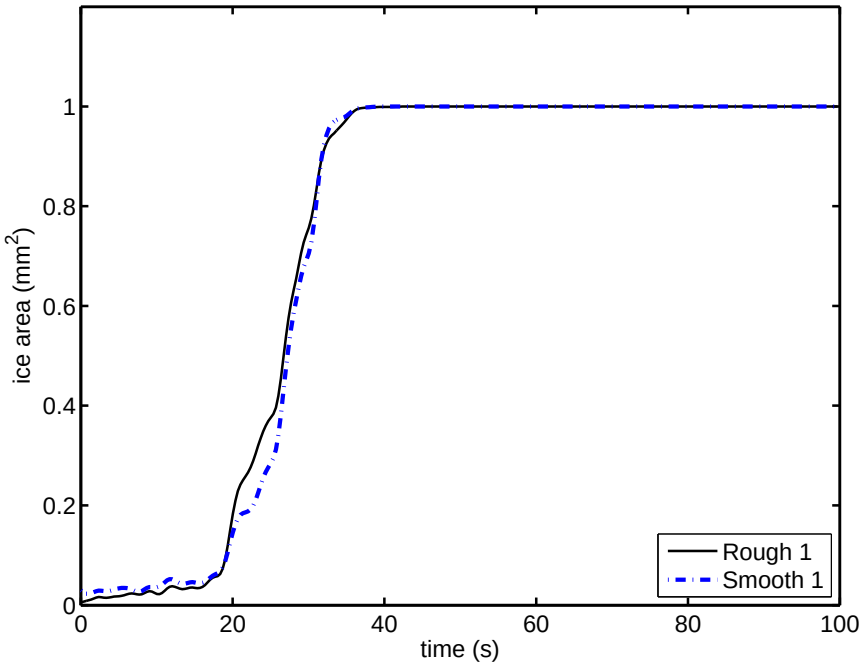

Figure E.23: Test FM5T1HP. Ice accretion area within region 1 on the flat plate specimen at test temperature −5 °C.

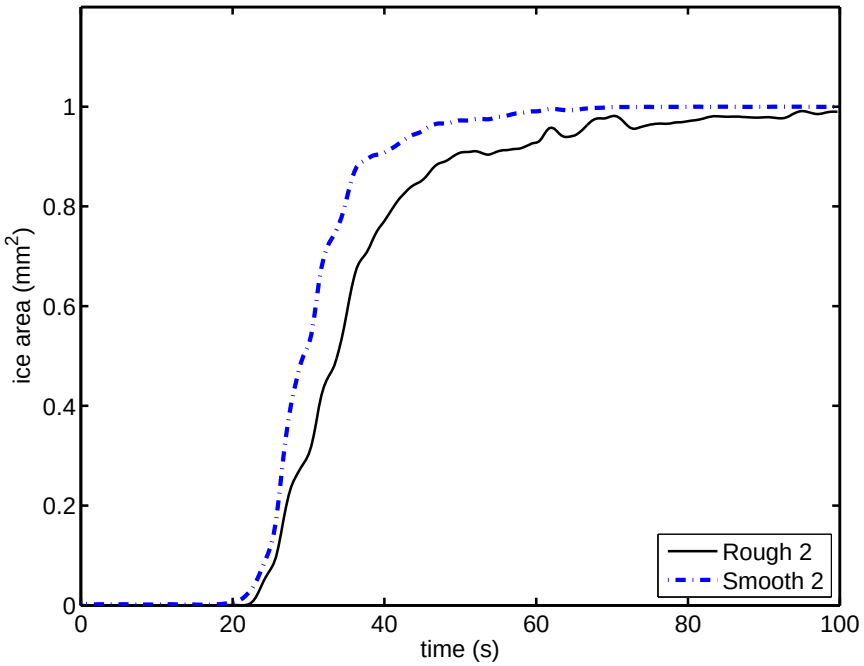

Figure E.24: Test FM5T1HP. Ice accretion area within region 2 on the flat plate specimen at test temperature −5 °C.

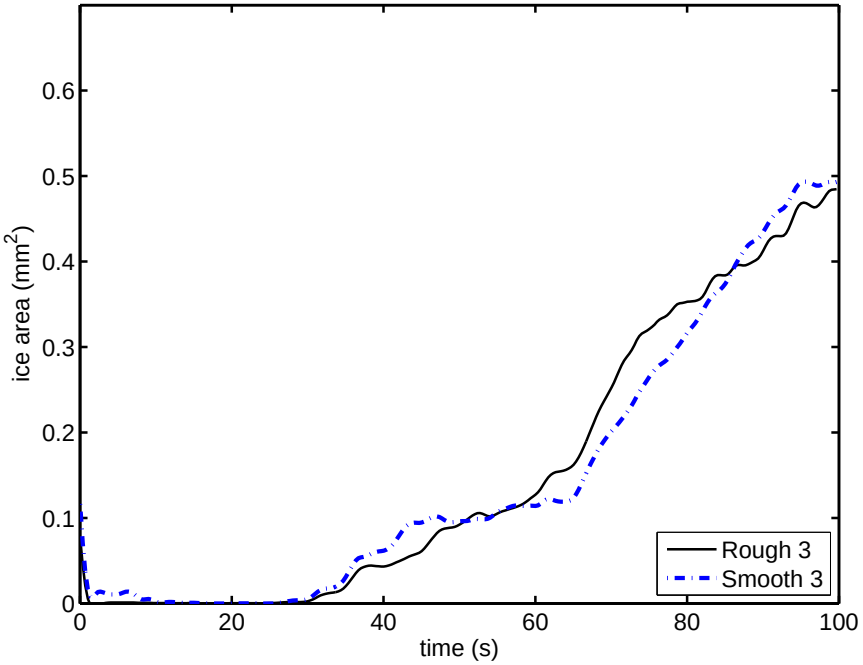

Figure E.25: Test FM5T1HP. Ice accretion area within region 3 on the flat plate specimen at test temperature −5 °C.

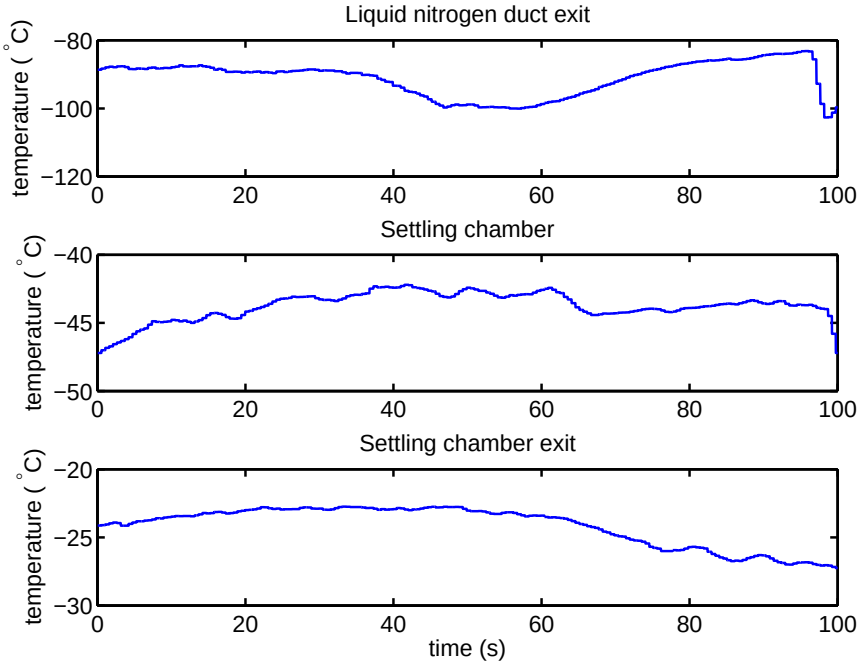

Figure E.26: Test FM5T2HP. Temperatures within the facility upstream of the wind tunnel duct. Specimen temperature −5 °C.

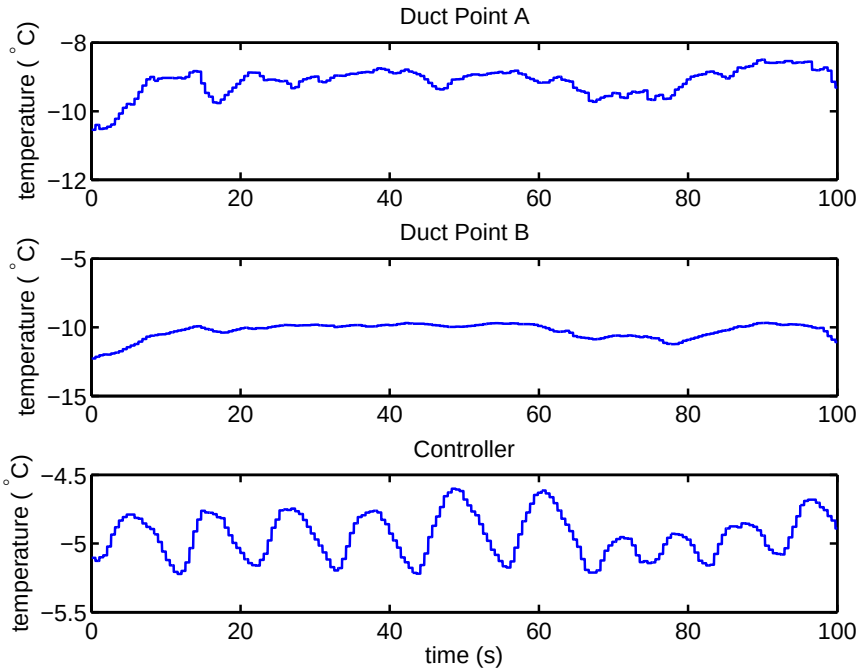

Figure E.27: Test FM5T2HP. Temperatures within the wind tunnel duct for the test specimen temperature of −5 °C.

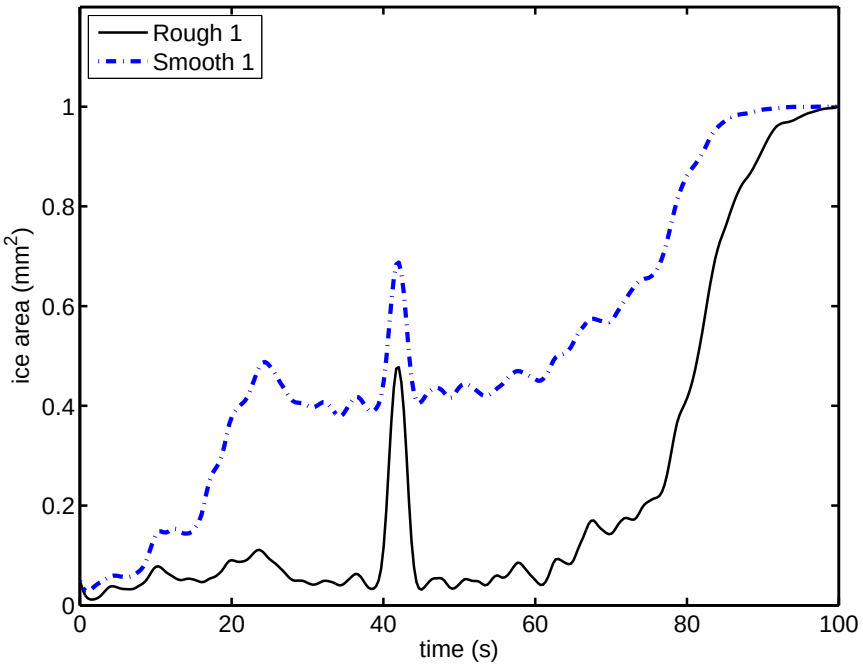

Figure E.28: Test FM5T2HP. Ice accretion area within region 1 on the flat plate specimen at test temperature −5 °C.

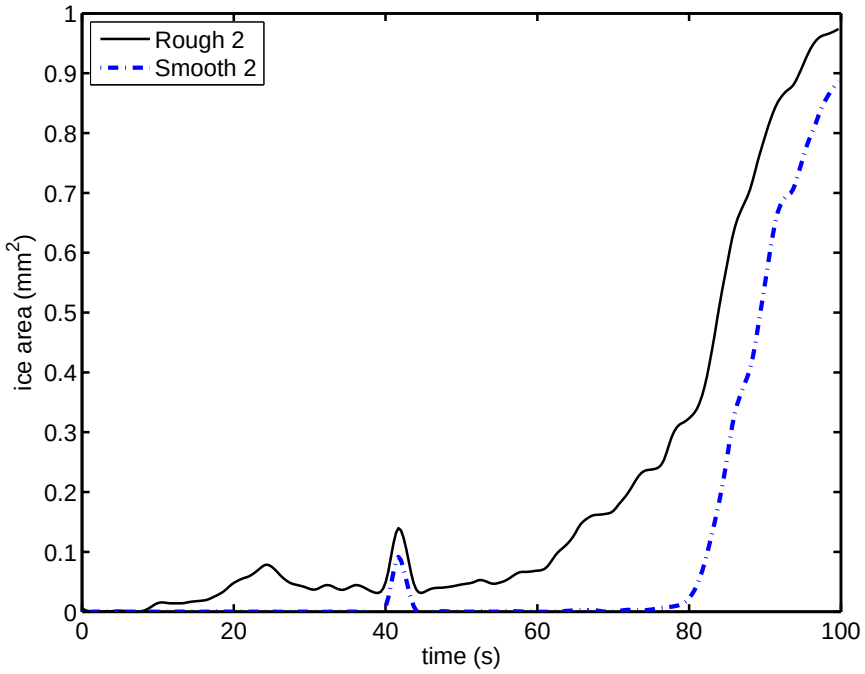

Figure E.29: Test FM5T2HP. Ice accretion area within region 2 on the flat plate specimen at test temperature −5 °C.

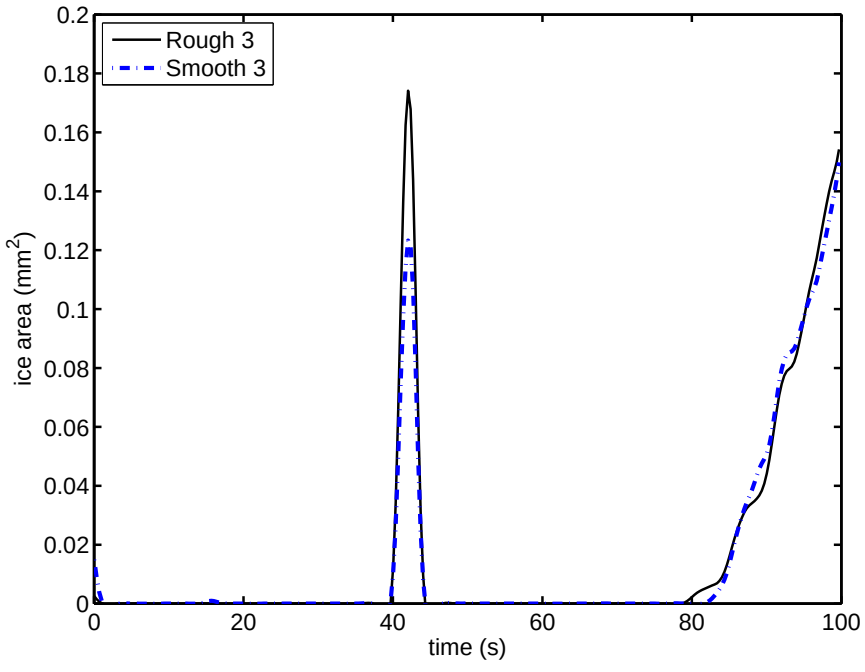

Figure E.30: Test FM5T2HP. Ice accretion area within region 3 on the flat plate specimen at test temperature −5 °C.

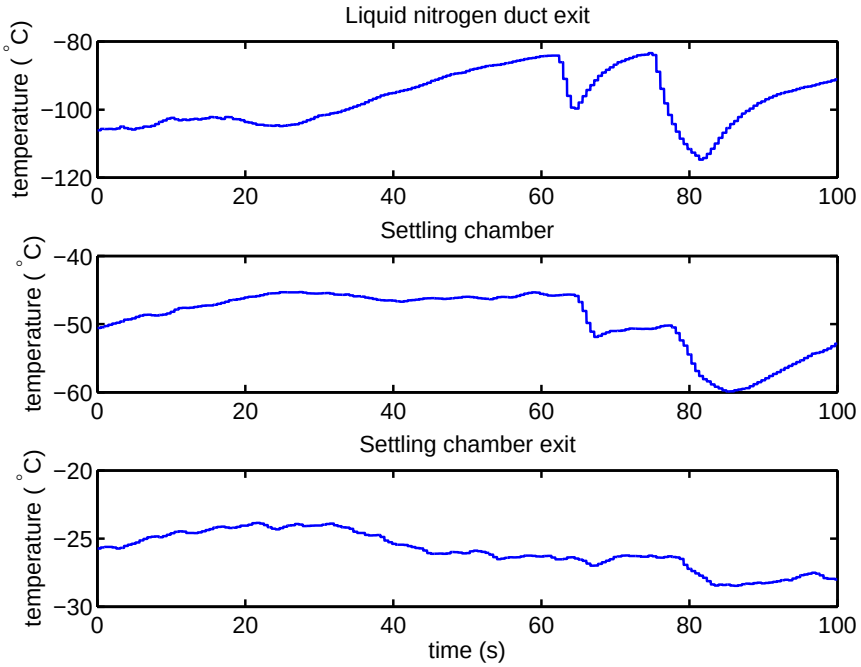

Figure E.31: Test FM5T3HP. Temperatures within the facility upstream of the wind tunnel duct. Specimen temperature −5 °C.

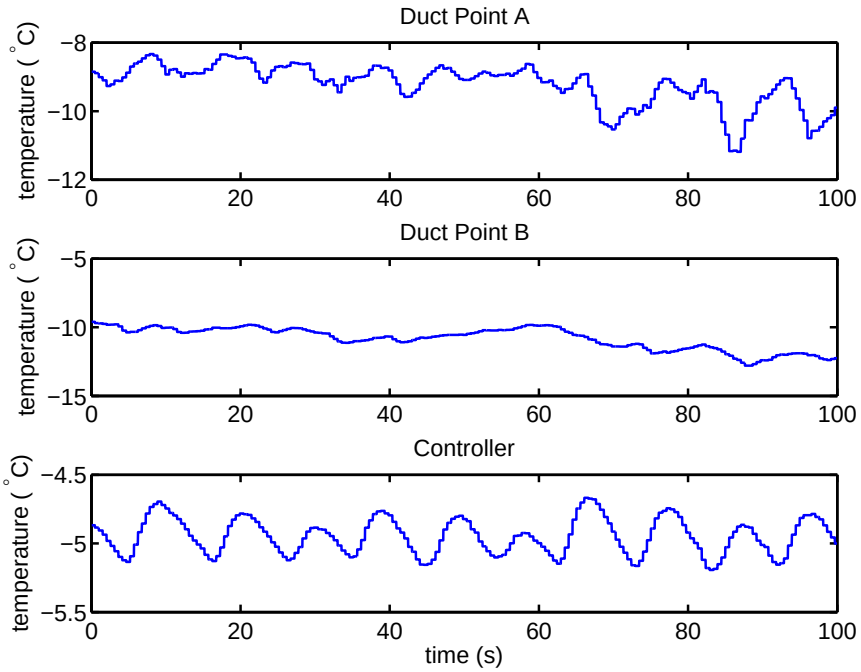

Figure E.32: Test FM5T3HP. Temperatures within the wind tunnel duct for the test specimen temperature of −5 °C.

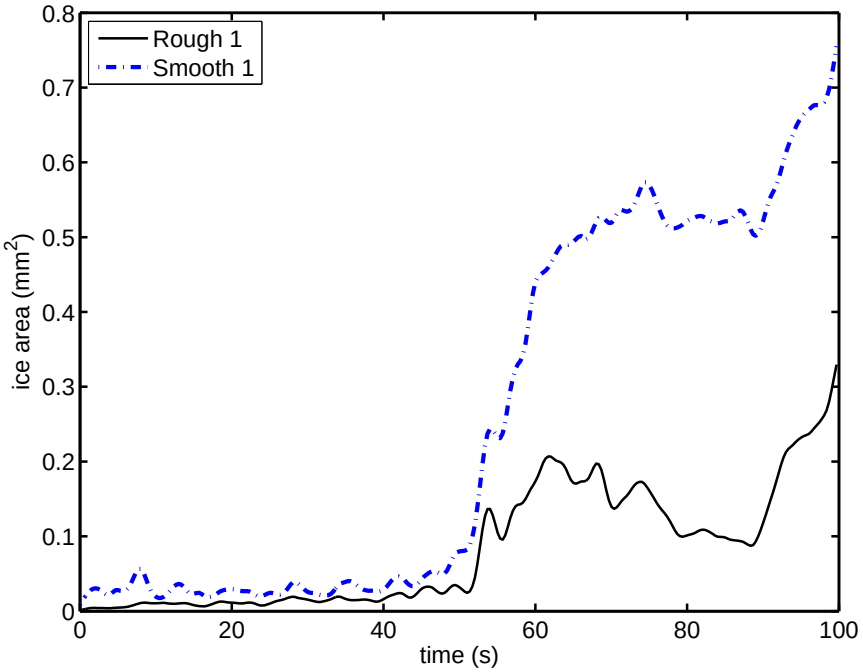

Figure E.33: Test FM5T3HP. Ice accretion area within region 1 on the flat plate specimen at test temperature −5 °C.

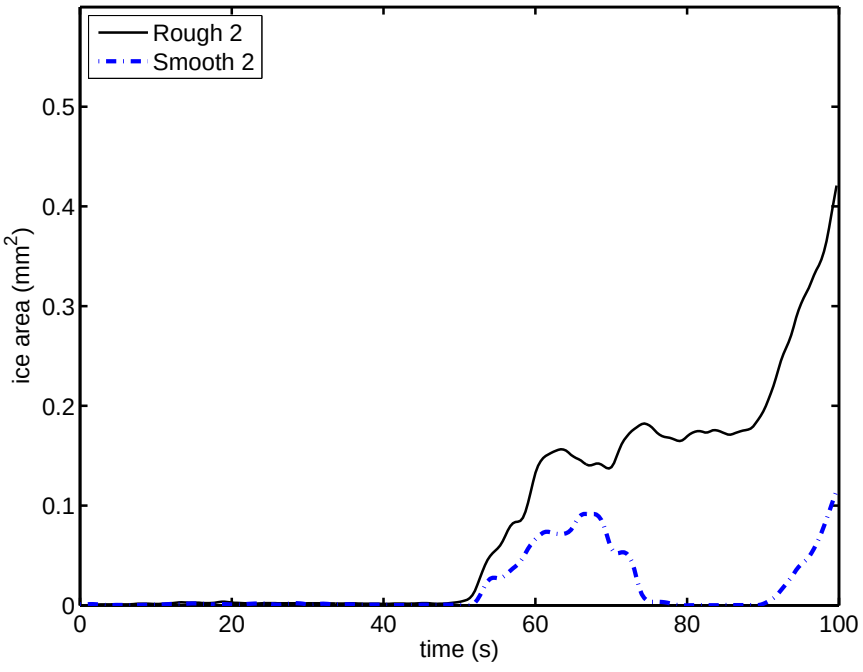

Figure E.34: Test FM5T3HP. Ice accretion area within region 2 on the flat plate specimen at test temperature −5 °C.

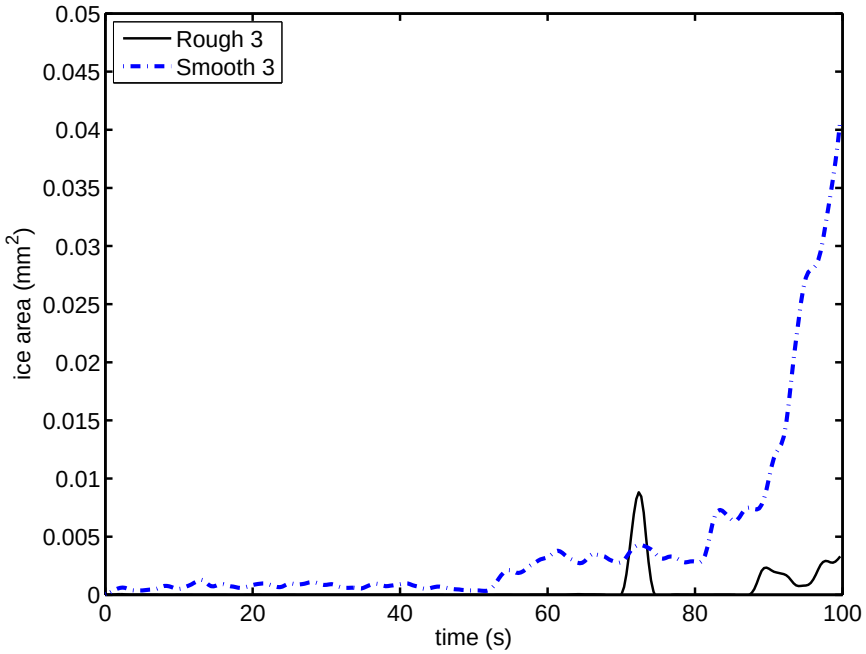

Figure E.35: Test FM5T3HP. Ice accretion area within region 3 on the flat plate specimen at test temperature −5 °C.

E.4 Surface Temperature 0 °C

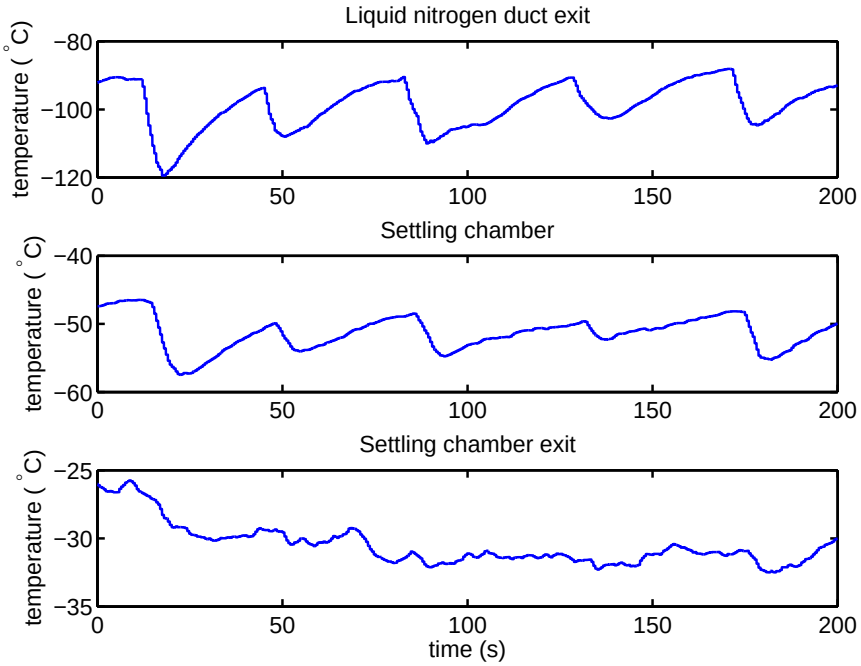

Figure E.36: Test F0T1HP. Temperatures within the facility upstream of the wind tunnel duct. Specimen temperature 0 °C.

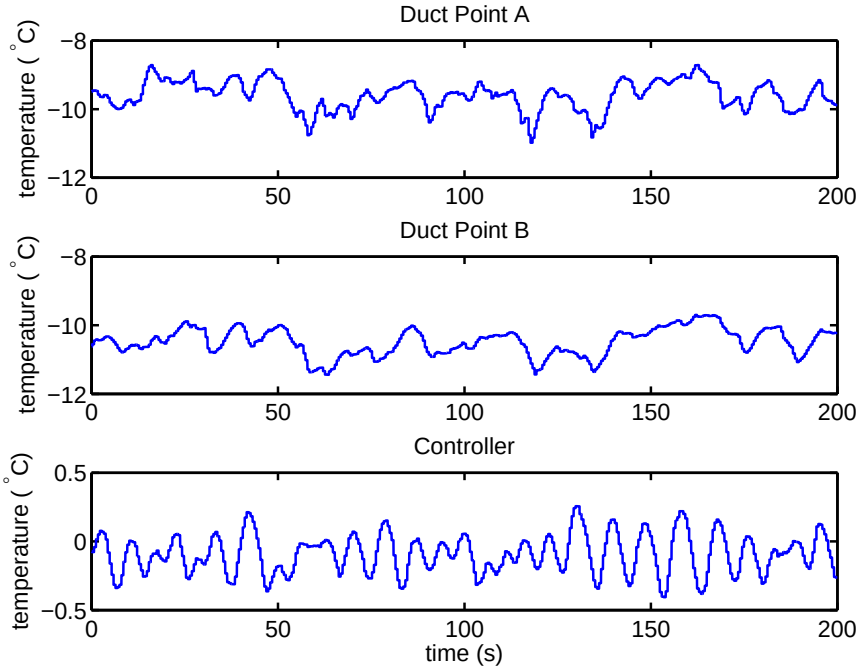

Figure E.37: Test F0T1HP. Temperatures within the wind tunnel duct for the test specimen temperature of 0 °C.

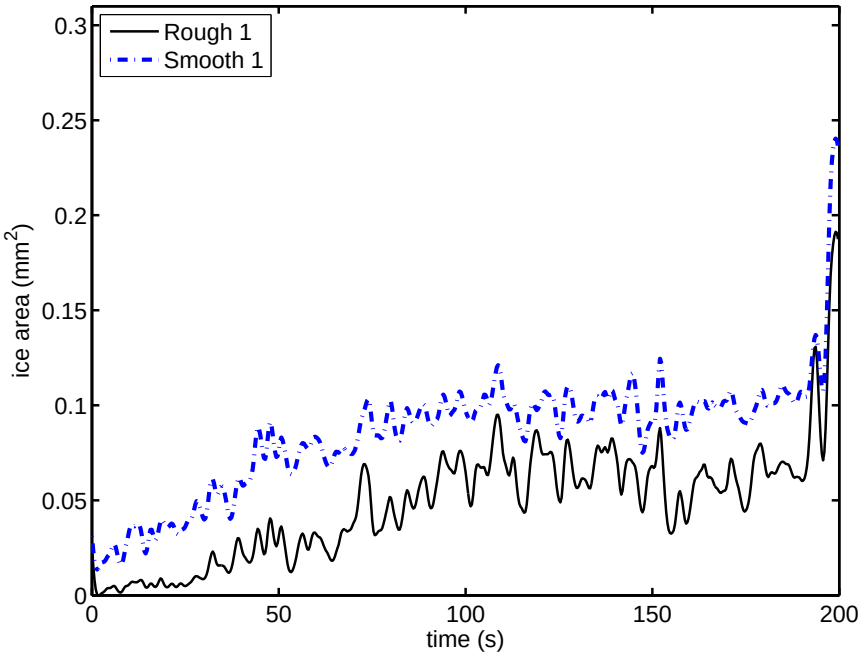

Figure E.38: Test F0T1HP. Ice accretion area within region 1 on the flat plate specimen at test temperature 0 °C.

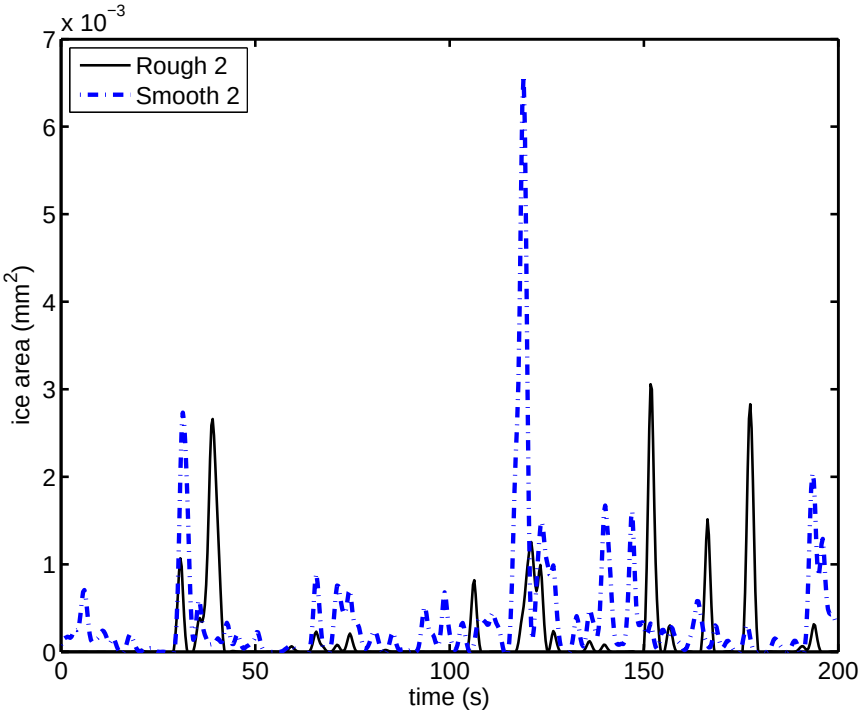

Figure E.39: Test F0T1HP. Ice accretion area within region 2 on the flat plate specimen at test temperature 0 °C.

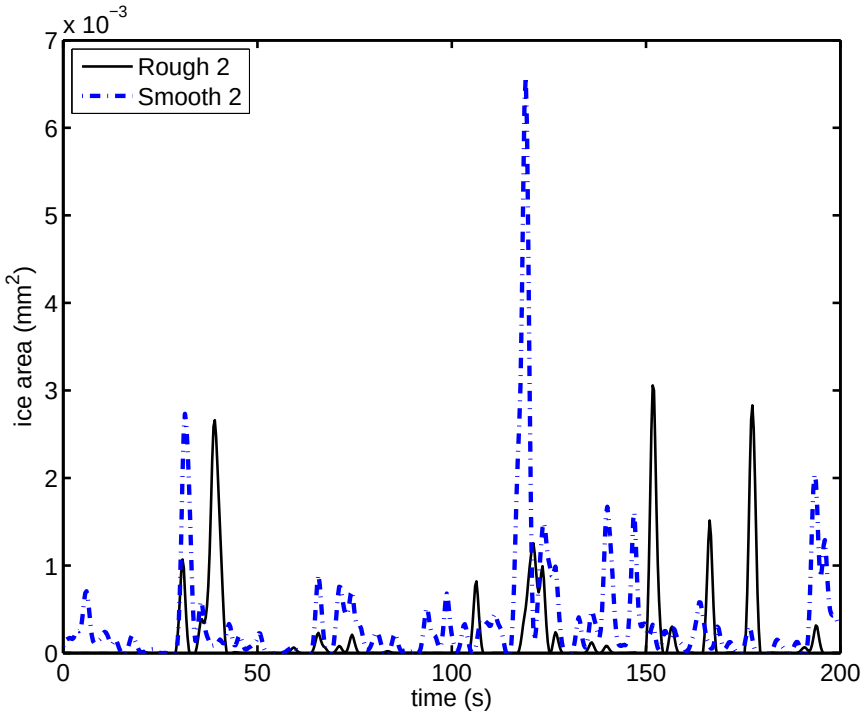

Figure E.40: Test F0T1HP. Ice accretion area within region 3 on the flat plate specimen at test temperature 0 °C.

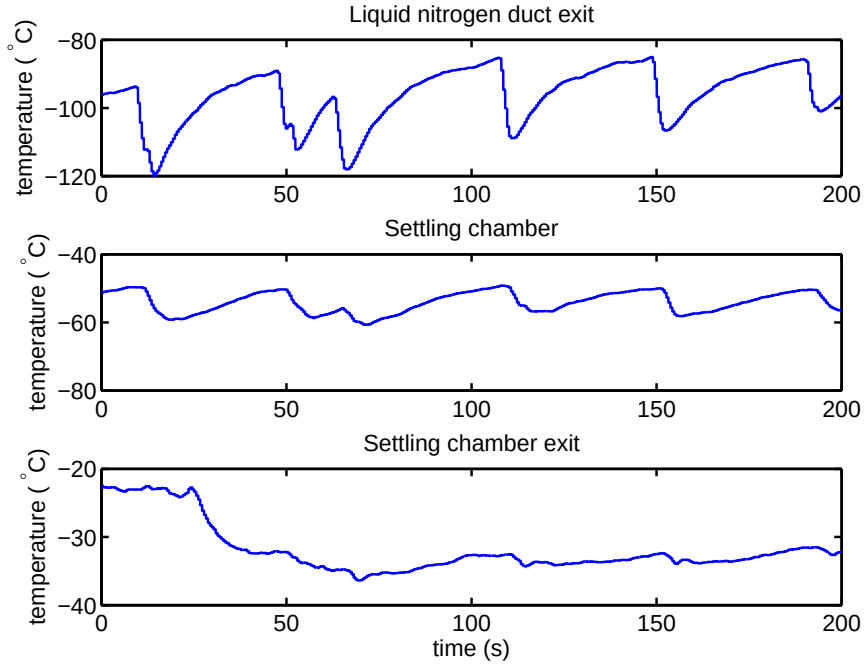

Figure E.41: Test F0T2HP. Temperatures within the facility upstream of the wind tunnel duct. Specimen temperature 0 °C.

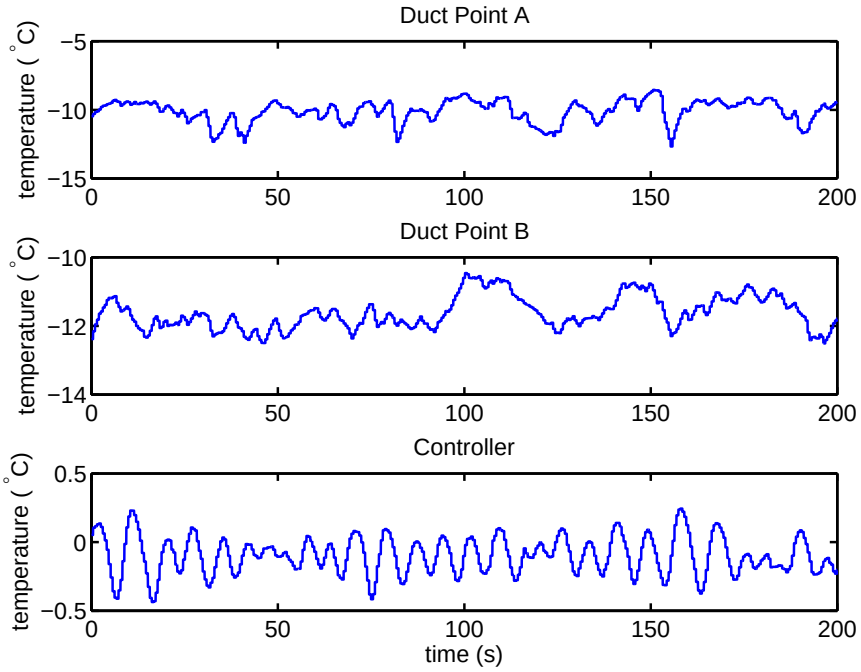

Figure E.42: Test F0T2HP. Temperatures within the wind tunnel duct for the test specimen temperature of 0 °C.

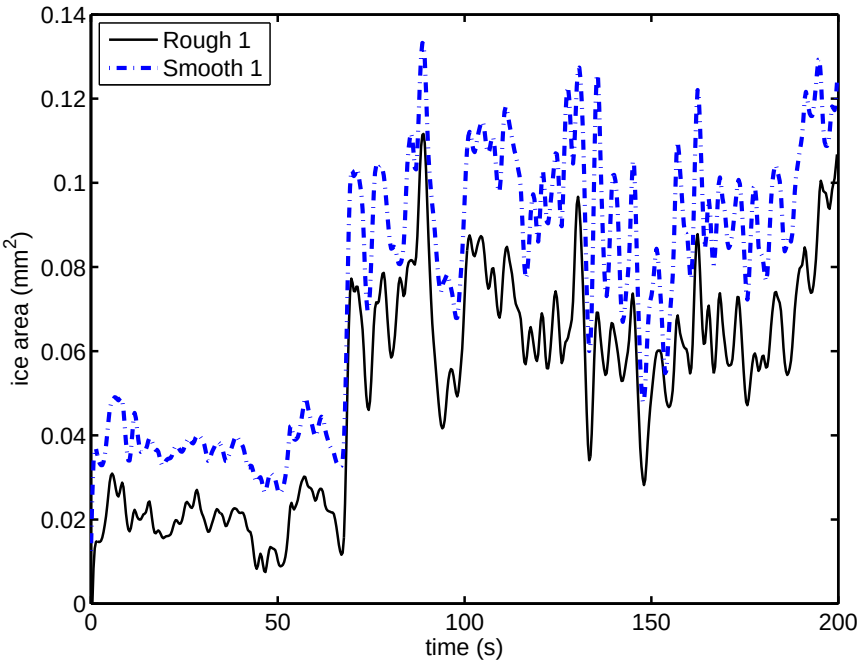

Figure E.43: Test F0T2HP. Ice accretion area within region 1 on the flat plate specimen at test temperature 0 °C.

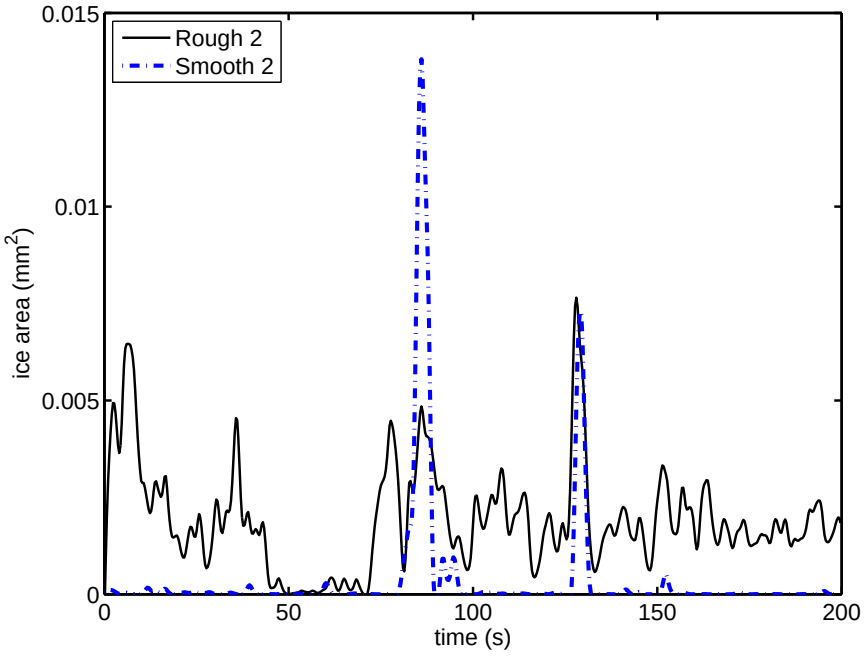

Figure E.44: Test F0T2HP. Ice accretion area within region 2 on the flat plate specimen at test temperature 0 °C.

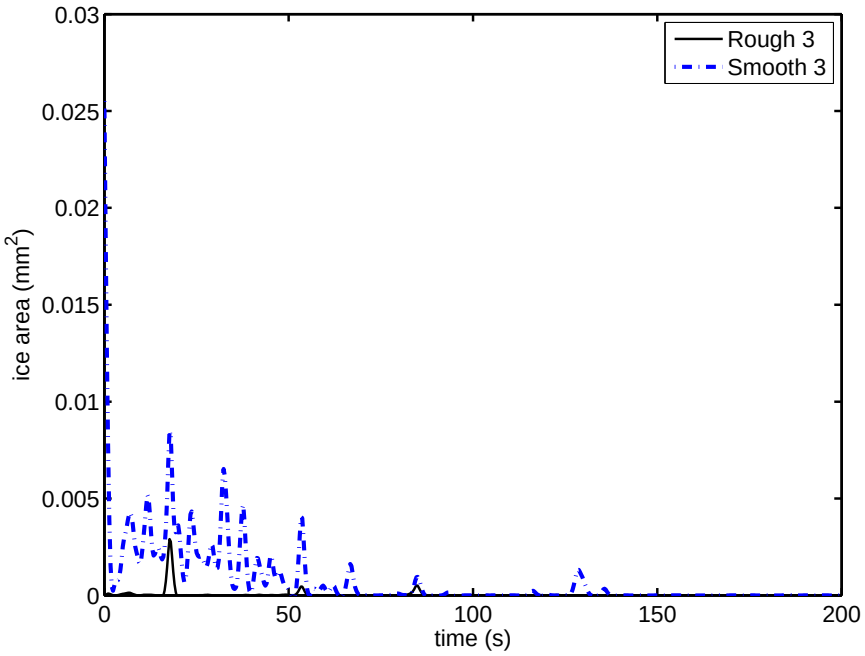

Figure E.45: Test F0T2HP. Ice accretion area within region 3 on the flat plate specimen at test temperature 0 °C.

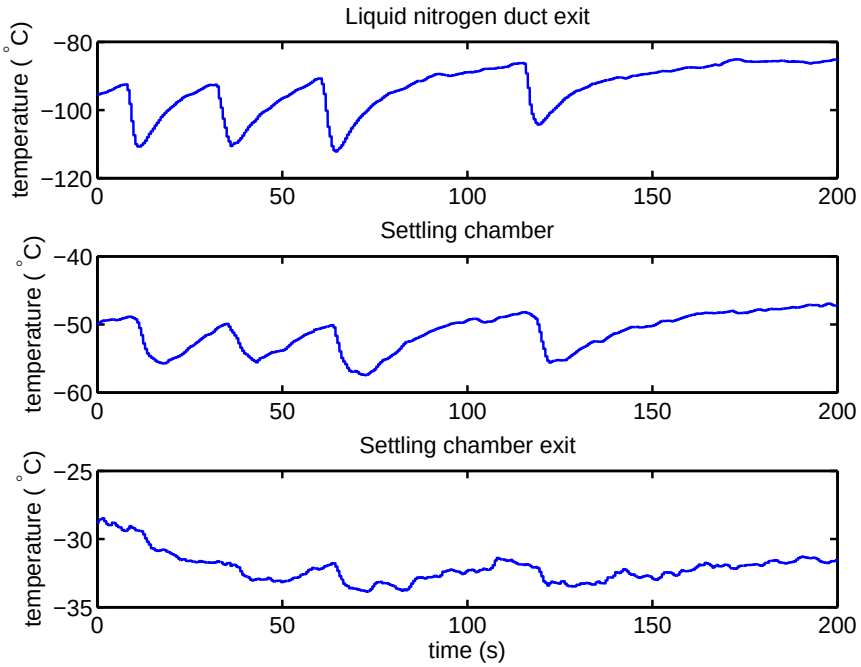

Figure E.46: Test F0T3HP. Temperatures within the facility upstream of the wind tunnel duct. Specimen temperature 0 °C.

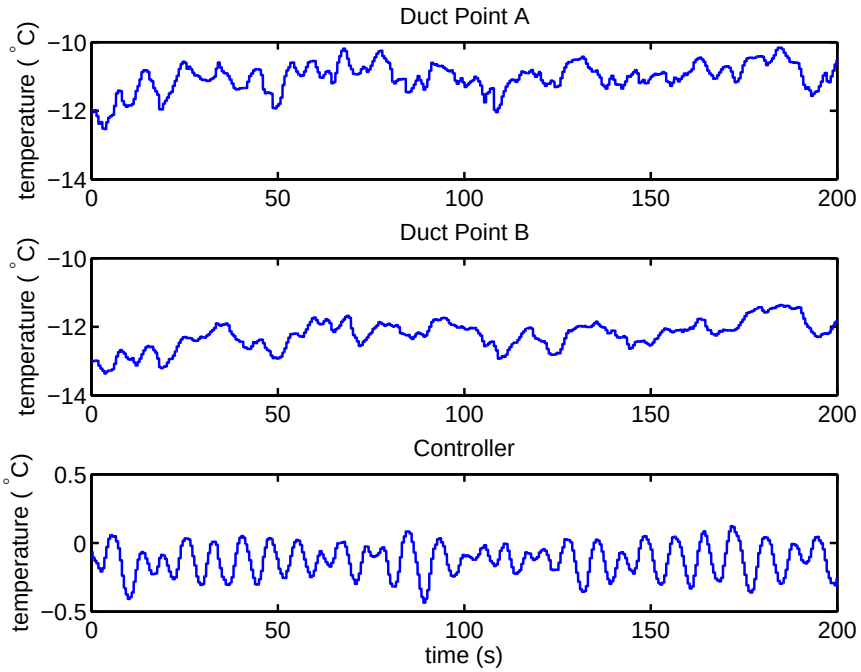

Figure E.47: Test F0T3HP. Temperature data acquisition reading of the specimen area for the surface at test temperature 0 °C.

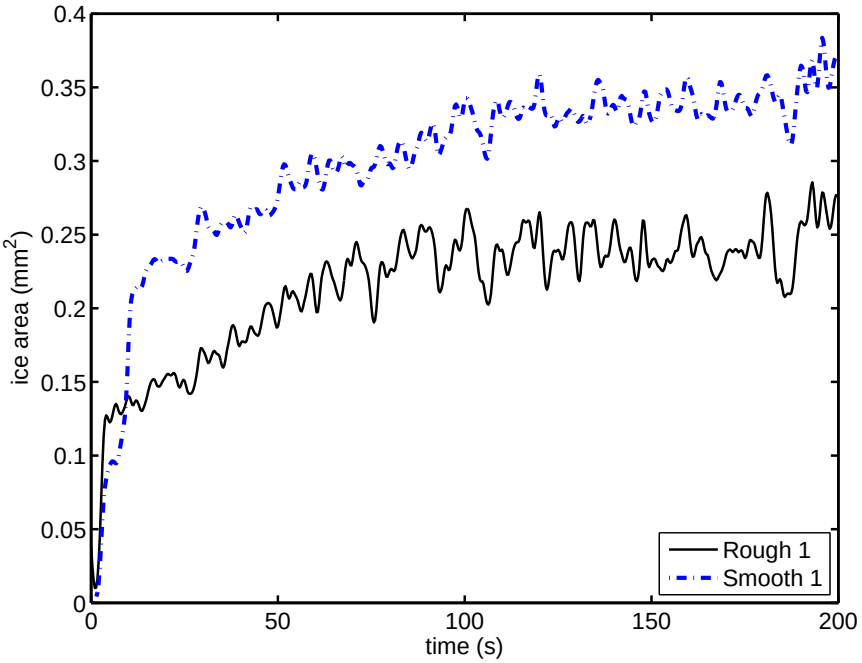

Figure E.48: Test F0T3HP. Ice accretion area within region 1 on the flat plate specimen at test temperature 0 °C.

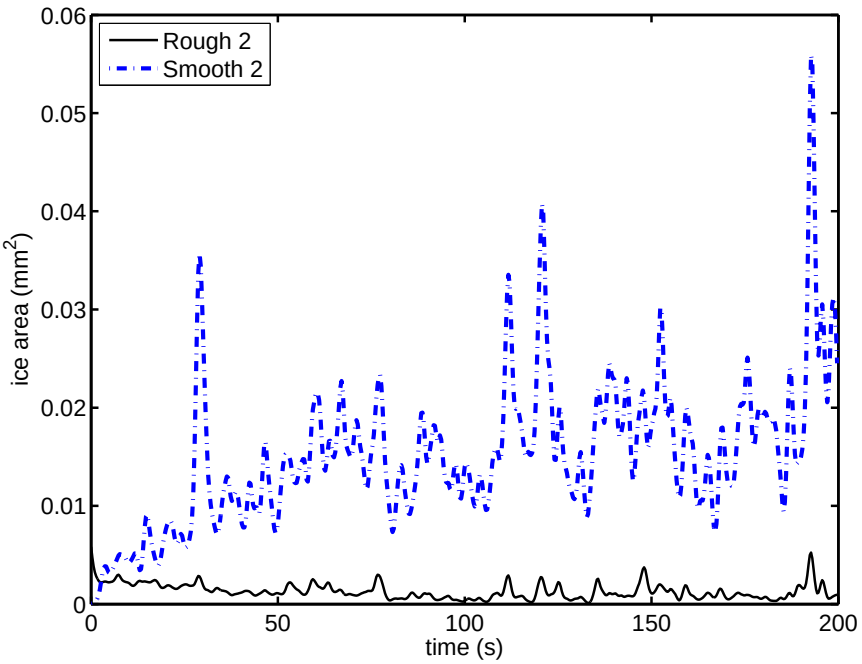

Figure E.49: Test F0T3HP. Ice accretion area within region 2 on the flat plate specimen at test temperature 0 °C.

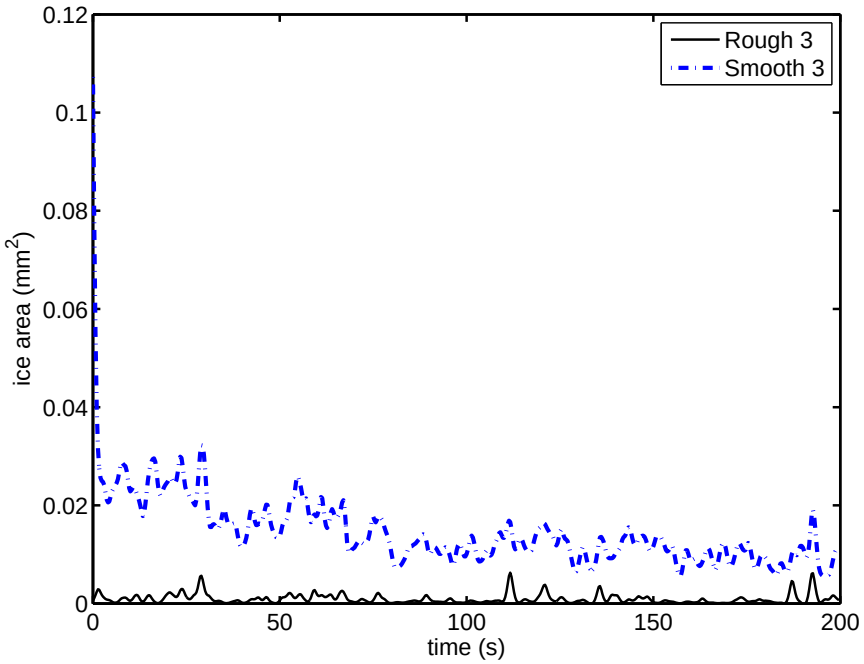

Figure E.50: Test F0T3HP. Ice accretion area within region 3 on the flat plate specimen at test temperature 0 °C.

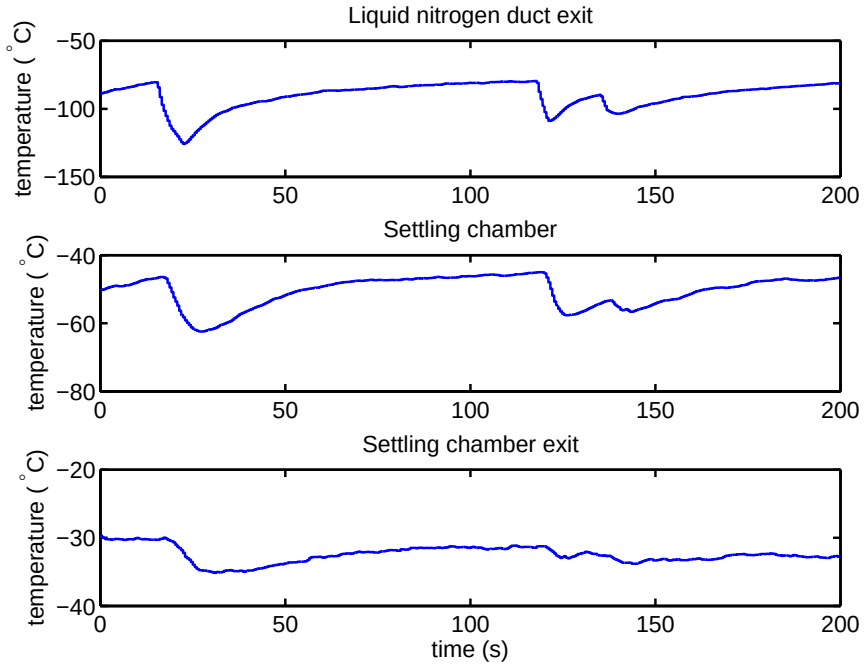

Figure E.51: Test F0T4HP. Temperatures within the facility upstream of the wind tunnel duct. Specimen temperature 0 °C.

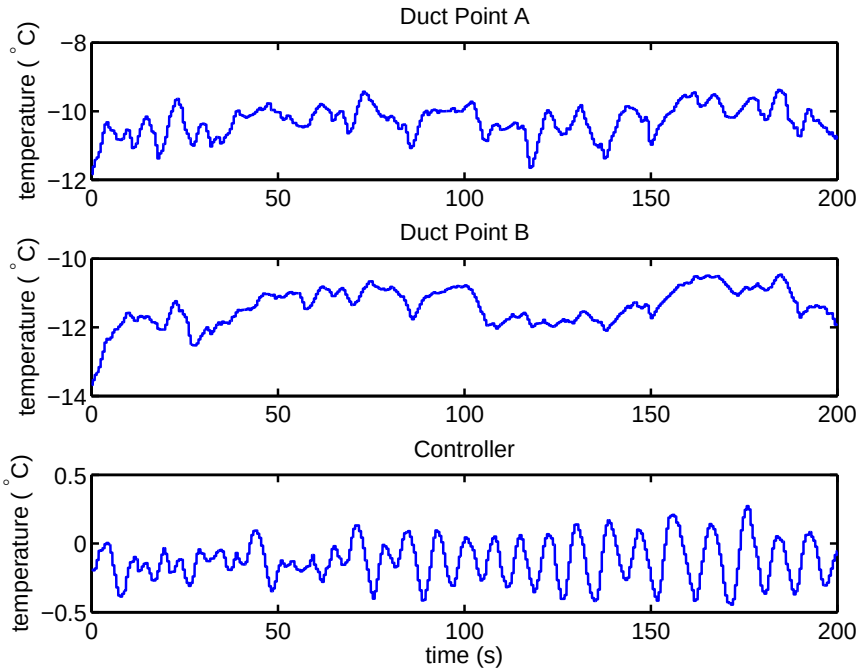

Figure E.52: Test F0T4HP. Temperatures within the wind tunnel duct for the test specimen temperature of 0 °C.

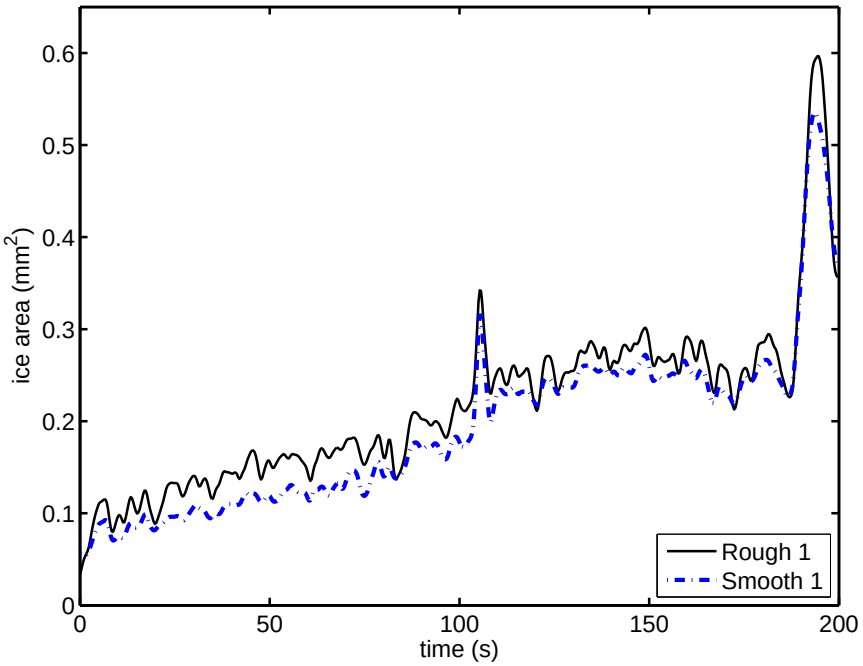

Figure E.53: Test F0T4HP. Ice accretion area within region 1 on the flat plate specimen at test temperature 0 °C.

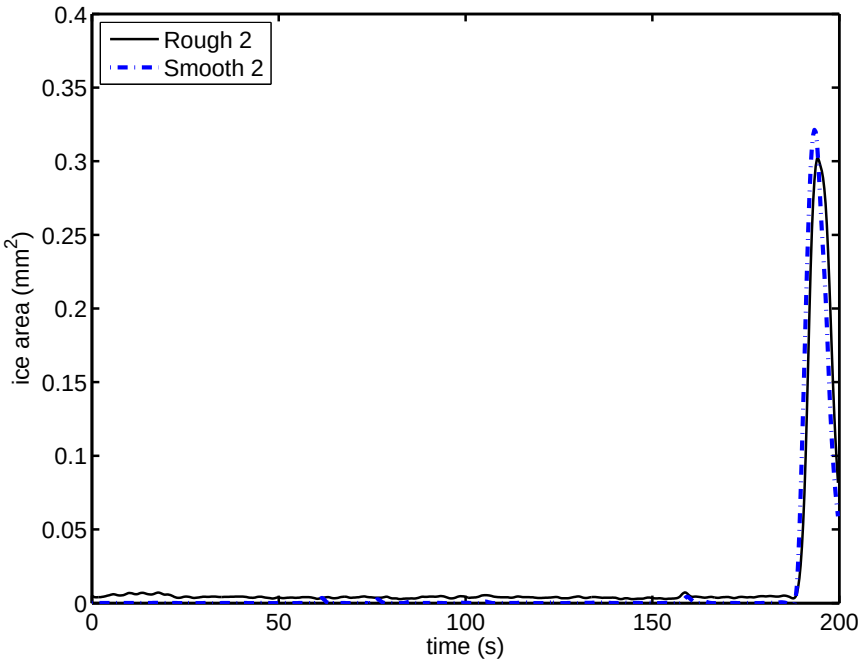

Figure E.54: Test F0T4HP. Ice accretion area within region 2 on the flat plate specimen at test temperature 0 °C.

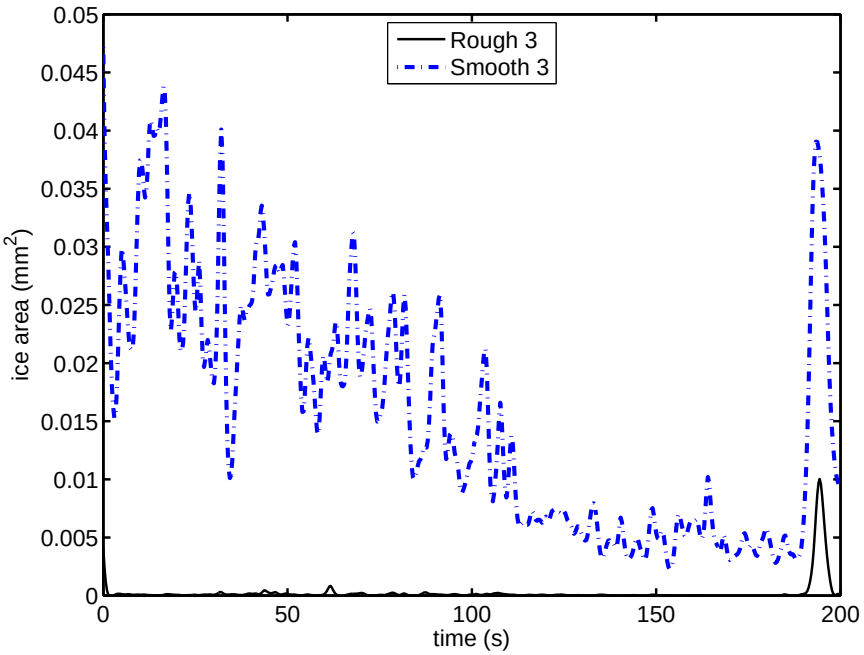

Figure E.55: Test F0T4HP. Ice accretion area within region 3 on the flat plate specimen at test temperature 0 °C.

E.5 Surface Temperature 5 °C

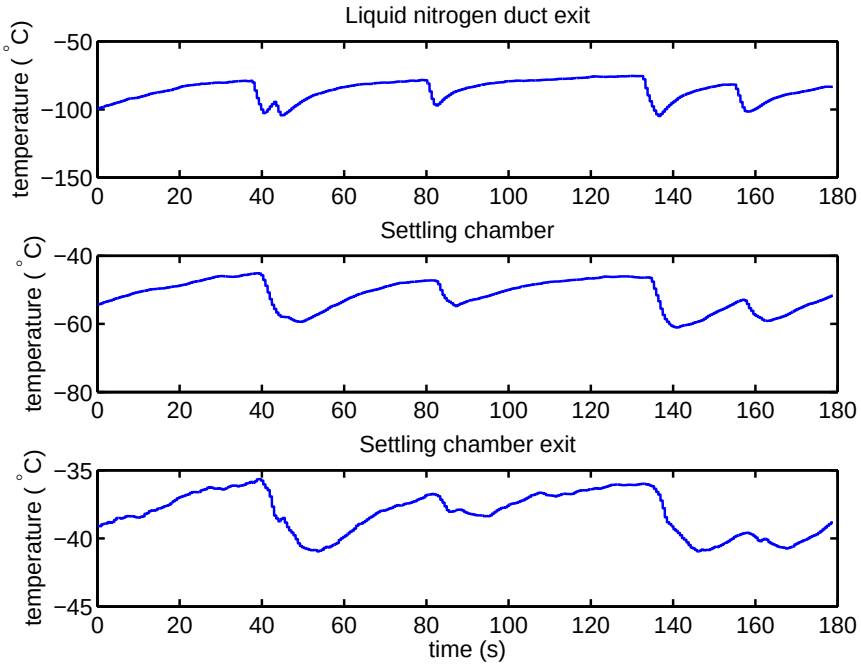

Figure E.56: Test FP5T1HP. Temperatures within the facility upstream of the wind tunnel duct. Specimen temperature 5 °C.

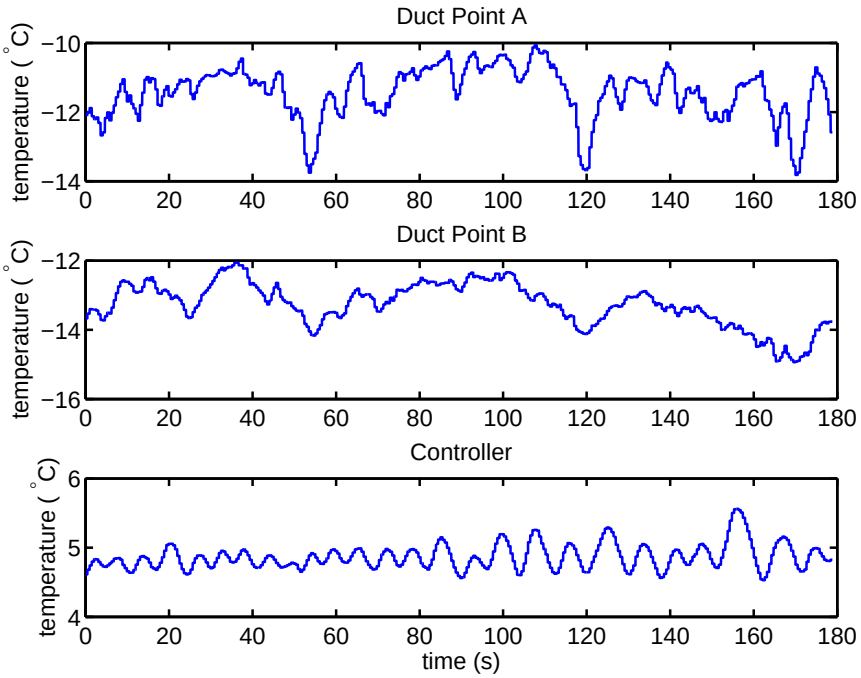

Figure E.57: Test FP5T1HP. Temperatures within the wind tunnel duct for the test specimen temperature of 5 °C.

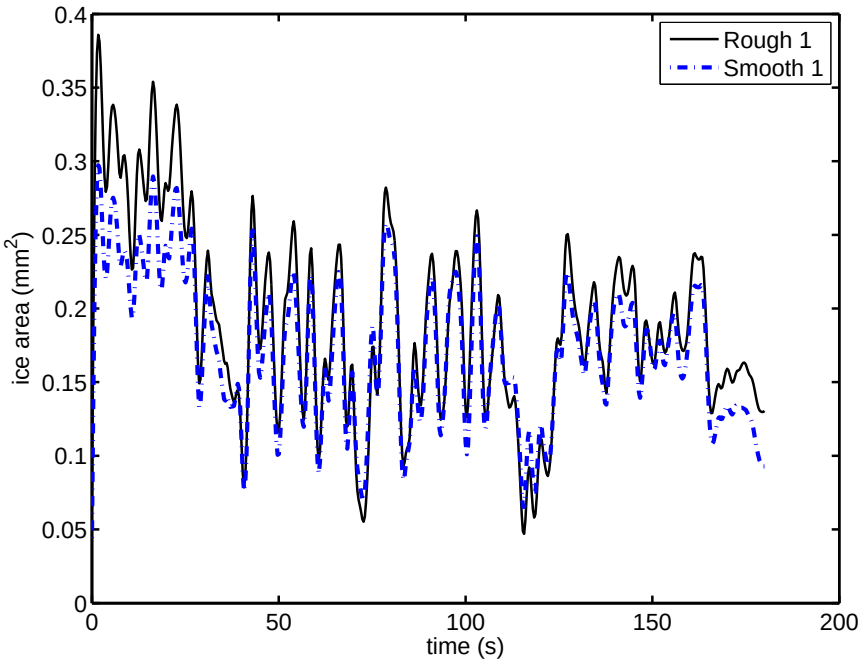

Figure E.58: Test FP5T1HP. Ice accretion area within region 1 on the flat plate specimen at test temperature 5 °C.

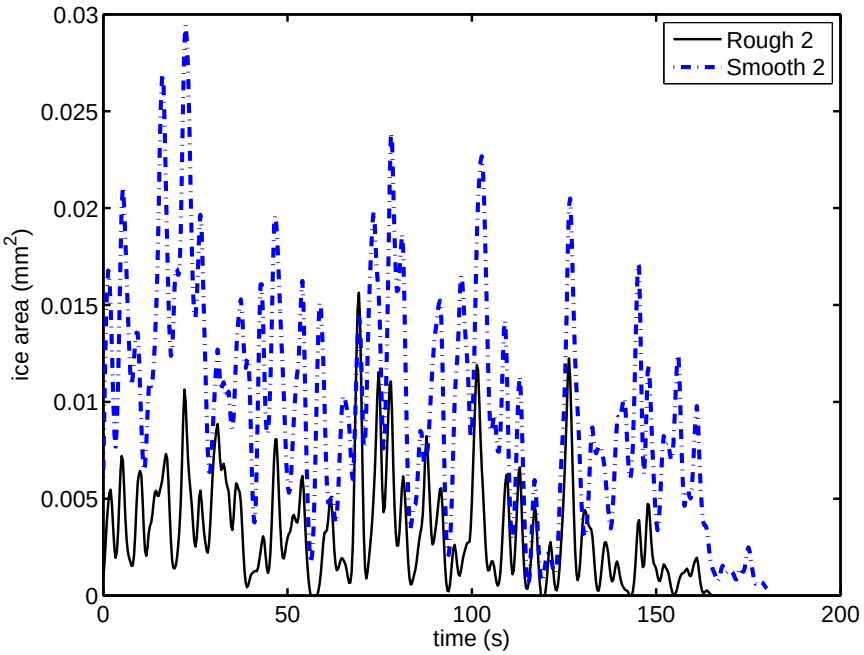

Figure E.59: Test FP5T1HP. Ice accretion area within region 2 on the flat plate specimen at test temperature 5 °C.

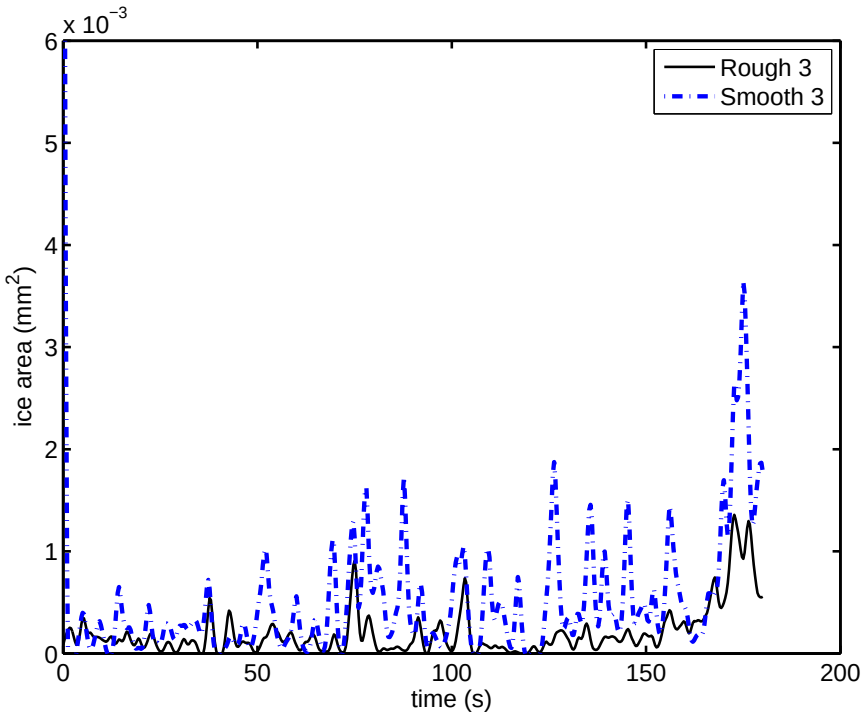

Figure E.60: Test FP5T1HP. Ice accretion area within region 3 on the flat plate specimen at test temperature 5 °C.

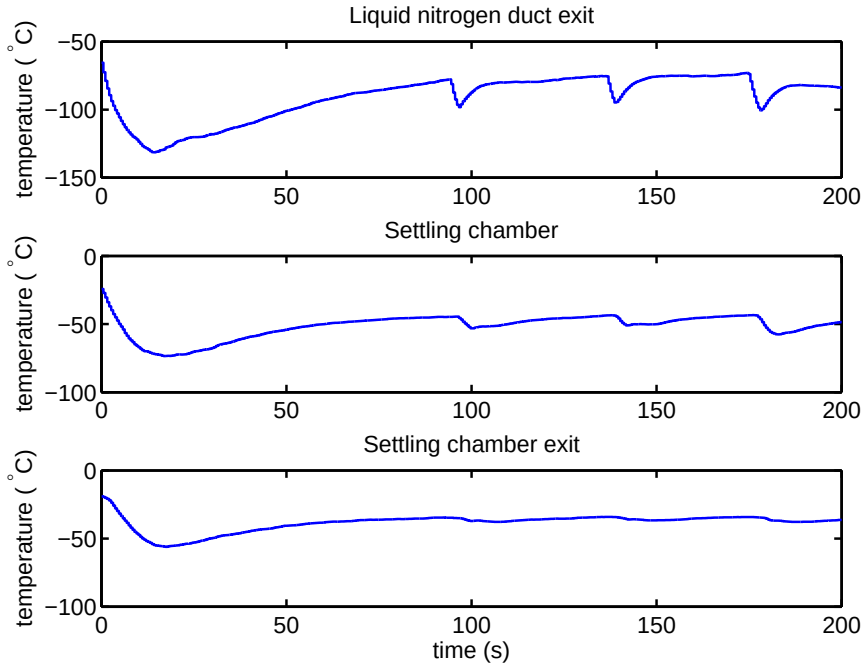

Figure E.61: Test FP5T2HP. Temperatures within the facility upstream of the wind tunnel duct. Specimen temperature 5 °C.

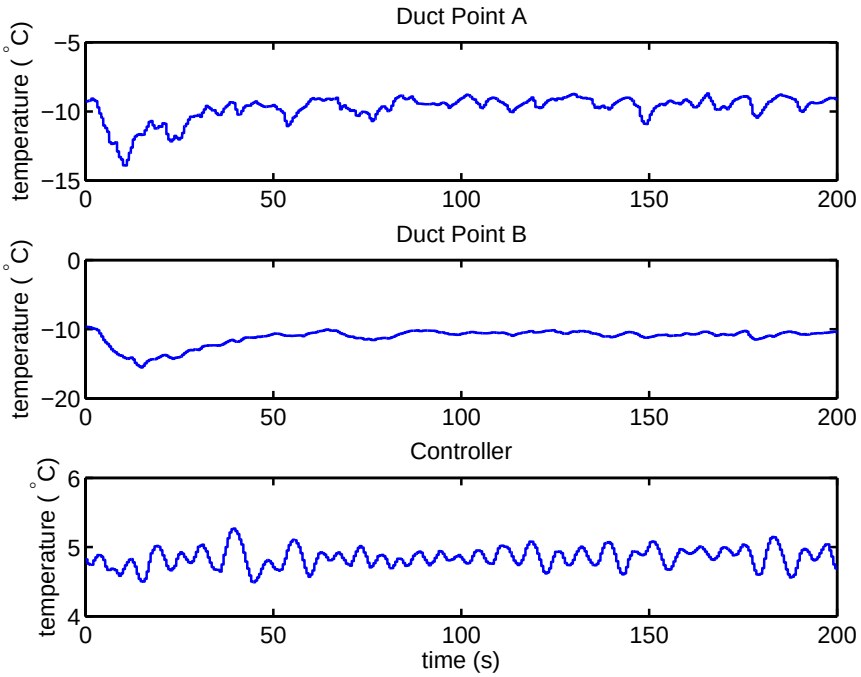

Figure E.62: Test FP5T2HP. Temperatures within the wind tunnel duct for the test specimen temperature of 5 °C.

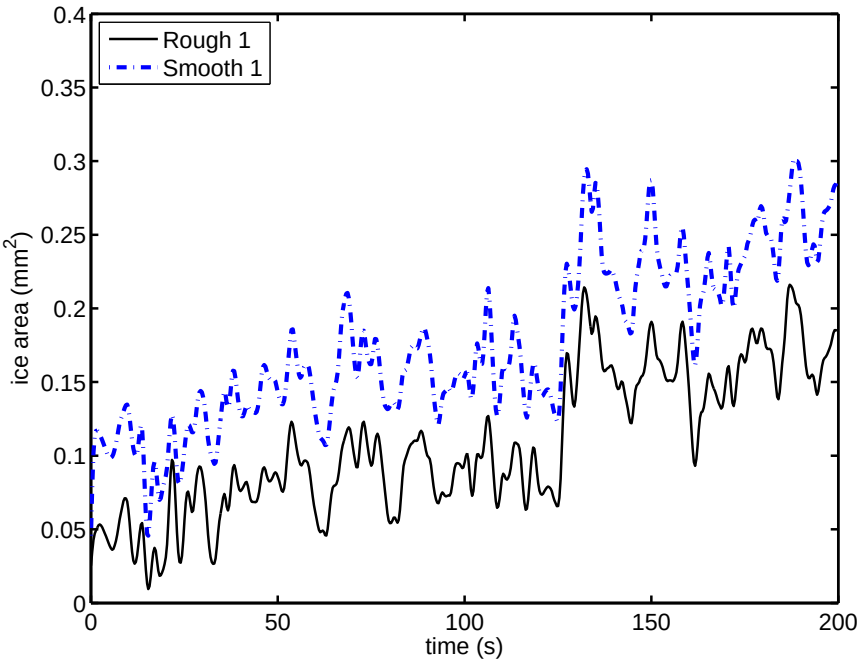

Figure E.63: Test FP5T2HP. Ice accretion area within region 1 on the flat plate specimen at test temperature 5 °C.

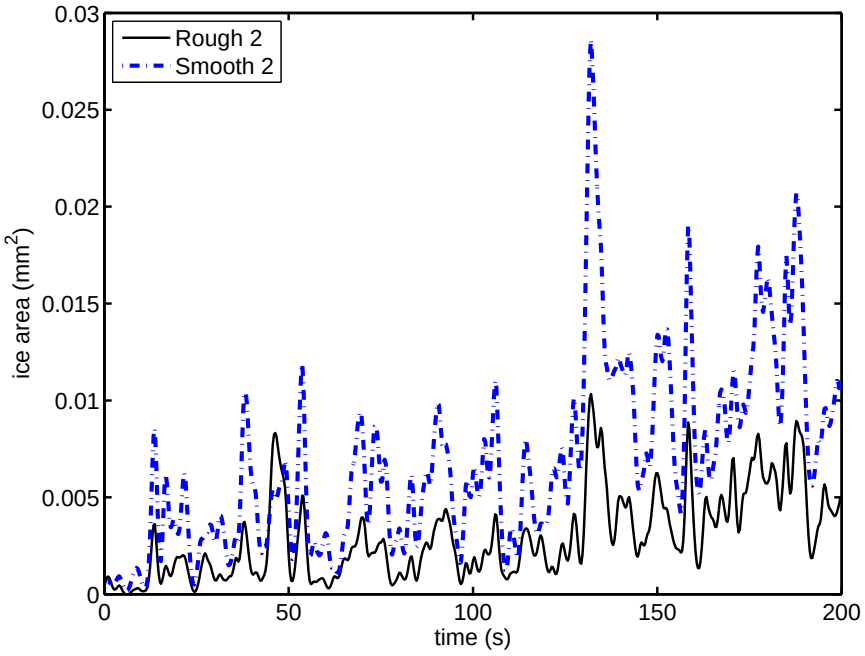

Figure E.64: Test FP5T2HP. Ice accretion area within region 2 on the flat plate specimen at test temperature 5 °C.

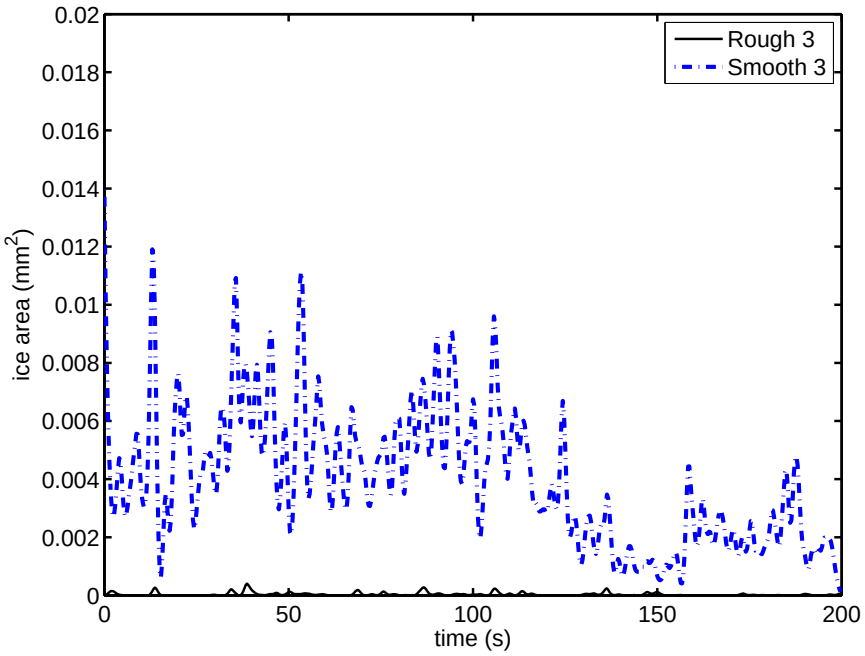

Figure E.65: Test FP5T2HP. Ice accretion area within region 3 on the flat plate specimen at test temperature 5 °C.

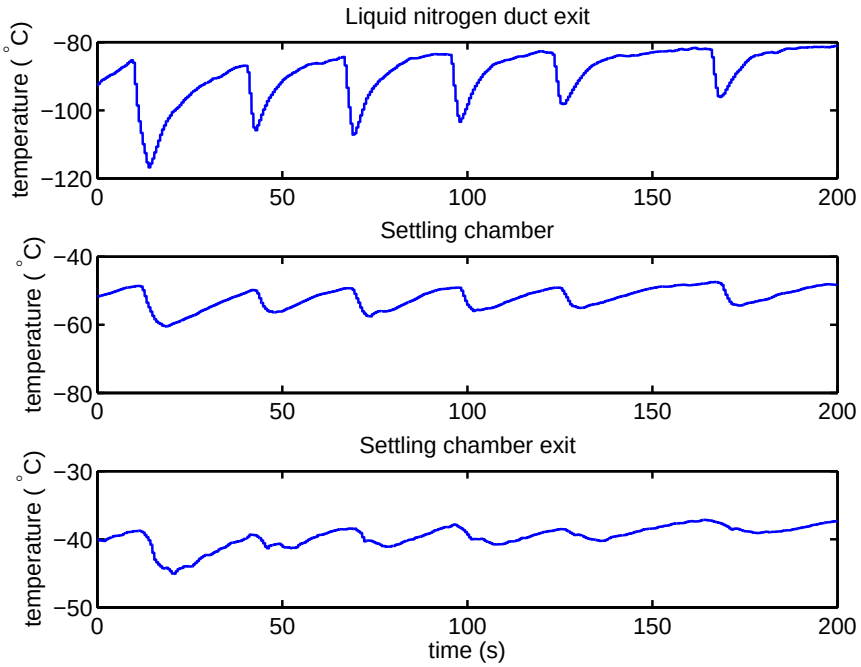

Figure E.66: Test FP5T3HP. Temperatures within the facility upstream of the wind tunnel duct. Specimen temperature 5 °C.

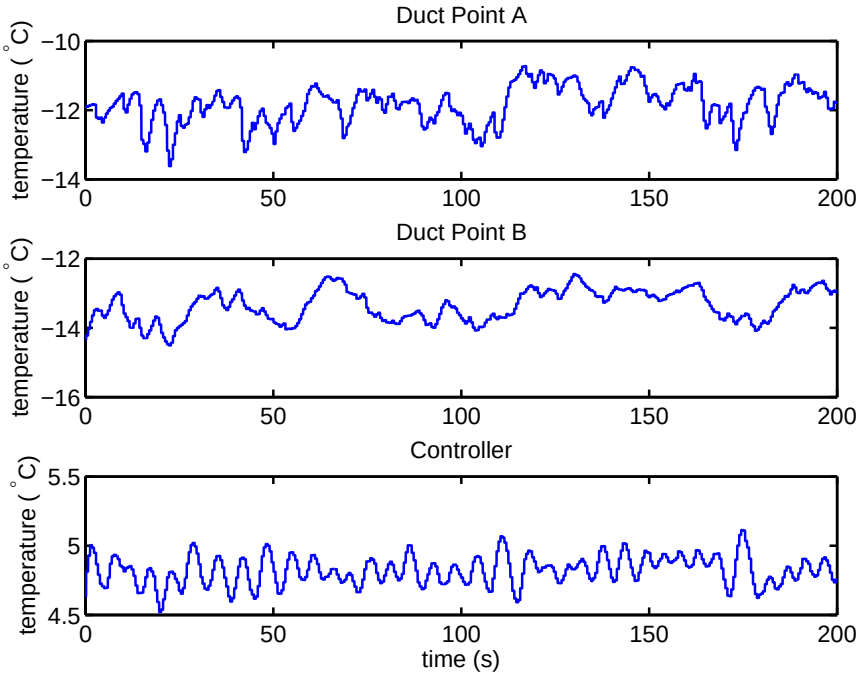

Figure E.67: Test FP5T3HP. Temperatures within the wind tunnel duct for the test specimen temperature of 5 °C.

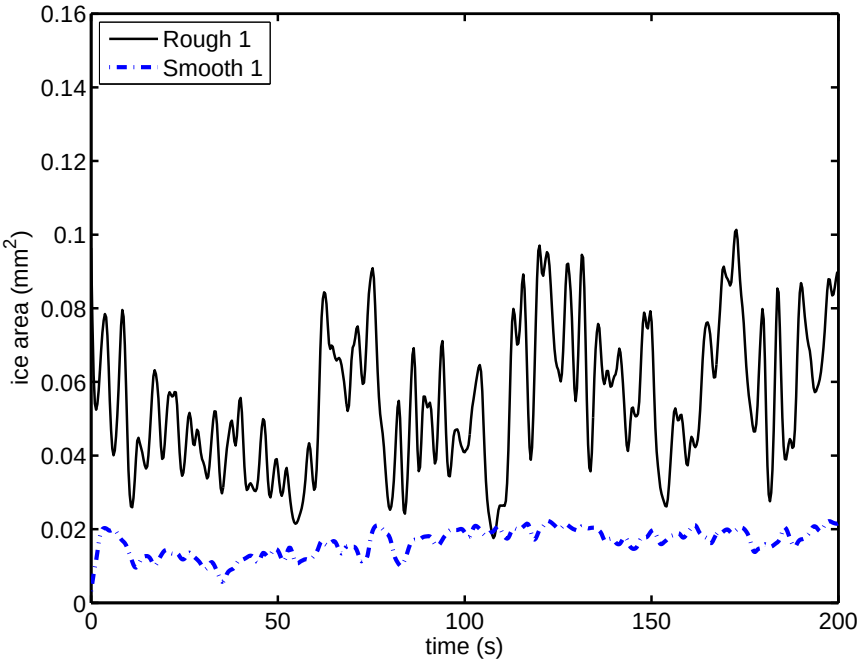

Figure E.68: Test FP5T3HP. Ice accretion area within region 1 on the flat plate specimen at test temperature 5 °C.

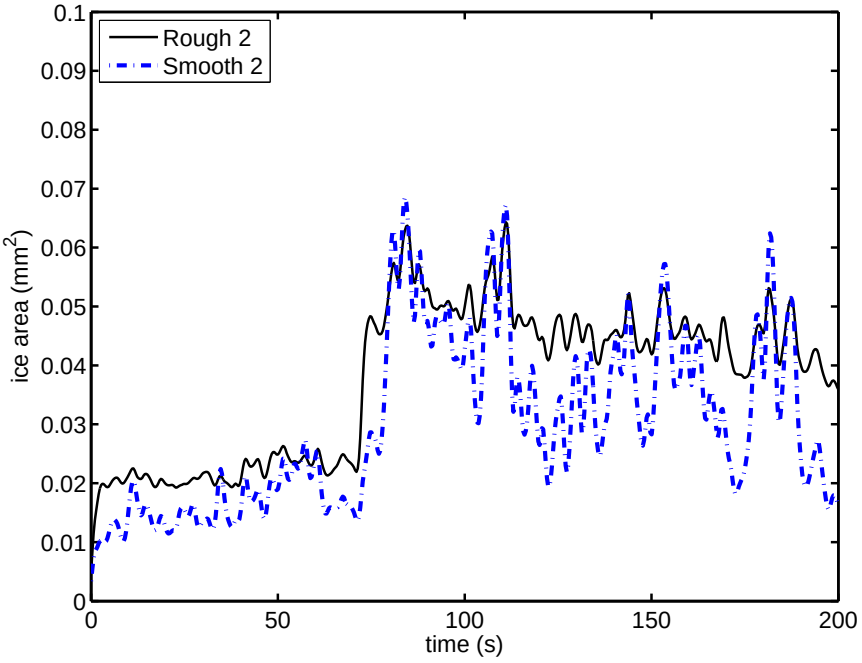

Figure E.69: Test FP5T3HP. Ice accretion area within region 2 on the flat plate specimen at test temperature 5 °C.

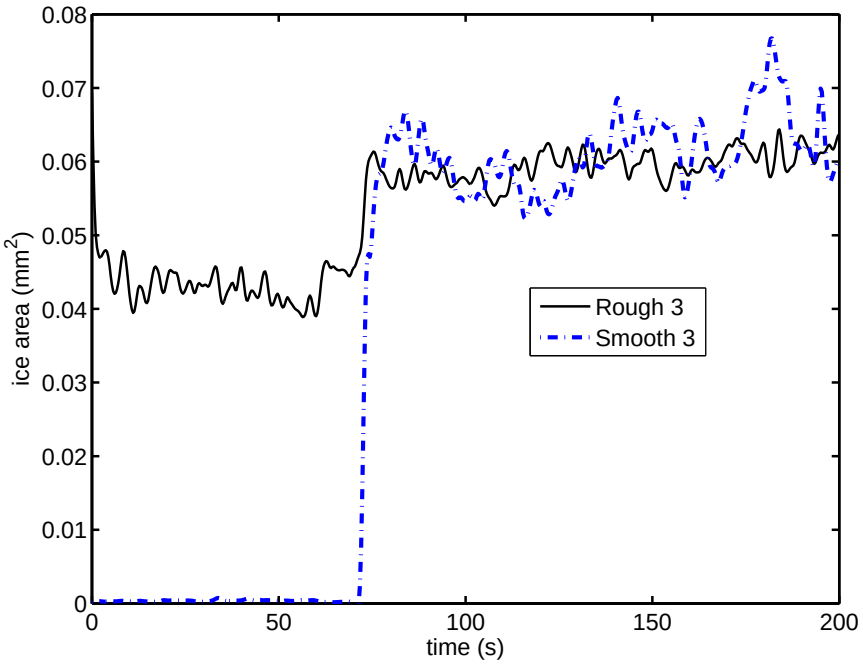

Figure E.70: Test FP5T3HP. Ice accretion area within region 3 on the flat plate specimen at test temperature 5 °C.